THE UNIVERSITY OF CALGARY

Fractures in Weak Snowpack Layers in Relation to Slab Avalanche Release

by

Alec François Guillaume van Herwijnen

A THESIS
SUBMITTED TO THE FACULTY OF GRADUATE STUDIES
IN PARTIAL FULFILLMENT OF THE REQUIREMENTS FOR THE
DEGREE OF DOCTOR OF PHILOSOPHY

DEPARTMENT OF CIVIL ENGINEERING

CALGARY, ALBERTA

February, 2005

UNIVERSITY OF CALGARY

FACULTY OF GRADUATE STUDIES

The undersigned certify that they have read, and recommend to the Faculty of Graduate Studies for acceptance, a thesis entitled "Fractures in Weak Snowpack Layers in Relation to Slab Avalanche Release" submitted by Alec François Guillaume van Herwijnen in partial fulfillment of the requirements for the degree of Doctor in Philosophy.

Supervisor, Dr. Bruce Jamieson
Department of Civil Engineering

Dr. Shawn Marshall
Department of Geography

Dr. Nigel Shrive
Department of Civil Engineering

Dr. Rob Stewart
Department of Geology and Geophysics

External examiner Dr. Ian McCammon
Snowpit Technologies

Date

Abstract

The vast majority of recreational avalanche incidents are caused by human-triggering of the slab avalanche. Specific snowpack characteristics, including hardness difference and difference in crystal size across the failure layer, associated with skier-triggered dry slab avalanches were identified. The relation of these snowpack variables with fracture initiation and fracture propagation, both of which are required for skier-triggering, was investigated. The properties of the slab overlying the weak layer, as well as the layer above the weak layer, were found to be important for fracture propagation in that the slab supplies the energy necessary to propagate the fracture through the weak layer. A classification system for fractures in stability tests was assessed. It was shown that incorporating such a descriptive classification system can improve the interpretation of these test results. Sudden fractures are more often the failure layer of slab avalanches than other fractures. Specific snowpack characteristics associated with the different fracture characters showed that sudden fractures are typically associated with snowpack conditions favouring both fracture initiation and fracture propagation. *In-situ* fractures in weak snowpack layers were photographed at 250 frames per second in 39 field tests. Displacement measurements of markers placed in the snow above weak layers showed that slope normal displacement (due to crushing of the weak layer) was observed in each fracture. The speed of propagating fractures was measured, ranging from 17 to 26 m/s. These observations were used to assess theoretical slab release models, suggesting that the fracture of the weak layer is coupled to a propagating flexural wave in the overlying slab that controls the speed of propagation.

Acknowledgements

This project would not have been possible without Dr. Bruce Jamieson, who provided guidance, training, funding, proofreading and countless very helpful discussions. I would like to acknowledge Crane Johnson for paving the road for the current research on fracture propagation. I thank Joachim Heierli for kindly sharing his work on fracture propagation. Many thanks to Antonia Zeidler, Cam Campbell and Dave Gauthier for great proofreading.

For collecting data for this project over the years, I owe thanks to all technicians and graduate students for their tireless digging: Ken Black, Cam Campbell, Tom Chalmers, Owen David, Joe Filippone, Michelle Gagnon, Ryan Gallagher, Torsten Geldsetzer, Brian Gould, Sue Gould, Phil Hein, Jill Hughes, Nick Irving, Crane Johnson, Greg Johnson, Alan Jones, Kalle Kronholm, Paul Langevin, Steve Lovenuik, Greg McAuley, Jennifer Olson, Andrew Rippington, Jordy Shepherd, Kyle Stewart, Ilya Storm, Adrian Wilson and Antonia Zeidler.

For daily advice and many good snow talks, I thank the Avalanche Control Section in Glacier National Park: Tom Chalmers, Eric Dafoe, Dean Flick, Jeff Goodrich, John Kelly, Bruce McMahon, Jim Phillips, Johan Schleiss, David Skjonsberg and Steve Thomas.

For their encouragement and support I would like to thank my parents, Otto and Anne-Marie van Herwijnen, my brother and sister and all my friends. Finally, I would like to thank Peggy Klein Klouwenberg for her patience and support over these years.

This thesis is part of an ongoing University-Industry Project funded by the BC

Helicopter and Snowcat Skiing Operators Association (BCHSSOA), the Natural Sciences and Engineering Research Council of Canada, Mike Wiegele Helicopter Skiing, Canada West Ski Areas Association (CWSAA) and the Canadian Avalanche Association. The supporting member of the BCHSSOA include Baldface Mountain Lodge, Bella Coola Heli Sports, Black Tusk Helicopter Inc., Canadian Mountain Holidays, Cariboo Snowcat Skiing and Tours, Cat Powder Skiing, Chatter Creek Mountain Lodges, Coast Range Helskiing, Crescent Spur Heli-skiing, Great Canadian Heli-skiing, Great Northern Snow Cat Skiing, Highland Powder Skiing, Island Lake Resort Group, Klondike Heliskiing, Last Frontier Heliskiing, Mica Heli Guides, Monashee Powder Adventures, Northern Escape Heli-skiing, Peace Reach Adventures, Powder Mountain Snowcats, Purcell Helicopter Skiing, R.K. Heli-Skiing, Retallack Alpine Adventures, Robson Helimagic, Selkirk Tangiers Heli-Skiing, Selkirk Wilderness Skiing, Snowwater Heli-skiing, TLH Heli-skiing, Valhalla Powdercats, Whistler Heli-Skiing and White Grizzly Adventures. The supporting members of Canada West Ski Areas Association include Apex Mountain Resort, Banff Mount Norquay, Big White Ski Resort, Hemlock Ski Resort, Intrawest Corporation, Kicking Horse Mountain Resort, Mt. Washington Alpine Resort, Silver Star Mountain Resorts, Ski Marmot Basin, Sun Peaks Resort, Sunshine Village, Whistler Blackcomb, Whitewater Ski Resort, and Resorts of the Canadian Rockies including Skiing Louise, Nakiska, Kimberley Alpine Resort and Fernie Alpine Resort.

Table of Contents

List of Tables

List of Figures

List of Symbols and abbreviations

1F	One finger (hand hardness)
$2L$	Length of shear band or deficit zone
4F	Four fingers (hand hardness)
a_c	Critical crack size
ASARC	Applied Snow and Avalanche Research, University of Calgary
a_x	Slope parallel marker acceleration
$a_{x_{max}}$	Maximum slope parallel marker acceleration
a_y	Slope normal marker acceleration
$a_{y_{max}}$	Maximum slope normal marker acceleration
B	Break (fracture character)
B_{slab}	Bridging index of the slab
CAA	Canadian Avalanche Association
CB	Cantilever beam
CCD	Charge-Coupled Device
Char	Fracture character
CR	Crusts
CT	Compression test
D	Depth measured vertically
d	Marker separation distance
DF	Decomposed and fragmented crystals
DH	Depth hoar
DHE	Drop hammer energy
DTT	Deep tap test
E	Crystal size
Ed	Edge of block (release type)
$\mathcal{E}$	Young's modulus
F	Fist (hand hardness)
FC	Faceted crystals
FFT	Fast Fourier transform
FPT	Fracture propagation test

$\mathcal{G}$	Shear modulus
g	Gravitational acceleration
H	Hand hardness ($H = 2^{h-1}$)
$\mathcal{H}$	Slab thickness measured perpendicular to the slope
h	Hand hardness index
I	Ice
K	Knife (hand hardness)
La	Layer above a particular snowpack layer (used as subscript)
Lb	Layer below a particular snowpack layer (used as subscript)
M	Most of block (release type)
N	Number of data
N_*	Width of moving average filter
NF	No fracture (fracture character)
P	Pencil (hand hardness)
p	Significance level
PC	Progressive compression (fracture character)
PP	Precipitation particles
Q1	First quartile
Q2	Second quartile
RG	Rounded Grains
RB	Rutschblock
RP	Resistant planar (fracture character)
R_p	Pearson product moment correlation coefficient
R_s	Spearman Rank order correlation coefficient
SC	Sudden collapse (fracture character)
SH	Surface hoar
SL	Snowpack layer
SP	Sudden planar (fracture character)
Storm	Storm snow layers (PP, DF and RG)

t	time
Th	Layer thickness
u_*	Cut-off frequency for low-pass FFT filter
V	Fracture speed estimate from avalanche video recorded with a standard video camera
v_x	Slope parallel marker speed
$v_{x_{max}}$	Maximum slope parallel marker speed
v_y	Slope normal marker speed
$v_{y_{max}}$	Maximum slope normal marker speed
$V_{\Delta x_*}$	Fracture speed obtained for slope parallel displacement $\Delta x_i(t) = \Delta x_*$
$\overline{V_{\Delta x}}$	Fracture speed obtained by averaging $V_{\Delta x_*}$ for a range of Δx_* values
$V_{\Delta y_*}$	Fracture speed obtained for slope normal displacement $\Delta y_i(t) = \Delta y_*$
$\overline{V_{\Delta y}}$	Fracture speed obtained by averaging $V_{\Delta y_*}$ for a range of Δy_* values
W	Whole block (release type)
WG	Wet grains
WL	Weak layer (used as subscript)
x	Slope parallel coordinate
X_0	Initial slope parallel position of marker
y	Slope normal coordinate
Y_0	Initial slope normal position of marker
ΔE_{La}	Difference in average crystal size between a particular snowpack layer and the layer above
ΔE_{Lb}	Difference in average crystal size between a particular snowpack layer and the layer below
Δh_{La}	Difference in hand hardness index with the layer above
Δh_{Lb}	Difference in hand hardness index with the layer below
Δt	Time between two frames ($= \frac{1}{250}$ s)
Δx	Slope parallel displacement
Δx_*	Given slope parallel displacement for fracture speed calculation
$\Delta x_i(t)$	Slope parallel displacement with time for Marker i
Δx_{max}	Maximum slope parallel displacement
Δy	Slope normal displacement
Δy_*	Given slope normal displacement for fracture speed calculation
$\Delta y_i(t)$	Slope normal displacement with time for Marker i

Δy_{max}	Maximum slope normal displacement
ϵ	Accuracy of displacement measurements
γ	Shear strain
ρ	Density
λ	Wavelength
ψ	Slope angle
Σ	Shear strength
τ	Shear stress
ν	Poisson's ratio
ω	Size of end zone of shear band

Chapter 1

Introduction

Each winter the snow returns to the mountains and so do avalanches. In Canada most snow avalanches have no effect on people, structures or roads. The majority start in the backcountry without human involvement. Avalanches do become a problem when there is potential to injure humans or damage property. The winter of 2003 was a cruel reminder of the destructive power of avalanches. It was the deadliest winter in history for recreationists in western Canada, with 29 avalanche-related fatalities. Over the last century, the number of avalanche victims on roads or in buildings has decreased significantly, whereas the number of avalanche victims during recreational activities has risen. However, Jamieson and Geldsetzer (1996: 7) note that the increase in recreational avalanche fatalities is low in proportion to the increase in people using the backcountry. This trend is likely the result of an increase in the knowledge of avalanches leading to better avalanche education and better pubic warning systems.

Since most recreationists rely on public avalanche bulletins for backcountry avalanche conditions, the ability to predict avalanche potential accurately for these bulletins is paramount. Studies on avalanche accidents show that the victims often trigger the avalanche themselves (Jamieson and Geldsetzer, 1996: 10), showing the importance of forecasting skier-triggered avalanches. Avalanche forecasters use a variety of information to determine the avalanche hazard, ranging from weather observations to snowpack information. This study is on field observations of fractures in

weak snowpack layers, with an emphasis on skier-triggered avalanches and fracture propagation, and therefore deals with the latter.

As explained later (Section 1.1), weak snow layers play an essential role in avalanching. The stability of a snowpack is largely dependent on the existence and the strength of weak layers, but also depends on slab properties and layering of the snowpack (e.g. Schweizer and Jamieson, 2001). Snowpack conditions must be favourable for fracture initiation and fracture propagation, both of which are required for slab avalanche release (Schweizer et al., 2003). Although there have been significant improvements in the understanding of snowpack properties affecting human-triggering, there is still a lack of physical understanding, supported by field measurements, on the complex interaction of various snowpack parameters and their relation to fracture initiation and especially fracture propagation. Furthermore, over the last few decades several theoretical models have been proposed to physically describe avalanche release (e.g. McClung, 1981; Bader and Salm, 1990). However, the only measurement on fracture propagation in a weak snow layer on low angle terrain (Johnson et al., 2004) was not in accordance with these models.

For this thesis, snowpack properties from snow profiles and stability tests affecting skier triggering were investigated. Furthermore, a partly new method was used to study fractures in weak snowpack layers through use of a portable high speed camera, providing direct observations of fractures in weak snowpack layers. Before formulating the objectives of this thesis, an overview of relevant snowpack processes, avalanche characteristics and snowpack tests is given.

1.1 The mountain snowpack

Snow crystals form in the atmosphere either by deposition of water vapour onto small particles or by accretion of super-cooled water droplets. Different shapes of crystals result from variations in temperature and supersaturation in the atmosphere (McClung and Schaerer, 1993: 37). The most common form is a stellar crystal with six arms (Figure 1.1a). Precipitation from multiple storms (snow or rain) throughout a winter produces a layered snowpack.

When snow is deposited it typically has a density of 40-100 kg m^{-3} (e.g. Keeler and Weeks, 1968). Wind may fragment the crystals forming relatively dense layers. Once on the ground, the properties of snow change significantly to build up a temporally variable snowpack. Apart from densification of the snow layers due to settlement of the snowpack, there are three main metamorphic processes that change the microstructure, and thus the mechanical properties of layers: rounding, faceting and melt-freeze metamorphism.

First, in the absence of a strong temperature gradient, typically less than 10^oC m^{-1}, freshly fallen dry snow will begin to decompose into rounded crystals (Figure 1.1b). The initial forms - usually dendritic - change into smaller particles, to reduce their specific surface, followed by the slow growth of larger particles at the expense of the smaller particles. This process, called rounding or equilibrium metamorphism, is associated with intergranular bonding and the gain of strength (Perla and Sommerfeld, 1987). Rounding is common when snowpack temperatures are at or below 0^oC and is faster when temperatures are close to the melting point. Usually, equilibrium metamorphism contributes to stability of the snowpack.

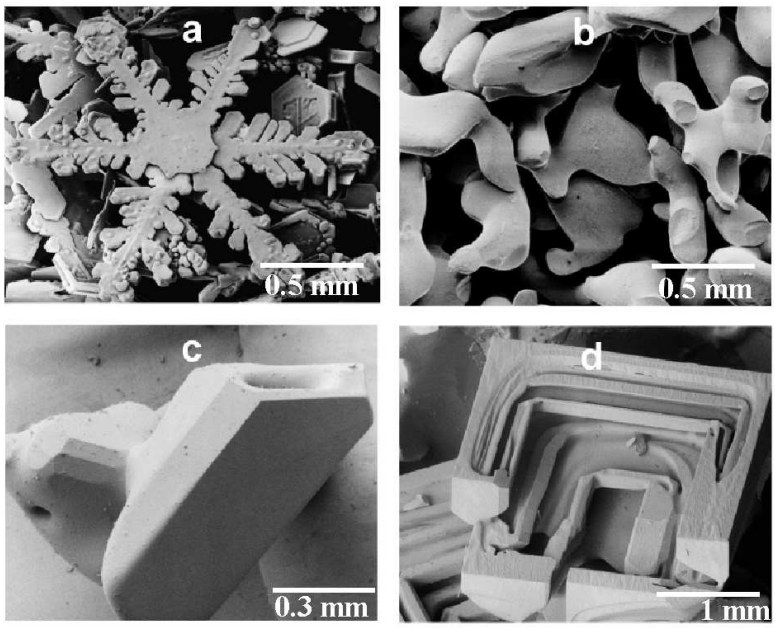

Figure 1.1: *Examples of snow crystals: a. Stellar snow crystal, b. Rounded snow crystals, c. Faceted snow crystal, d. Depth hoar. From http://emu.arsusda.gov/*

Faceting metamorphism, or kinetic growth, usually occurs when the temperature gradient is greater than about 10 K m^{-1} (Akitaya, 1974). This causes water vapour to move from warm to cold, usually upward through the snowpack. The water vapour is deposited as ice on the cooler surface of crystals, normally the bottom. Larger grains grow at the expense of smaller ones. Typically, decomposed fragments or rounded grains will grow into faceted crystals, characterized by flat faces and angular crystals (Figure 1.1c). If the strong temperature gradient persists, depth hoar, consisting of larger striated or hollow crystals, will form (Figure 1.1d). At typical densities, faceting metamorphism does not promote intergranular bonding and is therefore often associated with slow gain of strength, if any.

Rounding and faceting are metamorphic processes that occur in dry snow, with temperatures below 0°C. Melt-freeze metamorphism, on the other hand, is a result

of temperature cycles around 0^oC. It occurs when snow melts due to warm temperatures, rain or solar radiation. Liquid water assembles in concave areas (lower surface tension) and freezes to produce rounded forms. Again, smaller grains tend to disappear whereas larger grains tend to grow. Melt-freeze metamorphism is most relevant in spring and is not considered in this thesis.

Energy exchange between the snow surface and the atmosphere is another important process that can lead to the formation of surface hoar crystals, the solid equivalent of dew (McClung and Schaerer, 1993: 31). These relatively larger crystals (Figure 1.2) usually form on cold, relatively clear nights with light or no wind. The snow surface experiences radiant cooling causing water vapour from the air to deposit on the snow surface. When buried by subsequent snowfalls, layers of surface hoar can remain weak for an extended period of time, often playing an important role in avalanche formation. In the Columbia Mountains of Canada, surface hoar growth is relatively common during the winter months. Two to five buried surface hoar weak layers per winter can often be observed, and skiers can trigger avalanches on these weak layers for weeks after burial. Chalmers (2001) reports that the majority of avalanche activity on these layers typically occurs within the first 30 days after burial. In Figure 1.2 (b), a buried surface hoar weak layer is shown that is fractured on the left side of the photograph.

It is clear that a mountain snowpack can contain many different snow layers with distinctive properties. Some layers are weaker than the layers above and below, and more often associated with slab avalanching (Section 1.2). These layers are termed weak layers. Weak layers can be grouped into non-persistent and persistent weak layers (Jamieson and Johnston, 1992a).

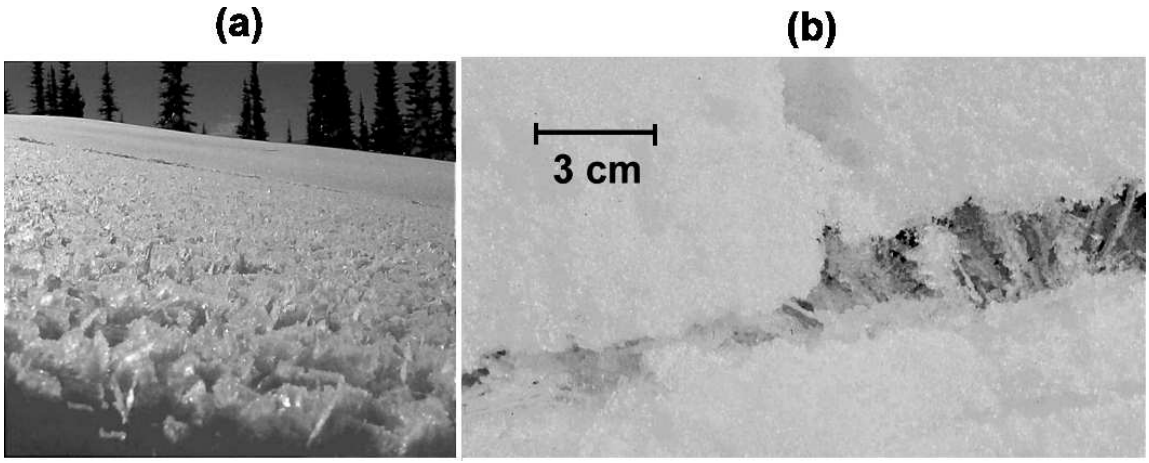

Figure 1.2: *Surface hoar produces persistent weak layer. (a) Surface hoar crystals for on the snow surface (Applied Snow and Avalanche Research University of Calgary (ASARC) photo). (b) A weak layer of buried surface hoar crystals that partly fractured (ASARC photo).*

Non-persistent weak layers, or storm snow instabilities, usually consist of precipitation particles which may remain weaker and lower in density than the adjacent layers during the initial stages of rounding. These layers tend to stabilize within a few days after burial, hence the name non-persistent. Skier-triggered avalanches on non-persistent weak layers are often less harmful to skiers because the avalanches are generally smaller as they typically involve low-cohesion snow and thinner slabs. Jamieson and Johnston (1992a) report that 6% of fatal avalanches in Canada, between 1972 and 1991, involved storm snow instabilities.

Persistent weak layers can remain weak for extended periods of time, sometimes months. All persistent weak layers consist of either surface hoar, faceted crystals or depth hoar. Persistent weak layers are usually referred to by their burial date. If, for instance, surface hoar crystals were buried by a snowfall on the 3rd of January 2002, the weak layer would be known as the 020103 SH layer. Persistent weak layers are

the main concern for skiers with regard to avalanche accidents in Canada (Jamieson and Geldsetzer, 1996). Seventy eight percent of fatal avalanches between 1972 and 1991 occurred on persistent weak layers.

1.2 Avalanche release

There are two types of avalanche release. Point release avalanches are similar to the failure of a cohesionless sand slope (Perla, 1980). The failure originates in one location when a small mass of snow fails and begins to move and entrain additional snow. As the mass descends, the avalanche spreads outwards in an inverted V shape (Figure 1.3a). There are few serious human related incidents caused by point releases.

Slab avalanches behave much differently. A cohesive slab of snow begins to slide before it breaks up (Figure 1.3b). Slab avalanches are the more hazardous of the two types. Jamieson and Johnston (1992a) report that 99% of fatal avalanches in Canada, between 1972 and 1991, were slab avalanches. Slab avalanches are more harmful to skiers because they are typically larger and harder to predict than loose snow avalanches, which typically occur during or soon after storms. On the other hand, skiers can trigger slab avalanches many days after storms, when skiing conditions are generally better. Slab avalanches are the focus of this study.

Some nomenclature with respect to fallen snow slabs has to be defined (Figure 1.4). The term weak layer was introduced earlier. The presence of a weak layer is a necessary, but not sufficient condition for slab avalanche formation (Bader and Salm, 1990). The bed surface is defined as the surface over which the slab slides. The bed surface can be the ground or older snow. The weak layer is always just above the

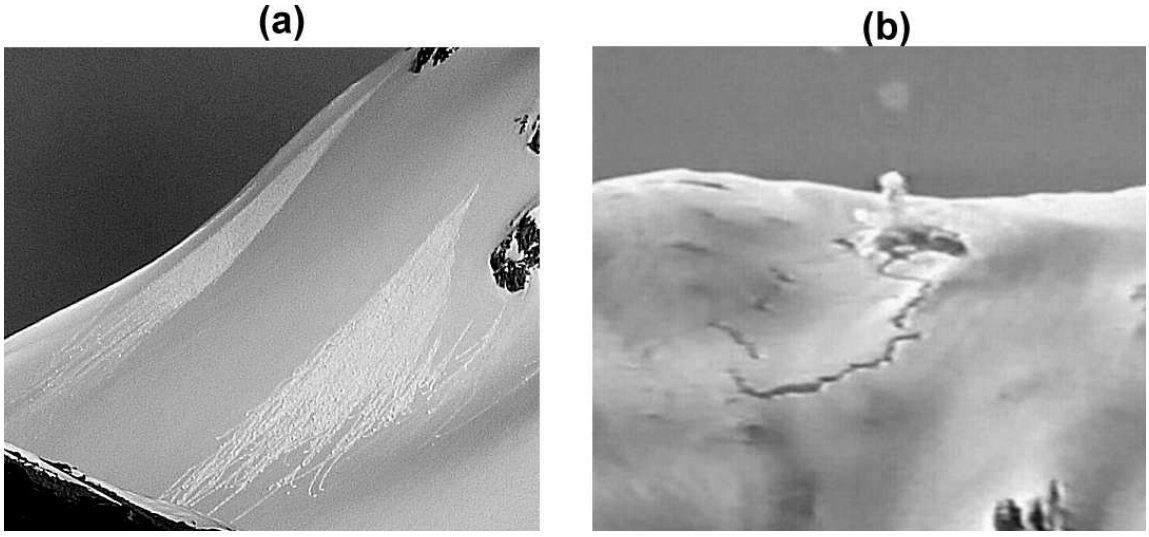

Figure 1.3: *Two types of avalanches: a. Point release avalanche (A. van Herwijnen photo). b. Slab avalanche triggered by an explosive (digitized from educational avalanche video with permission of photographer: Winning the avalanche game, 1994).*

bed surface and just under the slab. The breakaway wall at the top periphery of the slab is called the crown. The flanks are the left and right sides of the slab. The flanks are usually smooth surfaces, as is the crown. The lowest downslope fracture surface is termed the stauchwall.

Most avalanche paths have three distinct parts. The start zone is where the avalanche initiates. The slope angle there is usually between 30 and 50 degrees. The runout zone is where large avalanches decelerate and most of the debris is deposited. The track connects the starting zone with the runout zone. Large avalanches will initiate in the start zone, accelerate through the track and come to a stop in the runout zone. For smaller avalanche paths, the distinct zones are not always obvious.

The release of a slab avalanche requires an initial failure in the weak layer induced by a trigger, which then propagates outwards to release an avalanche. Slab avalanches

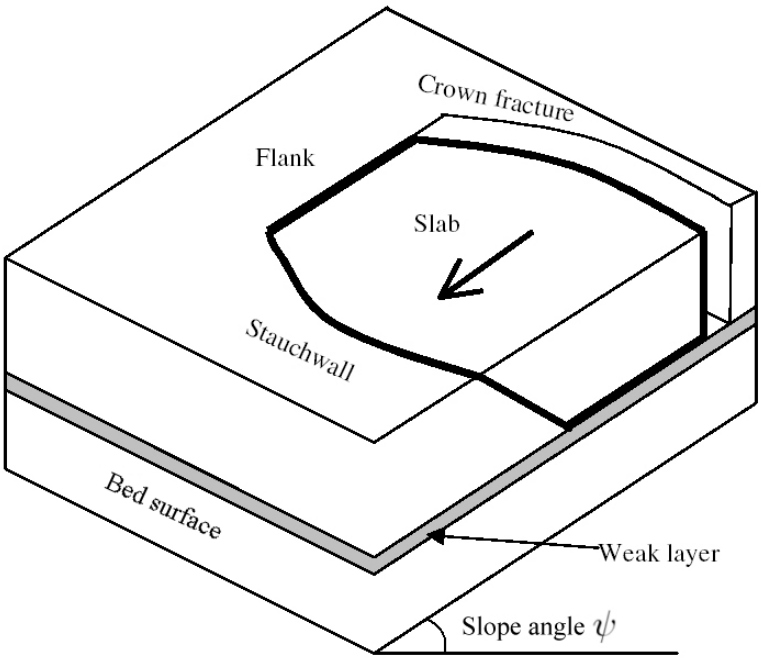

Figure 1.4: *Schematic of a slab avalanche release.*

can be triggered naturally or by an external load, referred to as artificial triggering. Natural triggers include snowfall, rain, changes in temperature and wind. However, at least 90% of recreational avalanche incidents were caused by artificial triggering of the slab avalanche (Jamieson, 2001). Artificial triggers include human inducing, over-snow vehicles and explosives. Three types of human-triggering can be identified: directly triggered, remotely triggered and a whumpf. When the slope on which the trigger is located avalanches, it is called a directly triggered avalanche. A remotely triggered avalanche is one where the trigger point is not located in the initial slab of snow that is released. The distance between the trigger point and the avalanche can be hundreds of metres. A fracture in a weak snow layer that propagates outwards from the trigger location, but does not release an avalanche is called a whumpf (Johnson et al., 2000b). Whumpfs occur on low angle terrain and often produce a

distinctive sound and downward displacement of the snow surface is often noticeable.

It is now commonly accepted that slab avalanche release starts with a shear failure in the weak layer initiated by a triggering mechanism (e.g. skiers, falling cornices, increased overburden from new snowfall, warming, etc). If the initial failure exceeds a critical length, it becomes a self-propagating brittle fracture until the slope parallel stress caused by the weight of the unsupported slab overcomes the peripheral strength of the slab (Schweizer et al., 2003). The critical length for fractures to become self-propagating has been estimated to be between 10 cm (rapid loading) and 10 m (slow loading) (Schweizer, 1999). Secondary fractures at the crown (tensile), flanks (tensile and shear) and stauchwall (compression) then release the slab from the slope.

Although the slab release mechanism is the same for the two types of triggers (i.e. natural and artificial), the loading rate and the area of loading are different. Natural triggers generally load the snow surface at slow rates over large areas, whereas artificial triggers typically apply localized near-surface rapid loading (Schweizer et al., 2003). This is important because the mechanical properties of snow are strain rate dependent (e.g. Narita, 1980). For most natural triggers (except cornice and ice falls), it is believed that a slow damage process at the bond scale creates a failure along the weak layer (McClung, 1979b). If this failure reaches a critical size, it will rapidly propagate along the weak layer, thereby releasing a slab avalanche. For skier triggering however, it is believed that skiers directly impart deformations in the weak layer which are large enough to create a propagating brittle fracture in the weak layer (Schweizer et al., 1995b).

Table 1.1: *Canadian avalanche size classification (CAA, 2002).*

Size	Destructive potential	Typical mass (metric tonnes)	Typical path length
1	Relatively harmless to people.	< 10 t	10 m
2	Could bury, injure or kill a person.	10^2 t	100 m
3	Could bury or destroy a car, damage a truck, destroy a small building or beak a few trees.	10^3 t	1000 m
4	Could destroy a railway car, large truck, several buildings or a forest area up to four hectares.	10^4 t	2000 m
5	Largest snow avalanche known. Could destroy a village or a forest of 40 hectares.	10^5 t	3000 m

1.2.1 Avalanche sizes

The size of an avalanche is an important indicator of its destructive power as well as its propagation propensity. Large slab avalanches are more destructive and are indicative of snowpack conditions favouring fracture propagation. Table 1.1 shows the Canadian avalanche size classification (CAA, 2002), which is used by many forecasting and skiing operations in Canada. Half sizes (e.g. size 1.5) are commonly recorded as well. Slab avalanches of size 0.5 are often recorded as signs of instability. However, these avalanches are relatively harmless to people.

1.3 Snowpack tests

Identifying weak snow layers is fundamental to identifying a snowpack prone to slab avalanche release. Different observation methods and tests are available to gain information about the snowpack. This section introduces the snow profile and six

Figure 1.5: *Determining the layer's hardness using the hand hardness measure of resistance (B. Jamieson photo).*

snowpack tests, namely the compression test, the rutschblock test, the shear frame test, the cantilever beam test, the deep tap test and fracture propagation test.

The snow profile is a systematic observation of snowpack layers made in a pit dug where the snowpack is undisturbed (CAA, 2002). It is widely used by avalanche professionals to gather information about the snowpack. Identification of weak layers is a primary objective. Thickness, crystal type, size and density are often recorded for each snow layer. A hardness measurement is also taken for each layer, using the "hand hardness" measure of resistance (Figure 1.5). The hardness is determined by inserting objects of different size in the snow. The objects from largest to smallest are: fist (F), four fingers (4F), one finger (1F), pencil (P) and knife (K). In addition, a temperature profile through the snowpack is measured.

1.3.1 Stability tests

Stability tests are commonly used by avalanche professionals, as well as recreationists, to identify potential weak layers and assess the stability of the overlying slab. These

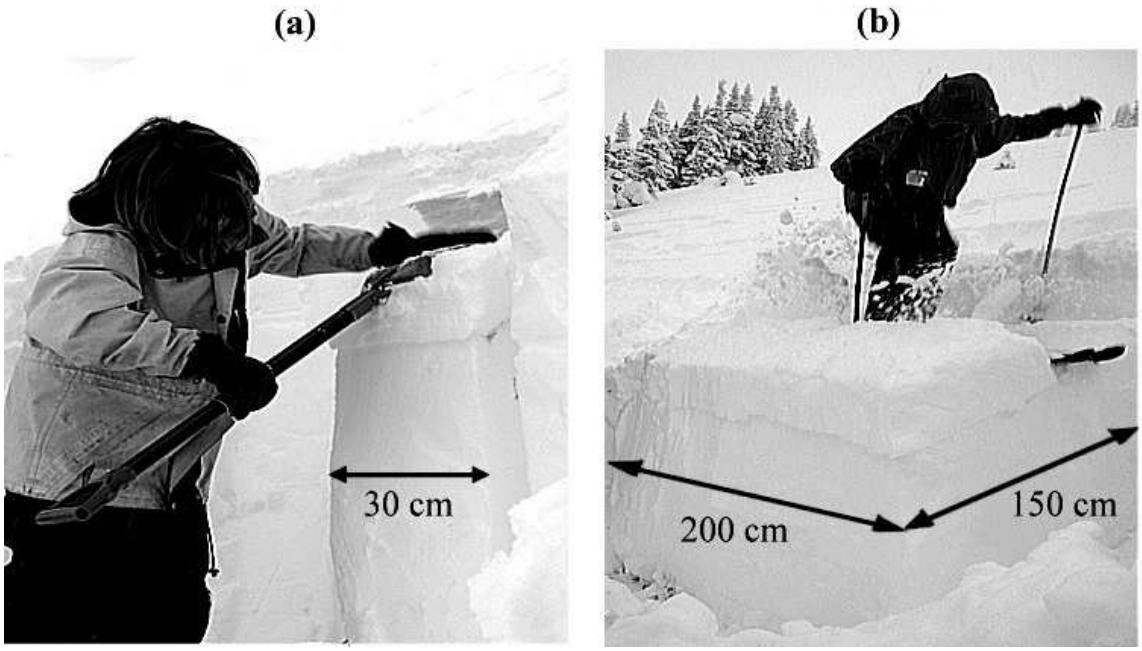

Figure 1.6: *Two stability tests commonly used to identify weak layers and evaluate the stability of the overlying slab. (a) The compression test (ASARC photo). (b) The rutschblock test (ASARC photo).*

tests, sometimes referred to as mechanical tests, consist of loading an isolated column of snow from the snow surface and observing whether or not any snowpack layer fractures. The two most widely used stability tests in Canada are the compression test (CT) and the rutschblock test (RB).

The compression test was developed by Parks Canada wardens in the 1970's (Jamieson, 1999). A 30 cm by 30 cm column of snow is isolated in the snow pit and subsequently loaded by tapping on a shovel placed on top of the column (Figure 1.6 (a)). When a weak layer fractures, a score is given to the fracture based on the number of taps. Compression tests are easy to perform and are widely used by avalanche professionals, as well as recreationists. Jamieson (1999) found that as the compression test score (number of taps) increases, the probability of skier-triggered

avalanches decreases. However, even for the highest loading step, the probability of triggering an avalanche was not zero, showing a practical limitation of this test. Variations of the compression test include the rammrutsch (Schweizer et al., 1995a), drop hammer (Stewart, 2002), stuffblock (Birkeland and Johnson, 1999) and quantified loaded column test (Landry et al., 2001).

The rutschblock (RB) test is a slope stability test first used by the Swiss army to find weak snow layers (Föhn, 1987). A block of snow, 2 m wide and 1.5 m downslope is isolated from the surrounding snowpack (Figure 1.6 (b)). The block is progressively loaded in six steps by a skier, ranging from preparing the block either by shovelling or cutting, to a skier jumping on the middle of the block. When a weak layer fractures, a score is assigned based on the loading step. The rutschblock test requires more time to perform than the compression test, and is therefore not as widely used by recreationists. However, because of the loading method and the size of the isolated block, it provides more valuable information with regards to skier-triggering than compression test results. The effectiveness of the rutschblock test as an evaluation of snowpack stability has been widely documented (e.g. Föhn, 1987; Jamieson and Johnston, 1992a). Low test scores are associated with poor stability and a high probability of skier-triggered avalanches. However, as for the compression test score, the probability of skier-triggering does not reduce to zero for the highest score.

Recently, researchers have developed formal classification systems for fractures in stability tests (e.g. Birkeland and Johnson, 1999; van Herwijnen and Jamieson, 2002), with the aim of improving the interpretation of these test results. Johnson and Birkeland (2002) proposed that observing the character of the fracture can provide

valuable information about the propagation propensity of the weak layer.

1.3.2 The shear frame test

Both the compression test and the rutschblock test are relatively easy to perform and do not require any special equipment. These tests are used to identify weak layers and qualify the stability of the overlying slab. The shear frame test on the other hand is used to measure the shear strength of a *known* weak layer. After the weak layer has been identified in a snow profile, or through use of stability tests, the overlying snow is carefully removed to within 40-50 mm of the weak layer. The shear frame, a sheet metal frame, is gently inserted into the overlying snow to within 2-5 mm of the weak layer. A force gauge is attached to a cord connected to the shear frame and pulled smoothly and quickly parallel to the slope, thereby measuring the shear strength of the weak layer (Jamieson and Johnston, 2001).

1.3.3 The cantilever beam test

The cantilever beam (CB) test is a test that is not widely used by avalanche professionals. The first use of the cantilever beam test on snow was reported by Perla in 1969. It is used to measure flexural strength of a beam of snow. The basic idea of the test is to isolate a snow beam in the snow pit (Figure 1.7 (a)), which is rapidly undercut with a saw or by digging the snow out from underneath the beam, until the beam fractures. In this test, common in engineering, the top of the beam is in tension, while the bottom is in compression (Johnson et al., 2000a). The length of the undercut is a measure of the tensile strength of the snow. B. C. Johnson (2000), performed modified cantilever beam tests by isolating cantilever beams containing

Figure 1.7: *Two snowpack tests not widely used by avalanche professionals. (a) The cantilever beam test is used to evaluate the flexural strength of the slab. (b) The deep tap test is an experimental test which gives a qualitative measure of the fracture propagation propensity of deeper weak layers.*

a weak layer. The overlying slab was undercut along the weak layer with a saw. Fractures were observed to propagate 30 to 60 cm horizontally along the weak layer before being stopped by a fracture through the slab.

1.3.4 The deep tap test and the fracture propagation test

The deep tap test (DTT) and the fracture propagation test (FPT) are experimental tests that are only used by the field staff of the University of Calgary. Both tests are used to give a qualitative measure of the fracture propagation propensity of deeper weak layers (Campbell, 2004). As for the compression test, a 30 by 30 cm column of snow is isolated in the snow pit. The weak layer that will be tested has to be identified in the column. All but 15 cm of snow above the weak layer, measured at the back of the column, is removed and a 5 cm deep notch along one of the side walls is cut into the weak layer. For the deep tap test, the column is then loaded using the

same loading steps as for the compression test (Figure 1.7 (b)). The FPT is almost identical to the DTT. The only difference is the loading method. Instead of using a shovel and tapping by hand, a drop hammer tester is used (Stewart, 2002). This tester consists of a horizontal plate with a vertical guiding rod attached to it and a weight (300 g or 1 kg). The drop hammer tester is positioned on the column of snow and the weight is dropped along the guide rod by increasing the drop height by five centimeters after each drop until the weak layer fractures.

1.4 Research objectives

The objectives for the research described in the thesis are as follows:

1. Determine snowpack properties that significantly affect skier-triggering, with an emphasis on fracture propagation.

2. Incorporate a descriptor of fracture character in stability tests and determine if this improves the interpretation of the test results.

3. Assess the usefulness of the deep tap test and the fracture propagation test as an index of propagation propensity by correlating the test results with avalanche activity in the surrounding areas.

4. Observe fractures in weak snowpack layers by using a high-speed camera and analyze the displacement of the overlying slab.

5. Obtain fracture speed measurements from photographed propagating fractures.

6. Assess theoretical models with field observations of fractures in weak snowpack layers from high speed photography.

Chapter 2

Current state of knowledge

In order to understand slab avalanche release, the mechanical properties of snow are reviewed. While fracture initiation is best understood in terms of applied stress and strength, fracture propagation is best understood in terms of stress intensity and fracture toughness. Both strength and fracture toughness are mechanical properties that depend on temperature, density, grain type and grain size (Schweizer et al., 2003). Studies on the mechanical properties of snow are very insightful and provide valuable information. However, most studies are laboratory studies performed on fine grained homogeneous snow. Snow cover stratigraphy, on the other hand, has been recognized as a key contributing factor for dry snow slab avalanche formation (Schweizer et al., 2003). Because of the extremely fragile nature of low-density layered snow, transporting specimens from the snowpack for study in the laboratory is often impractical. Field studies on the stratigraphy of the snowpack and its relation to slab release and skier-triggering are therefore indispensable.

For this thesis, field observations of fractures in weak snowpack layers were investigated. As mentioned in the introduction, this was done by investigating snowpack properties, from snow profiles and stability tests, in relation to skier triggering as well as by direct observations of fractures in weak snowpack layers through use of a portable high speed camera. In this review, a brief overview of the mechanical properties of snow is given (Section 2.1), followed by a summary of research on snowpack properties relevant to skier-triggering (Section 2.2). Studies on fracture

characterization in snowpack stability tests are assessed next (Section 2.3). In Section 2.4 theoretical slab avalanche release models are described, followed by a review of field measurements on propagating fractures (Section 2.5). Finally, Section 2.6 summarizes the studies that were reviewed.

2.1 Mechanical properties of snow

Laboratory studies on the mechanical properties of snow have shown that the behaviour of snow is highly strain rate dependent (Narita, 1980; McClung, 1977; Fukazawa and Narita, 1993; Schweizer, 1998). Snow is ductile at low strain rates, and brittle at higher strain rates. A transition from ductile to brittle behaviour is typically found at a strain rate of 10^{-4} to 10^{-3} s^{-1}. As brittle fracture and fracture propagation are essential parts of snow slab release, fracture toughness (related to the resistance of a material to crack propagation) is an essential property of snow. Measurements of fracture toughness have shown that snow has one of the lowest fracture toughnesses of materials (Kirchner et al., 2002).

The deformation behaviour of snow under uniaxial *tension* was studied in a series of cold lab experiments performed by Narita (1980). He found a clear distinction between brittle and ductile behaviour of snow, depending on strain rate. Brittle fracture took place at stain rates above about 10^{-4} s^{-1}, whereas ductile behaviour was observed in the $2\ 10^{-4}$ s^{-1} to $5.5\ 10^{-7}$ s^{-1} range. For brittle fracture, the resisting force increased linearly with increasing strain up to the point of rupture (Figure 2.1a). Two different types of ductile failure were observed. In the first, the linear stress-strain relation ceased after a characteristic strain (Figure 2.1b). Catastrophic failure

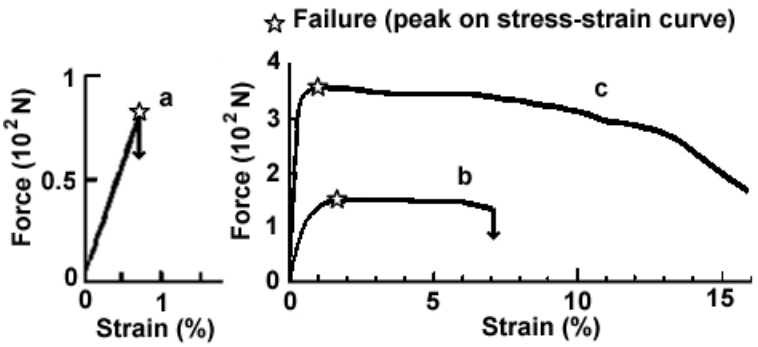

Figure 2.1: *Typical stress-strain curves for snow with a density between 290 and 450 kg m^{-3} under uniaxial tension for brittle behaviour (a) and ductile behaviour (b and c). After Narita (1980).*

was preceded by the appearance of small cracks throughout the entire specimen. The second type was relatively similar, with the important exception that the cracks appeared and grew, resulting in a decrease in transmitted stress with increasing applied strain (Figure 2.1c).

In 1977, McClung reported performing simple shear tests on homogeneous snow. In cold lab experiments, the snow specimen was placed in a direct shear apparatus and uniformly strained in the *ductile* range in plane strain and approximately simple-shear. Measurements of horizontal displacement, vertical displacement and applied horizontal load were recorded. The results fell into two basic categories. The first category of results showed a continuous increase in shear stress with horizontal displacement with no obvious peak (i.e. strain hardening; Figure 2.2a). The second category showed strain softening. In these tests the shear stress rose until a peak strength (i.e. failure) was reached (Figure 2.2b). The behaviour was found to be strain rate dependent. Samples that showed strain hardening at slow rates, exhibited strain softening at high strain rates. Additionally, he found that the peak and

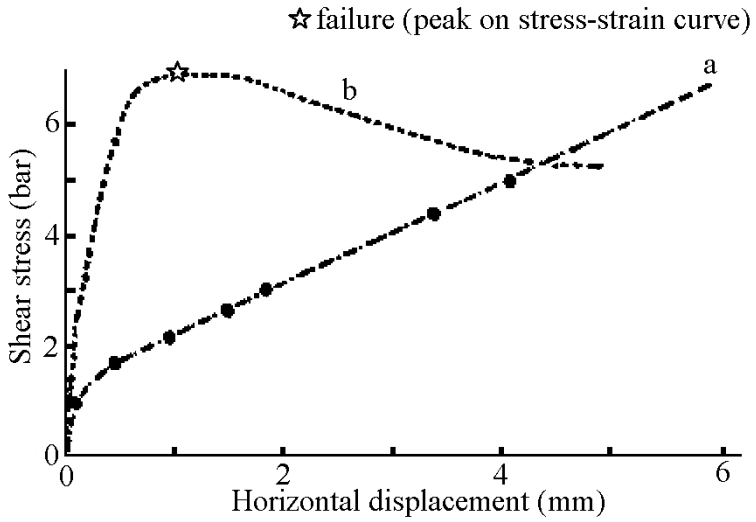

Figure 2.2: *Shear stress versus horizontal displacement of two similar snow samples at different strain rates showing strain hardening (a) and strain softening (b). After McClung (1977).*

residual strengths increased with normal load.

Fukuzawa and Narita (1993) studied the mechanical behaviour of depth hoar under *shear* stress. They "grew" depth hoar crystals in a laboratory by imposing a strong temperature gradient on a low density (170 to 190 kg m^{-3}) snow sample overlying a high density (360 to 390 kg m^{-3}) snow layer. Crushed fine grained snow was then precipitated on the depth hoar creating a three layered snow sample. Various strain rates were applied ranging from 10^{-5} to 10^{-3} s^{-1} at a temperature of -6^{o}C. At high strain rates the shear stress increased linearly with increasing strain, followed by brittle fracture. When lower stain rates were applied, the depth hoar deformed in a ductile manner. The shear stress increased gradually beyond the yield stress and small cracks began to appear in the layer of depth hoar. A peak in the shear stress was noticed whereafter stress decreased gradually, combined with more and larger cracks. From these results, a critical strain rate of ductile to brittle

transition was found between $8 \cdot 10^{-5}$ and $2 \cdot 10^{-4}$ s^{-1}.

Schweizer (1998) investigated the effects of loading rate and temperature on strength and shear modulus of natural snow in cold lab experiments. Snow samples composed of small rounded particles with a density of 290 kg m^{-3}, were placed in a direct simple-shear apparatus and subjected to shear deformations at different strain rates and at different temperatures. The test temperatures were -5^{o}C, -10^{o}C and -15^{o}C. As in previous studies, the mechanical properties of the specimen were rate dependent. For the snow tested, the transition from ductile to brittle was at a strain rate of 10^{-3} s^{-1}. Stiffness, the initial tangent to the stress strain curve, increased with increasing strain rate. Strength and toughness increased with increasing temperature. The most significant effect of temperature was found for the stiffness (i.e. shear modulus), which increased with decreasing temperature.

Föhn et al. (1998) studied the response of *in-situ* weak layers to the rapid pulling of a shear frame placed a few mm above the weak layer. An accelerometer and displacement sensor were attached to a shear frame in order to measure acceleration, displacement and applied force. They found that for rapid loading (i.e. loading time on the order of 0.1 s) the shear stress increased almost linearly with strain until the weak layer fractured, like a brittle material. The stress strain curve implied a quasi linear elastic behaviour up to the point of fracture:

$$\tau \approx \mathcal{G}\gamma \tag{2.1}$$

where τ is the shear stress, γ the shear strain and $\mathcal{G}$ is the shear modulus. The shear modulus is related to Young's modulus $\mathcal{E}$ by:

$$\mathcal{E} = 2(1 + \nu)\mathcal{G} \tag{2.2}$$

where ν is the Poisson's ratio. Using a Poisson's ratio of 0.1, Young's modulus ranged from 0.2 to 1.2 MPa. These values were lower than in previously published studies on dry coherent snow (e.g. Mellor, 1975; Shapiro et al., 1997), which was attributed to the granular nature of the tested snow. Furthermore, the relationship between grain shape and shear strength showed that weak layers composed of grains with euhedral features (e.g. solid faceted crystals) generally had lower shear strength than weak layers composed of smaller rounded grains.

Jamieson and Johnston (2001) made extensive *in-situ* measurements of weak layer shear strength using the shear frame. They provided shear strengths for weak layers by grain type and density. The shear strength of weak layers composed of faceted grains and depth hoar was consistently lower than for weak layers composed of partly decomposed and rounded grains with the same density, confirming earlier findings (Föhn et al., 1998). Moreover, the data showed an increase in strength with increasing density, in accordance with previous studies (e.g. Keeler and Weeks, 1968; Mellor, 1975; Perla et al., 1982).

Similar characteristics have been found for the strength of snow in tension. Jamieson and Johnston (1990) performed *in-situ* tensile tests of snowpack layers and reported an increase in tensile strength with increasing density, similar to previous studies (e.g. McClung, 1979a). Furthermore, Jamieson and Johnston (1990) found that the tensile strength of layers of faceted grains was approximately half that of layers of partly decomposed and rounded grains with the same density.

Cantilever beam tests (Section 1.3.3) performed on snow have been used to assess

the flexural strength of slabs (e.g. Perla, 1969; Johnson et al., 2000a). The beam number, which is an index for the flexural strength of the slab and is calculated from the length of the undercut, was found to increase with increasing slab density. B. C. Johnson (2000) performed modified cantilever beam tests by isolating cantilever beams containing a weak layer. The overlying slab was undercut along the weak layer with a saw. Fractures were observed to propagate 30 to 60 cm along the weak layer before being stopped by the fracture through the slab.

Even though fracture toughness was formally introduced in a theoretical slab avalanche release model by McClung in 1981, this important property has only recently been measured in snow. Kirchner et al. (2000) and Faillettaz et al. (2002) performed simple notched cantilever beam experiments in the field to measure the fracture toughness of snow in tension. The critical stress intensity factor, characteristic for brittle fracture, was found to increase with increasing density. Kirchner et al. (2002) measured the fracture toughness of snow in shear, finding an increase in fracture toughness with increasing density. Using notched cantilever beam experiments in the cold laboratory, Schweizer et al. (in press) found that the fracture toughness of snow also depends on the microstructure of the snow (density between 100 and 300 kg m^{-3}). Snow consisting of larger grains generally had a lower fracture toughness than fine grained snow. Furthermore, they found that the fracture toughness of snow decreased with increasing temperature up to about -8^{o}C. Above -6^{o}C the fracture toughness increased with increasing temperature.

The fracture toughness values obtained from *in-situ* notched cantilever beam tests performed by Failletaz et al. (2002) were also dependent on the cantilevered length. A possible explanation for this result was given by performing discrete element sim-

ulations of the cantilever beam experiments, considering snow as a cohesive granular material. This showed that due to the granular nature of snow the elastic energy was not stored homogenously throughout the snow, as in continuum media. The assumption of a geometry-independent fracture toughness was therefore not valid. However, snow can be considered a cellular solid rather than a granular material. Kirchner et al. (2001) applied foam theory to snow to describe the mechanical behaviour of snow. The concept of describing snow as an open cell foam appears promising, however Kirchner et al. (2001) noted that the subject is in its infancy, and foam fracture mechanics have not yet been developed.

2.2 Snow stratigraphy

In 1977, Perla reported the dimensions of slab avalanches, as well as some snowpack and terrain properties associated with avalanches from various unspecified triggers. Near the crown of slab avalanches the slope was typically 30 degrees or steeper, and the mean slab thickness was 67 cm. The article provided much needed field data on slab avalanches. Stethem and Perla (1980) confirmed these finding with similar measurements on 30 slab avalanches. Additionally, Stethem and Perla reported an average slab density of about 220 kg m^{-3} and found a wide variety of crystals in the failure layers. In many cases the crystals in the failure layers differed little from those in the adjacent layers. In 1993 Föhn summarized snowpack data of about 300 weak layers underlying slabs, 20% of which were identified by natural and skier-triggered avalanches and the remainder by snowpack tests such as the rutschblock test. He found that 60% to 70% of failure layers of slab avalanches were weak layers up to 6

cm thick, while the remaining failure layers were classified as weak interfaces. Eighty percent of the weak layers consisted of buried surface hoar, faceted crystals or depth hoar, whereas weak interfaces were usually adjacent to rounded grains or melt-freeze grains.

The first detailed study into snow cover characteristics that affect skier-triggering was performed by Jamieson and Johnston (1998). By comparing snow profiles observed next to skier-triggered slab avalanches with profiles from skier-tested slabs that were not triggered, they identified several snowpack parameters affecting skier-triggering. Specifically, they found that weak layers for skier-triggered start zones were generally softer (i.e. lower hand hardness) and weaker (i.e. lower shear strength) than weak layers in start zones that could not be skier-triggered.

Jamieson and Johnston (1998) also devoted special attention to remotely triggered avalanches and whumpfs. In contrast to skier-triggered start zones, remote trigger points, defined as a site outside an avalanche start zone where a person initiates a fracture that propagates along a weak snowpack layer, had deeper and denser slabs. These findings were confirmed by Johnson et al. (2000b) who also identified significant differences in weak layer thickness and maximum crystal size. Weak layers at remote trigger points were generally thicker and composed of larger crystals than weak layers in skier-triggered start zones. Field measurements also showed that the average vertical displacement of the slab at whumpf sites varied from 0.1 cm to 1 cm (Johnson et al., 2000b), which was caused by the collapse of the weak layer.

In 2001, three studies comprehensively summarized snowpack properties associated with skier-triggering (Schweizer and Jamieson, 2001; Schweizer and Lütschg, 2001; Schweizer and Wiesinger, 2001). Analysis of snow profile data next to skier-

triggered avalanches showed that weak layers of skier-triggered avalanches typically consisted of surface hoar, faceted crystals or depth hoar, as was reported in previous studies (e.g. Perla, 1977; Föhn, 1993). The crystals in the layer above and the layer below the weak layer were generally smaller and more rounded. Weak layers were usually soft (F to 4F) and the weak layer differed distinctly in grain size and hand hardness from the adjacent layers. The typical slab was approximately 50 cm thick, consisted of decomposed and fragmented particles or small rounded grains and was rather soft (4F). Furthermore, Schweizer and Wiesinger (2001) concluded that snow temperature and density are of limited value for revealing current potential instability of dry snow slabs. The snowpack properties associated with skier-triggered avalanches all have a clear physical relation to slab avalanche release. Slabs were generally soft, which enabled the skier to impart deformations to the softer weak layer efficiently (Schweizer and Lütschg, 2001). Slabs were relatively shallow, in accordance with field experiments which have shown that the skier's impact decreases with increasing depth (Schweizer et al., 1995b; Camponovo and Schweizer, 1996). A distinct hardness difference between the weak layer and the adjacent layers causes stress concentrations, which favours fracture initiation (Schweizer and Jamieson, 2001). Finally, distinct changes in crystal size are believed to indicate poor bonding between snowpack layers (Colbeck, 2001).

McCammon and Schweizer (2002) proposed to complement information on mechanical instability, such as shear strength measurements or stability test results, with information on structural instability (weak layer depth, weak layer thickness, grain type, grain size and hardness difference across the failure interface). Structural instability was defined as the tendency of the surrounding snowpack to concentrate

Table 2.1: *Highly significant snowpack parameters of instability and unstable ranges (from Schweizer and Jamieson, 2003a).*

Parameter	Critical range
Rutschblock score	< 4
Grain size difference	≥ 0.75 mm
Weak layer grain size	≥ 1.25 mm
Hardness difference	≥ 1.7
Weak layer hardness	$\leq$ F+

stresses at the weak layer and to propagate fractures along the weak layer. While no single parameter was a reliable predictor of instability, a simple count of the variables that were in the critical range (threshold sum) provided an approximate indicator of unstable conditions.

While these studies identified snowpack properties associated with skier-triggered avalanches, it was unclear whether these characteristics were unique for unstable profiles, or present in most profiles. Recently, Schweizer and Jamieson (2003a, 2003b) analyzed a large data set of snow profiles from 220 skier-triggered slopes and 204 slopes that were skied but not triggered. For the first time unstable ranges were identified for highly significant snowpack parameters (Table 2.1). The differences in crystal size and hand hardness between the weak layer and the adjacent layer on skier-triggered slopes were significantly larger than for weak layers on skier-tested slopes that were not triggered. Furthermore, unstable weak layers were significantly softer and consisted of larger crystals than stable weak layers.

Schweizer et al. (in press) explored a method based on the threshold sum approach to assess snowpack stability based on layer properties. Using the threshold values shown in Table 2.1 as well as a threshold range for the depth of the failure plane (18 cm to 94 cm), they report 77% accuracy when the primary weakness (i.e.

most critical layer in snowpack) was known. However, the threshold sum method was less successful at detecting the primary weakness, with an accuracy between 53% and 62%.

2.3 Fracture characterization in snowpack stability tests

Snow slope stability tests usually involve isolating a column or a block of snow, including a weak layer, and applying a sequence of increasing loads until a weak layer fractures. Therefore, slab properties and weak layer properties are tested simultaneously (Schweizer et al., 2003). The most commonly used stability tests in Canada are the rutschblock test and the compression test (Section 1.3.1). The *score* (i.e. the loading step at fracture) can be compared to avalanche activity on surrounding slopes to assess the validity of the test, which has been done for rutschblock tests (Föhn, 1987; Jamieson, 1995), as well as for compression tests (Jamieson, 1999). The probability of skier-triggering nearby slopes decreases as the stability test score increases. However, when the highest score in these tests is reached, the frequency of skier-triggering is not zero (i.e. false stable results), showing one limitation of such stability tests.

For decades, avalanche professionals have recognized that the stability test score is not the only test result relevant to avalanche forecasting. For instance, since 1981, the Canadian Avalanche Association's Guidelines for Weather, Snowpack and Avalanche Observations have assigned special attention to collapsing fractures in shovel tests (NRCC, 1981). Recently, avalanche researchers have been looking for ways to improve the interpretation of the stability test results by incorporating a

qualitative description of the character of fractures in weak layers. Johnson and Birkeland (2002) speculate that information about fracture character relates to fracture propagation propensity.

For the rutschblock test, Schweizer et al. (1995a) proposed a rating system for the type of release and character of the fracture plane. Schweizer and Wiesinger (2001) refined the descriptions for type of release (whole block, below the skis, only an edge) and fracture character (clean, partly clean, rough) in which "clean" implies planar. Schweizer and Jamieson (2003b) report that there is a significant difference in fracture character and release type in rutschblock tests between human triggered slopes and slopes not triggered. Rutschblock results near skier-triggered avalanches typically had a clean (i.e. planar) fracture surface and the whole block released.

Birkeland and Johnson (1999) introduced three levels of shear quality: Quality 1 is a fast, planar shear or a collapse, Quality 2 is an "average" shear and Quality 3 an irregular shear. Using data mostly from southwest Montana and northwest Wyoming, they report improved interpretation from stability test results, particulary those tests with high scores (Johnson and Birkeland, 2002). A stability test with a high score and with a clean Quality 1 shear is more likely to be related to signs of instability in the region than the same test score with an irregular Quality 3 shear. Many field workers in the United States now use this three level system and it has now been adopted in the snowpack observation guidelines for avalanche programs in the United States (Greene et al., 2004).

One of the limitations of this system is that the classification is somewhat subjective and experience with the system improves the reliability of the results. Furthermore, fast planar and collapsing fractures are described as Quality 1 fractures

even though these are substantially different types of fractures.

In a 1999 article on the compression test, Jamieson outlined a four level description of fracture character, used by researchers of the University of Calgary: Progressive Compression (PC), Thin Planar (TP), Sudden Collapse (SC) and non-planar Break (B). Five winters of stability test data with the four level description of fracture character were analyzed by van Herwijnen and Jamieson (2002). Over 6000 classified fractures from compression and rutschblock tests showed that the weak layer crystal type plays an important role in fracture character. Thin planar fractures were most commonly observed for weak layers composed of precipitation particles, decomposed fragments and rounded grains, as well as surface hoar crystals. Weak layers composed of depth hoar, or large well developed facets, were more likely to produce collapsing fractures. No significant difference in fracture character was found between the stability tests performed on slopes that were triggered and slopes that were not. However, a smaller number of stability tests performed on whumpf sites revealed that sudden collapse fractures were often associated with whumpfs. This indicates that fracture character provides some information about fracture propagation since whumpfs are generally regarded as good indicators of high instability (e.g. McClung and Schaerer, 1993: 135), as conditions are favourable for widespread fracture propagation.

2.4 Slab avalanche release models

Slab avalanche release is the result of four types of fractures: one in tension at the upper boundary of the slab (crown), two lateral breaks on the sides of the slab (flanks)

mostly in shear, one in compression at the lower boundary of the slab (stauchwall) and a fracture in the weak layer at the base of the slab (de Quervain, 1966). Prior to 1970, there was no consensus on which failure or fracture occurred first to release a slab avalanche. Bucher (1956) and Roch (1956) suggested that the primary failure can occur in any of these locations wherever stress exceeds strength. In addition, Roch (1956) reported that the failure in the weak layer could either be in shear or in compression. Haefeli (1967) believed that the tensile crown fracture was the initial and most important fracture. Bradley and Bowles (1967) focussed on compressive failure within a weak layer beneath the slab. Roch (1965) emphasized shear failure in the weak layer.

In 1970, Perla and LaChapelle (1970) assumed that the first *failure* for slab release occurs due to a loss of shear support in the weak layer. They argued, however, that the first *fracture* is a tensile fracture at the crown. They concluded that a reduction in shear support, possibly by yielding, leads to tensile fracture at the crown, followed by basal shear fracture. (Throughout this thesis, basal refers to the base of the slab and not the base of the snowpack.)

McClung (1979b, 1981, 1987) applied a one dimensional fracture mechanics model developed by Palmer and Rice (1973) for the growth of a shear band in clay. This approach specifies that a shear band is initiated at a stress concentration in the basal weak layer (Figure 2.3). Slow strain softening at the tip of the band follows, until a critical length is reached and the band propagates rapidly. The idea of having weaker parts within the weak layer is quite old. These weaker zones have been called shear perturbations (Perla and LaChapelle, 1970), deficit zones (Conway and Abrahamson, 1984), shear bands or slip surfaces (McClung, 1979b, 1981, 1987), super

weak zones (Bader and Salm, 1990), zones of localized weakness (Birkeland et al., 1995) or in general flaws or weak spots (Schweizer, 1999). These imperfections, and in particular their critical size, are considered a key parameter for stability. Gubler (1992) estimated the size to be on the order of 5 to 10 times the slab thickness, resulting in 0.5 to 50 m for typical slab thickness values.

Assuming that the main deformation is one dimensional and takes place in the sliding layer (Figure 2.3) and that the band length $2L$ is large compared to ω, the size of the end zone, and $\mathcal{H}$ the slab thickness perpendicular to the slope, McClung (1981) derived the mode II propagation condition:

$$\frac{(1-\nu)}{2\mathcal{G}}K_{II}^2 = \frac{\mathcal{H}(1-\nu)}{4\mathcal{G}}\left([\tau_g - \tau_r]\frac{L}{\mathcal{H}}\right)^2 = [\tau_p - \tau_r]\delta \tag{2.3}$$

with K_{II} the fracture toughness of snow in shear, $\tau_g = \rho g \mathcal{H} \sin\psi$ the shear stress due to the weight of the slab, τ_r the residual stress, τ_p the peak stress at the tip of the shear band, δ the displacement in the shear band from peak to residual stress and $\mathcal{G}$ the shear modulus of the slab (Figure 2.3). The two terms on the left are equivalent expressions for the driving term which provides the energy to drive the shear band. The term on the right provides the resistance to band extension. An important feature of the model proposed by McClung is that it suggests that snow slabs can fail under applied gravitational shear stress which is less than the peak strength of the snow in the weak layer.

The size of the end zone ω (Figure 2.3), is the characteristic length in which the shear stress falls from the peak to the residual value. This parameter was postulated to be the minimal length needed to initiate progressive failure. McClung (1981) estimated values between 0.5 m to 1 m. Using typical values of alpine snow, combined

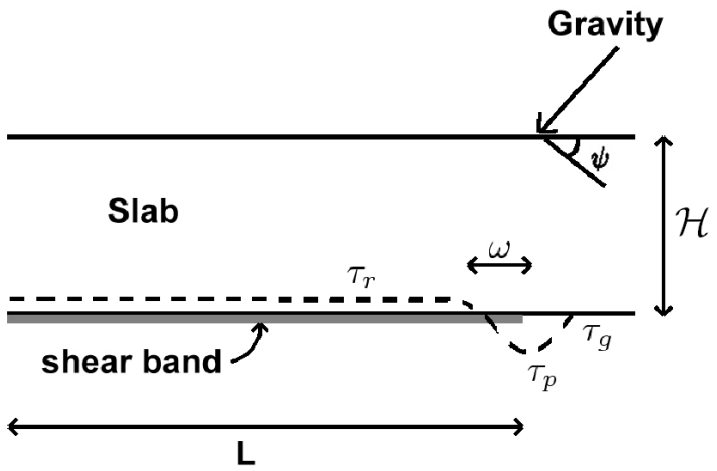

Figure 2.3: *Schematic of basal shear stress conditions for a slab underlain by a weak layer under strain softening. After McClung, 1979b.*

with results from laboratory experiments, Schweizer (1999) calculated an end zone length ranging from 0.2 m to 2.2 m. Smaller sizes are implied for more rapid loading (e.g. skier-triggering). However, the critical length of the deficit zone for fracture propagation must be a multiple of the end zone size and decreases with increasing ratio of peak stress to residual stress and increasing loading rate (Schweizer et al., 2003).

Bazant et al. (2003) expanded the model of McClung (1981) by incorporating nonlinear fracture mechanics effects. The main consequence of nonlinear fracture behaviour is that the fracture process zone at the crack tip has a certain finite length. This was taken into account by assuming the tip of an equivalent Linear Elastic Fracture Mechanics (LEFM) crack lies ahead of the actual crack tip by a certain distance c_f. Bazant et al. (2003) derived that $K_{II_c} \propto \tau_g\sqrt{\mathcal{H}}$ and the critical length a_c to drive *brittle* fracture should be on the order of the slab thickness (i.e. 0.2 to 1 m). Using field measurements (Perla, 1977), Bazant et al. (2003) suggested that

the fracture toughness at the base of the snow slab follows a power law $K_{II_c} = \propto \mathcal{H}^{1.8}$.

Bader and Salm (1990) explored fracture propagation in a weak layer. They introduced the term super weak zones as deficit zones where shear stresses from the overlying snow cannot be fully transmitted, similar to the idea of the shear band formally introduced by McClung (1979b). Based on expressions for stress and strain rate at the edge of the super weak zone, they applied a model to study shear failure and fracture. They concluded that without super weak zones, avalanche release is highly improbable, even with the local increase of stress by a skier. Furthermore, the model predicted that the critical length for brittle fracture propagation decreased with decreasing weak layer thickness. This result suggests that thinner weak layers are more prone to failure than thicker ones, which is not supported by field studies. Schweizer (1999) argued that the layer thickness is probably not relevant, since the deformation is expected to be concentrated at the upper or lower interface of the weak layer. Bader and Salm (1990) calculated the critical length for *ductile* failure propagation to be between 1 and 6 m, and the critical length for *brittle* fracture propagation was between 2 and 100 m. Using more realistic values for the properties of snow, Schweizer (1999) determined the critical length for *ductile* failure propagation to be between 0.1 and 3.1 m, whereas the critical length for *brittle* fracture propagation was between 5 and 35 m.

Louchet (2001) analyzed the stability of a basal crack as a Griffith problem, focussing on skier triggered slab avalanches. Snow was treated as a brittle ice foam that behaves in a elastic way prior to brittle fracture. A local overload, caused by a skier, may induce a crack in the weak layer, resulting in a tensile stress in the slab at the upper end of the sheared zone. Two release scenarios were introduced:

undercritical and overcritical triggering. For undercritical release, it was assumed that the crack in the weak layer gradually expands as the skier progresses across the slab up to the moment when tensile fracture takes place, as previously proposed by Perla and LaChapelle (1970). The second scenario required that the basal crack meets conditions for unstable crack growth before the tensile stress at the tip of the basal crack reaches the tensile strength. In this case the critical crack size a_c can be estimated as:

$$a_c = \frac{1}{\pi}\left(\frac{K_{IIc}}{\tau_g}\right)^2 \tag{2.4}$$

For typical values of K_{IIc} and τ_g the critical crack size a_c is approximately 0.3 to 1 m (Schweizer et al., 2003). However, as these values were determined with linear elastic fracture mechanics, they represent lower limits since the energy dissipated because of the plasticity of the material is not included. Louchet (2001) argued that independent of snow properties, the transition between the two triggering modes would occur at a critical slope angle of 35 degrees. In addition, residual friction on the basal crack surfaces increased the critical length for fracture propagation and the critical slope angle for the transition between the two triggering modes. However, there are no observations or data available to support the proposed transition in triggering modes.

In a review of dry slab avalanche release, Schweizer (1999) concluded that it was commonly accepted that slab avalanche release starts with an initial shear fracture in the weak layer. Clearly, the consensus on the initial fracture leading to slab avalanche release had evolved from an initial fracture in tension at the crown, as proposed by Perla and LaChapelle (1970), to an initial shear fracture in the weak layer, as first

proposed by McClung (1979b). However, compressive failure of the weak layer (collapse) has also been proposed as a possible mechanism for slab avalanche initiation. The brittle fracture of granular materials, such as snow, is interpreted as a result of shear at 45^0 to the compressive load (e.g. Kezdi, 1974: 183-185)

Bradley (1970) and Bradley and Bowles (1967) studied deep slab avalanches in the Rocky Mountains of Montana. They state that the initial failure is a compressive failure of the basal snow layer (depth hoar). Although McClung's work (1981) focused on shear failure in the basal weak layer, he acknowledged the importance of collapse in thick weak layers, which would subject the slab to bending stresses. In a parameter study on the supporting forces and stability of snow slabs, Lackinger (1989) proposed a possible failure mechanism for thick layers of depth hoar. Lackinger suggested that the collapse of the weak layer introduces bending forces in the overlying slab. The area of bending widens along with lateral propagation of the collapse until the tensile crown fracture interrupts the lateral and longitudinal force transmission, and the slab avalanche becomes inevitable.

In 2000, B. C. Johnson introduced a theory for fracture *propagation on horizontal terrain* similar to the idea put forward by Lackinger (1989). The theory is based on a compressive fracture of the weak layer, generating a flexural wave in the overlying slab. Energy is transferred through the slab, progressively collapsing the weak layer (Figure 2.4). This coupled process spreads outwards with the stiffness of the slab controlling the speed of propagation. Assuming an harmonic flexural wave in a beam and neglecting gravitational shear forces, the propagation speed is given by:

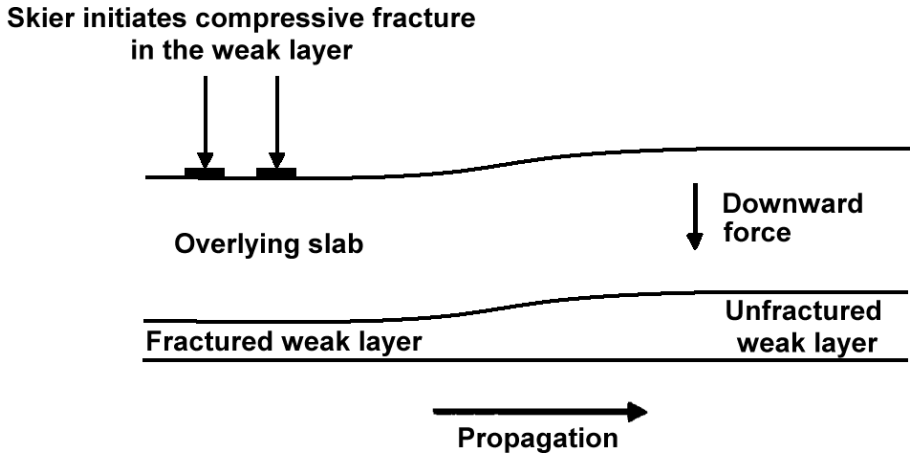

Figure 2.4: *Diagram showing initial collapse of the weak layer. The bending wave in the slab drives the fracture. After Johnson et al., 2000b.*

$$c = \frac{2\pi}{\lambda}\sqrt{\frac{\mathcal{E}I}{\rho A}} \tag{2.5}$$

with λ the wavelength, $\mathcal{E}$ the modulus of elasticity of the slab, I the moment of inertia, ρ the density of the slab and A the cross sectional area. This theory was developed as a result of fracture speed measurements on the site of a whumpf (see below). Moreover, field data showed that whumpfs and remotely triggered avalanches had thicker weak layers than non-remotely triggered avalanches (Johnson et al., 2000b). This supports the theory by emphasizing the significance of the compressive component, assumed larger for thicker weak layers, in fracture propagation on low angle terrain.

2.5 Field measurements on propagating fractures

There have been very few field measurements on propagating fractures in snow. In Antarctica and North America, several *observations* of firn quakes were reported and

described as a collapsing wave that can travel for many miles (DenHartog, 1982). Firn quakes are sudden collapses throughout a large area of perennial snow and are therefore similar to whumpfs (Section 1.2). Sorge (1933) experienced three firn quakes in Greenland during the winter of 1930-1931 and reported that snowpack layers at a depth of between 2 and 2.5 m appeared to have collapsed approximately 2.5 cm.

Benson (1962) reports that while traversing Greenland, collapses of soft layers were observed when walking or digging pits in undisturbed areas. In one case, a barrel dropped from an airplane penetrated the snow surface, initiating one of these collapses. The collapse of the weak layer started at the point of impact and spread, accompanied by a sound. DenHartog (1982) reports similar events in Antarctica. A 10 lb charge was set off in a 10 m hole. A vehicle at the shot point dropped noticeably. Another person located five miles away reported the arrival of a firn wave shortly after the explosion. The sound wave arrived only slightly before the snow wave, indicating that the propagation velocity was slightly lower that the speed of sound in the air.

Truman (1973) reported human triggered whumpfs in upper New York State. He reports being able to see the wave front travelling across the snow surface in conjunction with a continuous 'swishing' sound that could be heard travelling away from the trigger point and decreasing in intensity. Observations made at a location where propagation stopped revealed a discontinuity in the snow surface with the disturbed snow 1 to 2 cm lower that the undisturbed snow just ahead of the discontinuity and the snow depth at the time of observation was between 15 and 30 cm. An estimate for the speed of the waves (in those instances when the travelling wave front could

be seen) was 6 m/s.

The only measurement of the velocity of a propagating fracture on low angle terrain was carried out by Johnson at Bow Summit, Banff National Park, Canada (B. C. Johnson, 2000; Johnson et al., 2000b; Johnson et al., 2004) on the 19th of February 2000. Geophones, positioned on the snow surface, were used to measure the displacement of the slab resulting from a propagating fracture in a weak layer composed of buried surface hoar crystals. After a whumpf was successfully triggered by a person on snow-shoes, the vertical displacement of the slab was measured to be between 0.1 and 0.2 cm. The propagation speed was calculated to be 20±2 m/s.

2.6 Summary and relevance to this thesis

The mechanical behaviour of snow is highly rate dependent, as shown by laboratory studies and *in-situ* studies on the mechanical properties of snow. Snow is ductile at low strain rates, and brittle at higher strain rates. Furthermore, both strength and fracture toughness are mechanical properties that depend on temperature, density, grain type and grain size. Therefore, snow is "one of the most bewildering materials of engineering significance" (Mellor, 1975).

Snowpack characteristics associated with skier-triggered avalanches were identified in various studies. Recently, more detailed studies have summarized these properties more thoroughly, providing unstable ranges for significant snowpack variables. Typically the difference in crystal size and hand hardness between the weak layer and the adjacent layer on skier-triggered slopes were significantly larger than for weak layers on skier-tested slopes that were not triggered. Furthermore, unsta-

ble weak layers were significantly softer and consisted of larger crystals than stable weak layers. Finally, skier-triggered slabs were generally softer than stable slabs, and typically had a thickness less than 100 cm. The identified snowpack properties associated with skier-triggered avalanches have a clear physical relation to slab avalanche release, in particular fracture initiation. However, there is still a lack of understanding which snowpack properties affect fracture propagation. In Chapter 4, snowpack properties associated with skier-triggering are analyzed to confirm and expand previous findings and in particular investigate snowpack properties which influence fracture propagation.

Stability tests are very useful to identify potential weak layers, but can produce misleading results (i.e. false stable). Efforts have been made to incorporate a qualitative description of the character of fractures in stability tests, with the aim of improving the interpretation of test results for avalanche forecasting. Various characterization schemes have emerged, with distinct similarities. Fractures in stability tests associated with instabilities are typically described as fast, clean and planar or a collapse, whereas fractures in stability tests not associated with instabilities are described as rough, irregular, non planar or slow. It has been shown that incorporating a description of fracture character or release type in stability tests can reduce some of the uncertainties associated with stability test results. Furthermore, it has been proposed that information about fracture character relates to fracture propagation propensity. In Chapter 5 a classification scheme for fractures in snowpack stability tests, developed by Jamieson (1999) and refined by van Herwijnen and Jamieson (2003), is discussed. The objectives are to determine specific snowpack characteristics associated with the different fracture characters and assess if the proposed

classification system relates to fracture propagation propensity, thereby improving the interpretation of stability test results for avalanche forecasting.

Slab avalanche release models have evolved over the past four decades. Perla and LaChapelle (1970) were the first to suggest a single failure model for snow slabs. They assumed that the first fracture was in tension at the crown. Nowadays it is generally assumed that the first fracture is a shear fracture in the basal weak layer (McClung, 1987; Bader and Salm, 1990; Louchet, 2001). For natural avalanches, it is believed that shear failures start at flaws (i.e. deficit zones) in weak layers which grow due to strain softening until a critical length of approximately $0.2 - 10$ m is reached followed by rapid brittle fracture propagation. However, no obvious process is available for the formation of these deficit zones. In contrast to natural avalanches, it is believed that skiers can directly cause brittle fractures in weak snowpack layers (Schweizer et al., 1995a) up to a depth of roughly 100 cm. Schweizer (1999) concluded that deficit zones are probably not necessary for skier-triggering. As skiers impart substantial stress concentrations dynamically, the critical crack length for brittle fracture propagation for skier-triggering is believed to be on the order of 0.1 to 1 m.

Recent field measurements on a propagating fracture on low angle terrain suggest that slab avalanches could be the result of a compressive fracture (B. C. Johnson, 2000) of the weak layer. This led to the development of a theory for fracture propagation on low angle terrain based on a compressive fracture of the weak layer. This theory was supported by field data from remotely triggered slab avalanches and whumpfs. Furthermore, observations of firn quakes and human triggered whumpfs showed that fracture propagation on low angle terrain is usually associated with vertical displacement of the snow surface, ranging from 0.1 to 2.5 cm. In Chapter 6,

direct observations of fractures in weak snowpack layers through use of a portable high speed camera are described with the objective of obtaining displacement measurements at the time of fracture as well as fracture speed measurements, which is one way to assess theoretical models.

Chapter 3

Field Methods

In this chapter the study areas as well as the most important field methods are described. Specific field methods and analytical methods are further outlined in following chapters. In Section 3.1, the study areas are described. How slopes were chosen for snowpack observations is outlined in Section 3.2. These observations consisted of recording a snowprofile (Section 3.3), performing stability tests (Section 3.4), measuring the shear strength of weak layers (Section 3.5) and performing fracture propagation and deep tap tests (Section 3.6). Finally, observations performed on skier-tested slopes are outlined in Section 3.7.

3.1 Study area and data

Data for this study were mainly collected at three field stations in the Columbia Mountains of British Columbia, Canada from the years 1996-2004 (Figure 3.1 (a)). The Blue River field station, located in the Cariboo and Monashee Mountains, is operated in cooperation with Mike Wiegele Helicopter Skiing. The Rogers Pass field station, located in the Selkirk Mountains, is operated in cooperation with Glacier National Park (Parks Canada). The Bobby Burns field station, located in the Purcell Mountains to the southeast of Glacier National Park, was operated in cooperation with Canadian Mountain Holidays. Additionally, some field work was conducted at the Kicking Horse Mountain Resort, in the Purcell Mountains.

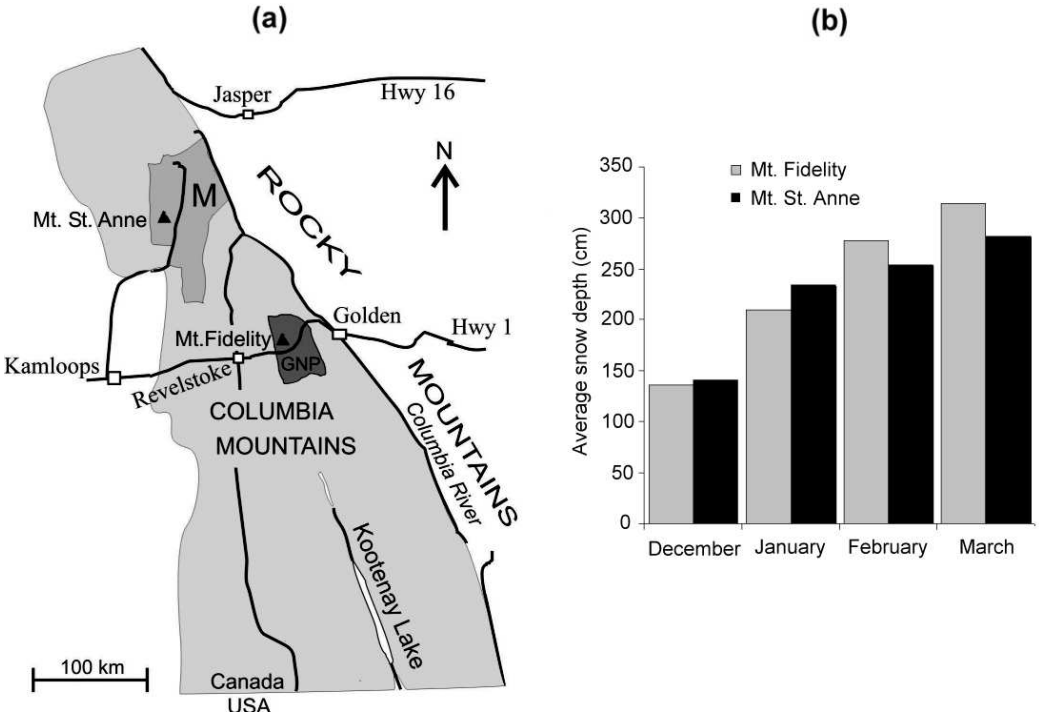

Figure 3.1: *(a) Map of the Columbia Mountains showing the area used by Mike Wiegele Helicopter Skiing (M) where the Blue River field station is located and Glacier National Park (GNP) where the Rogers Pass field station is located. Kicking Horse Mountain Resort is approximately 10 km west of Golden. The Bobby Burns field station is located to the southeast of GNP. (b) Five year average snowpack depth at Mt. Fidelity (1890 m) and Mt. St. Anne (1900 m) by month.*

Table 3.1: *Years of stability measurements and snowpack observations by location.*

Glacier National Park	Blue River	Bobby Burns	Kicking Horse Mountain Resort
1996-2004	1996-2004	1996-1998	2001-2004

The Columbia Mountains of British Columbia are characterized by a transitional climate with a heavy maritime influence (Hägeli and McClung, 2003). To the west the coastal snow climate is characterized by relatively warm temperatures and large amounts of precipitation. To the east, the Rocky Mountains, with a continental snow climate, typically have longer cold winters, with much less precipitation. The intermountain climate has transitional characteristics with more snow than the continental climate, and colder temperatures than the coastal climate. This allows persistent weak layers to develop and to be preserved over long periods of time. The snowpack at treeline is usually deeper than 2 m throughout the winter (Figure 3.1 (b)) and persistent weak layers are often composed of buried surface hoar or faceted crystals (Jamieson, 1995).

This thesis is part of an ongoing research project at the University of Calgary. Some of this work was only possible due to consistent measurements over a long time range. The author was involved in the field work during the winters of 2001-2002 to 2003-2004, mainly at Glacier National Park. Table 3.1 gives an overview of the years of data from stability measurements and snowpack observations used from different areas.

3.2 Site selection

For this study snowpack observations and tests were made in avalanche start zones and at regular study sites. In Blue River, the regular study site is located on Mt. St. Anne, at an altitude of 1900 m. The site can be accessed either by snowmobile or helicopter. Other sites were usually accessed by helicopter. In Glacier National

Park the regular study site is on Mt. Fidelity at an altitude of 1890 m. This site can be accessed by snowcat or by snowmobile. Other sites throughout the park were accessed by ski.

Regular study sites were visited frequently, typically once or more per week. Study sites were chosen in locations that are representative of the snowpack conditions common in surrounding avalanche terrain. Study sites were also chosen for their uniform snowpack, meaning that these sites are generally sheltered from the wind. Data from study sites were used to track changes in snowpack conditions over time and relate them to avalanche activity in surrounding terrain.

Unlike study sites, snowpack tests in avalanche start zones can only be related to recent avalanche activity on the same or adjacent slopes. Snowpack tests were made after the slope had been skier-tested (see below). In avalanche start zones, snowpack tests were made at a site typical of the start zone. If the slope was successfully skier-triggered, the area remaining for testing was reduced.

Site selection often included probing to determine the uniformity of snow depth and of major layers. Nevertheless, the primary concern when choosing start zone sites was the safety of the field workers. If conditions rendered a particular slope unsafe, another safer, and often smaller and/or less steep, slope was chosen.

3.3 Snowprofile observations

Manual snow profiles were performed at study sites and in avalanche start zones, according to the Canadian Avalanche Association's Observation Guidelines and Recording Standards (CAA, 2002). After a snowpit was dug, field researchers identified the

Figure 3.2: *Field researcher manually observing distinct changes in hardness throughout the snowpack to identify snowpack layers. ASARC photo.*

various snowpack layers. Some snowpack layers were identified visually (e.g. buried surface hoar layers), while the boundaries of most snowpack layers were identified by manually observing distinct changes in hardness within the snowpack (Figure 3.2). Most snowpack layers within approximately the upper 50 cm of the snowpack can accurately be identified this way. However, for deeper snowpack layers, many hardness transitions become more gradual and therefore observers often identify thicker snowpack layers with depth.

Once all snowpack layers were identified, various measurements were performed for each layer. This included depth measured vertically (D), hand hardness (h), density (ρ), grain form (F) and grain size (E) as well as layer thickness (Th). Site attributes were also recorded, including aspect, slope angle (ψ), elevation, vegetation zone, total snowpack depth, air temperature, wind, precipitation and sky conditions.

The depth of a layer was determined by measuring the vertical distance from the

snow surface to the lower boundary of the snowpack layer with an accuracy of 1 cm. The thickness was measured to the nearest mm for thin weak layers, whereas the thickness of thicker snowpack layers (i.e. > 5 cm) was measured to the nearest cm.

Grain forms were classified according to Colbeck et al. (1990): Precipitation Particles (PP), Decomposed and Fragmented crystals (DF), Rounded Grains (RG), Faceted Crystals (FC), Depth Hoar (DH), Wet Grains (WG), Surface Hoar (SH), Ice (I) and Crusts (CR). Crystal size was determined by looking at snow crystals extracted from the pit wall on a mm grid with an 8 X magnifier. The maximum and minimum representative crystal size was recorded. In the analysis, the average crystal size was used: $E = (E_{min} + E_{max})/2$. For the analysis, snowpack layers composed of PP, DF and RG were grouped in a category labelled *Storm* (i.e. non-persistent grain types). Snowpack instabilities in non-persistent snowpack layers are often referred to as storm snow instabilities. Furthermore, because the snowpack of the Columbia Mountains is generally thick (i.e. deeper than 150 cm), Depth Hoar is uncommon. Therefore, snowpack layers composed of DH were considered in combination with FC snowpack layers. Finally, SH layers were considered separately.

Density measurements were obtained by extracting snow samples using a 100 cm^3 cylindrical metal tube, with a diameter of 3.5 cm. After removal from the snow pit wall, the samples were weighed on a digital scale, with a precision of 0.1 g. Persistent weak layers were generally thin ($<$1 cm), making density measurements for these layers impractical. Therefore, there were almost no density measurements for persistent weak layers. Furthermore, it was usually not practical to measure the density of crusts.

Hand hardness measurements were performed more frequently, even for thin weak

Table 3.2: *Hand hardness index.*

Hand hardness Colbeck et al. (1990)	Hand hardness index h Geldsetzer and Jamieson (2000)
F	1
4F	2
1F	3
P	4
K	5

layers (e.g. SH) and crusts. The hardness is determined by inserting objects of different size in the snow with constant force. The objects from largest to smallest are: fist (F), four fingers (4F), one finger (1F), pencil (P) and knife (K). Intermediate values can be qualified with a "+" or "-" sign, giving fifteen levels ranging from F- to K+. For analysis, hand hardness measurements were indexed according to Table 3.2. Intermediate values were also allowed (e.g. 4F+ = 2.33). This index can be used to calculate the hand hardness H:

$$H = \frac{F_{constant}}{A_{fist}} M^{h-1} \tag{3.1}$$

where $F_{constant}$ is the approximately constant force applied manually, A_{fist} is the area of a gloved fist and M a constant (Geldsetzer and Jamieson, 2000). In this way, the hand hardness increases step wise by a factor of M (corresponding to a decrease in area of 1/M), using fist resistance as a base. Jamieson (1995) used a factor of $M = 2$, whereas Geldsetzer and Jamieson (2000) used a factor of $M = 4$. In order to adequately analyze hand hardness data, the proportionality factor M in Equation 3.1 was determined. As can be seen in Figure 3.3, taking $M = 2$ resulted in a nearly linear relation between the shear strength and the hand hardness as expected

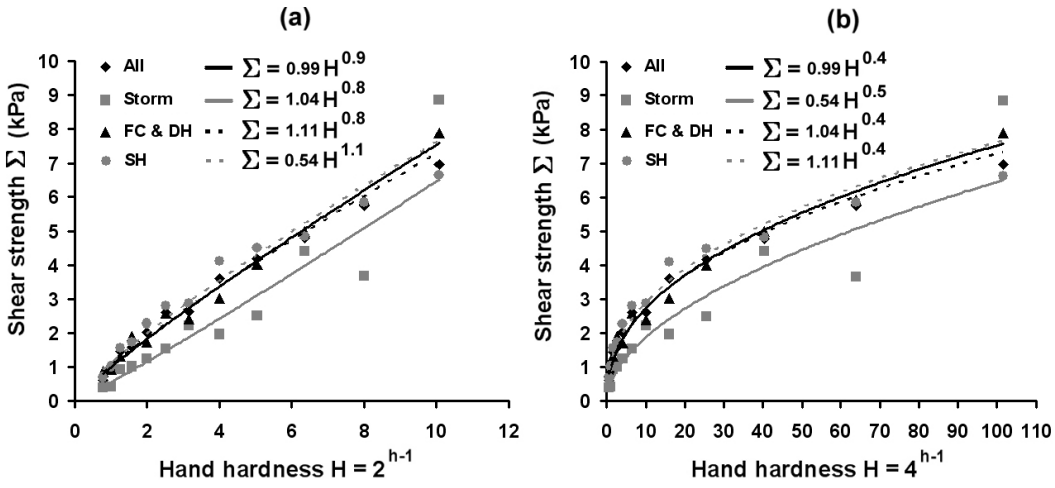

Figure 3.3: *Mean shear strength by hand hardness H given by Equation 3.1, for all snowpack layers as well as by grain group. (a) Hand hardness calculated with $M = 2$. (b) Hand hardness calculated with $M = 4$.*

(Jamieson, 1995), whereas taking $M = 4$ resulted in non-linear relationship between the shear strength Σ and the hand hardness. Throughout this thesis, H is calculated based on $M = 2$.

3.4 Stability tests

At each profile site, field observers typically performed three compression tests and usually a rutschblock test (see Figure 1.6). For the compression test, a column of snow 30 cm by 30 cm was isolated in the snowpit (CAA, 2002). The column was deep enough to expose potential weak layers (typically 1 to 1.5 m). Any fractures that occurred while isolating the column were assigned a score of 0. Once isolated, a shovel was placed squarely on top of the column. The first loading sequence was to tap the shovel blade ten times with the fingertips, only moving the hand from the wrist. Fractures within the first ten taps were rated as "easy". The second step

Table 3.3: *Loading steps and rutschblock scores (CAA, 2002)*

Rutschblock score	**Loading Step**
1	The block slides during digging or cutting
2	The skier approaches the block from above and gently steps down onto the upper part of the block (within 35 cm of the upper wall)
3	Without lifting the heels, the skier drops from a straight leg to a bent knee position, pushing downwards and compacting the surface layers
4	The skier jumps up and lands in the same compacted spot
5	The skier jumps again onto the same compacted spot
6	The skier steps down another 35 cm, almost to mid-block, and pushes once then jumps three times.
7	No failure

was to tap the shovel ten times with the fingertips, moving the arm from the elbow. Fractures that occur during the second loading sequence were rated as "moderate". The last loading sequence was to tap the shovel ten times with a close fist, moving the arm from the shoulder, and resulting fractures were rated as "hard". When a fracture appeared, a score was given based on the number of taps preceding the fracture.

Rutschblock tests were performed according to the Canadian Avalanche Association's Observation Guidelines and Recording Standards (CAA, 2002). After all potential failure planes were identified, a block of snow was isolated, by digging and/or by cutting with a 1.2 m long saw. The height of each block was sufficient to test all failure planes likely to be skier triggered (typically 0.6 to 1.2 m). The dimensions of the rutschblock were 2 m across and 1.5 m up-slope when the side walls were shovelled. If a saw was used to cut the side walls, the dimensions of the

Table 3.4: *Descriptive classification of fracture character in stability tests (van Herwijnen and Jamieson, 2003).*

Fracture character	**Code**	**Fracture characteristics**
Progressive Compression	PC	Fracture usually crosses column with one loading step, followed by gradual compression of the layer with subsequent loading steps
Resistant Planar	RP	Planar or mostly planar fracture that requires more than one loading step to cross column and/or block does not slide easily on weak layer.
Sudden Planar	SP	Planar fracture suddenly crosses column with one loading step and the block slides easily* on weak layer.
Sudden Collapse	SC	Fracture suddenly crosses column with one loading step and causes noticeable slope normal displacement.
Non-planar Break	B	Irregular fracture

* Block slides off column on steep slopes. On low angle slopes, hold sides of block and note resistance to sliding.

block were 2.1 m across the front of the block and 1.9 m across the back. This tapering reduced friction on the side walls, which might influence the score. Once isolated, the block was loaded according to Table 3.3. As an addition to the stability test score, avalanche researchers from the University of Calgary started systematically classifying fractures in stability tests in 1997, using a four level description of fracture character (Jamieson, 1999; van Herwijnen and Jamieson, 2002). After analyzing data from five winters of using this system, it was refined in December 2002 (van Herwijnen and Jamieson, 2003). Presently a five level description of fracture character (Table 3.4) is used by field workers of the University of Calgary, as well as by several avalanche safety operations in Canada. Additionally, during the winter of 2003-2004 observers recorded the release type of rutschblock tests as whole block

Figure 3.4: *Measurement of the shear strength of a weak layer with a shear frame. ASARC photo.*

(W), most of the block (M) or only an edge (Ed).

3.5 Shear frame test

The shear strength of weak layers was measured with a shear frame as described in Jamieson and Johnston (2001). After the weak layer of interest was identified in the snowpit, the overlying snow was removed so that the frame was filled when pushed into the snow to within 2-5 mm of the weak layer (Figure 3.4). Because snow adjacent to the layer might bond to the frame, a blade was used to cut around the frame. A force gauge attached to a cord on the shear frame was pulled smoothly and quickly ($<$ 1 s) in order to cause brittle fracture in the weak layer. The maximum force was recorded.

The size of the shear frame was either 0.01 m^2 or 0.025 m^2. Typically, the larger frame was used. However, for very soft slabs, or weak layers underlying very hard layers, using the smaller frame was advantageous. An average of 12 shear frames per weak layer were pulled. The shear strength Σ is the average maximum force of the twelve measurements divided by the frame area. The shear strength is then adjusted for size effects of the shear frame (Sommerfeld, 1980) by multiplying the obtained value by 0.63.

3.6 Fracture propagation test and deep tap test

The deep tap test (DTT) and the fracture propagation test (FPT) are prototype field tests that were introduced during the winter of 2002-2003. These tests were intended to index the fracture propagation propensity of a specific weak layer. Like the compression test, the deep tap test and the propagation test use a 30 x 30 cm isolated snow column. However, once the target weak layer was identified, the test column was levelled so that all but 15 cm (measured at the back wall) of snow above the weak layer was removed (Figure 3.5 (a)). To ensure that little applied energy was lost, and/or the test column was not ruined, the remaining 15 cm of snow on top of the weak layer has to be unlikely to crush during testing. Damping snow of at least one-finger (1F) hardness was usually adequate (Campbell, 2004). This is important for the validity of the assumption that most of the energy applied during loading reaches the weak layer. The weak layer was then notched 5 cm on the right side of the column with a snow saw to simulate a crack in the weak layer with the idea that sufficient additional applied energy will cause the crack (notch) to propagate

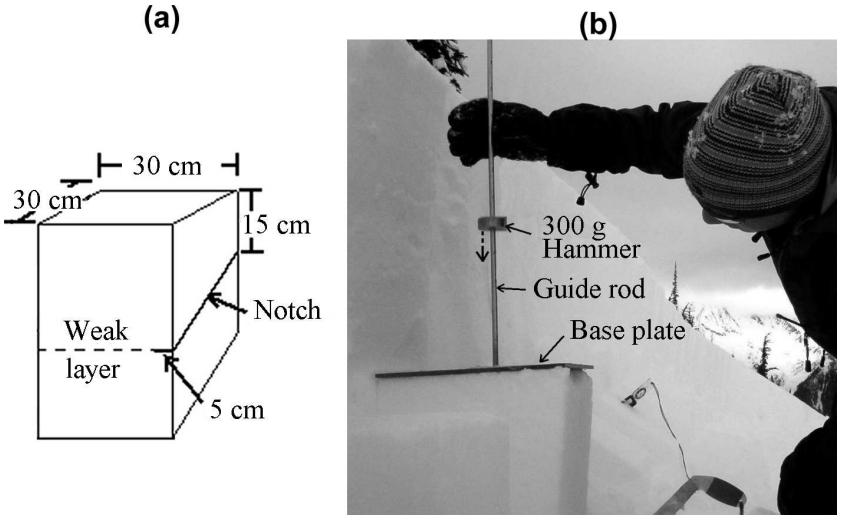

Figure 3.5: *(a) The test column dimensions and preparation steps (notch and levelling) for the fracture propagation test or the deep tap test. (b) The drop hammer tester being used on a fracture propagation test. After Campbell (2004).*

(Campbell, 2004).

For the deep tap test, the isolated column was loaded using the same loading steps as for the compression test (i.e. 30 manual taps). For the fracture propagation test, a drop hammer tester (Stewart, 2002) was used to load the test column. The drop hammer tester (Figure 3.5 (b)) consists of a 30 x 30 cm horizontal base plate, with a vertical guide rod mounted in the centre, and 300 g or 1 kg hammers used for loading. An appropriate hammer weight was chosen based on practice test results and mounted on the guide rod. The hammer was then dropped from successive 5 cm height increments, starting from 5 cm, until the fracture propagated across the entire test column. The drop height (d) which caused the fracture to propagate was recorded. For analysis, the drop height was converted to energy, termed drop hammer energy (DHE):

$$DHE = \frac{dgm}{w(l/\cos\psi)} \tag{3.2}$$

where g is the acceleration due to gravity, m is the mass of the hammer used, w is the width of the test column, l is the length of the test column measured horizontally and ψ is the slope angle. This equation assumes all the energy from the drop hammer tester reaches the weak layer. Therefore, all deep tap tests and fracture propagation tests with visible crushing of the overlying snow and/or fractures in layers other than the target weak layer were rejected.

3.7 Skier-tested slopes

Test skiing a slope is also considered to be an effective stability test (McClung and Schaerer, 1993: 130). A skier adds dynamic stress to the snow by his or her weight during descent, thereby testing the stability of any underlying weak layers. Safety measures must always be observed when carrying out these tests. Field observers regularly performed ski tests on small slopes that were judged safe given the snowpack conditions at the time (Figure 3.6). For safety reasons, ski tests were limited to terrain free of terrain traps and snowpack conditions unlikely to produce an avalanche larger than Size 1.5, introducing a bias in the data.

On each skier-tested slope a snow profile, three compression tests, and usually a rutschblock test were observed. Furthermore, on most skier-tested slopes 12 shear frame tests were performed on the primary weakness. The *primary weakness* was identified by field observers as being the snowpack layer most susceptible to skier-triggering. It was the failure layer of a slab avalanche when the skier-tested slope

Figure 3.6: *Field observer performing a ski test on a relatively small slope, which was judged safe under the present snowpack conditions (ASARC photo).*

was triggered. On skier-tested slopes that were not triggered, the primary weakness was most often identified through the use of stability tests or it was identified by field observers based on experience and recent avalanche activity.

Additionally, fracture line profiles were observed on slopes where skiers had accidently triggered a slab avalanche. These avalanches were reported to research staff by a guide or a park employee and investigated within one or two days after the event occurred. If snowpack conditions had changed substantially since the avalanche was triggered, the data were not used.

When conditions were favourable to whumpfing (Section 1.2), field researchers travelled to sites where whumpfs were expected. When a whumpf occurs, a distinct sound is heard and the movement of the overlying slab often causes vegetation pro-

truding through the surface to move. At whumpf sites a snow profile was observed outside the area where the weak layer had fractured. Furthermore, three compression tests were performed and usually shear frame tests. At nine whumpf sites, an additional profile was observed inside the area where the weak layer had fractured. This provided information about the amount of vertical displacement of the overlying slab during fracture by comparing the weak layer thickness in the undisturbed area with the thickness of the fractured weak layer.

Chapter 4

Snowpack properties associated with skier-triggering

4.1 Introduction

Snow stability evaluation is considered as the essential element of avalanche forecasting (McClung and Schaerer, 1993: 124). Stability evaluation for avalanche forecasting relies on weather and snowpack data as well as avalanche observations. Snowpack data, consisting of stability tests and snow profiles, become crucial information in the absence of avalanche occurrence data. In this chapter, snowpack properties from snow profiles are analyzed with respect to skier triggering. Stability test results, in particular those from compression tests, are analyzed in the next chapter.

Earlier field studies on snowpack properties summarized snowpack and terrain properties associated with avalanches, most of which released naturally (e.g. Perla, 1977). Jamieson and Johnston (1998) performed the first detailed study of snow cover characteristics that affect skier-triggering. Since then, various studies have examined the role of snowpack parameters in skier-triggered avalanches with increasing detail (see Section 2.2). Based on the comparison of stable and unstable snow profiles, Schweizer and Jamieson (2003b) showed that there are significant variables that indicate instability. They found the following snowpack variables to be indicative of instability: weak layer grain size and hand hardness, difference in hardness across

the failure interface and difference in grain size across the failure interface. Whereas these variables are likely to affect slab avalanche release in terms of fracture initiation (i.e. stress transmission, stress concentration in the weak layer and strength of the weak layer), the relation between these snowpack variables and fracture propagation is less clear. In a recent review on snow avalanche formation, Schweizer et al. (2003) state that the properties of the overlying slab have to be considered, in particular for fracture propagation. However, no further explanation is given. The goal in this chapter is to shed some light on the relationship of various snowpack parameters with skier-triggering and in particular with fracture propagation.

Since this thesis is part of an ongoing research project at the University of Calgary, some of the data used in the analysis below were also used in previously published studies on snowpack properties associated with skier-triggered slab avalanches: Jamieson and Johnston, 1998; Johnson et al., 2000b; ; Schweizer and Jamieson, 2001, 2003a and 2003b; Schweizer et al., in press. The analysis presented here was intended to corroborate and expand previous findings with data from over 500 profiles from skier-tested slopes (both skier-triggered and not triggered), whumpfs and remotely triggered slab avalanches. Furthermore, there were also some important differences in methodology. In previous research, differences in crystal type and hand hardness between the weak layer and the adjacent layer were taken across the failure interface (e.g. Schweizer and Jamieson, 2003b). The failure interface was defined as the boundary between the weak layer and *either* of the adjacent layers. If the failure interface was not reported in the profile, first the maximum difference in hand hardness and second the maximum difference in crystal size were considered, to choose either the layer above or below the weak layer as the adjacent layer. Therefore, there

was an inherent bias towards larger values of the hand hardness difference and the crystal size difference. Furthermore, only snowpack properties from one adjacent layer were considered. In the present analysis, the differences in hand hardness and crystal size between the weak layer and *both* the adjacent layers as well as snowpack properties from *both* the adjacent layers are considered separately.

This chapter is organized as follows. The data and specific methods for the analysis are described first (Section 4.2). Since 1996, researchers at the University of Calgary have collected many snow profile data containing a wealth of information. The typical distribution as well as results from correlation analysis of these snowpack data are reported in Sections 4.3.1 and 4.3.2. Results from the statistical comparison of stable and unstable snowpack characteristics with respect to skier-triggering are outlined in Sections 4.3.3 and 4.3.4. Furthermore, in Section 4.3.5 snowpack properties from remotely triggered avalanches, whumpfs and medium and large skier-triggered slab avalanches (i.e. $>$ Size 2; Table 1.1) are compared to snowpack properties from small skier-triggered slab avalanches (i.e. $\leq$ Size 2). These three types of slab avalanches are considered separately from small skier-triggered slab avalanches because they represent snowpack conditions which favour fracture propagation. A summary of the results is given in Section 4.4, followed by a discussion of the significant snowpack parameters in Section 4.5. Finally some brief conclusions are drawn in Section 4.6.

Table 4.1: *Number of observations for the each measured snowpack variables.*

Variable	Symbol	Unit	N
Depth	D	cm	19722
Thickness	Th	cm	19722
Density	ρ	kgm^{-3}	8501
Hand hardness index	h	˜	19120
Crystal Type	F	˜	17663
Crystal Size	E	mm	15752
Shear strength	Σ	Pa	1674

4.2 Data and methods

A database consisting of 1780 snow profiles observed since 1996 by researchers of the University of Calgary was analyzed to determine typical distributions of snowpack parameters and correlations between various snowpack parameters by grain group. In total, 19722 snowpack layers were recorded with information about depth (D), thickness (Th), crystal type (F), crystal size (E), hand hardness index (h), density (ρ) and shear strength (Σ). However, not all variables were recorded in each profile and for each layer. The number of observations for each snowpack parameter are shown in Table 4.1.

There were relatively fewer density measurements partly because it was not possible to measure the density of thin snowpack layers (i.e. $Th < 3$ cm) and it is often difficult to measure the density of crusts. Furthermore, there were far fewer shear strength data. The shear strength was only measured consistently for persistent weak layers on regular study sites. Furthermore, shear strength measurements were also performed on the primary weakness (see below) on skier-tested slopes.

For the identification of typical distributions and correlations of snowpack variables affecting skier-triggering, only data up to a depth of 150 cm measured from the

snow surface were considered. This was done because the distribution of the data was affected by both the depth of the snow pits (mean = 120 cm) and to a lesser extent, the total snow depth (Figure 3.1 (b)). Furthermore, most of the data were collected within the upper 150 cm of the snowpack (93 %), and this range encompasses the typical range of depths for skier-triggering (e.g. Camponovo and Schweizer, 1996; Schweizer and Jamieson, 2003b).

Differences in snowpack properties between an arbitrary snowpack layer (SL) and the layer above (La) were considered separately from those with the layer below (Lb). The hand hardness difference was taken as the difference in hand hardness index between the adjacent layers and the snowpack layer: $\Delta h_{La} = h_{La} - h_{SL}$ and $\Delta h_{Lb} = h_{Lb} - h_{SL}$. Crystal size differences were obtained by subtracting the average crystal size of the adjacent layers from the snowpack layer crystal size: $\Delta E_{La} = E_{SL} - E_{La}$ and $\Delta E_{Lb} = E_{SL} - E_{Lb}$.

Pearson product-moment linear correlations (Walpole et al., 2002, p. 392) were used to determine associations between snowpack properties. This correlation technique requires that the data to be measured on at least an interval scale (e.g. crystal size). Spearman Rank order correlations (Walpole et al., 2002, p. 620) were used to determine associations between snowpack properties measured on an ordinal scale (e.g. hand hardness). The correlation coefficient, R_p for the Pearson product moment correlation and R_s for the Spearman Rank order correlation, ranges from -1 to 1, with -1 and 1 indicating perfect correlations, and 0 indicating no correlation. All correlation coefficients are considered significant at the $p < 0.05$ level.

A subset of the large data set consisted of 520 profiles observed next to skier-triggered slabs (279) and on skier-tested slopes that did not release a slab avalanche

(241). These data were used to compare stable and unstable snowpack characteristics. One hundred fifty-six of these skier-triggered slabs were directly triggered avalanches (either skier-tested slopes that were skier-triggered or accidently triggered slab avalanches), 44 were remotely triggered slab avalanches and 66 were whumpfs (see Section 1.2). Additionally, five profiles were observed at the trigger point of remotely triggered slab avalanches, and nine profiles at whumpf sites inside the whumpfed area where the weak layer had fractured.

In order to compare stable and unstable snowpack variables from skier-tested slopes, two data sets were constructed. The first data set contained data from all snowpack layers observed on skier-tested slopes and next to accidently triggered slab avalanches. Snowpack layers that were the failure layer of skier-triggered slab avalanches were termed "unstable". All other snowpack layers were considered "stable". This data set was used to compare stable and unstable snowpack parameters without selection bias since each snowpack layer was considered a potential weak layer (WL). The second data set only contained data from primary weaknesses of stable and unstable profiles. The primary weakness was the snowpack layer considered the most susceptible to skier-triggering (Section 3.7). It was identified as being the failure layer of a skier-triggered slab or through use of stability tests. Primary weaknesses that were the failure layer of a slab avalanche are referred to as "unstable".

In order to assess snowpack variables associated with snowpack conditions favouring fracture propagation, unstable primary weaknesses were analyzed in more detail. Snowpack variables from primary weaknesses associated with skier-triggered slabs that were not remotely triggered and smaller or equal to Size 2 (Table 1.1) were con-

trasted with snowpack variables from primary weaknesses associated with remotely triggered slab avalanches, whumpfs and skier-triggered slab avalanches larger than Size 2. In the remainder of this chapter, *small avalanches* will refer to slab avalanches not remotely triggered that were smaller or equal to Size 2. *Large avalanches* will refer to slab avalanches not remotely triggered that were larger than Size 2.

The robust non-parametric Mann-Whitney U-test was used (Walpole et al., 2002, p. 605) to contrast stable and unstable snowpack parameters. Furthermore, this test was also used to compare snowpack properties from small avalanches with snowpack properties from whumpf sites, remotely triggered avalanches and large avalanches. The non-parametric Mann-Whitney U-test compares the medians of two non-normal distributions. It is especially useful when dealing with ordinal data (e.g. hand hardness). All types of weak layers were contrasted collectively and the three categories of weak layers were analyzed separately as well (*Storm*, FC and DH, and SH).

Slab properties were also calculated. The hand hardness of the slab (H_{slab}) was calculated as the weighted average of the hand hardness of the snowpack layers comprised in the slab above the snowpack layer under consideration or the primary weakness:

$$H_{slab} = \frac{\Sigma_i (H_i \cdot Th_i)}{Th_{slab}} \tag{4.1}$$

with Th_{slab} the slab thickness ($\Sigma_i Th_i = Th_{slab}$), H_i the hand hardness of slab layer i of thickness Th_i. Using Equation 3.1, the hand hardness H_{slab} was converted to the corresponding hand hardness index h_{slab}. The difference in hand hardness index between the weak layer and the slab was calculated as $\Delta h_{slab} = h_{slab} - h_{WL}$. Furthermore, a "bridging index" was calculated by multiplying the slab thickness by

the hardness (Schweizer and Jamieson, 2003b): $B_{slab} = h_{slab}Th_{slab}$.

4.3 Results

In this section, the results from the statistical analysis of the various data sets are described. First, the typical distributions of snowpack variables are considered. Most snowpack variables were non-normally distributed and some are ordinal data (e.g. hand hardness). Therefore the distributions were described by the median and the first (Q1) and third (Q3) quartiles, where 25% of the data are less than Q1 and 25% of the data are greater than Q3. The results are described for each grain group separately.

Second, results from the correlation analysis are presented for the following snowpack variables: depth of the layer, layer thickness, density, crystal size, hand hardness, differences in crystal size, differences in hand hardness and shear strength.

Third, stable and unstable snowpack parameters are contrasted using the non-parametric Mann-Whitney U-test. Various snowpack properties from the weak layer, the overlying slab, the adjacent layers and differences in snowpack variables between the adjacent layers and the weak layer are described. This is followed by the results of the comparison of snowpack variables from stable and unstable primary weaknesses.

Finally, snowpack variables from remotely triggered slab avalanches, whumpfs and large skier-triggered slab avalanches are compared to snowpack properties from small skier-triggered slab avalanches, using the non-parametric Mann-Whitney U-test.

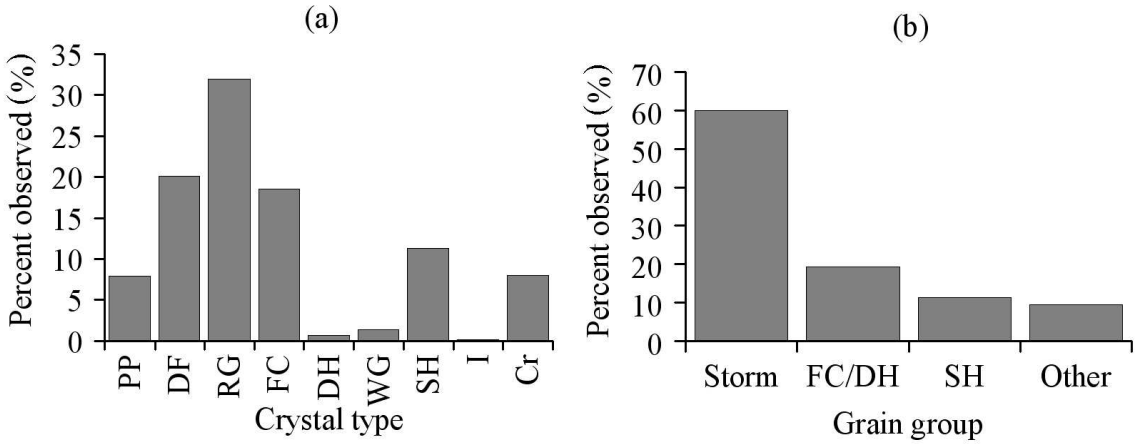

Figure 4.1: *(a) Frequency of observed layers by grain type. (b) Frequency of observed layers by grain group classified as Storm (PP, DF and RG), FC and DH, SH and Other (WG, I and CR).*

4.3.1 Typical distributions of snowpack variables

The distribution of the data by grain type is shown in Figure 4.1 (a). As expected for a snowpack from the Columbia Mountains, snowpack layers were predominantly composed of PP, DF and RG (7.8%, 20.1% and 31.9%, respectively). Eighteen percent of the snow-pack layers were composed of faceted crystals, and only 0.6% of depth hoar (DH). Furthermore, buried Surface Hoar (SH) layers were relatively common (11 %), which is a well known fact about this snow climate (e.g. Hägeli and McClung, 2003). Finally, crusts (CR) were also commonly observed (8.2 %). The distribution of the data by grain group is shown in Figure 4.1 (b). As expected, most snowpack layers were *Storm* layers (60 %)

An overview of descriptive statistics for measured snowpack properties by grain group is given in Table 4.2. The median thickness of SH layers (1 cm) was much lower than that of *Storm* layers (10 cm) and FC and DH layers (9 cm). Furthermore, the ranges of values for the layer thickness for *Storm* layers and layers of FC and DH

Table 4.2: *Descriptive statistics for snowpack layer properties by grain group, showing the number of data points (N), the lowest value (Min), the lower quartile (Q1), the median, the upper quartile (Q2) and the highest value recorded (Max). Snowpack properties shown are layer thickness (Th), density (ρ), hand hardness index (h), differences in hand hardness (Δh_{La} and Δh_{Lb}), crystal size (E), differences in crystal size (ΔE_{La} and ΔE_{Lb}) and shear strength (Σ).*

	Storm					
Parameter	N	Min	Q1	Median	Q3	Max
Th (cm)	9875	0.1	5	10	16	99
ρ (kg m^{-3})	6345	10	123	178	238	438
E (mm)	9596	0.1	0.6	1.0	1.3	5
h	9808	F-	4F-	1F	P-	K+
Σ (kPa)	226	0.02	0.58	1.06	2.08	11.79
ΔE_{La} (mm)	7445	-44.3	-0.6	-0.1	0.0	4.0
ΔE_{Lb} (mm)	8203	-44.3	-0.5	0.0	0.3	4.0
Δh_{La}	9794	-4	-1	-0.33	0	4
Δh_{Lb}	10505	-3.66	-0.33	0.33	0.66	4.33
	FC and DH					
Parameter	N	Min	Q1	Median	Q3	Max
Th (cm)	3160	0.1	4	9	16	93
ρ (kg m^{-3})	1535	23	203	249	288	430
E (mm)	3074	0.3	0.8	1.0	1.5	10
h	3129	F-	4F+	1F	P-	K+
Σ (kPa)	261	0.06	1.20	1.83	3.01	11.70
ΔE_{La} (mm)	2566	-34.3	-0.5	0.0	0.3	7.0
ΔE_{Lb} (mm)	2135	-24.0	-0.5	-0.1	0.0	3.0
Δh_{La}	2951	-4	-0.66	0	0.66	4
Δh_{Lb}	2624	-3.33	-0.33	0.33	1	4
	SH					
Parameter	N	Min	Q1	Median	Q3	Max
Th (cm)	1872	0.1	0.5	1	1	6
E (mm)	1827	0.4	3.0	5.0	7.5	45
h	1651	F-	4F-	4F+	1F	K+
Σ (kPa)	1069	0.06	1.17	2.26	3.94	16.42
ΔE_{La} (mm)	1582	-2.5	2.5	4.3	6.8	44.3
ΔE_{Lb} (mm)	1520	-3.0	2.5	4.3	6.5	44.3
Δh_{La}	1619	-2.33	0.33	1	1.33	3.66
Δh_{Lb}	1627	-1.66	0.33	1	1.66	4

were much larger than for buried SH layers, which ranged in thickness from 0.1 to 6 cm. Consequently, no density measurements were available for SH layers. However, the density of layers composed of FC and DH (median 249 kg m^{-3}) was generally higher than that of *Storm* layers (median 178 kg m^{-3}).

The median hand hardness was lowest for buried SH layers (4F+). Furthermore, the distribution of hand hardness data for SH layers was skewed towards lower values, as can be seen by the lower values of $Q1$ and $Q3$ in Table 4.2. The median hardness difference on the other hand, was lowest for *Storm* snow layers (-0.33 for both Δh_{La} and Δh_{Lb}) and highest for SH layers (1 for both Δh_{La} and Δh_{Lb}). The differences in hand hardness by grain group are shown in Figure 4.2. As can be seen, most surface hoar layers were softer than the adjacent snow layers, since the hardness difference was generally positive. This was not the case for *Storm* layers or FC and DH layers, since a large portion of the hardness difference data was negative (Figure 4.2). Furthermore, Δh_{La} was significantly lower than Δh_{Lb} for *Storm* snow layers ($N = 16221$, U-test $p = 10^{-8}$) as well as for FC and DH layers ($N = 6335$, U-test $p = 10^{-6}$). However, this was not the case for SH layers (N =3389, U-test $p = 0.44$).

The median crystal size for *Storm* snow layers (1 mm) was similar to that for FC and DH layers (1 mm). Buried surface hoar crystals on the other hand, were typically much larger (median 5 mm). Furthermore, the range of values for the crystal size was much larger for SH crystals than for other types of crystals (Table 4.2). The differences in crystal size between snowpack layers and adjacent layers by grain type are shown in Figure 4.3. Clearly, the difference in crystal size between SH layers and adjacent layers was much larger than for other types of snowpack layers. Moreover, the typical range of crystal size differences was much larger for SH layers. This is

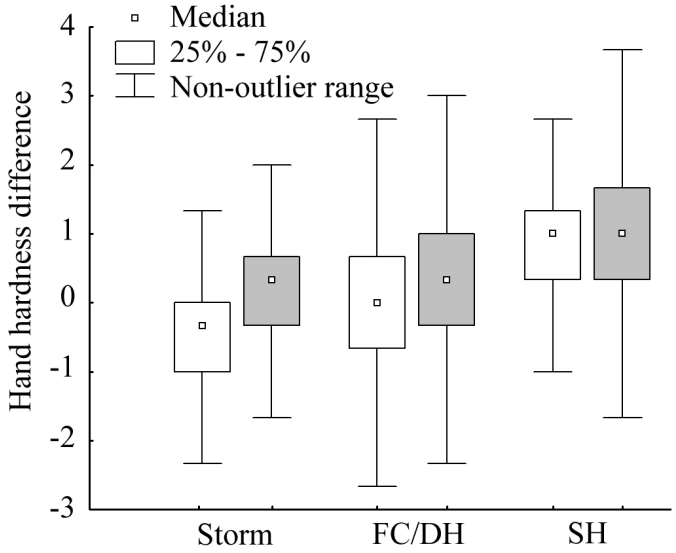

Figure 4.2: *Hand hardness difference between the layer above and the snowpack layer (white boxes) and the layer below and the snowpack layer (grey boxes), by grain group.*

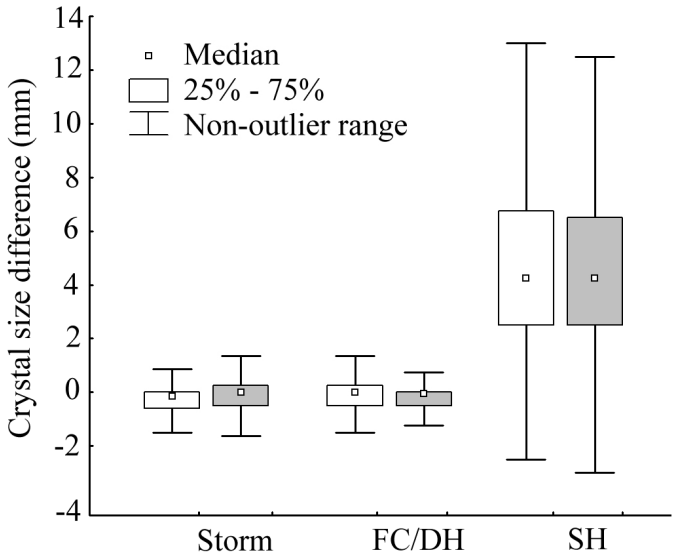

Figure 4.3: *Crystal size difference between the layer above and the snowpack layer (black and white) and the layer below and the snowpack layer (grey), by grain group.*

understandable since SH crystals are generally larger than other types of crystals (Table 4.2).

Finally, the median measured shear strength was lowest for *Storm* layers, and highest for buried SH layers. However, shear strength data were biased. The shear strength of weak layers composed of buried Surface Hoar layers was measured more often and up to a greater depth than for other snowpack layers. Furthermore, shear frame measurements were only performed on snowpack layers that were considered potential failure layers for slab avalanches. Therefore, only strength data for relatively weak snowpack layers were available.

4.3.2 Correlation analysis

Depth

An overview of the correlation between snowpack variables and depth is given in Table 4.3. The density, hand hardness and shear strength of snowpack layers exhibited significant positive correlations with depth, regardless of grain group. This comes as no surprise, since it is a well known fact that the density of snowpack layers increases with depth (e.g. McClung and Schaerer, p. 64, 1993). Furthermore, the hardness as well as the shear strength of snowpack layers are known to depend on density (e.g. Mellor, 1975), hence the significant positive correlations. This means that in general, the density, the hand hardness and the shear strength of snowpack layers increase with depth (Figure 4.4). However, the correlation coefficients of the correlations between H and D and between ρ and D were largest for *Storm* layers (R_p = 0.75 and $R_p = 0.79$, respectively), indicating that these snowpack layers generally increased in hardness and density more rapidly with increasing depth than FC and

Table 4.3: *Overview of correlation statistics between measured snowpack variables and depth by grain group. The number of observations (N), the correlation coefficient (R_p for the Pearson correlation and R_s for the Spearman correlation) and the significance (p) are given for each variable.*

	Depth		
Parameter	*Storm*	FC DH	SH
Th	N=9875 R_p=0.38 $p < 10^{-8}$	N=3160 R_p=0.33 $p < 10^{-8}$	N=1873 R_p=-0.11 p=10^{-7}
ρ	N=5978 R_p=0.75 $p < 10^{-8}$	N=1535 R_p=0.65 $p < 10^{-8}$	- - -
E	N=9595 R_p=-0.36 $p < 10^{-8}$	N=3074 R_p=0.29 $p < 10^{-8}$	N=1827 R_p=-0.06 p=0.012
H	N=9808 R_s=0.79 $p < 10^{-8}$	N=3129 R_s=0.50 $p < 10^{-8}$	N=1651 R_s=0.60 $p < 10^{-8}$
Σ	N=224 R_p=0.52 $p < 10^{-8}$	N=261 R_p=0.35 $p < 10^{-8}$	N=1069 R_p=0.66 $p < 10^{-8}$
ΔE_{La}	N=7444 R_p=-0.11 $p < 10^{-8}$	N=2566 R_p=0.06 p=0.003	N=1582 R_p=0.01 p=0.587
ΔE_{Lb}	N=8202 R_p=-0.18 $p < 10^{-8}$	N=2135 R_p=-0.02 p=0.356	N=1520 R_p=-0.06 p=0.029
Δh_{La}	N=8299 R_s=0.01 p=0.255	N=2951 R_s=0.10 p=10^{-7}	N=1619 R_s=0.27 $p < 10^{-8}$
Δh_{Lb}	N=8997 R_s=-0.26 $p < 10^{-8}$	N=2624 R_s=-0.18 $p < 10^{-8}$	N=1627 R_s=-0.03 p=0.287

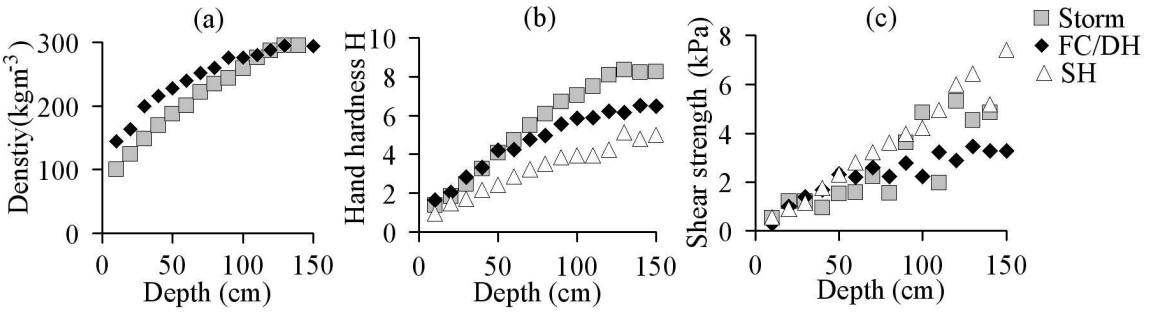

Figure 4.4: *Snowpack variables by depth for each grain group. (a) Median density by depth. (b) Median hand hardness by depth. (c) Median shear strength by depth.*

DH or buried SH (Figure 4.4 (a) and (b)). A similar trend was not found for the shear strength, which was only measured for weak layers. However, as mentioned earlier, the shear strength data were biased since more shear strength measurements were performed on buried SH layers and up to a greater depth. Nevertheless, as can be seen in Figure 4.4 (c), the shear strength of buried SH layers generally increased more with depth than for FC and DH layers.

The thickness of *Storm* layers and FC and DH layers had a significant positive correlation with depth (Table 4.3), indicating that these layers were generally thicker at greater depth. Although settlement of the snowpack causes layers to decrease in thickness, observers generally identify thicker snowpack layers with depth (see Section 3.3). For buried SH layers, on the other hand, there was a weak negative correlation between layer thickness and depth (R_p = -0.11), as well as a very weak negative correlation between crystal size and the depth. On the other hand, there was a general trend for deeper *Storm* layers to be composed of smaller crystals (Table 4.3). This is not surprising since this category is composed of PP, DF and RG. Precipitation particles (PP) are relatively large crystals (i.e. typically 1 to 4 mm) generally found in the upper snowpack. These dendritic crystals are deposited

during snowfall and begin changing into smaller rounded particles (i.e. DF and RG) as soon as they are on the snow surface and get buried by subsequent snowfall (Section 1.1).

The crystal size of FC and DH layers, on the other hand, had a positive correlation with depth. In the Columbia Mountains, typically there are two types of faceted crystals present in the snowpack. There usually is a facet-crust combination that forms in early winter (November), which is often referred to as the November facets (e.g. Jamieson et al., 2001). These facet-crust combinations often form when dry snow falls on top of a wet snow layer (Jamieson, 2004). In this process, latent heat from the wet snow layer produces a large temperature gradient in the overlying snow until the wet layer freezes, driving the faceting process (Colbeck and Jamieson, 2001). If conditions are right, this can produce well-developed facets (i.e. 2-3 mm) which can remain in the snowpack throughout the winter (Jamieson et al., 2001). On the other hand, smaller faceted crystals form near the surface as a result of near surface faceting (e.g. Birkeland, 1998). These faceted crystals form when extreme near-surface temperature gradients, caused by radiative cooling, diurnal faceting or melt-layer faceting, drive the kinetic metamorphism process in the upper snowpack layers. Typically, these faceted crystal are relative small (i.e. 0.5-1 mm).

Differences in crystal size between snowpack layers and the adjacent layers were not strongly influenced by the depth of the snowpack layer. Only ΔE_{La} and ΔE_{Lb} correlated negatively with the depth of *Storm* layers (R_p = -0.11 and R_p = -0.18, respectively), indicating that as these layers get buried deeper in the snowpack, the difference in crystal size between *Storm* layers and the adjacent layers decreases. Similarly, the differences in hand hardness did not correlate strongly with depth

(Table 4.3). For buried SH layers and FC and DH layers, Δh_{La} exhibited a weak positive correlation with depth (R_s = 0.10 and R_s = 0.27, respectively), indicating that the difference in hardness increases with depth. On the other hand, Δh_{Lb} exhibited a weak negative correlation with depth for *Storm* layers and FC and DH layers (R_s = -0.26 and R_s = -0.18, respectively).

Layer thickness

An overview of the correlation between snowpack variables and layer thickness is given in Table 4.4. Thicker *Storm* layers and thicker FC and DH layers generally had a higher density (Table 4.4). However, the correlations were not strong (R_p = 0.12 and R_p = 0.16, respectively). Furthermore, there were stronger correlations between layer thickness and depth as well as between density and depth for these snowpack layers (Table 4.3). Therefore, the correlation between the density and the layer thickness was caused by a combined effect of an increase in recorded layer thickness and density with depth. For the same reasons, there was a significant negative correlation between E and Th for *Storm* layers (Figure 4.5) and significant positive correlations between H and Th for *Storm* layers and FC and DH layers.

As seen in Table 4.4, the thickness of buried SH layers generally increased with increasing crystal size (Figure 4.5). Since buried SH layers are composed of only one layer of crystals (e.g. Figure 1.2) this was expected. Furthermore, there was a negative correlation between hand hardness and layer thickness, indicating that the hardness of buried SH layers typically decreases for thicker layers. Consequently, the shear strength of buried SH layers also decreased with increasing layer thickness for these snowpack layers.

Table 4.4: *Overview of correlation statistics between measured snowpack variables and layer thickness by grain group. The number of observations (N), the correlation coefficient (R_p for the Pearson correlation and R_s for the Spearman correlation) and the significance (p) are given for each variable.*

	Layer thickness		
Parameter	Storm	FC DH	SH
ρ	N=5978 R_p=0.12 $p < 10^{-8}$	N=1535 R_p=0.16 $p < 10^{-8}$	- - -
E	N=9595 R_p=-0.19 $p < 10^{-8}$	N=3074 R_p=0.02 p=0.362	N=1827 R_p=0.55 $p < 10^{-8}$
H	N=9808 R_s=0.16 $p < 10^{-8}$	N=3129 R_s=0.18 $p < 10^{-8}$	N=1651 R_s=-0.23 $p < 10^{-8}$
Σ	N=224 R_p=-0.11 p=0.105	N=261 R_p=-0.12 p=0.051	N=1069 R_p=-0.24 $p < 10^{-8}$
ΔE_{La}	N=7444 R_p=-0.04 p=0.001	N=2566 R_p=0.02 p=0.285	N=1582 R_p=0.53 $p < 10^{-8}$
ΔE_{Lb}	N=8202 R_p=-0.04 p=0.001	N=2135 R_p=0.02 p=0.285	N=1520 R_p=0.55 $p < 10^{-8}$
Δh_{La}	N=8299 R_s=-0.14 $p < 10^{-8}$	N=2951 R_s=-0.20 $p < 10^{-8}$	N=1619 R_s=0.21 $p < 10^{-8}$
Δh_{Lb}	N=8997 R_s=0.08 $p < 10^{-8}$	N=2624 R_s=-0.12 $p < 10^{-8}$	N=1627 R_s=0.22 $p < 10^{-8}$

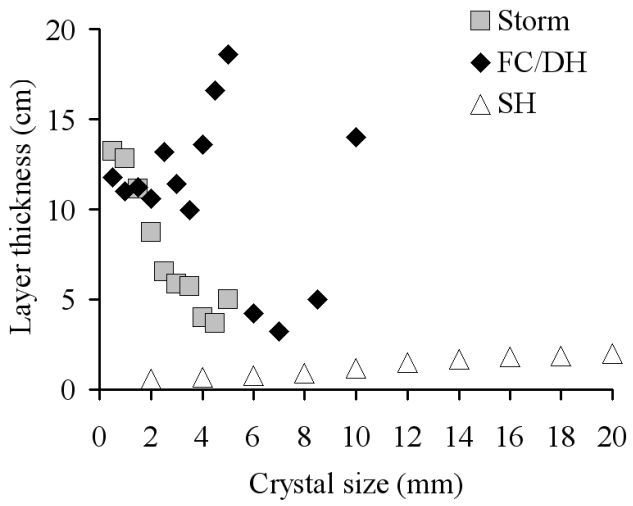

Figure 4.5: *Layer thickness by crystal size for each grain group.*

Differences in crystal size between snowpack layers and the adjacent layers did not correlate strongly with layer thickness, except for SH layers. For these layers there was a positive correlation between crystal size differences and layer thickness. This was no surprise since layer thickness for SH layers had a positive correlation with crystal size.

Finally, thicker *Storm* layers and FC and DH layers typically had lower hand hardness differences than thin layers (Table 4.4). This was expected since there was a positive correlation between hand hardness and layer thickness for these layers. However, the correlation coefficients were not very high. On the other hand, thicker SH layers were generally softer than the adjacent layers, as can be seen by the stronger positive correlation between Δh_{La} and Th and Δh_{Lb} and Th in Table 4.4.

Density

An overview of the correlation between snowpack variables and density is given in Table 4.5. It comes as no surprise that the hand hardness and the shear strength had significant positive correlations with density. This indicated that snowpack layers of greater density are generally harder and have higher shear strength. These relationships have long been recognized (e.g. Keeler and Weeks, 1968). Furthermore, there was a negative correlation between the density of *Storm* layers and the crystal size, indicating that layers with larger crystals typically had a lower density. On the contrary, the density of FC and DH layers typically increased with crystal size (Table 4.5). However, as for the layer thickness, these correlations were significantly affected by the depth of the layer. For *Storm* layers, the density increased with depth, whereas the crystal size typically decreased with depth. The combination of these two effects led to a decrease in density for *Storm* layers with larger crystals. For FC and DH layers on the other hand, both the density and the crystal size increased with depth, hence the positive correlation between E and ρ for these snowpack layers.

The density of snowpack layers only correlated weakly with ΔE_{La} and Δh_{La} for *Storm* layers. Both correlation coefficients were negative (R_p = -0.20 and R_s = -0.07, respectively), indicating that both ΔE_{La} and Δh_{La} tended to decrease with increasing density. On the other hand, there were no significant correlations between density and ΔE_{La} and Δh_{La} for FC and DH layers (Table 4.5).

Finally, differences in crystal size and hand hardness between snowpack layers and the layer below correlated more strongly with density than differences with the layer above. Furthermore, all correlation coefficients were negative (Table 4.5), indicating that both ΔE_{Lb} and Δh_{Lb} decreased with increasing density, regardless of

Table 4.5: *Overview of correlation statistics between measured snowpack variables and density by grain group. The number of observations (N), the correlation coefficient (R_p for the Pearson correlation and R_s for the Spearman correlation) and the significance (p) are given for each variable. No density measurements were available for buried SH layers.*

	Density	
Parameter	Storm	FC DH
E	N=5912 R_p=-0.46 $p < 10^{-8}$	N=1521 R_p=0.22 $p < 10^{-8}$
H	N=5974 R_s=0.88 $p < 10^{-8}$	N=1534 R_s=0.74 $p < 10^{-8}$
Σ	N=43 R_p=0.60 p=10^{-5}	N=49 R_p=0.40 p=0.005
ΔE_{La}	N=4704 R_p=-0.20 $p < 10^{-8}$	N=1322 R_p=0.04 p=0.203
ΔE_{Lb}	N=5257 R_p=-0.20 $p < 10^{-8}$	N=1165 R_p=-0.09 p=0.004
Δh_{La}	N=5087 R_s=-0.07 p=10^{-7}	N=1445 R_s=-0.00 p=0.912
Δh_{Lb}	N=5534 R_s=-0.36 $p < 10^{-8}$	N=1310 R_s=-0.36 $p < 10^{-8}$

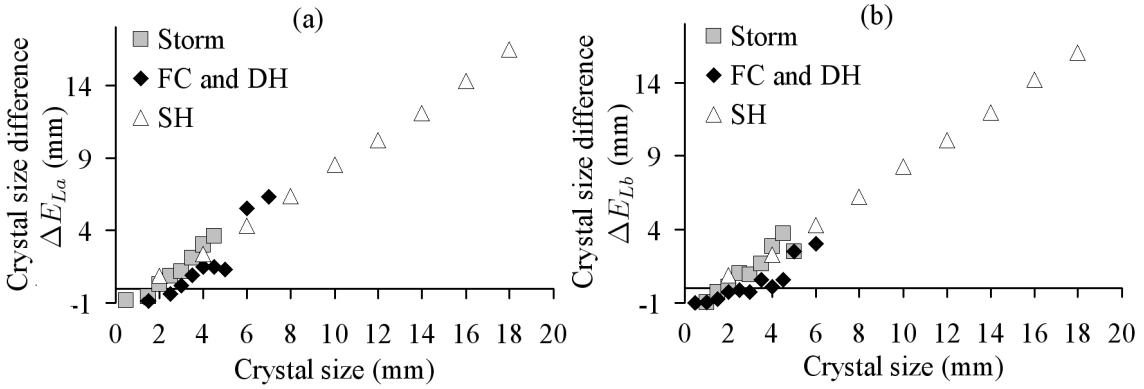

Figure 4.6: *Median difference in crystal size by crystal size of the snowpack layer for each grain group. (a)* ΔE_{La} *by* E*. (b)* ΔE_{Lb} *by* E*.*

grain group.

Crystal Size

An overview of the correlation between snowpack variables and crystal size is given in Table 4.6. The hand hardness of snowpack layers significantly correlated with the size of the crystals. Negative correlations between hand hardness and crystal size indicate that *Storm* layers and buried SH layers composed of larger crystals were generally softer (Table 4.6). For layers of FC and DH however, there was no significant correlation between hardness and crystal size. This was probably due to a combined effect of crystal size and depth. As described earlier, layers composed of smaller FC crystals were typically shallow layers, which are generally soft. Larger facets were typically associated with deeper snowpack layers, which tend to be harder. However, when only larger faceted crystals were considered (i.e. > 1 mm), a significant negative correlation emerged as well ($N = 1258$, $R_s =$ -0.16, $p = 10^{-8}$).

As expected, crystal size differences between the snowpack layers and the ad-

Table 4.6: *Overview of correlation statistics between measured snowpack variables and crystal size by grain group. The number of observations (N), the correlation coefficient (R_p for the Pearson correlation and R_s for the Spearman correlation) and the significance (p) are given for each variable.*

	Crystal size		
Parameter	Storm	FC DH	SH
H	N=9534 R_s=-0.47 $p < 10^{-8}$	N=3046 R_s=-0.04 p=0.053	N=1616 R_s=-0.28 $p < 10^{-8}$
Σ	N=219 R_p=-0.01 p=0.999	N=259 R_p=0.11 p=0.089	N=1062 R_p=-0.22 $p < 10^{-8}$
ΔE_{La}	N=7444 R_p=0.24 $p < 10^{-8}$	N=2566 R_p=0.14 $p < 10^{-8}$	N=1582 R_p=0.99 $p < 10^{-8}$
ΔE_{Lb}	N=8202 R_p=0.24 $p < 10^{-8}$	N=2135 R_p=0.11 $p < 10^{-8}$	N=1520 R_p=0.99 $p < 10^{-8}$
Δh_{La}	N=8091 R_s=0.15 $p < 10^{-8}$	N=2878 R_s=0.34 $p < 10^{-8}$	N=1585 R_s=0.30 $p < 10^{-8}$
Δh_{Lb}	N=8739 R_s=0.25 $p < 10^{-8}$	N=2560 R_s=0.12 $p < 10^{-8}$	N=1593 R_s=0.24 $p < 10^{-8}$

jacent layers correlated very well with crystal size (Figure 4.6), regardless of grain group. However, the correlations were strongest for buried SH layers (Table 4.6), indicating that the size of the buried Surface Hoar crystals predominantly determines the magnitude of the crystal size differences with the adjacent layers. Furthermore, snowpack layers composed of larger crystals typically had greater differences in hand hardness (Table 4.6). This comes as no surprise since there were negative correlations between crystal size and hand hardness, regardless of grain group.

Hand hardness

An overview of the correlation between snowpack variables and hand hardness is given in Table 4.7. As expected, the shear strength correlated well with hand hardness for all grain groups (Table 4.7). Typically, harder snowpack layers had a higher shear strength (see Figure 3.3). Furthermore, the hand hardness and crystal size differences had negative correlations with the hand hardness, for all grain groups. These negative correlations show that there were smaller differences in crystal size and hardness for harder snowpack layers. Furthermore, the correlation coefficients were generally stronger for differences relative to the layer below than for the layer above (Table 4.7).

As can be seen in Figure 4.7, both Δh_{La} and Δh_{Lb} decreased with increasing hand hardness H, regardless of grain group. However, Δh_{La} and Δh_{Lb} decreased more rapidly for *Storm* layers and FC and DH layers than for buried SH layers.

Table 4.7: *Overview of correlation statistics between measured snowpack variables and hand hardness by grain group. The number of observations (N), the correlation coefficient (R_p for the Pearson correlation and R_s for the Spearman correlation) and the significance (p) are given for each variable.*

	Hand hardness		
Parameter	Storm	FC DH	SH
Σ	N=208 R_s=0.64 p $< 10^{-8}$	N=249 R_s=0.48 p $< 10^{-8}$	N=988 R_s=0.63 $p < 10^{-8}$
ΔE_{La}	N=7406 R_s=-0.06 p=10^{-6}	N=2546 R_s=-0.06 p=0.003	N=1397 R_s=-0.20 p $< 10^{-8}$
ΔE_{Lb}	N=8166 R_s=-0.32 p $< 10^{-8}$	N=2118 R_s=-0.14 p $< 10^{-8}$	N=1347 R_s=-0.28 $p < 10^{-8}$
Δh_{La}	N=8299 R_s=-0.14 p $< 10^{-8}$	N=2951 R_s=-0.35 $p < 10^{-8}$	N=1619 R_s=-0.25 $p < 10^{-8}$
Δh_{Lb}	N=8997 R_s=-0.44 p $< 10^{-8}$	N=2624 R_s=-0.57 $p < 10^{-8}$	N=1627 R_s=-0.46 $p < 10^{-8}$

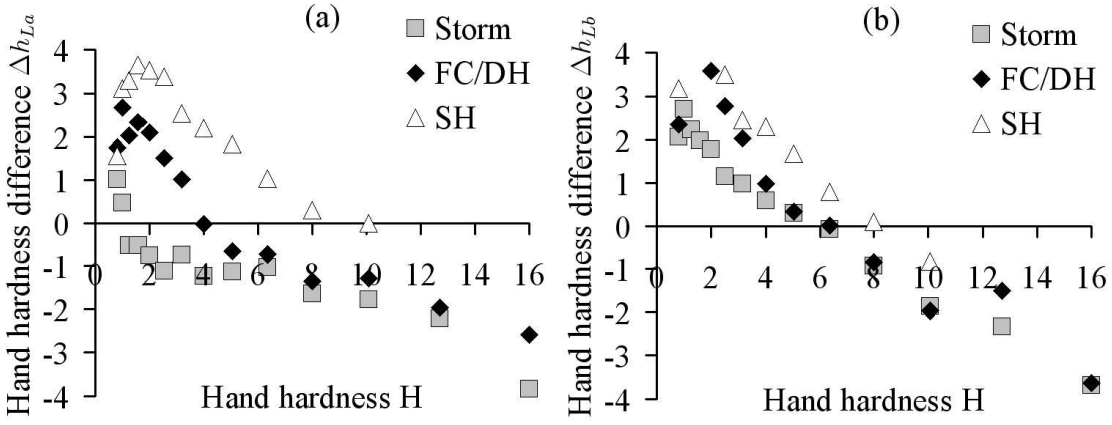

Figure 4.7: *Median difference in hand hardness between the snowpack layer and the adjacent layers by hand hardness of the snowpack layer for each grain group. (a) Δh_{La} by H. (b) Δh_{Lb} by H.*

4.3.3 Comparing stable and unstable profiles

An overview of the statistical comparison of stable and unstable snowpack properties is given in Tables 4.8 and 4.9. Many snowpack variables were highly significant factors for all three categories of weak layers as well as for the combined data set (All). These and several other variables are discussed in more detail below. Special attention is devoted to the frequency of skier-triggering. The frequency of skier-triggering for a specific variable was calculated as the percentage of the total number of observations that were classified as unstable (i.e. $N_{Unstable}/N_{total}$).

Weak layer properties are considered first, followed by slab properties, properties of the adjacent layers and finally differences in snowpack variables between the weak layer and the adjacent layers. No shear strength data were included in this part of the analysis, since these data were only available for primary weaknesses.

Weak layer properties

Figure 4.8 shows the frequency of skier-triggering by grain type as well as by grain group. Buried SH layers had the highest frequency of skier-triggering (25%). The frequency of skier-triggering for other grain types was much lower (Figure 4.8 (a)). Furthermore, no snowpack layers composed of Wet Grains (WG), Ice (I) or Crusts (CR) were the failure layers of slab avalanches. Similarly, when looking at the frequency of skier-triggering by grain group (Figure 4.8 (b)), the frequency of skier-triggering was much higher for SH (25%) layers than for *Storm* layers (2%) or FC and DH layers (3.5%).

Most snowpack properties from unstable weak layers were significantly different from stable snowpack layer properties. As can be seen in Tables 4.8 and 4.9, the

Table 4.8: *Comparison of stable and unstable snowpack variables for the combined data set (All) and for Storm layers. For each variable, the number of observations (N) as well as the median (Med.) is shown. Stable and unstable profiles are contrasted (U-test) and the level of significance (p) is given. Variables that were highly significant ($p < 0.05$) for all weak layers as well as for each grain group (see Table 4.9) are marked with two asterisks. One asterisk denotes variables that were significant for all weak layers as well as for two grain groups.*

	All					*Storm*				
	Unstable		Stable			Unstable		Stable		
Vari.	N	Med.	N	Med.	p	N	Med.	N	Med.	p
$^{**}D_{WL}$	156	42	4677	60	$< 10^{-8}$	57	29	2583	54	$< 10^{-8}$
$^{**}Th_{WL}$	156	1.0	4677	10.0	$< 10^{-8}$	57	1.5	2583	11.0	$< 10^{-8}$
$^{**}E_{WL}$	151	2.25	3547	1.00	$< 10^{-8}$	55	1.50	2511	1.00	$< 10^{-8}$
$^{**}h_{WL}$	137	4F	4425	1F+	$< 10^{-8}$	52	F+	2556	1F	$< 10^{-8}$
ρ_{WL}	15	121	1989	169	0.032	11	102	1454	154	$< 10^{-8}$
$^{*}h_{slab}$	151	1.95	3986	2.30	0.032	54	1.47	2174	1.96	0.027
ρ_{slab}	90	123	2375	132	0.212	26	108	1432	120	0.050
$^{*}B_{slab}$	151	91	3986	122	0.010	55	35	2002	90	10^{-6}
$^{**}\Delta h_{slab}$	134	0.67	3882	-0.97	$< 10^{-8}$	49	1.03	2155	-0.81	$< 10^{-8}$
$^{**}Th_{La}$	153	10.6	4135	9.0	$< 10^{-8}$	55	10.0	2203	9.0	$< 10^{-8}$
E_{La}	122	1.00	3218	1.00	0.001	44	1.00	1961	1.00	0.880
h_{La}	151	1F-	3884	1F	0.074	54	4F	2122	1F-	0.007
$^{**}\rho_{La}$	82	160	1695	160	0.032	22	130	1079	140	$< 10^{-8}$
$^{**}Th_{Lb}$	154	10.9	4144	9.5	$< 10^{-8}$	56	9.0	2355	9.0	$< 10^{-8}$
$^{*}E_{Lb}$	107	0.75	3275	1.00	10^{-5}	40	0.75	2153	1.00	0.012
h_{Lb}	151	1F+	3903	1F+	0.119	56	1F	2278	1F+	0.460
$^{**}\rho_{Lb}$	67	180	1608	179	0.032	20	142	1042	161	$< 10^{-8}$
$^{**}\Delta E_{La}$	121	1.50	2820	0.00	$< 10^{-8}$	43	0.25	1946	-0.05	10^{-6}
$^{**}\Delta E_{Lb}$	106	2.50	2875	0.00	$< 10^{-8}$	39	0.50	2127	0.00	$< 10^{-8}$
$^{**}\Delta h_{La}$	134	0.67	3773	-0.33	$< 10^{-8}$	49	0.33	2556	-0.67	$< 10^{-8}$
$^{**}\Delta h_{Lb}$	135	1.33	3781	0.33	$< 10^{-8}$	51	1.00	2556	0.33	$< 10^{-8}$

Table 4.9: *Comparison of stable and unstable snowpack variables for FC and DH layers and buried SH layers. For each variable, the number of observations (N) as well as the median (Med.) is shown. Stable and unstable profiles are contrasted (U-test) and the level of significance (p) is given. Variables that were highly significant ($p < 0.05$) for all weak layers as well as for each grain group (see Table 4.8) are marked with two asterisks. One asterisk denotes variables that were significant for all weak layers as well as for two grain groups.*

	FC and DH					SH				
	Unstable		Stable			Unstable		Stable		
Vari.	N	Med.	N	Med.	p	N	Med.	N	Med.	p
$^{**}D_{WL}$	29	59	802	83	10^{-4}	69	52	214	69	10^{-4}
$^{**}Th_{WL}$	29	1.0	802	11.0	$< 10^{-8}$	69	1.0	214	0.8	0.003
$^{**}E_{WL}$	28	1.50	777	1.00	0.002	68	6.00	208	4.50	10^{-6}
$^{**}h_{WL}$	26	1F-	792	1F+	10^{-4}	59	4F	152	1F-	10^{-7}
ρ_{WL}	4	240	327	225	0.746	-	-	-	-	-
$^{*}h_{slab}$	29	2.70	771	2.66	0.746	68	2.18	206	2.54	0.001
ρ_{slab}	15	157	455	160	0.862	49	117	138	154	0.001
$^{*}B_{slab}$	29	167	735	228	0.099	54	123	180	243	10^{-4}
$^{**}\Delta h_{slab}$	26	0.15	805	-0.84	10^{-4}	59	0.72	146	-0.01	0.015
$^{**}Th_{La}$	29	11.0	772	7.0	$< 10^{-8}$	69	10.9	212	9.9	0.002
E_{La}	19	1.00	661	1.00	0.101	59	0.75	184	0.75	0.383
h_{La}	29	1F+	732	1F+	0.561	68	1F+	205	P-	10^{-4}
$^{**}\rho_{La}$	13	189	260	213	10^{-5}	47	153	120	200	0.001
$^{**}Th_{Lb}$	28	5.0	645	9.2	10^{-7}	69	13.0	210	11.0	0.003
$^{*}E_{Lb}$	10	1.00	540	1.25	$< 10^{-8}$	57	0.75	174	0.75	0.050
h_{Lb}	28	P+	612	P-	0.002	67	1F+	204	P-	0.076
$^{**}\rho_{Lb}$	5	274	217	245	10^{-5}	42	190	108	227	0.002
$^{**}\Delta E_{La}$	19	0.50	650	0.00	10^{-4}	59	5.10	181	3.75	10^{-4}
$^{**}\Delta E_{Lb}$	10	0.00	533	-0.15	$< 10^{-8}$	57	5.25	172	3.75	10^{-5}
$^{**}\Delta h_{La}$	26	0.67	724	0.00	0.001	59	1.00	145	0.67	0.016
$^{**}\Delta h_{Lb}$	25	1.67	606	0.33	10^{-6}	59	1.00	147	1.00	0.001

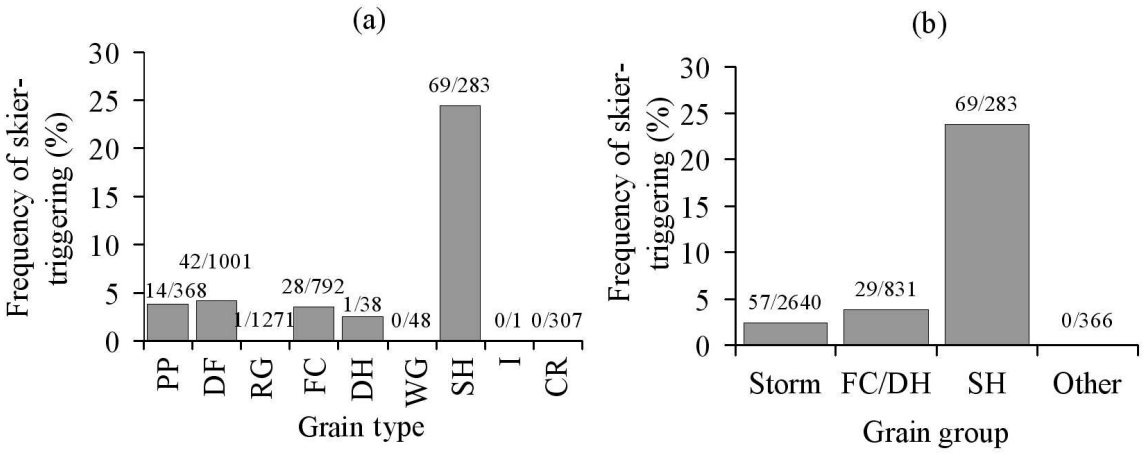

Figure 4.8: *(a) Frequency of skier-triggering by grain type. (b) Frequency of skier-triggering by grain group. The number of unstable weak layers (i.e. failure layer of slab avalanche) as well as the total number of observed snowpack layers for each category of grain type or grain group is shown above the bars.*

depth, thickness and hand hardness of unstable weak layers were significantly lower than for stable snowpack layers. This shows that unstable snowpack layers are generally thin shallow weak layers that are relatively soft. Furthermore, unstable snowpack layers generally had larger crystals than stable snowpack layers. However, some differences were observed between the three different categories of weak layers.

In Figure 4.9 the frequency of skier-triggering by depth is shown for each grain group. There generally was a decrease in frequency of skier-triggering for deeper weak layers. Furthermore, the frequency of skier-triggering was highest for snowpack layers between 20 and 30 cm, regardless of grain group. However, weak layers composed of FC and DH or buried SH remained unstable at greater depth than *Storm* layers.

The thickness of unstable weak layers was generally much lower than for stable snowpack layers (Tables 4.8 and 4.9), with the exception of buried SH layers. For the latter, unstable weak layers were generally thicker than stable weak layers (Table

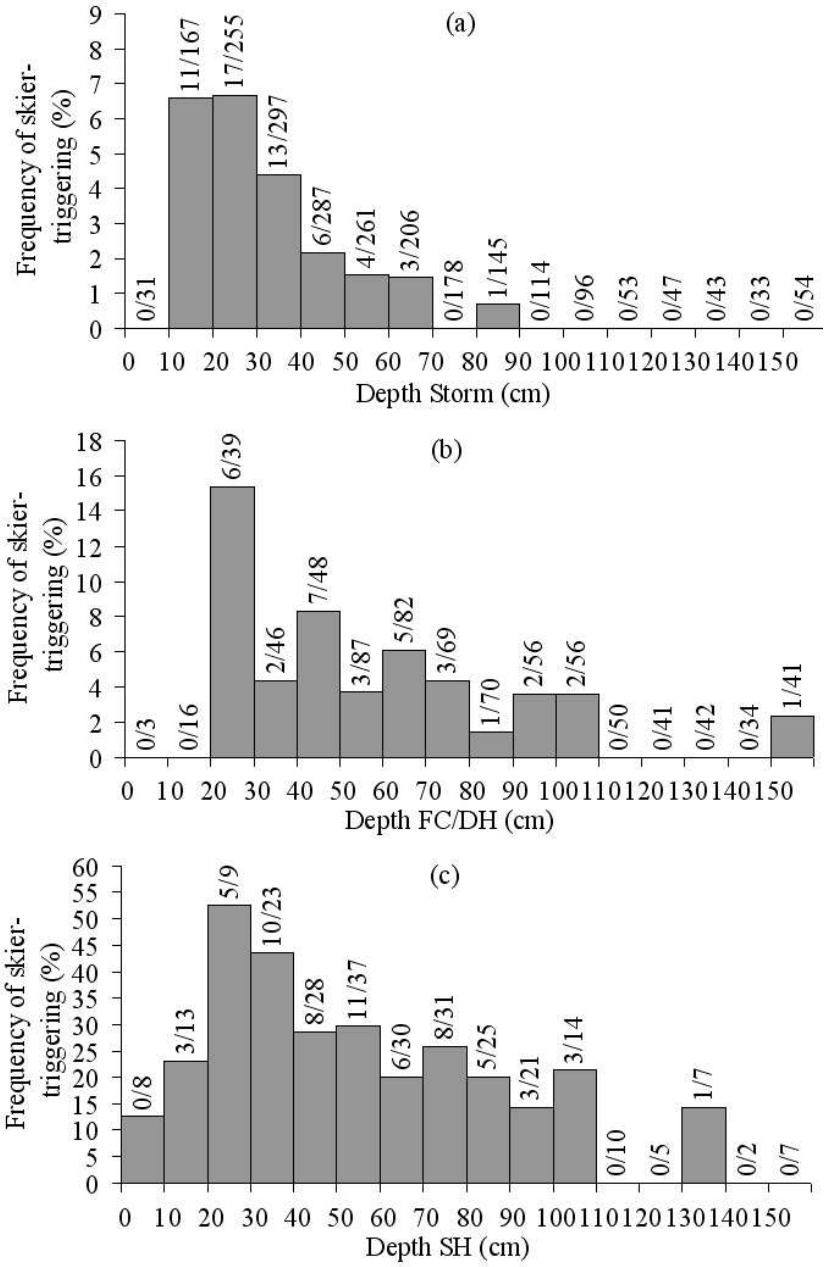

Figure 4.9: *Frequency of skier-triggering by depth for each grain group. The data were sorted in 10 cm intervals. (a) Storm layers. (b) FC and DH layers. (c) Buried SH layers. Above each bar, the number of unstable snowpack layers and the total number of observed snowpack layers are shown.*

4.9).

Crystal size was also a significant indicator of instability. Snowpack layers composed of large crystals were more often the failure layer of slab avalanches (Tables 4.8 and 4.9). An increasing trend in the frequency of skier-triggering was observed with increasing crystal size, regardless of crystal type. However, since surface hoar crystals were typically much larger than other grain types (Table 4.2), the influence of crystal size on stability was only apparent for larger values of E_{wl} than for *Storm*, and FC and DH layers. As seen in Tables 4.8 and 4.9, the median crystal size for unstable buried SH layers was 6 mm, much larger than for *Storm* layers (1.5 mm) and FC and DH layers (1.5 mm).

The hand hardness of snowpack layers was also a significant variable. As can be seen in Figure 4.10, the frequency of skier-triggering decreased with increasing hand hardness in the combined data set. Furthermore, no snowpack layers with a hand hardness greater than 1F+ were the failure layer of a slab avalanche. Similar trends in frequency of skier-triggering were observed for each grain group.

Finally, density was only a significant variable for *Storm* layers. However, since most unstable weak layers were thin, the density of these unstable layers could not be measured. Furthermore, as mentioned earlier, no density measurements were available for buried SH layers.

Slab properties

The difference in hand hardness between the slab and the weak layer was the only significant slab variable in the combined data set as well as for each grain group. This shows that unstable slabs were generally harder than the underlying weak layers.

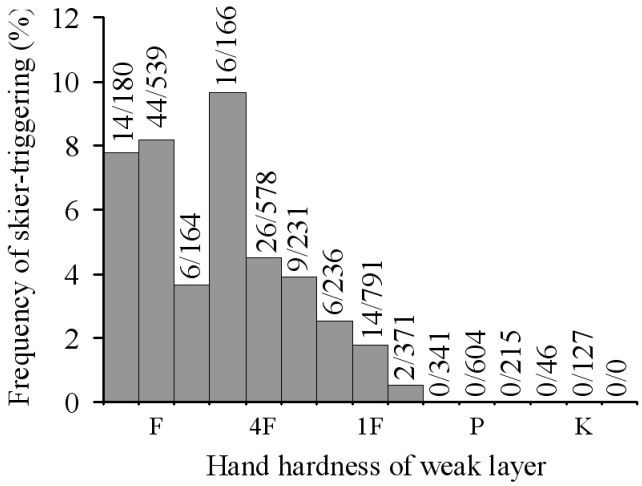

Figure 4.10: *Frequency of skier-triggering by hand hardness of the weak layer for the combined data set. The number of unstable weak layers and the total number of observed weak layers for each hand hardness step are shown above the bars.*

Additionally, slab hardness and bridging were significant variables in the combined data set as well as for *Storm* layers and buried SH layers. In Figure 4.11, the frequency of skier triggering is shown for these three slab variables.

Unstable slabs were generally softer than stable slabs, except for FC and DH layers for which there was no significant difference in hand hardness index between stable and unstable slabs (Table 4.9). As can be seen in Figure 4.11 (a), there was a maximum in the frequency of skier-triggering for a slab hardness of 4F-. For slabs harder than 4F-, the frequency of skier-triggering decreased. Similar trends were found for *Storm* layers and buried SH layers, and to a lesser extent for FC and DH layers. In general, the frequency of skier-triggering reached a maximum for a slab hardness between 4F and 1F and decreased with increasing slab hardness.

Since both the slab hardness and the weak layer depth were significant variables, it was not surprising that the bridging index B_{slab} was also a significant slab variable.

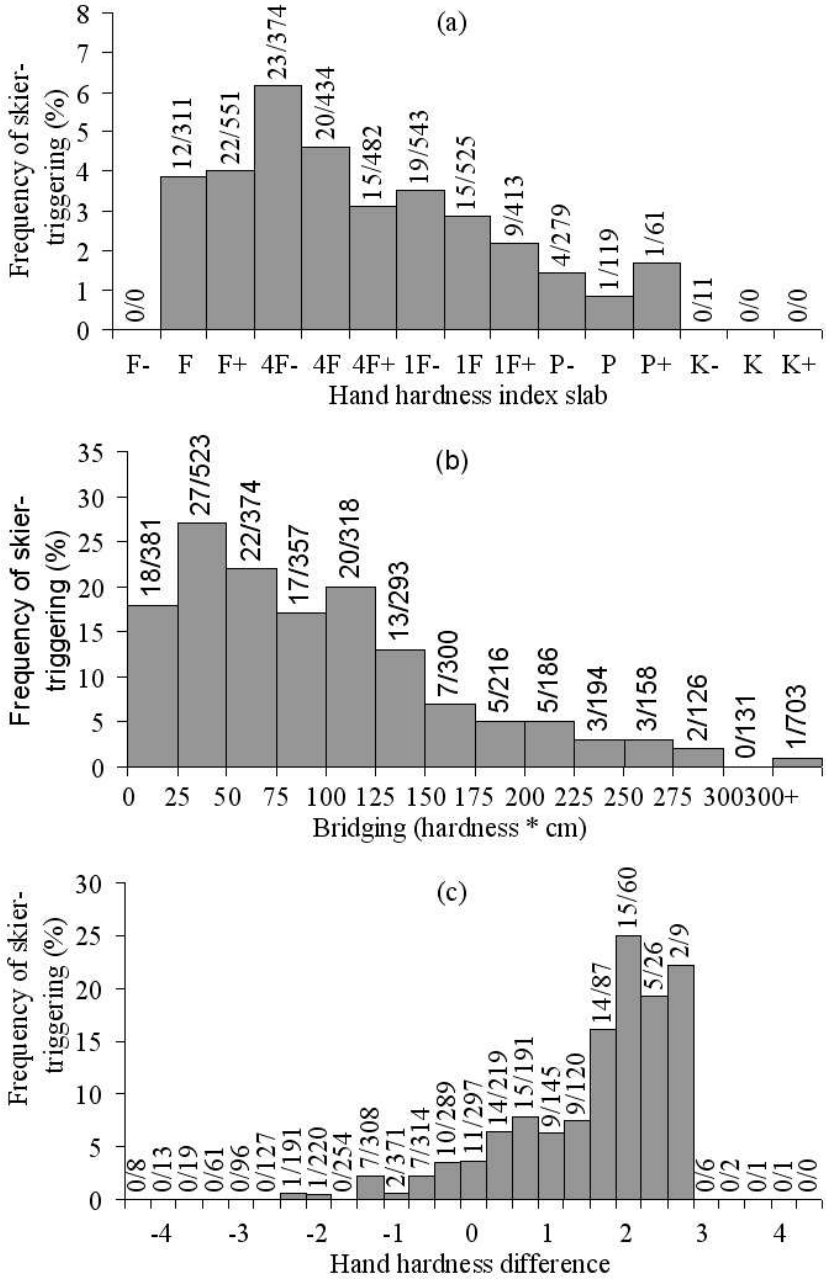

Figure 4.11: *Frequency of skier-triggering for three slab variables that were highly significant in the combined data set as well as for Storm layers and buried SH layers. (a) Hardness index of the slab (h_{slab}). (b) Bridging ($B_{slab} = h_{slab}Th_{slab}$). (c) Hardness difference between the slab and the weak layer (Δh_{slab}). The number of skier-triggered slabs and the total number of skier-tested slabs for each interval are shown above the bars.*

As can be seen in Figure 4.11 (b), the frequency of skier-triggering decreased with increasing B_{slab} after reaching a maximum for B_{slab} between 125 and 150 hardness*cm. Similar trends were observed for each grain group, with typically a maximum in the frequency of skier-triggering for B_{slab} between 100 and 150 hardness*cm.

Finally, the difference in hand hardness index between the slab and the weak layer was the most significant slab variable. There was a significant increase in frequency of skier-triggering with increasing Δh_{slab}, as seen in Figure 4.11 (c). However, for large values of Δh_{slab} (i.e. $\Delta h_{slab} > 3$) the frequency of skier-triggering dropped to zero since there were few observations in that range. On the other hand, for values of $\Delta h_{slab} < 0$ many data were available, yet the frequency of skier-triggering was very low. This shows that the vast majority of unstable slabs were harder than the weak layer. Very similar trends were observed for each grain group, with an increase in frequency of skier-triggering with increasing Δh_{slab} up to a value of $\Delta h_{slab} \approx 3$.

Properties of the layers adjacent to the weak layer

In Figure 4.12, the frequency of skier-triggering by grain type for the adjacent layers is shown. The frequency of skier-triggering was highest when the layer above the weak layer was composed of DF crystals (6%), followed by RG (4%), PP (3.5%) and FC crystals (2.5%). Occasionally, the layer above an unstable weak layer was a crust (Figure 4.12 (a)). On the other hand, the frequency of skier-triggering was highest when the layer below the weak layer was a crust (12%), followed by WG (10%), RG (4.5%), FC (3.5%) and DF (3%).

Layers adjacent to unstable weak layers were significantly different in the thickness and density compared to layers adjacent to stable snowpack layers (Tables 4.8

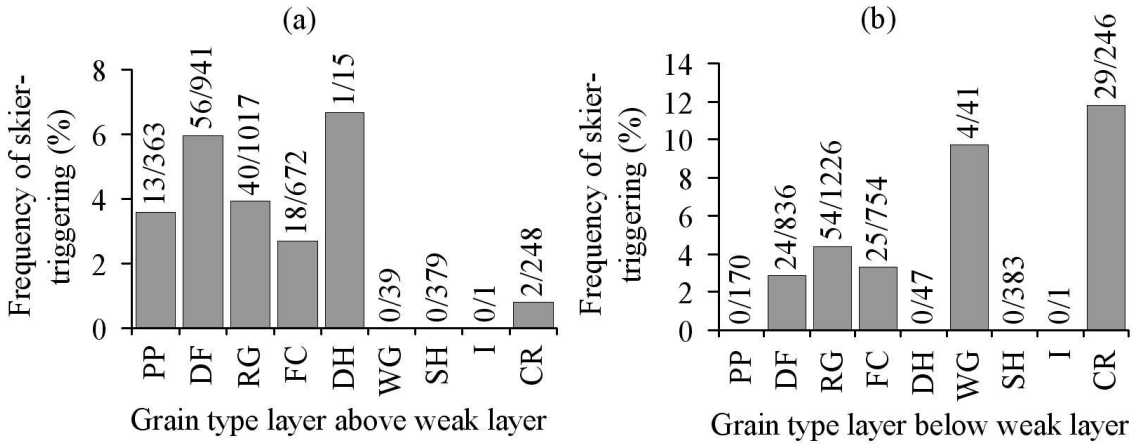

Figure 4.12: *Frequency of skier-triggering by grain type of the layer above (a) and the layer below (b) the weak layer for the combined data set. The number of observations linked to a skier-triggered avalanche as well as the total number of observations are shown above the bars.*

and 4.9). Both the layer above and the layer below unstable weak layers were generally thicker than for stable weak layers, regardless of grain group. As seen in Figure 4.13 for the combined data set, there was a slight increase in frequency of skier-triggering with increasing Th_{La} and Th_{Lb}.

The density of layers above unstable weak layers was generally lower than ρ_{La} for stable weak layers. Similarly, for *Storm* layers and buried SH layers, the density of the layer below unstable weak layers was generally lower than ρ_{Lb} for stable weak layers. On the other hand, ρ_{Lb} for unstable FC and DH layers was typically larger than for stable FC and DH weak layers. However, for FC and DH weak layers, layers below unstable weak layers (54%) were often a crust, for which density was rarely measured due to sampling difficulty.

There was no significant difference in E_{La} between unstable and stable weak layers. On the other hand, E_{Lb} was typically smaller for unstable weak layers than

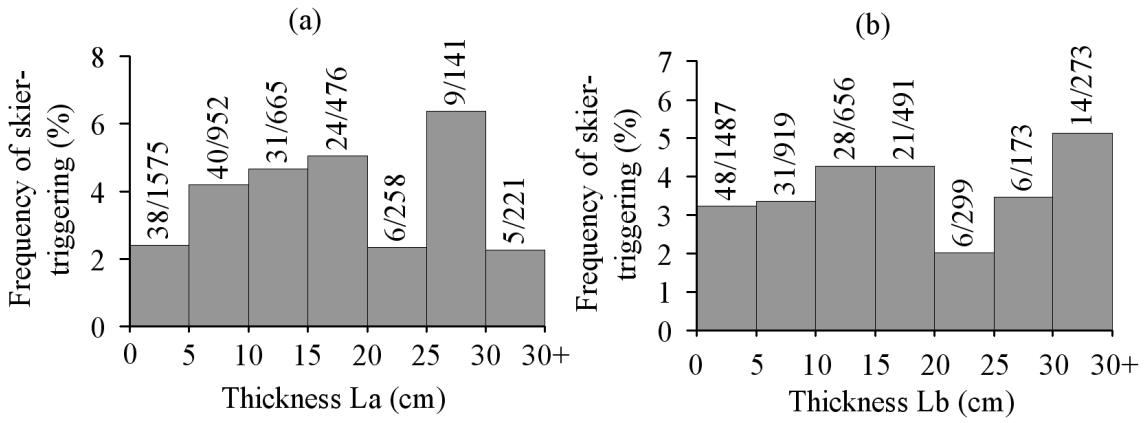

Figure 4.13: *Frequency of skier-triggering by layer thickness of the layer above (a) and the layer below (b) for the combined data set. The data were sorted in 5 cm intervals. The number of observations linked to a skier-triggered avalanche as well as the total number of observations are shown above the bars.*

for stable weak layers (Tables 4.8 and 4.9), suggesting that a weak layer is less stable when the layer below consists of smaller crystals.

Both h_{La} and h_{Lb} were not significant variables. However, when looking at the frequency of skier-triggering for these two variables, obvious trends emerged, similar for each grain group. In Figure 4.14, the frequency of skier-triggering by hand hardness of the adjacent layers is shown for the combined data set. The frequency of skier-triggering showed and increasing trend with increasing h_{La} until a maximum was reached for h_{La} typically between 4F and 1F. Thereafter, the frequency of skier-triggering decreased with increasing h_{La}. On the other hand, the frequency of skier-triggering marginally increased with increasing h_{Lb} (Figure 4.14 (b)) and was highest for h_{Lb} = K for all grain groups.

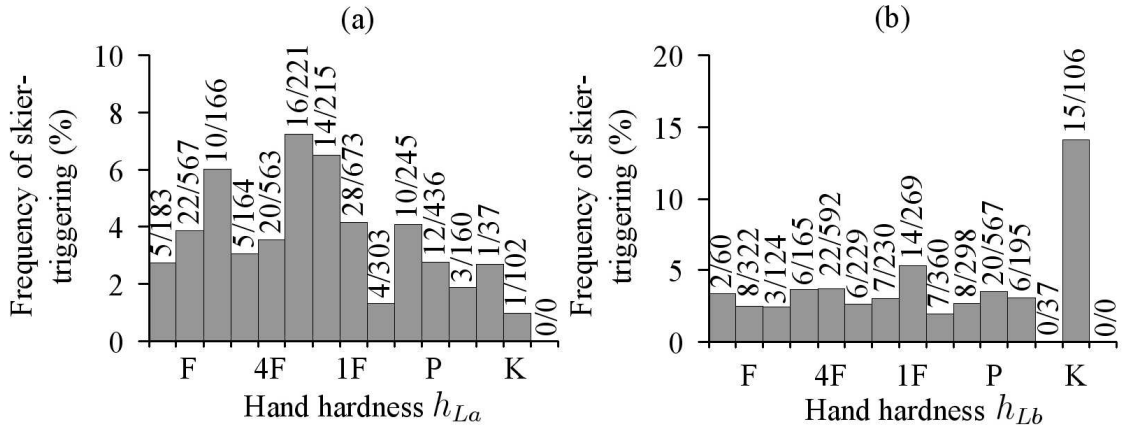

Figure 4.14: *Frequency of skier-triggering by hand hardness index of the layer above (a) and the layer below (b) for the combined data set. The number of observations linked to a skier-triggered avalanche as well as the total number of observations for each hardness step are shown above the bars.*

Differences in snowpack properties between the adjacent layers and the weak layer

Differences in snowpack properties between the adjacent layers and the weak layer were all highly significant variables with respect to skier-triggering. Typically, ΔE_{La} and ΔE_{Lb} were greater for unstable weak layers than for stable weak layers. Furthermore, there was an increase in frequency of skier-triggering with increasing crystal size difference, regardless of grain group. However, the magnitude of the difference in crystal size varied greatly by grain group. As seen in Tables 4.8 and 4.9, the median value of ΔE_{La} and ΔE_{Lb} for *Storm* layers (0.25 and 0.5 mm, respectively) was similar to that of FC and DH layers (0.5 and 0 mm, respectively), but much smaller than for buried SH layers (5.1 and 5.25 mm, respectively). This comes as no surprise since buried SH crystals were typically much larger than other types of crystals (Table 4.2).

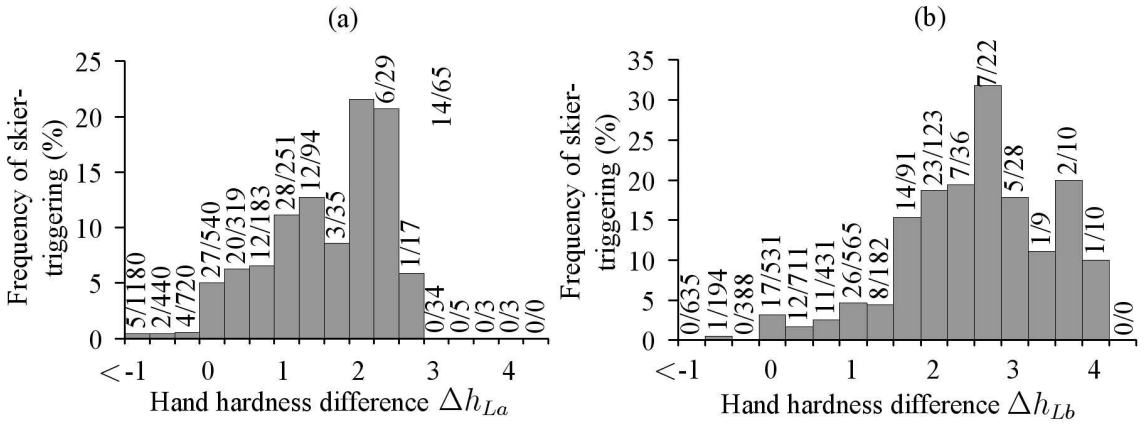

Figure 4.15: *Frequency of skier-triggering by hand hardness difference ΔE_{La} (a) and ΔE_{Lb} (b) for the combined data set. and the layer below (b). The number of observations linked to a skier-triggered avalanche as well as the total number of observations for each hardness step are shown above the bars.*

Generally, the hardness differences between the adjacent layers and the weak layer were greater for unstable weak layers than for stable weak layers. However, as for the differences in crystal size, there was a difference in the magnitude of Δh_{La} for different grain groups, but not for Δh_{Lb}. As seen in Table 4.8 and 4.9, the median difference in hand hardness Δh_{La} for *Storm* layer was -0.67, whereas it was larger for unstable SH weak layers (0.67). Nevertheless, as shown in Figure 4.15, there was an increase in the frequency of skier-triggering with increasing Δh_{La} and Δh_{Lb}. Similar trends were observed for each grain group, with a maximum in the frequency of skier-triggering for Δh_{La} and Δh_{Lb} between 2 and 3.

4.3.4 Comparing stable and unstable primary weaknesses

An overview of the statistical comparison of stable and unstable primary weaknesses is given in Tables 4.10 and 4.11. Four snowpack variables were highly significant for all three grain groups as well as for the combined data set: E_{WL}, Σ, ρ_{La} and ρ_{Lb}.

Table 4.10: *Comparison of stable and unstable primary weaknesses for the combined data set (All) and for Storm layers. For each variable, the number of observations (N) as well as the median (Med.) is shown. Stable and unstable profiles are contrasted (U-test) and the level of significance (p) is given. Variables that were significant ($p < 0.05$) for all weak layers (see Table 4.11) as well as for each grain group are marked with two asterisks. One asterisk denotes variables that were significant for all weak layers as well as for two grain groups.*

	All					*Storm*				
	Unstable		Stable			Unstable		Stable		
Vari.	N	Med.	N	Med.	p	N	Med.	N	Med.	p
$^{*}D_{WL}$	156	42	241	54	10^{-5}	57	29	109	50	$< 10^{-8}$
Th_{WL}	156	1.0	241	1.0	0.980	57	1.5	109	1.0	0.970
$^{**}E_{WL}$	151	2.25	236	1.50	10^{-6}	55	1.50	108	1.00	0.015
$^{*}h_{WL}$	137	F	210	F+	$< 10^{-8}$	52	F	98	F+	$< 10^{-8}$
ρ_{WL}	15	121	38	152	0.026	11	102	28	140	$< 10^{-8}$
$^{**}\Sigma$	119	0.64	171	1.41	$< 10^{-8}$	38	0.47	66	1.00	10^{-6}
$^{*}h_{slab}$	151	1.95	206	2.32	0.027	54	1.47	83	1.95	0.037
ρ_{slab}	90	123	158	137	0.051	26	108	74	120	0.001
$^{*}B_{slab}$	151	91	206	128	0.001	55	35	88	75	0.001
$^{*}\Delta h_{slab}$	134	0.51	183	-0.10	10^{-5}	49	1.35	76	0.38	10^{-5}
Th_{La}	153	10.6	238	10.0	0.844	55	10.0	108	10.0	0.891
E_{La}	124	1.00	176	0.75	0.067	44	1.00	70	1.00	0.146
$^{*}h_{La}$	151	F+	205	4F-	0.001	54	F	84	F+	0.002
$^{**}\rho_{La}$	82	160	149	175	0.027	22	130	71	140	$< 10^{-8}$
Th_{Lb}	154	10.9	217	11.0	0.988	56	9.0	90	10.0	0.780
E_{Lb}	135	1.00	184	1.00	0.359	47	1.00	73	1.00	0.703
$^{*}h_{Lb}$	151	4F-	207	4F-	0.002	56	F+	85	4F-	0.003
$^{**}\rho_{Lb}$	67	180	113	201	0.027	20	142	47	163	$< 10^{-8}$
ΔE_{La}	123	1.25	175	0.50	0.001	43	0.25	70	0.00	0.215
$^{*}\Delta E_{Lb}$	132	1.50	183	0.50	10^{-6}	46	0.50	72	0.00	10^{-4}
$^{*}\Delta h_{La}$	134	0.67	182	0.33	10^{-4}	49	0.33	98	0.00	10^{-5}
Δh_{Lb}	135	1.33	184	1.00	0.005	51	1.00	98	0.67	10^{-4}

Table 4.11: *Comparison of stable and unstable primary weaknesses for FC and DH layers and buried SH layer. For each variable, the number of observations (N) as well as the median (Med.) is shown. Stable and unstable profiles are contrasted (U-test) and the level of significance (p) is given. Variables that were significant ($p < 0.05$) for all weak layers as well as for each grain group (see Table 4.10) are marked with two asterisks. One asterisk denotes variables that were significant for all weak layers as well as for two grain groups.*

	FC and DH					SH				
	Unstable		Stable			Unstable		Stable		
Vari.	N	Med.	N	Med.	p	N	Med.	N	Med.	p
$^{*}D_{WL}$	29	59	52	57	0.606	69	52	78	66	0.017
Th_{WL}	29	1.0	52	1.5	0.794	69	1.0	78	1.0	0.151
$^{**}E_{WL}$	28	1.50	51	1.00	0.004	68	6.00	77	4.50	10^{-4}
$^{*}h_{WL}$	26	F+	50	F+	0.276	59	F	62	F+	10^{-5}
ρ_{WL}	4	240	10	201	0.429	-	-	-	-	-
$^{**}\Sigma$	24	1.10	40	1.50	0.027	57	0.74	64	1.87	10^{-5}
$^{*}h_{slab}$	29	2.70	51	2.61	0.429	68	2.18	72	2.43	0.014
ρ_{slab}	15	157	30	143	0.665	49	117	53	157	0.003
$^{*}B_{slab}$	29	167	51	181	0.783	54	123	64	201	0.008
$^{*}\Delta h_{slab}$	26	0.52	49	0.05	0.187	59	0.99	58	0.19	0.001
Th_{La}	29	11.0	50	9.0	0.780	69	10.9	78	11.5	0.151
E_{La}	21	1.00	43	1.00	0.177	59	0.75	63	0.75	0.296
$^{*}h_{La}$	29	4F-	50	4F-	0.714	68	4F-	71	4F-	0.005
$^{**}\rho_{La}$	13	189	26	204	10^{-7}	47	153	51	193	0.014
Th_{Lb}	28	5.0	51	11.0	0.525	69	13.0	76	12.9	0.129
E_{Lb}	24	1.00	46	1.00	0.436	64	0.75	65	1.00	0.191
$^{*}h_{Lb}$	28	4F	51	4F	0.378	67	4F-	71	4F-	0.006
$^{**}\rho_{Lb}$	5	274	20	270	10^{-4}	42	190	46	231	0.002
ΔE_{La}	21	0.50	42	0.25	0.207	59	5.10	63	4.00	0.014
$^{*}\Delta E_{Lb}$	23	0.25	46	0.00	0.078	63	5.25	65	3.75	0.002
$^{*}\Delta h_{La}$	26	0.67	48	0.33	0.215	59	1.00	57	0.67	0.006
Δh_{Lb}	25	1.67	49	1.00	0.123	59	1.00	57	1.00	0.227

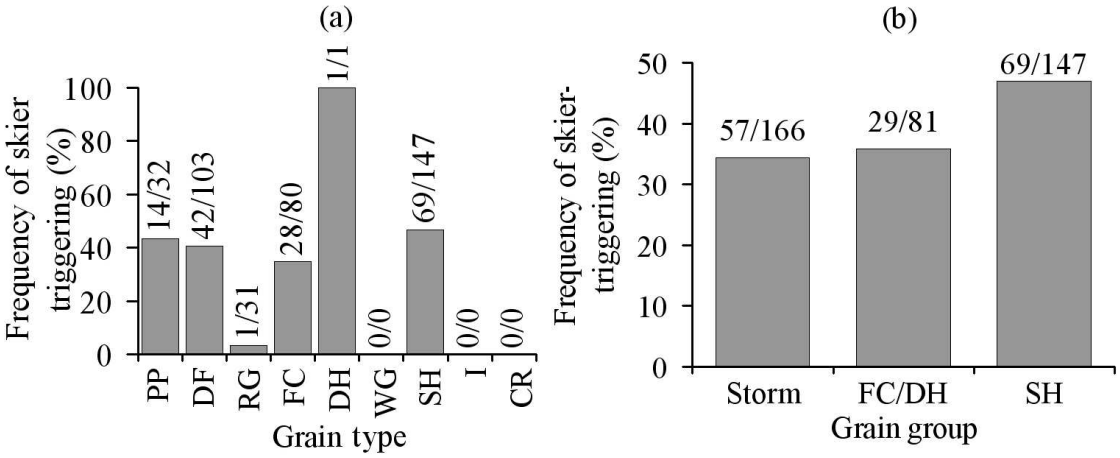

Figure 4.16: *(a) Frequency of skier-triggering by grain type of the primary weakness. (b) Frequency of skier-triggering by grain group. The number of unstable primary weaknesses (i.e. failure layer of slab avalanche) as well as the total number of observed primary weaknesses for each category of grain type or grain group is shown above the bars.*

Weak layers that were the failure plane of slab avalanches were generally composed of larger crystals, had lower shear strength and the adjacent layers generally had a lower density. Furthermore, nine additional snowpack variables were highly significant for the combined data set as well as for two out of three grain groups. The properties of the primary weakness are considered first, followed by slab properties, properties of the adjacent layers and finally differences in snowpack variables between the primary weakness and the adjacent layers are discussed. Shear strength data were included in this part of the analysis.

Properties of the primary weakness

Figure 4.16 shows the frequency of skier-triggering for primary weaknesses by grain type as well as by grain group. The frequency of skier-triggering was highest for primary weaknesses composed of Depth Hoar (DH) crystals, yet there was only one

data point. The frequency of skier-triggering for buried SH was second highest (47%), closely followed by PP (44%), DF (41%) and FC (35%). On the other hand, the frequency of skier-triggering of primary weaknesses composed of rounded grains (RG) was much lower (3%) and no primary weaknesses were composed of WG, I or CR. Furthermore, buried SH weak layers had the highest frequency of skier-triggering (47%) by grain group, followed by FC and DH weak layers (36%) and *Storm* weak layers (34%).

Many properties of unstable primary weaknesses were significantly different from stable primary weaknesses. The crystal size and shear strength were both significant variables in the combined data set as well as for all grain groups. Primary weaknesses composed of large crystals were more often the failure layer of slab avalanches. As can be seen in Figure 4.17, there was an increase in the frequency of skier-triggering with increasing E_{WL}, regardless of grain group. However, since surface hoar crystals were generally large crystals (Table 4.2), the effect of crystal size on stability became apparent for larger values of E_{wl} than for *Storm*, and FC and DH weak layers (Figure 4.17). Furthermore, unstable primary weaknesses generally had lower shear strength than stable primary weaknesses (Tables 4.10 and 4.11) and a decrease in frequency of skier-triggering was observed with increasing shear strength, regardless of grain group.

The depths of unstable primary weaknesses were significantly shallower than for stable primary weaknesses (Tables 4.10 and 4.11). This was not the case for FC and DH layers. However, when looking at the frequency of skier-triggering by depth, there was a trend for decreasing skier-triggering with increasing depth, regardless of grain group. As before (i.e. Figure 4.9), the frequency of skier-triggering by depth

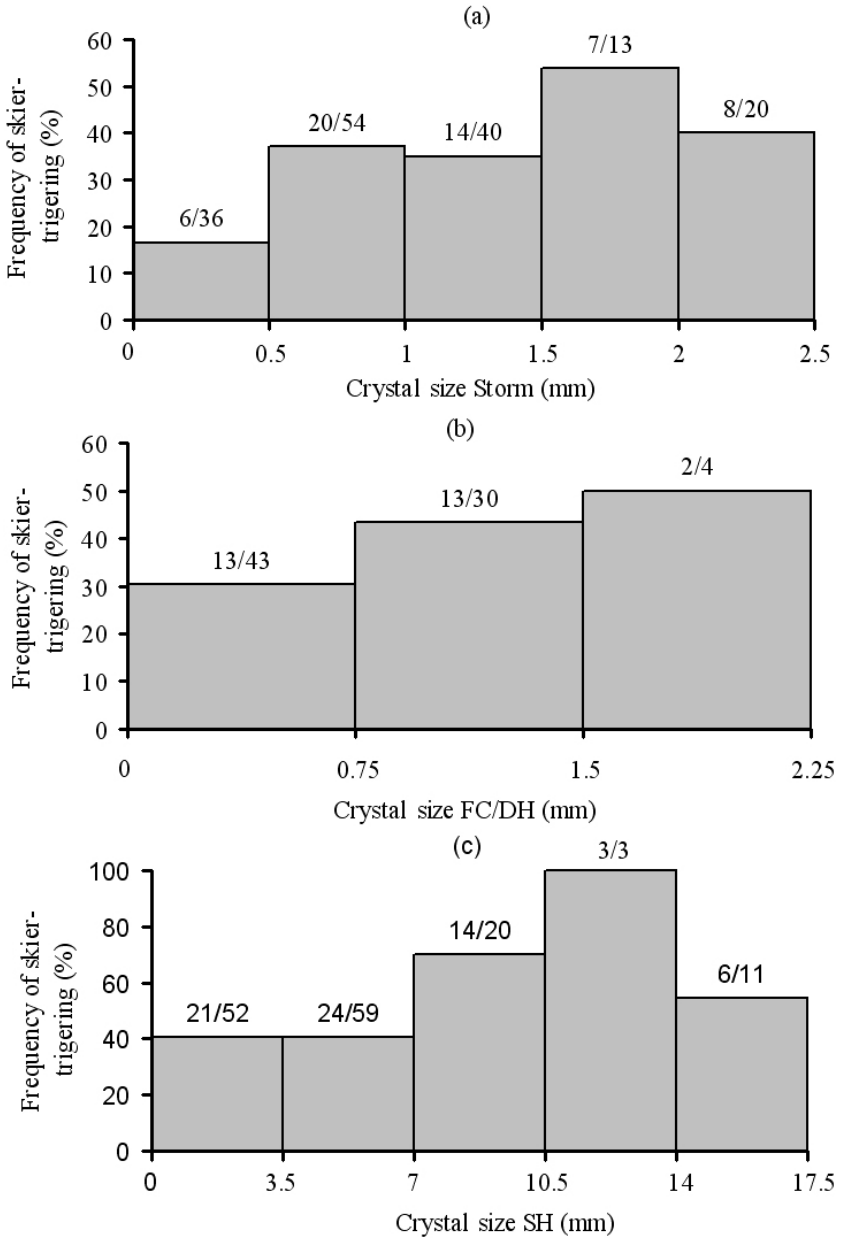

Figure 4.17: *Frequency of skier-triggering by crystal size of the primary weakness for each grain group. The data were sorted in 0.5 mm intervals for Storm layers, 0.75 mm for FC and DH layers and 3.5 mm for SH layers. The number of unstable primary weaknesses as well as the total number of observed primary weaknesses for each interval is shown above the bars.*

decreased more rapidly for *Storm* primary weaknesses than for persistent primary weaknesses, where the decrease in frequency of skier-triggering was more gradual.

Finally, the hand hardness of the primary weakness was also a significant variable in the combined data set as well as for buried SH and *Storm* primary weaknesses. As can be seen in Figure 4.18, the frequency of skier-triggering decreased with increasing hand hardness for these weak layers. Furthermore, despite the fact that there was no significant difference in hand hardness between stable and unstable FC and DH primary weaknesses (Table 4.11), the frequency of skier-triggering showed the same decreasing trend with increasing hand hardness. Moreover, no primary weaknesses harder than 1F were the failure layer of a slab avalanche.

Slab properties

No slab properties were significantly different in the combined data set as well as for all three grain groups (Tables 4.10 and 4.11). Nevertheless, h_{slab}, B_{slab} and Δh_{slab} were significant variables in the combined data set as well as for *Storm* and buried SH primary weaknesses. Furthermore, general trends in the frequency of skier-triggering of slab variables were comparable for each grain group and similar to those shown earlier (i.e. Figure 4.11).

Skier-triggered slabs were generally softer than skier-tested slabs that were not triggered. Furthermore, there was a decrease in the frequency of skier-triggering with increasing slab hardness for all grain groups, similar to that shown in Figure 4.11 (a). Likewise, B_{slab} was generally lower for unstable slabs than for stable slabs. However, there typically was a maximum in the frequency of skier-triggering for a bridging between 100 and 150 hardness*cm, as shown in Figure 4.19. Finally, the difference

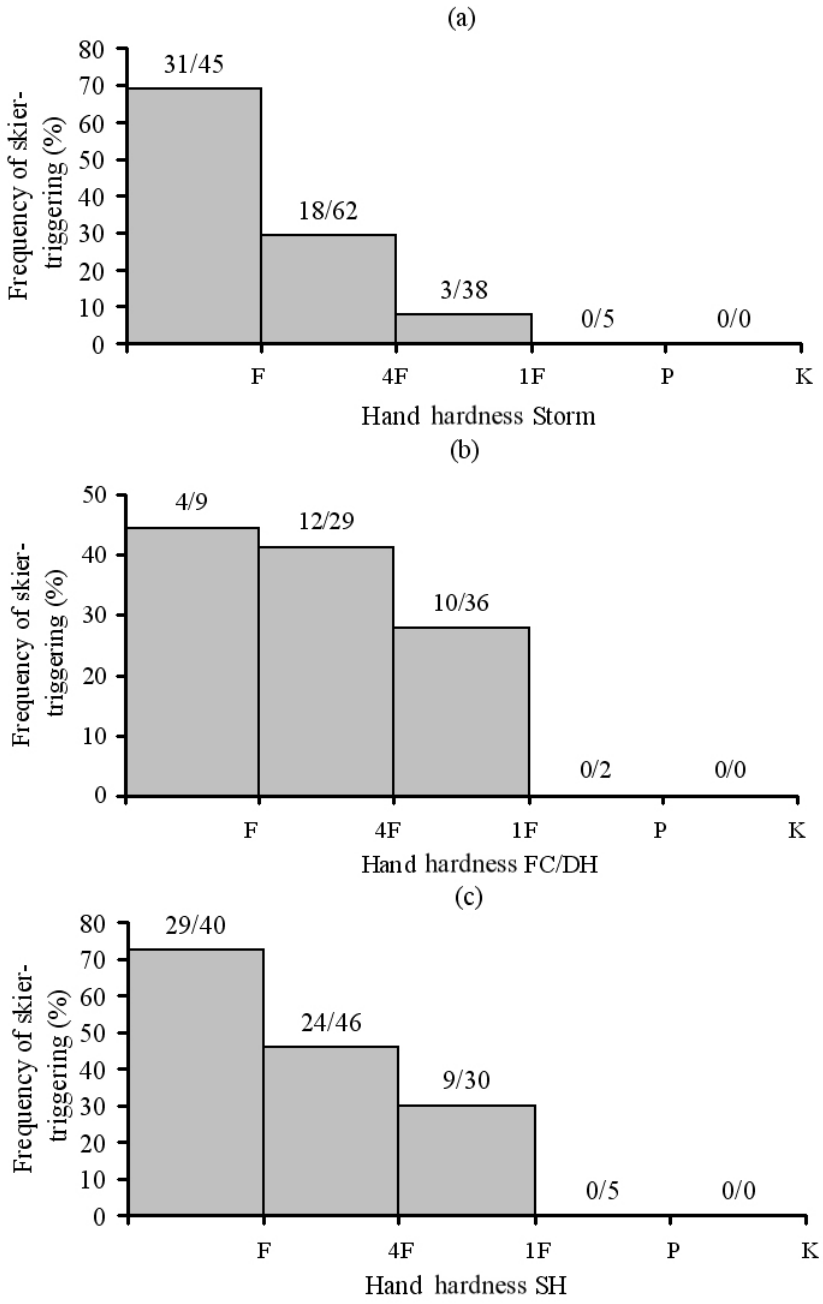

Figure 4.18: *Frequency of skier-triggering by hand hardness of the primary weakness for each grain group. (a) Storm primary weaknesses. (b) FC and DH primary weaknesses. (c) Buried SH primary weaknesses. The number of unstable primary weaknesses as well as the total number of observed primary weaknesses for each hardness step is shown above the bars.*

in hand hardness between the slab and the primary weakness was typically larger for unstable slabs than for stable slabs (Tables 4.10 and 4.11). Moreover, there was an increase in the frequency of skier-triggering with increasing Δh_{slab} up to a value of $\Delta h_{slab} \approx 2.5$, similar to that shown earlier in Figure 4.11 (c), regardless of grain group.

Properties of the layers adjacent to the primary weakness

In Figure 4.20, the frequency of skier-triggering by grain type for layers adjacent to primary weaknesses is shown for the combined data set. The frequency of skier-triggering was highest when the layer above the primary weakness was composed of DF crystals (55%), followed by PP (54%), FC (42%), RG (31%) and CR (28%). On the other hand, the frequency of skier-triggering was highest when the layer below the weak layer was composed of WG (67%), followed by DF (44%), FC (43%), RG (42.5%) and CR (40%).

Both ρ_{La} and ρ_{Lb} were significant variables in the combined data set as well as for each grain group (Tables 4.10 and 4.11). The density of the layers adjacent to unstable primary weaknesses was generally lower than for stable primary weaknesses, regardless of grain group. Furthermore, both h_{La} and h_{Lb} were also significant variables, except for primary weaknesses composed of FC and DH. However, the observed trends in the frequency of skier-triggering by h_{La} and h_{Lb} were similar for each grain group.

Figure 4.21 shows the frequency of skier-triggering by h_{La} and h_{Lb} for the combined data set. There was a decrease in the frequency of skier-triggering for increasing h_{La}. However, contrary to Figure 4.14 (a), the maximum frequency of skier-triggering

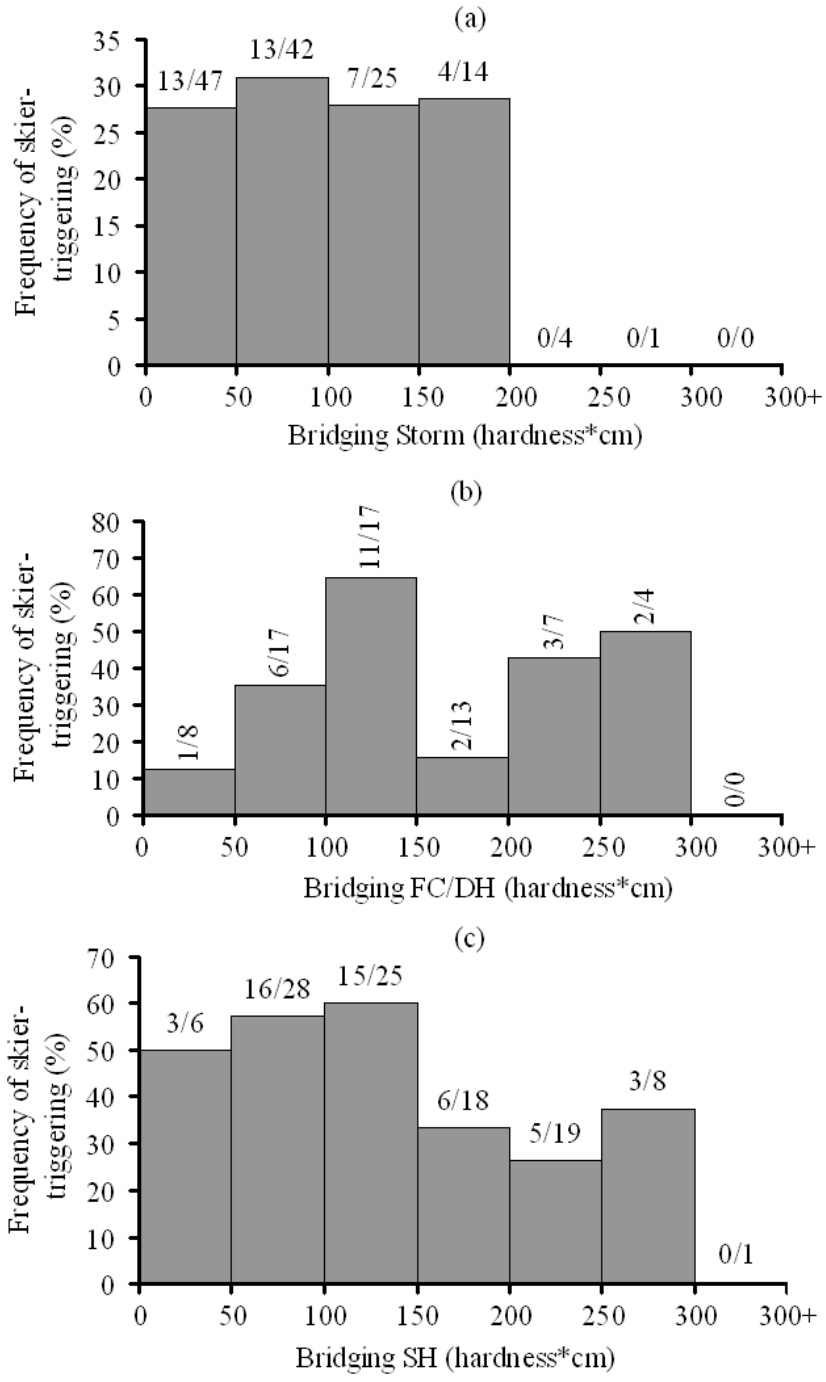

Figure 4.19: *Frequency of skier-triggering by B_{slab} for each grain group. (a) Storm primary weaknesses. (b) FC and DH primary weaknesses. (c) Buried SH primary weaknesses. The number of unstable slabs as well as the total number of observed slabs for each hardness step is shown above the bars.*

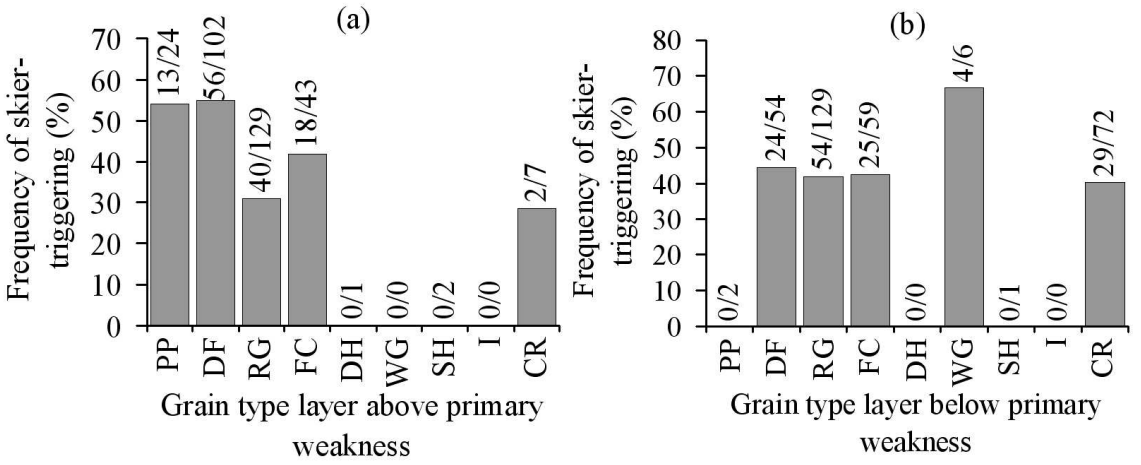

Figure 4.20: *Frequency of skier-triggering by grain type of the layer above (a) and the layer below (b) the primary weakness for the combined data set. The number of observations linked to a skier-triggered avalanche as well as the total number of observations are shown above the bars.*

was observed for h_{La} = F. Likewise, the frequency of skier-triggering decreased with increasing h_{Lb}. However, for h_{Lb} = K the frequency of skier-triggering increased again, similar to Figure 4.14 (b).

Finally, no significant differences in layer thickness and crystal size of the adjacent layers were observed between stable and unstable primary weaknesses (Tables 4.10 and 4.11).

Differences in snowpack properties between the adjacent layers and the primary weakness

No differences in snowpack properties between the adjacent layers and the primary weakness were statistically significant in the combined data set and for all three grain groups (Tables 4.10 and 4.11). Nevertheless, ΔE_{Lb} and Δh_{La} were significant variables in the combined data set as well as for *Storm* and buried SH primary weaknesses. Furthermore, general trends in the frequency of skier-triggering were

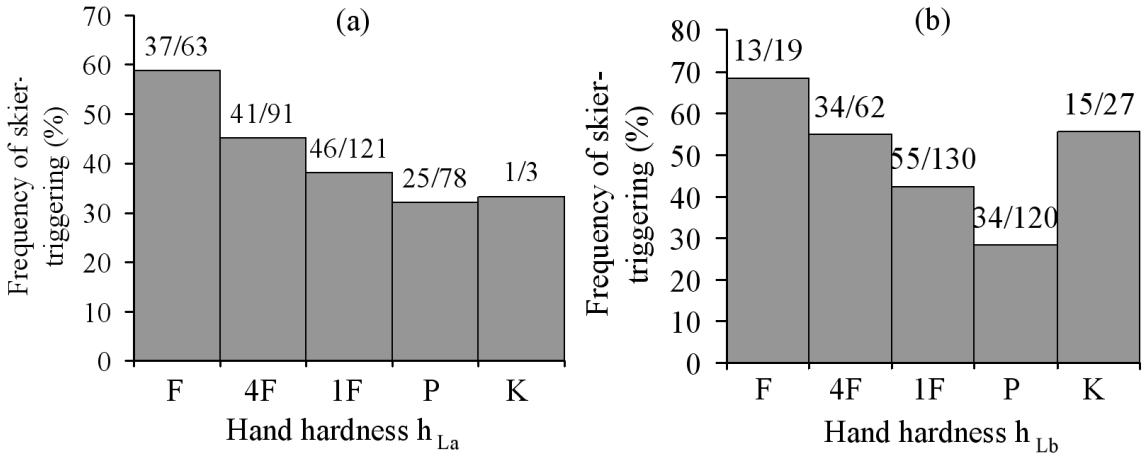

Figure 4.21: *Frequency of skier-triggering by hand hardness index of the layer above (a) and the layer below (b) the primary weakness for the combined data set. The number of observations linked to a skier-triggered avalanche as well as the total number of observations for each hardness step are shown above the bars.*

comparable for each grain group and very similar to those shown earlier for the hand hardness difference (i.e. Figure 4.15).

Figure 4.22 shows the frequency of skier-triggering by ΔE_{La} for each grain group. There was an increase in the frequency of skier-triggering with increasing ΔE_{La}, regardless of grain group. However, the magnitude of the difference in crystal size varied greatly by grain group. For *Storm* and FC and DH primary weaknesses, the frequency of skier-triggering reached a maximum value for ΔE_{La} below 1.5 mm. On the other hand, the frequency of skier-triggering for buried SH primary weaknesses reached a maximum for much larger values of ΔE_{La} (Figure 4.22 (c)).

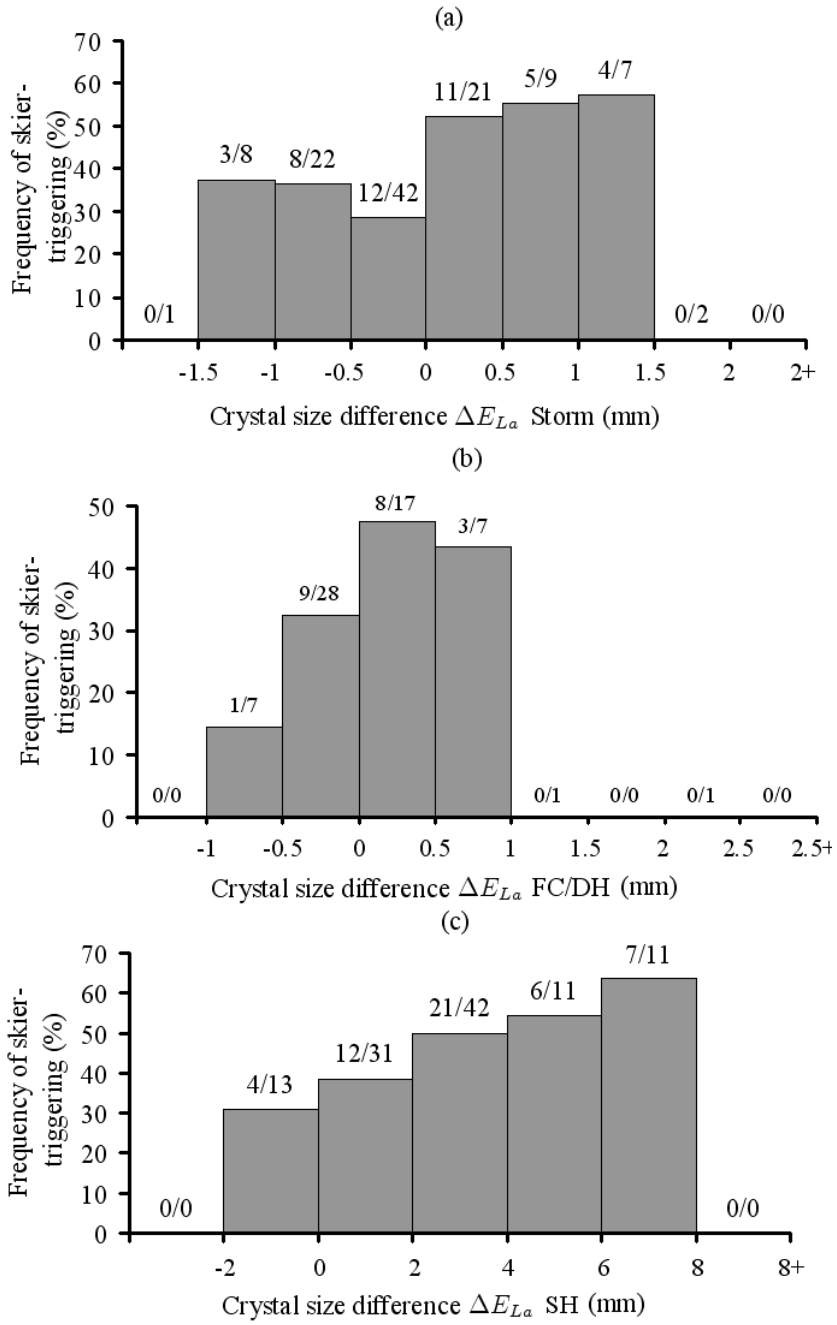

Figure 4.22: *Frequency of skier-triggering by ΔE_{La} by grain group. (a) Storm primary weaknesses sampled at an interval of 0.5 mm. (b) FC and DH primary weaknesses sampled at an interval of 0.5 mm. (c) Buried SH primary weaknesses sampled at an interval of 2 mm. The number of observations linked to a skier-triggered avalanche as well as the total number of observations for each hardness step are shown above the bars.*

4.3.5 Snowpack conditions favouring fracture propagation

The comparison of snowpack variables from remotely triggered avalanches (Sr), whumpfs and large skier-triggered slabs with snowpack variables from small slab avalanches is shown in Table 4.12. Only data from the primary weakness were considered. Since most primary weaknesses were persistent weak layers, which are named after their burial date, the age of these weak layers was also considered in the analysis (Age_{WL}, in days).

Many snowpack variables were significantly different and these are discussed in more detail below. As before, weak layer properties are considered first, followed by slab properties, properties of the adjacent layers and differences in snowpack variables between the weak layer and the adjacent layers are described. Furthermore, snowpack properties from five trigger points of remotely triggered slab avalanches are compared to fracture line data from remotely triggered avalanches, and ten profiles at whumpf sites inside the whumpfed area where the weak layer had fractured are compared to profiles observed outside whumpfed areas. Finally, results from the correlation analysis between various snowpack variables and the size of slab avalanches and the estimated width (W) are presented. Both the size and width of slab avalanches were estimated in the field by research technicians.

Weak layer properties

In Figure 4.23, the frequency of observation of weak layer grain type is shown. The crystal type of weak layers involved in remotely triggered slab avalanches, whumpfs and large slab avalanches consisted mainly of persistent weak grain types (i.e. FC, DH and SH) and were rarely composed of PP or DF crystals.

Table 4.12: *Comparison of snowpack properties from remotely triggered avalanches (Sr), whumpfs and large slab avalanches (Sc > Size 2) with small slab avalanches (Sc ≤ Size 2). Two asterisks denote variables that were highly significant ($p < 0.05$) for all three types of slab avalanches. One asterisk denotes variables that were highly significant for two types of slab avalanches.*

	Sc ≤ Size 2		Sr			Whumpf			Sc > Size 2		
variable	N	Median	N	Median	p	N	Median	p	N	Median	p
$^{*}Age_{wl}$	78	11	38	11	0.152	64	14	10^{-4}	10	16	$< 10^{-8}$
$^{**}D_{wl}$	140	38	44	64	10^{-7}	65	58	10^{-6}	16	75	10^{-4}
Th_{Wl}	140	1	44	1	0.564	65	1.8	0.003	16	1	0.293
$^{*}E_{Wl}$	137	2	44	5	0.024	64	7	10^{-5}	14	4.5	0.072
$^{*}h_{Wl}$	125	4F	40	1F-	0.099	64	1F-	0.003	12	1F	0.002
$^{*}\rho_{Wl}$	14	121	2	231	$< 10^{-8}$	9	200	$< 10^{-8}$	1	240	-
$^{**}\Sigma$	107	6.2	39	1.2	10^{-4}	46	1.0	0.004	12	1.6	10^{-4}
$^{**}h_{slab}$	136	1.8	48	2.3	0.005	65	2.4	10^{-4}	15	2.8	0.001
$^{**}B_{slab}$	136	78	48	159	10^{-6}	65	135	10^{-7}	15	195	10^{-5}
$^{**}\rho_{slab}$	81	115	33	135	0.035	38	139	0.005	9	192	$< 10^{-8}$
Δh_{slab}	122	0.33	40	0.47	0.365	64	0.52	0.142	12	0.57	0.662
Th_{La}	137	10.9	44	10	0.496	65	9	0.368	16	8.8	0.853
$^{**}E_{La}$	109	1	34	0.75	$< 10^{-8}$	54	0.8	$< 10^{-8}$	13	0.75	10^{-6}
$^{**}h_{La}$	136	1F	44	P-	10^{-4}	63	P-	10^{-7}	15	P-	10^{-4}
$^{**}\rho_{La}$	73	151	25	190	0.002	33	188	10^{-4}	9	240	$< 10^{-8}$
Th_{Lb}	138	10.9	43	10	0.535	59	10	0.849	16	10.9	0.698
$^{**}E_{Lb}$	96	0.75	31	1	$< 10^{-8}$	35	1	$< 10^{-8}$	11	0.75	10^{-5}
$^{*}h_{Lb}$	136	P-	43	P-	0.056	59	P	0.035	15	P+	0.017
$^{**}\rho_{Lb}$	60	178	18	224	0.005	25	248	10^{-4}	7	250	$< 10^{-8}$
$^{*}\Delta E_{La}$	108	1	34	4.5	0.037	53	6	0.001	13	3.75	0.082
ΔE_{Lb}	95	2.1	31	4.5	0.172	34	8.5	0.002	11	5	0.167
$^{*}\Delta h_{La}$	122	0.67	40	1.33	0.014	63	1	10^{-4}	12	1	0.277
Δh_{Lb}	123	1.33	39	1.67	0.230	58	1.33	0.658	12	1.33	0.877

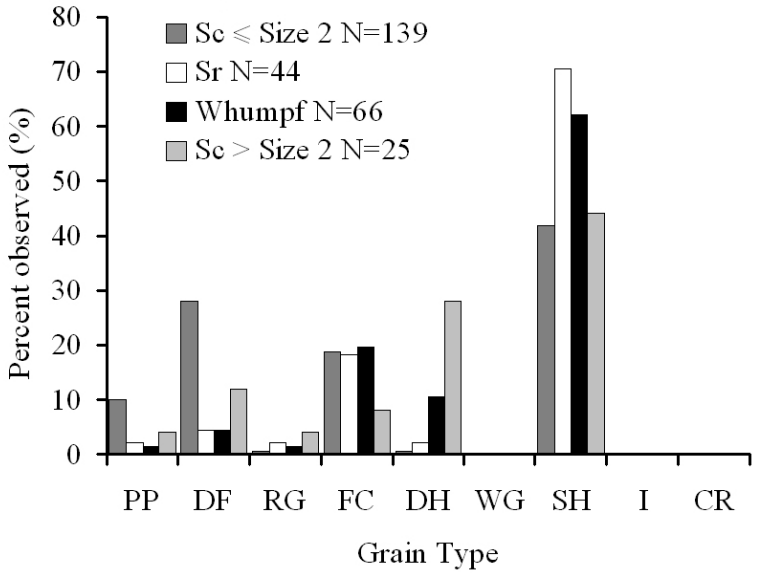

Figure 4.23: *Frequency of observation of grain type for small avalanches (dark grey; Sc ≤ Size 2)), remotely triggered avalanches (white; Sr), whumpfs (black) and large avalanches (light grey; Sc > 2). The number of observations N is also shown.*

Weak layers at sites of remotely triggered slab avalanches, whumpfs and large skier-triggered slab avalanches were significantly deeper and stronger than weak layers associated with small skier-triggered slabs (Table 4.12). Furthermore, the weak layer crystals were also significantly larger for remotely triggered slab avalanches and whumpfs. There was also a significant difference in weak layer density (Table 4.12), indicating that weak layers involved in remotely triggered slab avalanches and whumpfs generally had a higher density. However, very few measurements were available. Finally, persistent weak layers associated with whumpfs and large slab avalanches were significantly older than weak layers that were the failure plane of small slab avalanches.

The thickness of the weak layer was significantly higher for whumpfs than for

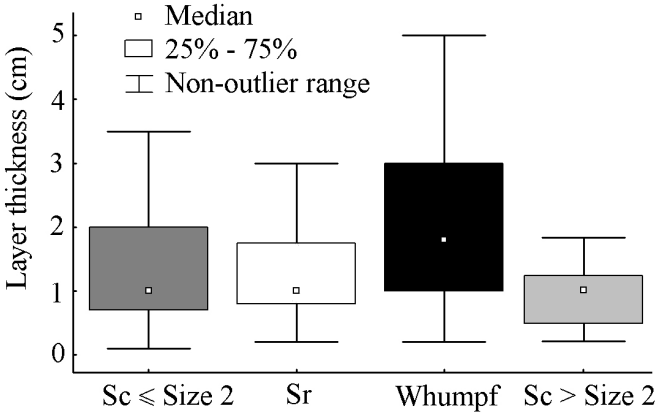

Figure 4.24: *Weak layer thickness for small slab avalanches (dark grey), remotely triggered slab avalanches (white), whumpfs (black) and large slab avalanches (light grey).*

small slab avalanches (Table 4.12). The median weak layer thickness for whumpfs was 1.8 cm, whereas Th_{WL} had a median of 1 cm for remotely triggered avalanches and for small and large slab avalanches (Table 4.12). Furthermore, as can be seen in Figure 4.24, weak layers involved with whumpfs had a wider range of thicknesses.

Slab properties

The hardness, bridging and density of the slabs were significantly higher for whumpfs, remotely triggered and large slab avalanches than for small slab avalanches (Table 4.12). As seen in Figure 4.25, the range of slab hardness for whumpfs, remotely triggered and large slab avalanches was more narrow than for small slab avalanches. Furthermore the slab hardness data for these avalanches was skewed towards higher values of h_{slab}. Finally, the majority of slab hardness data from remotely triggered slab avalanches and whumpfs was within the 4F to 1F range. Similar characteristics were observed for B_{slab} and ρ_{slab}. For remotely triggered slab avalanches, whumpfs and large slab avalanches, B_{slab} typically ranged from 100 to 200 hard-

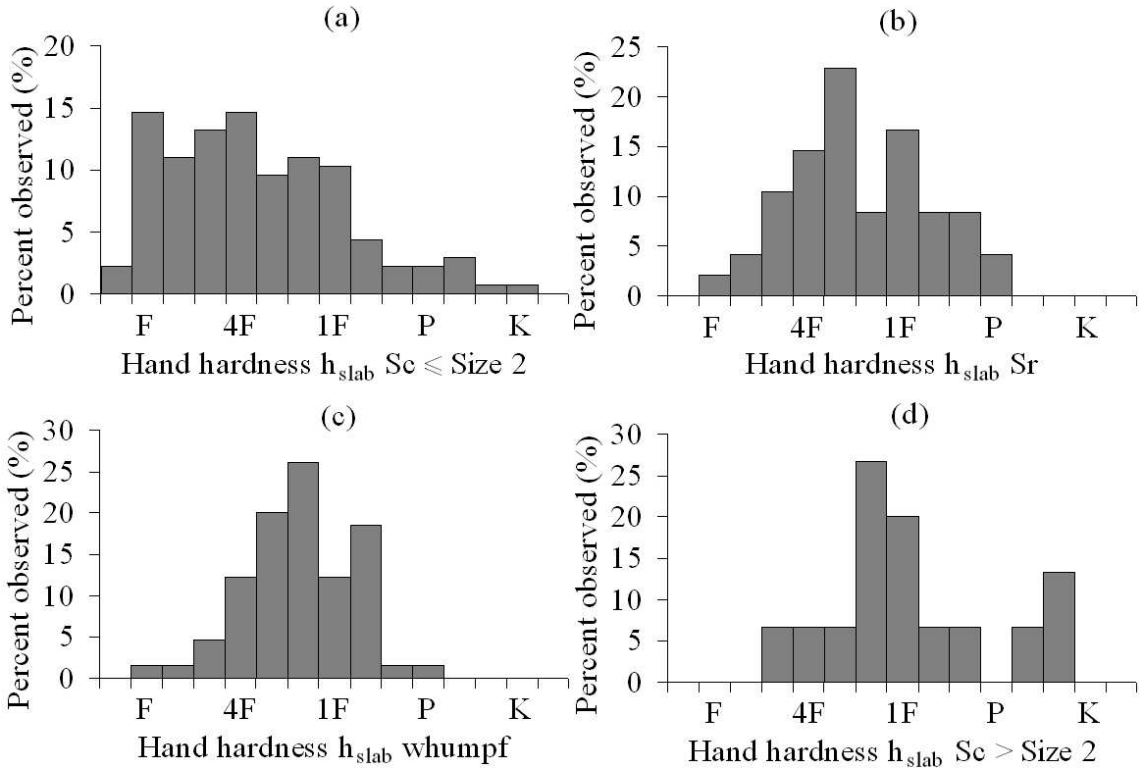

Figure 4.25: *Frequency of observation of slab hardness. (a) Small skier-triggered slab avalanches. (b) Remotely triggered slab avalanches. (c) Whumpfs. (d) Large skier-triggered slab avalanches.*

ness*cm, whereas B_{slab} was generally lower than 100 hardness*cm for small slab avalanches.

Properties of the layers adjacent to the weak layer

In Figure 4.26, the frequency of observation by grain type for the layers adjacent to the weak layer is shown. There were not many differences in crystal type of the adjacent layers. Nonetheless, the layer above the weak layer involved in whumpfs and large slab avalanches consisted more often of rounded grains (RG) or a crust (CR), whereas the layers below the weak layer consisted more often of faceted crystals (FC) or a crust (CR). The layer above the weak layer involved in remotely triggered

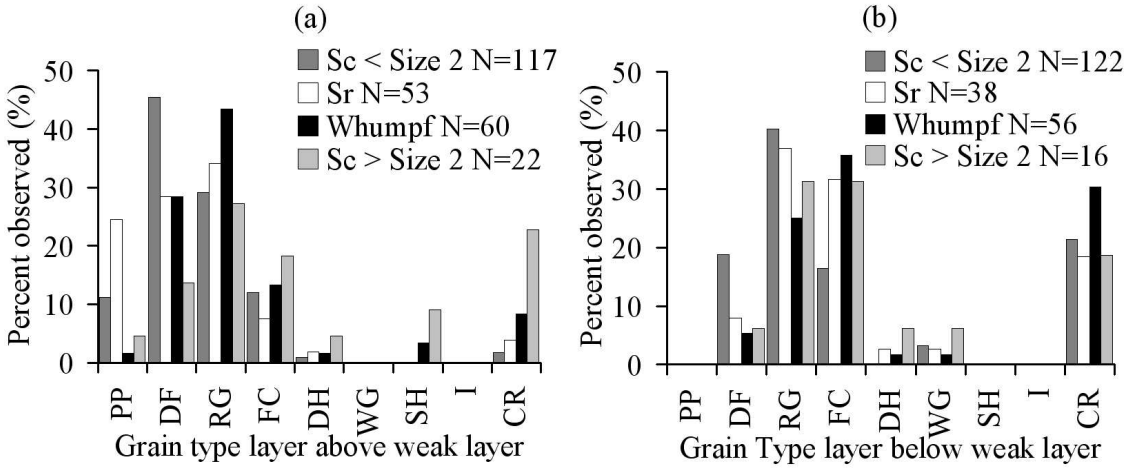

Figure 4.26: *Frequency of observation of grain type for directly skier-triggered slab avalanches (dark grey), remotely triggered avalanches (light grey) and whumpfs (black). The number of observations N is also shown.*

slab avalanches was relatively more often composed of precipitation particles (PP) and the layer above weak layers involved in small slab avalanches was more often composed of DF crystals.

The crystal size of the layers adjacent to weak layers associated with remotely triggered slab avalanches, whumpfs and large slab avalanches was significantly different from small slab avalanches (Table 4.12). However, the crystals of the layer above the weak layer were significantly smaller, whereas the crystals of the layer below were significantly larger (Table 4.12).

As can be seen in Figure 4.27, the density of the adjacent layers was typically larger for remotely triggered slab avalanches, whumpfs and large slab avalanches than for small slab avalanches. Furthermore, the differences were most pronounced for large slab avalanches. This is also seen by the higher significance level for ρ_{La} and ρ_{Lb} for large slab avalanches in Table 4.12.

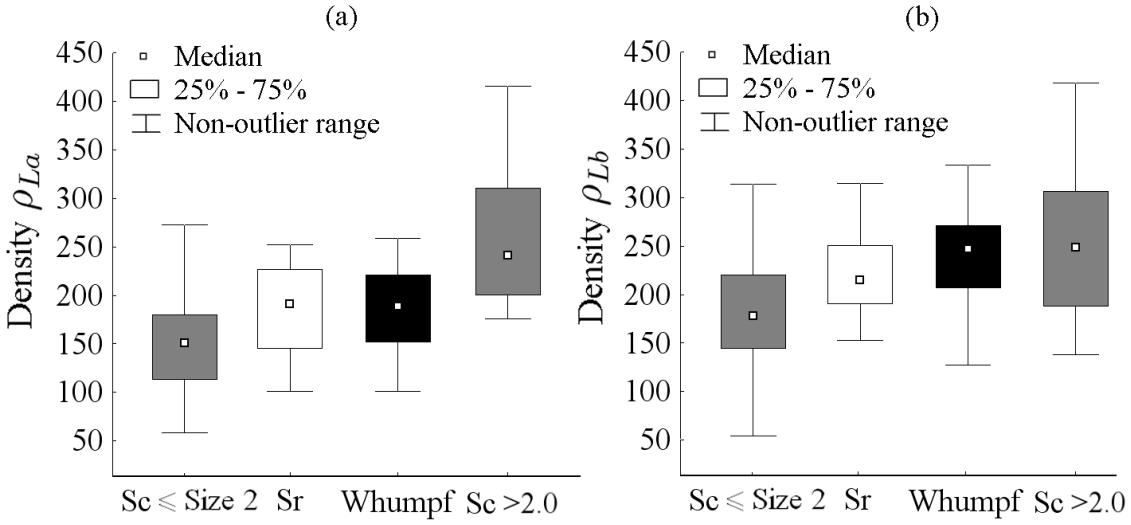

Figure 4.27: *Density of the layers adjacent to the weak layer for directly skier-triggered slab avalanches (dark grey), remotely triggered avalanches (light grey) and whumpfs (black). (a) Density of the layer above the weak layer (La). (b) Density of the layer below the weak layer (Lb).*

Finally, the hand hardness of the layer above the weak layer was significantly higher for whumpfs, remotely triggered and large avalanches. The same was true for the layer below the weak layer, except for remotely triggered slab avalanches (Table 4.12).

Differences in snowpack properties between the adjacent layers and the weak layer

The difference in hand hardness between the layer above and the weak layer was the most significant variable (Table 4.12). As can be seen in Figure 4.28 (a), Δh_{La} was generally larger for remotely triggered slab avalanches and whumpfs than for small and large slab avalanches. This was not the case for Δh_{Lb} (Figure 4.28 (b)), for which there was no significant difference (Table 4.12) between the various types of

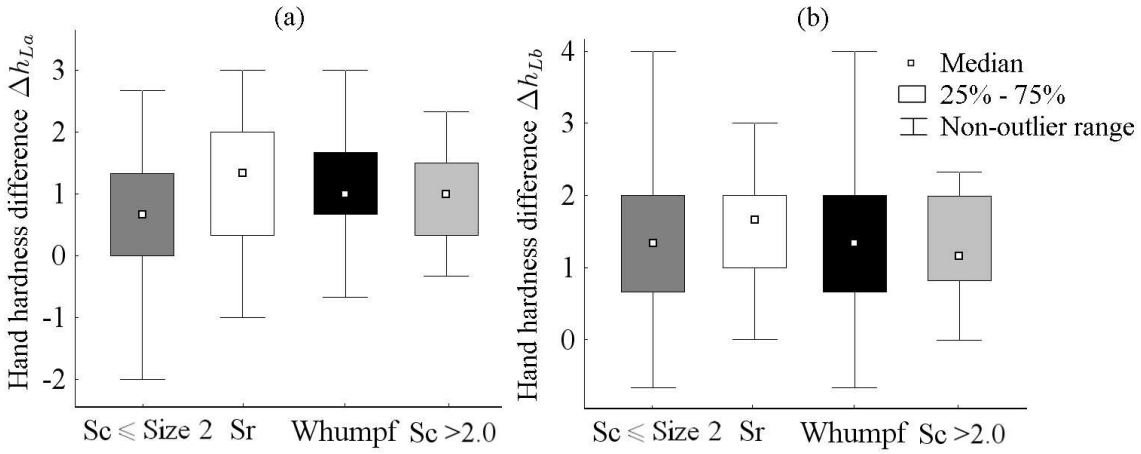

Figure 4.28: *Difference in hand hardness between the adjacent layers and the weak layer for directly skier-triggered slab avalanches (dark grey), remotely triggered avalanches (light grey) and whumpfs (black). (a) Difference in hand hardness between the layer above and the weak layer. (b) Difference in hand hardness between the layer below and the weak layer.*

slab avalanches.

Differences in crystal size between the adjacent layers and the weak layer were only significant variables for whumpfs. This indicated that the crystals from the weak layer associated with whumpfs were generally much larger than the crystals in the adjacent layers. As can be seen in Table 4.12, the median value of ΔE_{La} and ΔE_{Lb} was much larger for whumpfs (6 and 8.5 mm, respectively) than for small slab avalanches (1 and 2.1, respectively). This comes as no surprise since most weak layers associated with whumpfs and remotely triggered avalanches were buried SH layers (Figure 4.23).

Comparison of snowpack properties between the trigger point and the fracture line of remotely triggered slab avalanches

For five remotely triggered slab avalanches, profiles were observed at the trigger point as well as at the fracture line (i.e. crown). The depth of the weak layer at the trigger point was generally slightly shallower than at the fracture line (4 of 5), as seen in Figure 4.29 (a). This indicates that remotely triggered slab avalanches are generally initiated in areas where the snowpack is relatively thin. Furthermore, the weak layer at the trigger point was typically thinner than at the fracture line (3 of 5, Figure 4.29 (b)). However, two of these weak layers were thick layers of depth hoar ($>$ 20 cm). Finally, the hardness of the weak layer at the trigger point was equal or lower than at the fracture line (5 of 5, Figure 4.29 (c)), indicating that at the trigger point the weak layer was typically weaker than at the fracture line.

The properties of the layers adjacent to the weak layer on the other hand, did not differ much from those of the layers adjacent to the weak layer at the fracture line. Similarly, little difference was observed between the slab properties at the trigger point and those at the fracture line.

Comparison of snowpack properties between whumpfed and unwhumpfed areas

Nine profiles were observed inside the area of a whumpf, where the weak layer had fractured. There were no significant differences in snowpack properties between the whumpfed and unwhumpfed profiles, except for the change in weak layer thickness. The thickness of the weak layer inside the whumpfed area was always lower than in the undisturbed area, showing that during fracture (i.e. whumpfing) there was

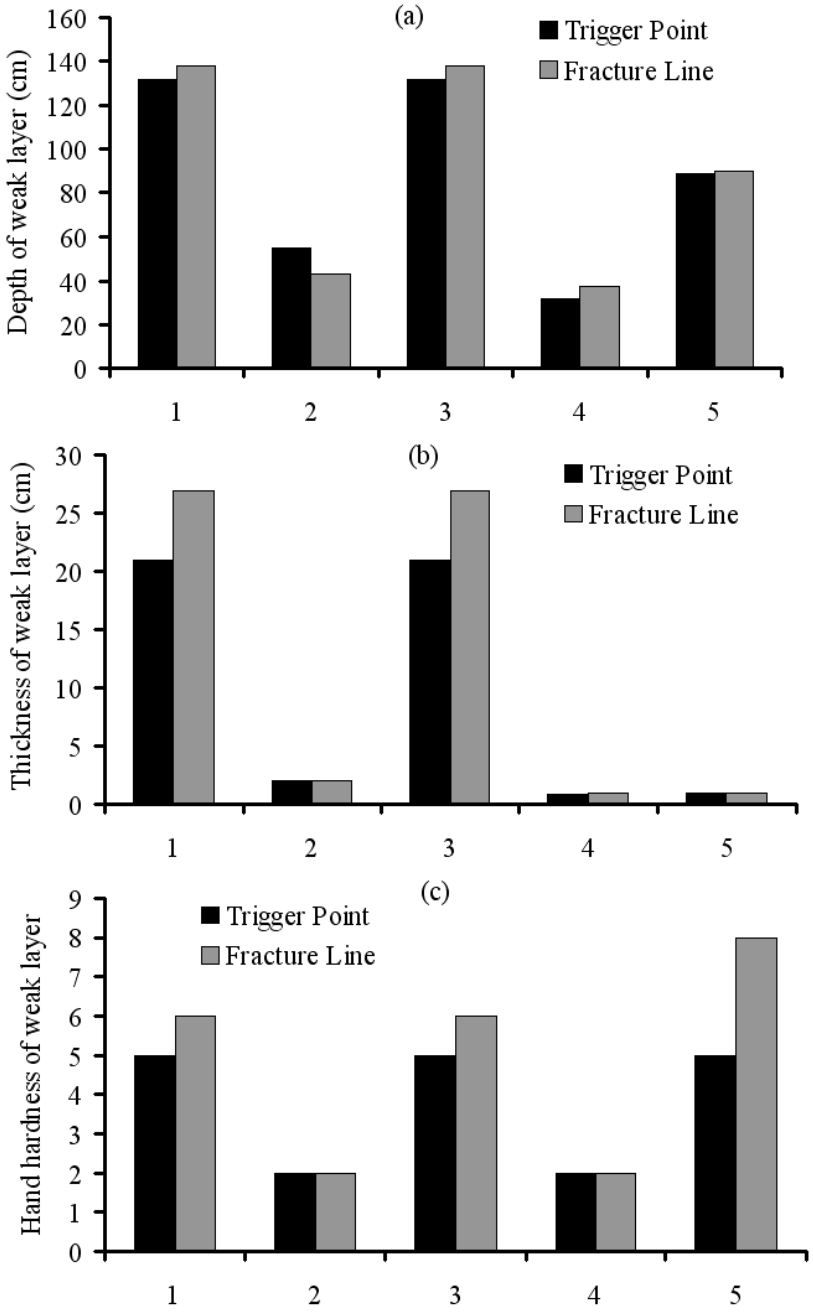

Figure 4.29: *Comparison of weak layer properties between the trigger point and the fracture line of five remotely triggered slab avalanches. (a) Weak layer depth. (b) Weak layer thickness. (c) Weak layer hand hardness.*

Table 4.13: *Measured difference in weak layer thickness between whumpfed and unwhumpfed sites. The depth of the weak layer (D_{WL}), weak layer crystal type (F_{WL}) and size (E_{WL}), the thickness of the weak layer in the undisturbed snowpack (Th_{WL}) and the amount of collapse obtained from the whumpfed area are shown (ΔTh_{WL}).*

D_{WL} (cm)	F_{WL}	E_{WL} (mm)	Th_{WL} (cm)	ΔTh_{WL} (cm)
68	SH	12	1.3	0.8
67	SH	12.5	2.5	0.5
26	SH	14	3	1.5
141	DH	3	28.5	14.5
42	SH	15	2	0.5
49.2	SH	9	1.2	0.2
64.5	SH	7.5	1.5	0.8
55.2	SH	6	0.7	0.2
58.2	SH	6	0.3	0.1

collapse of the weak layer. The amount of collapse was taken as the difference in weak layer thickness between the undisturbed site and the whumpfed site. In Table 4.13 the measured change in weak layer thickness is shown. The amount of collapse ranged from 0.1 cm to 14.5 cm for a thick weak layer composed of DH crystals.

Correlation between snowpack variables and avalanche size and width.

An overview of the correlation between various snowpack variables and the size and width of the investigated slab avalanches is given in Table 4.14. Since there was a strong significant positive correlation between the size of the slab avalanches and the width ($N = 191$, $R_s = 0.71$, $p = 10^{-32}$), it comes as no surprise that the correlations between snowpack variables and avalanche size and width were very similar. Both the size and the width of the investigated slab avalanches had significant positive correlation with many snowpack variables: B_{slab}, D_{WL}, h_{La}, h_{slab}, ρ_{La}, Σ, ρ_{slab}, h_{WL}, h_{Lb}, ρ_{Lb}, Δh_{La}, ΔE_{La} and E_{WL}. However, the strongest correlations were with slab properties and properties of the layer above the weak layer. The only significant

Table 4.14: *Correlation between snowpack variables and avalanche size and width. Snowpack variables marked with an asterisk were correlated with the width of slab avalanches using the Spearman Rank order correlation.*

	Avalanche Size (CAA, 2002)				Width		
Variable	N	R_s	p	Variable	N	R_p	p
B_{slab}	151	0.60	$4\ 10^{-16}$	$^{*}B_{slab}$	130	0.64	$4\ 10^{-16}$
D_{WL}	156	0.57	10^{-14}	D_{WL}	134	0.52	10^{-14}
h_{La}	151	0.47	$2\ 10^{-9}$	$^{*}h_{La}$	130	0.55	$2\ 10^{-9}$
h_{slab}	151	0.43	$3\ 10^{-8}$	$^{*}h_{slab}$	130	0.55	$3\ 10^{-8}$
ρ_{La}	82	0.56	$6\ 10^{-8}$	ρ_{La}	75	0.65	$6\ 10^{-8}$
Σ	119	0.46	10^{-7}	Σ	106	0.50	10^{-7}
ρ_{slab}	90	0.50	$4\ 10^{-7}$	ρ_{slab}	84	0.62	$4\ 10^{-7}$
h_{WL}	137	0.37	$9\ 10^{-6}$	$^{*}h_{WL}$	116	0.46	$9\ 10^{-6}$
h_{Lb}	151	0.33	$3\ 10^{-5}$	$^{*}h_{Lb}$	129	0.37	$3\ 10^{-5}$
ρ_{Lb}	67	0.42	$3\ 10^{-4}$	ρ_{Lb}	61	0.34	$3\ 10^{-4}$
Δh_{La}	134	0.26	0.002	$^{*}\Delta h_{La}$	130	0.29	0.002
ΔE_{La}	121	0.24	0.009	ΔE_{La}	130	0.25	0.009
E_{WL}	151	0.19	0.022	E_{WL}	130	0.21	0.023
ΔE_{Lb}	106	0.19	0.051	ΔE_{Lb}	84	0.19	0.051
Δh_{Lb}	135	0.10	0.265	$^{*}\Delta h_{Lb}$	84	0.18	0.265
E_{Lb}	107	0.03	0.749	E_{Lb}	93	0.04	0.749
Th_{Lb}	154	0.01	0.890	Th_{La}	132	0.03	0.959
Th_{La}	153	0.00	0.969	Th_{WL}	134	-0.01	0.823
Th_{WL}	156	-0.02	0.823	Th_{Lb}	132	-0.10	0.890
E_{La}	122	-0.25	0.006	E_{La}	107	-0.35	0.006

negative correlation was with E_{La}, indicating that skier-triggered slab avalanches were generally smaller for larger E_{La}.

4.4 Summary of results

Results from the typical distributions of snowpack variables showed that snowpack layers with different grain types often have different physical characteristics (Section 4.2). *Storm* layers were typically relatively hard (median 1F), thick (median 10 cm) and composed of small grains (median 1 mm). Furthermore, the differences in grain size and hand hardness between *Storm* layers and the adjacent layers were generally small (Table 4.2). Similar characteristics were found for FC and DH layers, although the density of FC and DH layers was typically higher than for *Storm* layers of comparable depth. On the other hand, buried SH layers were generally thin (median 1 cm) snowpack layers composed of large crystals (median 5 mm). Moreover, differences in crystal size and hand hardness between the adjacent layers and buried SH layers were typically much larger than for *Storm* layers and FC and DH layers (Figure 4.2 and Figure 4.3).

The cross correlation analysis has shown that there were many correlations between various snowpack variables (Section 4.3.2). The density, hand hardness and shear strength were found to increase with depth for all grain groups. Furthermore, the hand hardness and the shear strength had significant positive correlations with density, and there was a significant positive correlation between the shear strength and the hand hardness. These correlations have long been recognized in various studies (e.g. Gold, 1956; Mellor, 1975; Jamieson, 1995; Shapiro et al., 1997). However,

some differences were observed between the various grain groups (e.g. Figure 4.4), showing the importance of grain type and grain size. Furthermore, the importance of grain size was emphasized by the negative correlation between hand hardness and crystal size, showing that snowpack layers composed of larger crystals generally have a lower hand hardness, and thus a lower shear strength. This was especially true for buried SH layers, for which there also was a positive correlation between layer thickness and crystal size (e.g. Figure 4.5). Finally, both ΔE_{La} and ΔE_{Lb} were significantly affected by the crystal size of the snowpack layers (e.g. Figure 4.6), which comes as no surprise. Likewise, differences in hand hardness between a particular layer and the adjacent layers were influenced by the hardness of the particular layer in that harder layers generally had smaller differences in hand hardness (e.g. Figure 4.7).

The comparison of stable and unstable snowpack variables has shown that many measured and calculated snowpack variables were indicative of instability in the combined data set and for each grain group (Section 4.3.3). For the weak layer, the significant variables were: depth, thickness, crystal type and size, and hand hardness. Unstable weak layers were generally shallow, thin, soft layers composed of relatively large crystals, most often buried SH. Furthermore, the difference in hand hardness between the slab and the weak layer was generally large for unstable slabs (Figure 4.11 (c)). The layers adjacent to the weak layer were generally of lower density for unstable weak layers than for stable weak layers. Finally, differences in crystal size and hand hardness were typically larger for unstable weak layers (Table 4.8). Furthermore, three additional variables, h_{slab}, B_{slab} and E_{Lb}, were significant in the combined data set and for two out of three grain groups. The slab was generally

softer, with typically a bridging value between 100 and 150 hardness*cm (e.g. Figure 4.11(b)) and the crystals in the layer below were generally smaller for unstable weak layers (Table 4.8).

From the comparison of stable and unstable primary weaknesses (Section 4.3.4), five variables emerged as significantly different in the combined data set and for each grain group: the crystal type and size of the primary weakness, the shear strength of the primary weakness and the density of the adjacent layers. Unstable primary weaknesses were predominantly composed of large persistent crystals (e.g. Figure 4.16) with low shear strength. Furthermore, the density of the layer above and the layer below the primary weakness was generally lower for unstable primary weaknesses (Tables 4.10 and 4.11). Primary weaknesses composed of FC and DH did not exhibit many significant differences in snowpack properties, showing that assessing the stability for these weak layers is more complex. On the other hand, many additional snowpack variables were significant in the combined data set as well as for *Storm* and buried SH primary weaknesses: D_{WL}, h_{WL}, h_{slab}, B_{slab}, Δh_{slab}, h_{La}, h_{Lb},ΔE_{Lb} and Δh_{La}.

The comparison of remotely triggered slab avalanches, whumpfs and large skier-triggered slab avalanches with small skier-triggered slab avalanches (Section 4.3.5) showed that the following snowpack variables were significant: D_{WL}, Σ, h_{slab}, B_{slab}, ρ_{slab}, E_{La}, h_{La}, ρ_{La}, E_{Lb}, ρ_{Lb}. Whumpfs, remotely triggered slab avalanches and large skier-triggered slab avalanches generally had deeper weak layers with higher shear strength than weak layers associated with small skier-triggered slabs. Furthermore, the hand hardness of the slab, the bridging and the density of the slab were typically larger. The layers adjacent to the weak layer were generally also of higher density.

Finally, weak layers associated with whumpfs, remotely triggered slabs and large slab avalanches were generally older than weak layer associated with small skier-triggered avalanches. Additionally, six more variables were significantly different for at least two types of slab avalanches: E_{WL}, h_{WL}, ρ_{WL}, h_{Lb}, ΔE_{La} and Δh_{La} (Table 4.12).

The comparison of snowpack properties measured at the trigger point of remotely triggered avalanches showed that the weak layer was generally shallower and softer than at a site representative of the fracture line. Furthermore, the amount of vertical displacement caused by the fracture of weak layers at whumpf sites was measured and ranged from 0.1 to 14.5 cm, with a median of 0.5 cm. Finally, the correlation of snowpack variables with the size and width of the investigated slab avalanches showed that many snowpack variables had significant positive correlations. The strongest correlations however, were with snowpack variables from the overlying slab and the layer above the weak layer.

A schematic overview of the trends in the frequency of skier-triggering by snowpack variables of the weak layer, the slab and the adjacent layers is given in Figure 4.30. Only trends that were observed for each grain group as well as in the combined data set are shown. In general, an increase in frequency of skier-triggering was observed with shallow weak layers (i.e. $D_{WL} < 20$ cm), whereas a decrease in frequency of skier-triggering was observed for deep weak layers (see Figure 4.9). However, deeper unstable weak layers were generally associated with larger skier-triggered slab avalanches.

The frequency of skier-triggering decreased with increasing h_{WL} (see Figure 4.18). As expected, similar trends were also found for the shear strength. On the other hand, an increase in frequency of skier-triggering was observed with increasing E_{WL}

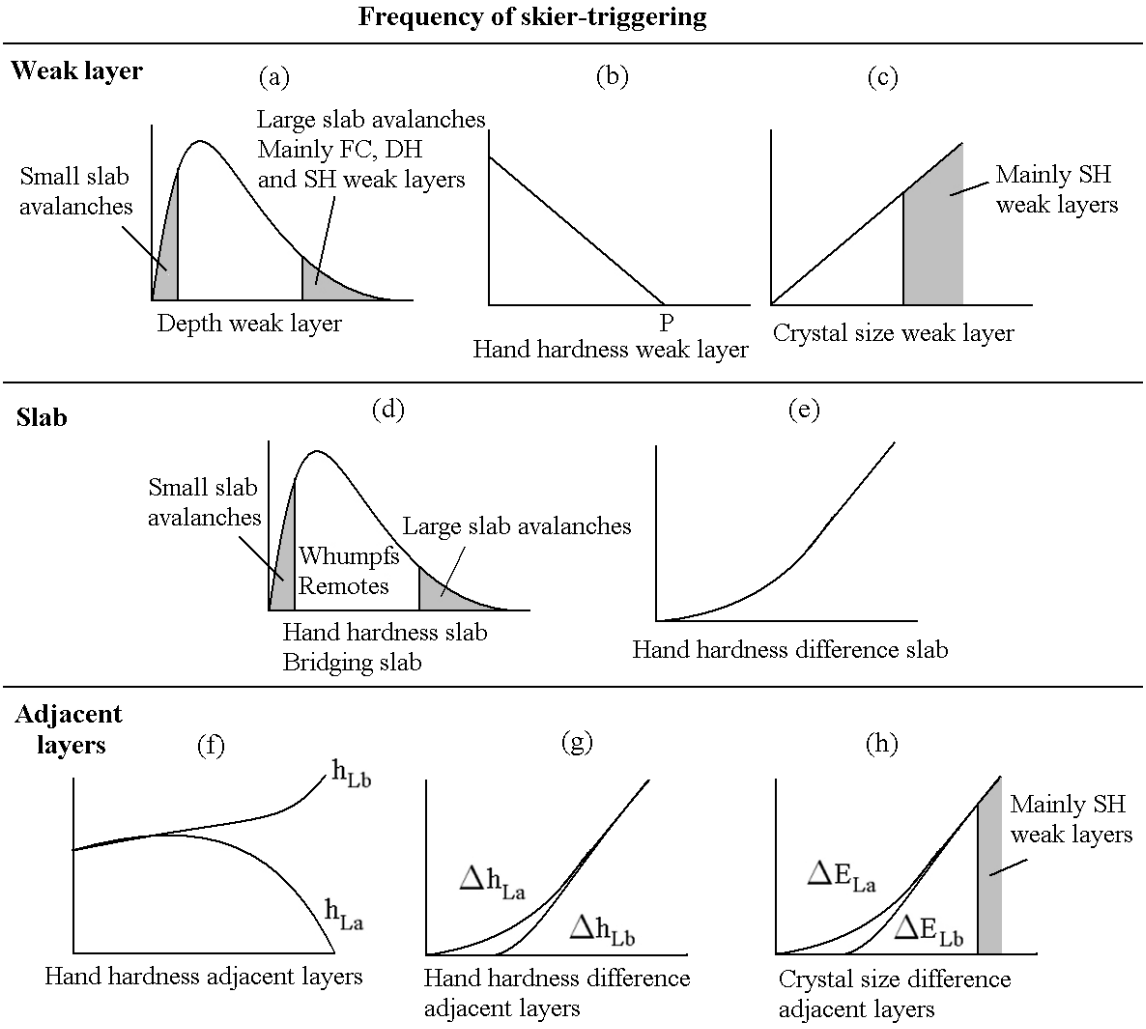

Figure 4.30: *Schematic overview (not to scale) of the observed frequency of skier-triggering (vertical axis) by snowpack variables. (a) Depth of the weak layer. (b) Hand hardness of the weak layer. (c) Crystal size of the weak layer. (d) Hand hardness and bridging of the slab. (e) Difference in hand hardness between the slab and the weak layer. (f) Hand hardness of the adjacent layers. (g) Difference in hand hardness between the adjacent layers and the weak layer. (h) Differences in crystal size between the weak layer and the adjacent layers.*

(see Figure 4.17), Δh_{slab} (see Figure 4.11 (c)), ΔE_{La} (see Figure 4.22), ΔE_{Lb}, Δh_{La} (see Figure 4.15 (a)) and Δh_{Lb} (see Figure 4.15 (b)). Furthermore, consistent trends were observed in the frequency of skier-triggering by h_{slab} and B_{slab}. For these variables, the frequency of skier-triggering was observed to increase until a maximum was reached, followed by a decrease in frequency of skier-triggering (e.g. Figure 4.11 (a) and (b); Figure 4.14 (a)). Finally, the hardness of the layer above did not affect stability in the same manner as the hardness of the layer below. Whereas the frequency of skier-triggering decreased for large values of h_{La}, it increased for large values of h_{Lb}.

4.5 Discussion

The snowpack variables that were found to be significant in the combined data set and for at least two out of three grain groups were similar to those identified in recent studies (e.g. Schweizer and Jamieson, 2001, 2003a and 2003b; Schweizer et al., in press). However, important differences were found by considering the differences in snowpack properties between both the adjacent layers and the weak layer separately. This had not been done in previous studies. Furthermore, the analysis has shown that some measured and calculated variables were not significant for each grain group. Finally, by looking at the frequency of skier-triggering, the association of the various parameters with stability was observed.

In order for a skier to trigger a slab avalanche, a skier has to initiate a fracture in a weak layer which then propagates along the weak layer until the slab is released. In this section, the significant snowpack variables are discussed with an emphasis

on their relation to fracture initiation and fracture propagation, both of which are required for slab avalanche release (Schweizer et al., 2003). However, because these data are solely from the Columbia Mountains of British Columbia, the present results should be considered representative of that specific snow climate and caution should be exerted before applying these findings to other snow climates.

4.5.1 Weak layer properties

Unstable weak layers were predominantly composed of buried SH crystals, followed by FC and DH and then *Storm* layers. Persistent grain types have long been recognized as playing a key role in avalanche formation (e.g. Perla, 1977) and these findings come as no surprise. It is a well known fact that persistent weak layers are more prone to avalanching than non-persistent weak layers and can remain unstable over extended periods of time.

The depth of the weak layer relates to the ease of fracture initiation. Shallow weak layers can easily be fractured by skiers as additional stress introduced in the snowpack overcomes the strength of the weak layer. However, for deeper weak layers, the skier's stress strongly decreases, reducing the frequency of fracture initiation. Schweizer and Camponovo (2001) measured the stress below a skier, and showed that it roughly decreases as $\frac{1}{D}$, which is consistent with the observed decrease in frequency of skier-triggering with increasing depth (Figure 4.9).

On the other hand, the frequency of skier-triggering for shallow weak layers (i.e. < 20 cm) was low. This is partly because skis typically penetrate the snow surface by 20 to 30 cm (Jamieson, 1995). Therefore, skiers seldom trigger slab avalanches on weak layers within the upper 20 cm of the snowpack, since ski penetration causes

the weak layer as well as the overlying slab to fracture. This is shown schematically in Figure 4.31 (a). While skiers can easily fracture shallow weak layers, the overlying slab has low stiffness (soft) and has very low strength. Additional stress induced by the skier will therefore lead to brittle fractures in the slab. The slab can therefore not efficiently deliver stress to the crack tip, and fracture propagation is impeded. This is consistent with the author's field observations in that skier-triggered slab avalanches on shallow weak layers are infrequent and generally very small (Size 1 or smaller) and do not propagate much further than the length of the skis (i.e. one to two metres; Figure 4.31 (b)).

By performing a finite element simulation of a layered snowpack, Schweizer (1993) showed that stress concentrations occur at layer transitions in the snowpack, particularly at the transition from a stiff (hard) to a less stiff (soft) layer. He found that stress concentrations increased as the difference in hardness between both layers increased. Furthermore, he found that stress concentrations were even more pronounced in thin weak layers. This is consistent with the fact that unstable weak layers were generally thin layers that were significantly softer than the adjacent layers, promoting stress concentrations in the weak layer, thereby facilitating fracture initiation (Sections 4.3.3 and 4.3.4). However, some significant differences were observed for buried SH weak layers. For these layers, there was an increase in frequency of skier-triggering with increasing layer thickness. Furthermore, whumpfs were typically associated with thicker weak layers, predominantly composed of persistent grain types. This indicates that thicker persistent weak layers are favourable to fracture propagation. This is consistent with the theory proposed by B. C. Johnson (2000) for fracture propagation on low angle terrain by emphasizing the importance of the

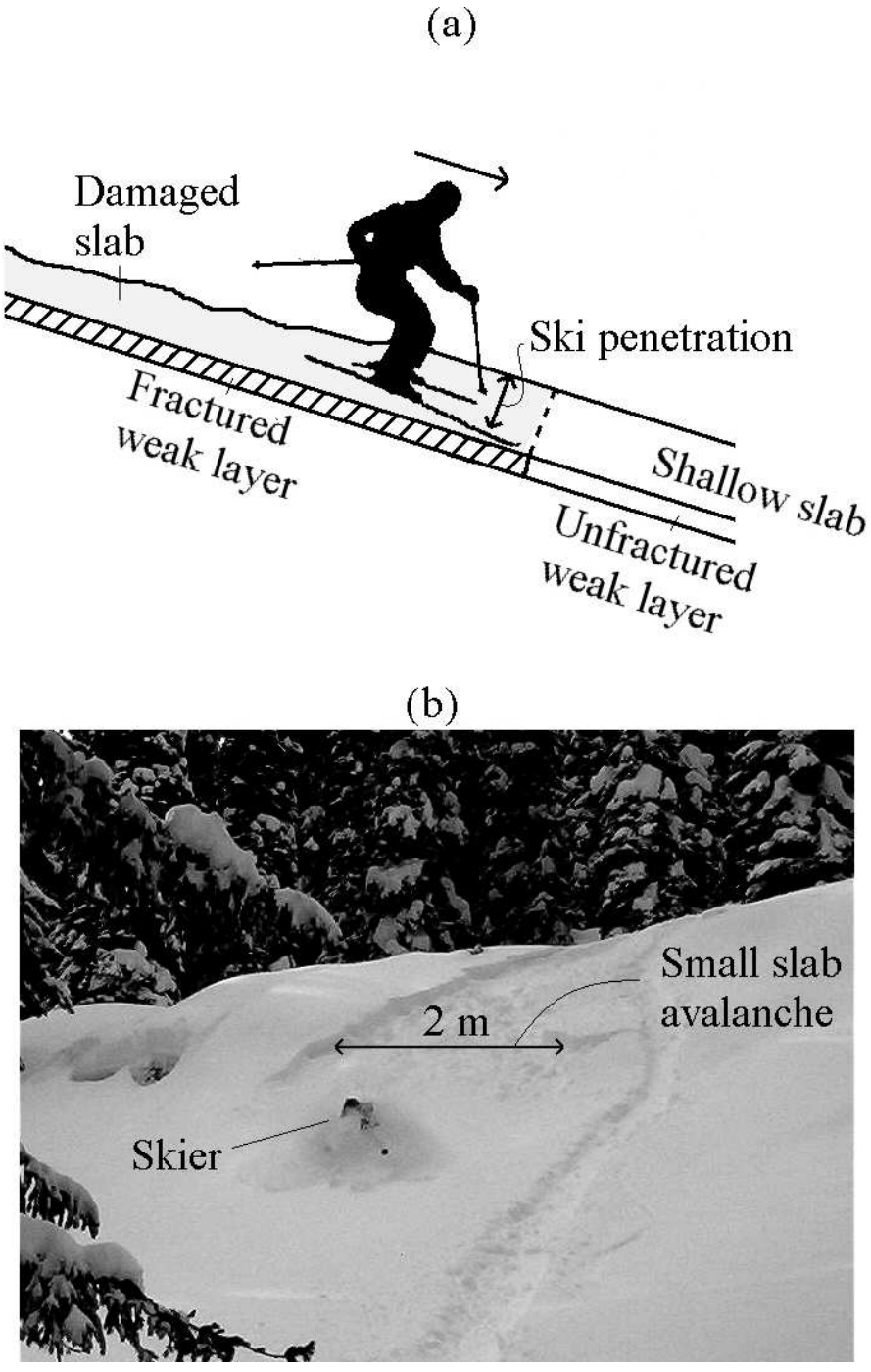

Figure 4.31: *(a) Schematic representation of a skier fracturing a shallow weak layer as well as the overlying soft slab, thereby impeding fracture propagation. (b) Photo of skier, with significant ski penetration, who just triggered a very small slab avalanche (approximately 2 m wide) on a shallow buried SH layer (approximately 30 cm deep), showing very little fracture propagation (A. van Herwijnen photo).*

compressive component during fracture (i.e. collapse of the weak layer), introducing bending in the slab.

Skier-triggered avalanches were less frequent for harder weak layers and no weak layers harder than 1F+ were skier-triggered. The hand hardness of the weak layer, which typically increases with depth, relates to the shear strength of that layer. This shows that harder weak layers generally have a higher shear strength and are deeper in the snowpack. Therefore, fracture initiation is impeded for harder weak layers as more stress is required to fracture the weak layer while less stress reaches the weak layer.

Finally, weak layers composed of larger crystals were more often associated with skier-triggered slab avalanches (Figure 4.17). This is attributed to the fact that layers composed of larger crystals typically had a lower hand hardness, and thus a lower shear strength (Section 4.6). Therefore, fractures can be initiated more easily in weak layers composed of larger crystals. Furthermore, there was also a positive correlation between crystal size and differences in grain size with the adjacent layers. Colbeck (2001) described a theoretical framework for bond growth between snow crystals of dissimilar sizes. He showed that large differences in grain size indicate poor bonding. Weak layers composed of larger crystals will generally not bond well to the surrounding snow, inducing stress concentrations at the bond scale, which facilitates fracture.

4.5.2 Slab properties

Generally speaking, there are two requirements for skier-triggering (Figure 4.32): fracture initiation and fracture propagation. The depth of the weak layer influences

whether or not a skier can induce sufficient stress to initiate a fracture in the weak layer (see above). Additionally, the depth of the weak layer also influences weak layer properties (i.e. hand hardness and strength) as well as the slab hardness. Schweizer (1993) noted that thick hard layers in the snowpack form a sort of bridge by spreading the induced stress over a larger lateral distance, thereby decreasing the stress at the depth of the weak layer. Therefore, fracture initiation for deeper weak layers is further impeded by harder and thicker slabs.

Fracture propagation on the other hand requires the slab to be cohesive (stiff enough) to supply energy to the crack tip (see above). Therefore, with regards to fracture propagation, slab properties typically improve with increasing weak layer depth, since the slab becomes more cohesive (larger h_{slab}). This is shown conceptually in Figure 4.32 and the grey area under both curves is the frequency of skier-triggering. This is in good accordance with the trend observed in the frequency of skier-triggering by depth shown in Figure 4.9. Furthermore, for the same reasons, similar trends were observed in the frequency of skier-triggering by h_{slab} (Figure 4.11 (a)) and B_{slab} (Figure 4.11 (b)).

The comparison of remotely triggered avalanches, whumpfs and large slab avalanches with small skier-triggered avalanches further accentuated the importance of slab hardness for fracture propagation. The distribution of the slab hardness data for these occurrences (Figure 4.25), which are associated with snowpack conditions favourable for fracture propagation, was centred around 4F to 1F, coinciding with the maximum frequency of skier-triggering by h_{slab} shown in Figure 4.11 (a). This shows that thicker, harder slabs favour fracture propagation, which supports the strong positive correlations of D_{WL}, h_{slab} and B_{slab} with the size and width of skier-

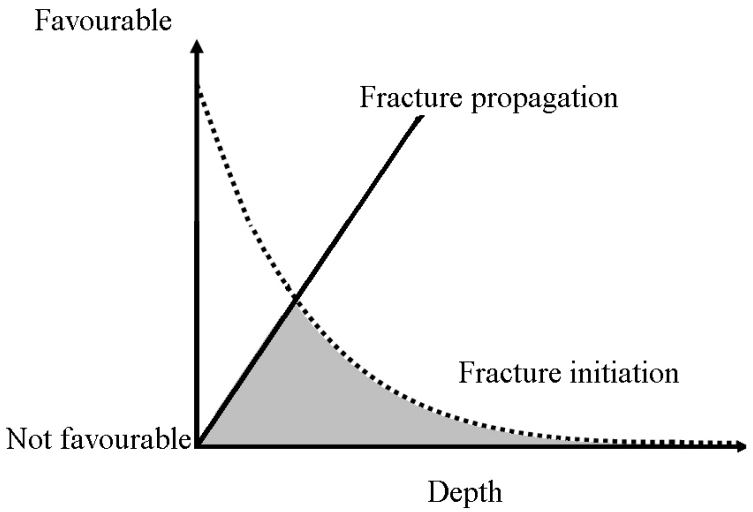

Figure 4.32: *Schematic representation of the influence of weak layer depth on fracture initiation and fracture propagation. Conditions for fracture initiation become less favourable with increasing depth whereas conditions for fracture propagation improve. The grey area under the curves represents the expected frequency of skier-triggering by depth.*

triggered slab avalanches (Section 4.3.5).

Föhn et al. (1998) showed that in the brittle range, the shear stress increased almost linearly with strain until the weak layer fractured, hence $\tau = \mathcal{G}\gamma$, here γ is the shear strain and $\mathcal{G}$ is the shear modulus, which is related to the elastic modulus by $\mathcal{E} = 2(1+\nu)\mathcal{G}$. Furthermore, Föhn et al. found that the shear strain up to the point fracture was approximately constant. Since the hand hardness of snowpack layers is approximately proportional to the shear strength, hand hardness can therefore be considered an index of the elastic modulus of that layer. However, the stress state in the slab over a dynamically propagating fracture is unknown. Fuller (in press) reported that slabs that had fractured but did not slide downslope were often taller than the unreleased part, which he attributed to an elastic response of the slab to

unloading. Furthermore, he stated that this was especially apparent for deeper and harder slabs. Here, the elastic stain energy released by the fracture in the weak layer is approximated by the pre-fracture shear strain energy U of the slab. For shearing stresses this is given by (e.g. Beer and Johnston, 1985: 478):

$$U = \int \frac{\tau^2}{2\mathcal{G}} dV \tag{4.2}$$

where τ is the shear stress, $\mathcal{G}$ is the shear modulus, and the pre-fracture elastic shear strain is assumed to be constant in the slab over the subsequent fracture in the weak layer. For a fracture of length $2a$ and unit width, the strain energy of half the crack length is given by:

$$U = \int_0^a \frac{\tau^2}{2\mathcal{G}} \mathcal{H} dx = \int_0^a \frac{\mathcal{G}\gamma^2}{2} \mathcal{H} dx = \frac{a\gamma^2}{2} \mathcal{G}\mathcal{H} \tag{4.3}$$

where $\mathcal{H}$ is the slope normal slab depth. Hence, the elastic strain energy of the slab is proportional to $\mathcal{G}\,\mathcal{H}$, or $\mathcal{E}\,\mathcal{H}$. Since supporting the correlation of bridging (B_{slab}) with avalanche size (Section 4.3.5). The bridging index B_{slab} combines both the thickness of the slab (closely related to $\mathcal{H}$) and the slab hardness (related to $\mathcal{E}$), hence it can be thought of as an index of the elastic strain energy capacity of the slab, supporting the correlation of bridging with avalanche size (Section 4.3.5).

4.5.3 Properties of the adjacent layers

The density of both the adjacent layers were significant variables in all statistical comparisons. In general, the density of the adjacent layers was lower for unstable weak layers. However, for whumpfs, remotely triggered and large slab avalanches, the

density of the adjacent layers was typically larger than for small skier-triggered slabs. Furthermore, no distinct trends were observed in the frequency of skier-triggering by density of the adjacent layers. This indicates that the significant difference in density of the adjacent layers was likely influenced by the depth of the weak layer. As discussed earlier, the density of snowpack layers typically increases with depth. Unstable weak layers were typically shallower than stable weak layers. Therefore, it is not surprising that both ρ_{La} and ρ_{Lb} were lower for unstable weak layers. On the other hand, the weak layers associated with whumpfs, remotely triggered and large avalanches were generally deeper and older than small skier-triggered slab avalanches, hence the significantly larger ρ_{La} and ρ_{Lb} (Table 4.12).

The hardness of the layers adjacent to the weak layer on the other hand, exhibited trends in the frequency of skier-triggering and there were substantial differences between the layer above and the layer below the weak layer. The frequency of skier-triggering by h_{la} (Figure 4.14 (a)) had characteristics that were very similar to the frequency of skier-triggering by h_{slab}. This is expected, since the layer above the weak layer is the lowest layer in the slab. Therefore, the hand hardness and density of the layer above the weak layer affect both fracture initiation and fracture propagation in a similar manner as the hand hardness and the density of the slab. As described earlier, an increase in hardness will hinder fracture initiation by bridging, whereas conditions for fracture propagation are improved (Figure 4.32). On the other hand, very low hand hardness favours fracture initiation yet fracture propagation is impeded. Furthermore, the density and the hand hardness of the layer above also had significant positive correlations with the size and width of the skier-triggered slab avalanches, indicating that an increase in density and hand hardness of the

layer above the weak layer favours fracture propagation, as for the slab.

The properties of the layer below the weak layer did not affect fracture initiation and propagation in the same manner. This is highlighted by the increase in frequency of skier-triggering with increasing h_{Lb} (Figure 4.14 (b)), with a maximum for h_{Lb} = K. Indeed, as the layer below the weak layer increases in hand hardness, stress concentrations in the weak layer are increased, facilitating fracture initiation and propagation (see below). Furthermore, layers below unstable weak layers were more often a crust than the layer above the weak layer (Figure 4.12). This also indicates that the layer below the weak layer mainly acts as a stress concentrator. Whereas a hard layer above the weak layer would impede fracture initiation by bridging, a hard layer below the weak layer increases the stress concentrations favouring fracture propagation without impeding fracture initiation.

4.5.4 Differences in snowpack properties between the adjacent layers and the weak layer

From the above, it is clear that a typical unstable snowpack consists of a thin weak layer overlain by a cohesive slab and on top of a stiff layer. On the basis of interfacial fracture mechanics, Schweizer and Camponovo (2001) suggested that fracture propagation depends on the difference in stiffness between the weak layer and the adjacent layers. According to Wei et al. (1996), the interface fracture energy decreases as the relative modulus of the weak layer ($\mathcal{E}_{WL}/\mathcal{E}_{adjacent}$) increases. As mentioned earlier, hand hardness can be considered an index of elastic modulus. An increase in hand hardness difference therefore indicates a decrease in the relative modulus of the weak layer. On the basis of interfacial fracture mechanics, one would therefore ex-

pect fracture propagation to be more likely with increasing hand hardness difference. This is in good accordance with the observed increase in frequency of skier-triggering with increasing hand hardness difference (Figure 4.15). Furthermore, Δh_{La} was significantly larger for remotely triggered slab avalanches and whumpfs, showing that larger differences in hand hardness between the layer above and the weak layer favour fracture propagation.

Finally, as described earlier, large differences in crystal size indicate that there is poor bonding between the adjacent layers and the weak layer (Colbeck, 2001), consistent with an increase in frequency of skier-triggering with increasing grain size difference (Figure 4.22), for all grain groups.

4.6 Concluding remarks

The above results support findings of similar studies on skier-triggered slab avalanches (Schweizer and Wiesinger, 2001; Schweizer and Jamieson, 2001, 2003a and 2003b; Schweizer et al., in press). Weak layer properties, as well as slab properties and grain size and hand hardness differences were found to be indicative of instability. However, the present study investigated the snow cover variables in more detail, in particular the properties of the layers adjacent to the weak layer, which were considered separately. Furthermore, the results were discussed with an emphasis on fracture initiation and fracture propagation, both of which are required for slab avalanche release. However, since snow is such a complex material, as shown by the correlation analysis, the influence of snowpack variables on fracture initiation and fracture propagation are complex. Nevertheless, some important conclusions can be

drawn.

In order for a skier to initiate a fracture in a weak layer, sufficient stress has to reach the weak layer in order to overcome the strength of the weak layer. The amount of skier-induced stress at the weak layer is affected by the depth of the weak layer (D_{WL}) as well as the hardness, and therefore the density, of the snow layers above the weak layer (the slab and the layer above), hence these variables affect fracture initiation. The hand hardness of the weak layer is related to the strength, and is therefore related to fracture initiation. Finally, the thickness of the weak layer and differences in hand hardness and crystal size between the weak layer and the adjacent layers indicate stress concentrations, and therefore also influence fracture initiation (Section 4.5.1).

For fracture propagation, the energy consumed by the fracture must be less than or equal to the amount of energy released. Interfacial fracture mechanics suggests that the fracture energy decreases as the relative modulus of the weak layer increases. Since hand hardness can be thought of as an index of elastic modulus, differences in hand hardness also relate to fracture propagation (Section 4.5.4). The energy released during fracture was approximated with the elastic strain energy in the slab prior to fracture, which is proportional to the thickness and the stiffness of the slab (Section 4.5.2). Therefore, the hardness, the thickness and the bridging of the slab, as well as the hardness of the layer above the weak layer, relate to fracture propagation. More energy is released by thick, stiff slabs, favouring fracture propagation. On the other hand, shallow, soft slabs have low strength and are easily damaged by skiers. Even though skiers can readily fracture underlying weak layers, these slabs generally cannot efficiently transmit stresses to the crack tip, and widespread fracture

propagation is impeded (Section 4.5.1). For the Columbia Mountains, a typical slab hardness between 4F and 1F was found to be ideal for fracture propagation, while still allowing fractures to be initiated by a skier.

Chapter 5

Fracture character in stability tests

5.1 Introduction

Stability tests (Section 3.4) are widely used by avalanche workers and researchers to identify potential failure layers for slab avalanches and evaluate the stability of the overlying slab. For decades, avalanche professionals have recognized that the test score (i.e. loading step) is not the only result relevant to avalanche forecasting. Additional information about the character of the fracture can provide valuable information. For instance, since 1981, the Canadian Avalanche Association's Guidelines for Weather, Snowpack and Avalanche Observations have assigned a special code (STC) for collapsing fractures in shovel tests (NRCC, 1981).

Systems for classifying fractures have been proposed since the late 1990's. In 1999, Birkeland and Johnson proposed a three level shear quality description: Quality 1 is a clean fast shear or a collapse, Quality 2 is an average shear and Quality 3 an irregular shear. Johnson and Birkeland (2002) summarized six years of shear quality data from stuffblock, compression and rutschblock tests. Comparing the data with nearby signs of instability in the area, they reported improved interpretation of stability test results, particularly for tests with high scores. In Switzerland, a rating system for the fracture type (clean, partly clean, rough) in stability tests and the release type for rutschblock tests (whole block, most of the block or only an edge of the block) is in use (Schweizer and Wiesinger, 2001). Schweizer and Jamieson (2003a)

report a significant difference in fracture character and release type in rutschblock tests between human triggered slopes and slopes not triggered.

Using the rating system described in Section 3.4, over 4500 fractures observed in stability tests performed in the Columbia Mountains of western Canada were analyzed. The objectives are to determine specific snowpack characteristics associated with the different fracture characters and to assess if the proposed system can improve the interpretation of stability test results for avalanche forecasting. The main focus is on compression test results. Results from the rutschblock test, the deep tap test and the fracture propagation test are described as well.

Parts of the analysis presented in this chapter have been published previously. After the first winter of using the refined fracture classification system, preliminary results were published in "Avalanche News" (van Herwijnen and Jamieson, 2003), a revue published by the Canadian Avalanche Association. More recently, results from the analysis of fracture character in compression tests were presented at the International Snow Science Workshop in Jackson Hole, Wyoming. A paper will be published in the proceedings of this conference (Spring 2005) and has also been submitted for publication in a special issue of Cold Regions Science and Technology.

This chapter is organized as follows. First the data and specific methods for the analysis are described. Second, an overview of the results is presented. Special attention is given to identifying snowpack characteristics associated with the different types of fractures. This is followed by a discussion of the results and finally conclusions are drawn.

5.2 Methods

In 1997 researchers from the University of Calgary started systematically classifying fractures in stability tests (Figure 1.6) performed in the Columbia mountains of British Columbia, Canada, using a four level description of fracture character (Jamieson, 1999; van Herwijnen and Jamieson, 2002). After analyzing data from five winters, this system was refined in December 2002 (van Herwijnen and Jamieson, 2003). Presently a five level description of fracture character (Table 3.4) is used by field workers of the University of Calgary, as well as by several avalanche safety operations in Canada.

The definitions of PC, SC and B fractures have not changed since introduced in 1997. Therefore, some of the older data were used the analysis. In all, 4621 fractures in over 2200 compression tests were classified as PC (38%), RP (9%), SP (15%), SC (30%) and B (8%).

At each test site (regular study plot sites or skier-tested slopes) field researchers usually performed three compression tests and observed a snow profile, providing information about crystal type (F), crystal size (E), layer thickness (Th), density (ρ), depth (D) and hand hardness (h) of snowpack layers (CAA, 2002). This information was used to relate snowpack properties to fracture character in compression tests. Each layer that failed in a compression test is referred to as a "weak layer" (WL). Special attention was given to weak layer properties as well as to the properties of the layers above (La) and below (Lb) the weak layer. Also important are differences in snowpack properties between the weak layer and the adjacent layers (previous chapter), namely the differences in crystal size (ΔE_{La} and ΔE_{Lb}) and the differences

in hand hardness (Δh_{La} and Δh_{Lb}).

Over 1000 compression tests, resulting in 2512 fractures, were performed on 441 skier-tested slopes since 1997. However, only 980 of these fractures were classified using the new classification system (Table 3.4). Including whumpfs and remotely triggered avalanches, 160 of these slabs were skier-triggered.

Until December 2002, non-planar fractures (B) were only systematically recorded when associated with the failure plane of a slab avalanche. This introduces a strong bias towards skier-triggered slab avalanches for these fractures. Therefore, all non-planar breaks recorded before December 2002 were not included in the stability analysis.

As in the previous chapter, two data sets were constructed in order to compare stable and unstable fracture character data from skier-tested slopes. The first data set contained fracture character data from all compression test results performed on skier-tested slopes. Fractures in compression tests that were on the failure plane of an adjacent triggered slab avalanche are referred to as "unstable" (190 classified fractures). All other fractures in compression tests performed on skier-tested slopes are labelled "stable" (790 classified fractures). This enabled an objective comparison of stable and unstable data, without targeting specific weak layers. However, the data set was unbalanced, with the majority of fractures being "stable" fractures. The second data set only contained data from stable and unstable primary weaknesses, which was the snowpack layer considered most susceptible to skier-triggering (Section 3.7).

Deep tap tests (DTT) and fracture propagation tests (FPT) were regularly performed on persistent weak layers on the study slopes at Mt. St. Anne and Mt.

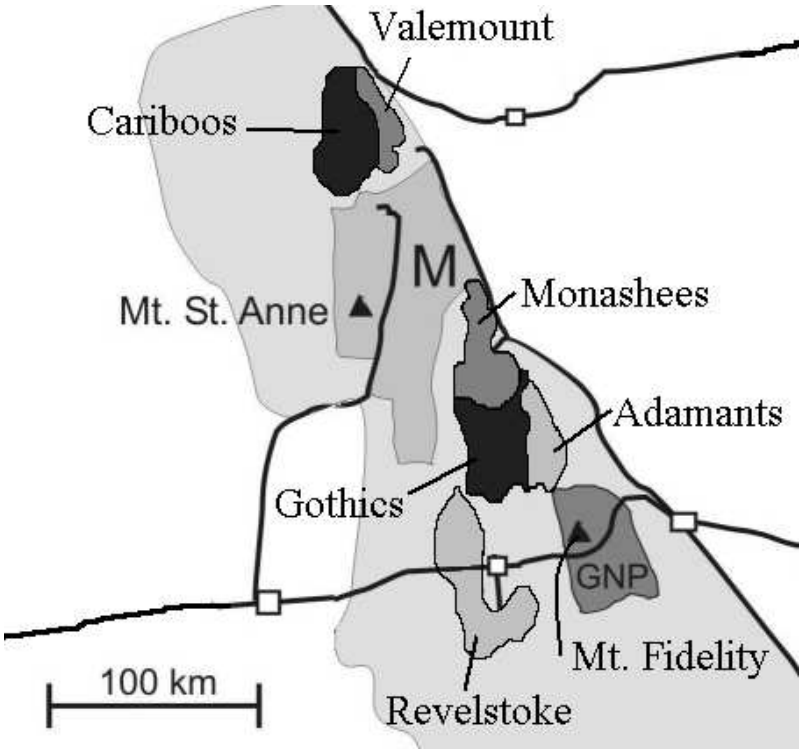

Figure 5.1: *Map showing the area used by Mike Wiegele Helicopter Skiing (M) where the Blue River field station is located and Glacier National Park (GNP) where the Rogers Pass field station is located. Regular study site observations at Mt. Fidelity were correlated with avalanche activity in the CMH Revelstoke, CMH Adamants and CMH Gothics areas. Regular study site observations performed at Mt. St. Anne were correlated with avalanche activity in at CMH Valemount, CMH Cariboos and Mike Wiegele heli-skiing areas.*

Fidelity. Fracture character observations were also recorded for these tests. Usually, three deep tap tests and three fracture propagation tests were performed next to each other on each weak layer of interest. In total, 237 deep tap tests and 178 fracture propagation tests were performed.

In order to determine whether the score of these tests (i.e. number of taps or drop hammer energy (DHE)) related to the propagation propensity of persistent weak layers, avalanche activity in the surrounding areas was compared to the test

score (Figure 5.1). Information about avalanche activity in the vicinity was obtained from guides or park service employees as well as from several heli-ski operators (Mike Wiegele Heli-skiing and Canadian Mountain Holidays (CMH)). Regular study site observations performed at Mt. Fidelity in Glacier National Park were correlated with avalanche activity in the park as well as with avalanche activity in the CMH Revelstoke, CMH Adamants and CMH Gothics areas. Regular study site observations performed at Mt. St. Anne were correlated with avalanche activity in the CMH Valemount, CMH Cariboos and Mike Wiegele heli-skiing areas.

5.3 Results

5.3.1 Snowpack properties associated with fracture character

Figure 5.2 shows the frequency of each type of fracture since the new characterization scheme was introduced in the winter of 2002-2003. In the Columbia Mountains, fractures in compression tests were most often classified as SP fractures (39%), followed by RP (22%), SC (16%), PC (13%) and finally B (9%); only one percent of observed fractures were not classified (Figure 5.2 (a)).

For rutschblock tests on the other hand, the majority (83%) of fractures were classified as Sudden Planar (Figure 5.2 (b)). Furthermore, only one fracture in a rutschblock test was classified as PC and one as B. This is likely because University of Calgary field researchers usually observe fractures in rutschblock tests on the front wall. Progressive fractures, such as PC and RP fractures, are therefore difficult to observe. If observations were made on the side wall, there would probably be more PC and RP fractures.

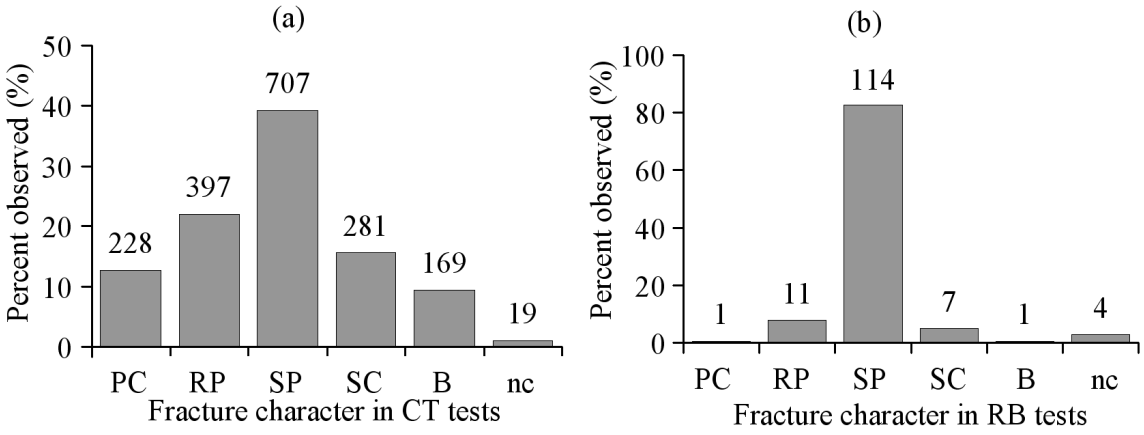

Figure 5.2: *Frequency of observation of each fracture character in compression tests (a) and rutschblock tests (b). The percentage of fractures that were not classified (nc) is also shown.*

An overview of descriptive statistics of various snowpack properties by fracture character, for the weak layer as well as the adjacent layers, is given in Tables 5.1 and 5.2.

Table 5.1: *Descriptive statistics for snowpack properties of the weak layer (WL) and the adjacent layers (La and Lb) for PC, RP and B fractures. The number of observations (N), Median (Med), and 90% range ($R_{90\%}$)* are also shown.*

	PC			RP			B		
Variable	N	Med	$R_{90\%}$	N	Med	$R_{90\%}$	N	Med	$R_{90\%}$
D_{WL} (cm)	1748	15	5 - 40	397	27	7 - 61	382	49	16 - 122
E_{WL} (mm)	659	1.5	0.8 - 6.0	257	1.0	0.5 - 2.5	185	1.3	0.5 - 7.0
h_{WL}	715	F	F- to 1F	255	4F-	F- to 1F	187	4F+	F to P-
ρ_{WL} ($kg\,m^{-3}$)	419	97	54 - 192	193	118	75 - 208	92	176	90 - 280
Th_{WL} (cm)	724	8.0	0.2 - 23.0	257	11.0	0.5 - 36.5	193	8.0	0.2 - 41.0
CT score	1748	7	1 - 20	397	12	1 - 26	382	21	6 - 29
E_{La} (mm)	400	1.5	0.8 - 3.0	165	1.3	0.5 - 2.5	154	1.0	0.5 - 2.5
h_{La}	524	F	F- to P	206	4F-	F- to K-	181	P	F to P+
ρ_{La} ($kg\,m^{-3}$)	284	99	54 - 226	120	116	50 - 244	128	170	78 - 295
Th_{La} (cm)	528	6.0	1.0 - 16.5	209	6.0	1.0 - 21.0	182	11.0	1.0 - 27.0
E_{Lb} (mm)	621	1.0	0.5 - 2.0	217	1.0	0.4 - 5.5	141	1.0	0.4 - 2.5
h_{Lb}	716	4F	F- to P-	256	4F+	F to P+	184	1F+	4F to K
ρ_{Lb} ($kg\,m^{-3}$)	464	131	61 - 242	157	143	75 - 272	127	227	117 - 344
Th_{Lb} (cm)	720	10.9	1.5 - 25.0	256	9.0	0.3 - 33.0	184	13.0	2.0 - 35.0
ΔE_{La}	399	0.0	-1.5 to 4.5	165	-0.3	-1.0 to 1.5	152	0.3	-1.0 to 6.5
ΔE_{Lb}	616	0.4	-0.7 to 5.0	217	0.3	-1.8 to 1.3	136	0.2	-0.5 to 6.0
Δh_{La}	515	0	-1 to 2	204	-0.33	-1 to 2	175	0.33	-1 to 2
Δh_{Lb}	708	0.66	-0.33 to 2	254	0.66	-0.33 to 2.33	177	1	-0.33 to 2.33

* The 90% range is defined as the middle 90% of the data. Five percent of the data are below, and five percent of the data are above $R_{90\%}$.

Table 5.2: *Descriptive statistics for snowpack properties of the weak layer (WL) and the adjacent layers (La and Lb) for SP and SC fractures. The number of observations (N), Median (Med), and 90% range ($R_{90\%}$)* are also shown.*

	SP			SC		
Variable	N	Med	$R_{90\%}$	N	Med	$R_{90\%}$
D_{WL} (cm)	707	52	18 - 121	1387	40	3 - 135
E_{WL} (mm)	515	4.5	0.5 - 14.0	857	2.5	0.8 - 17.0
h_{WL}	513	4F	F to 1F	888	4F	F- to 1F+
ρ_{WL} ($kg\,m^{-3}$)	107	170	102 - 248	396	185	59 - 291
Th_{WL} (cm)	517	1.3	0.3 - 27.0	900	5.0	0.5 - 22.0
CT score	707	18	3 - 28	1387	13	1 - 26
E_{La} (mm)	444	0.8	0.4 - 2.0	653	1.0	0.4 - 2.7
h_{La}	503	P	F to P+	840	P	F to K-
ρ_{La} ($kg\,m^{-3}$)	358	200	110 - 302	575	185	66 - 314
Th_{La} (cm)	503	10.0	1.5 - 33.0	848	6.0	1.0 - 21.0
E_{Lb} (mm)	363	0.8	0.4 - 1.5	641	1.0	0.5 - 2.0
h_{Lb}	501	1F+	4F to K-	740	1F	F to P+
ρ_{Lb} ($kg\,m^{-3}$)	308	230	160 - 320	503	219	87 - 319
Th_{Lb} (cm)	503	10.0	1.0 - 26.8	748	10.0	1.5 - 26.0
ΔE_{La}	445	4.0	-0.5 to 13.0	649	3.5	-1.0 to 18.5
ΔE_{Lb}	358	4.3	-0.5 to 14.3	630	3.3	-0.5 to 17.8
Δh_{La}	502	0.66	-1 to 2.33	833	0.33	-0.66 to 2.33
Δh_{Lb}	494	1	0 to 3	718	0.33	-0.33 to 2.33

* The 90% range is defined as the middle 90% of the data. Five percent of the data are below, and five percent of the data are above $R_{90\%}$.

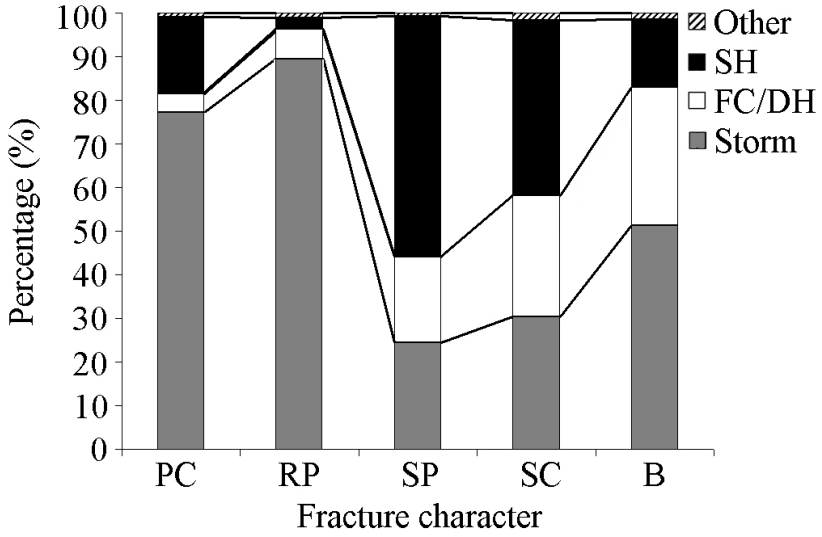

Figure 5.3: *Percentage of weak layer grain type by fracture character in compression tests. Weak layers consisting of either Precipitation Particles (PP), Decomposed Fragments (DF) or Rounded Grains (RG) were grouped in one category labelled* Storm*. Surface Hoar (SH), Faceted Crystals (FC) and Depth Hoar (DH) are each in separate groups. Wet Grains (WG), Crusts (Cr) and Ice (I) were grouped in a category named* Other*.*

Weak layer properties

Figure 5.3 shows the percentage of weak layer grain types by fracture character in compression tests. The percentage of weak layers consisting of *Storm* snow (PP, DF and RG) was greatest for PC (77%) and RP (89%) fractures. On the other hand, most sudden fractures (SP and SC) fractured in weak layers consisting of persistent snow crystals (FC, DH and SH). Finally, there were approximately as many storm snow weak layers (51%) as persistent weak layers (47%) associated with non-planar breaks.

Persistent snow crystals, especially surface hoar and depth hoar crystals, are usually larger than grains in non-persistent weak layers (Section 4.3.1). Therefore,

Table 5.3: *Comparison of weak layer thickness for SP and SC fractures for persistent weak layers consisting of buried SH and FC. The significance level (p) for the U-test is also given.*

	SP		SC		
Crystal Type	N	Med	N	Med	p
Surface Hoar	289	1.0 cm	350	1.3 cm	$< 10^{-8}$
Faceted Crystals	103	2.0 cm	181	15.0 cm	$< 10^{-8}$

the median weak layer crystal size, as well as the 90% range, were larger for SP and SC fractures than for PC, RP and B fractures (Tables 5.1 and 5.2).

The median depth for PC and RP fractures (15 and 27 cm, respectively) was lower than that for SP, SC and B fractures (52, 40 and 49 cm, respectively). Moreover, the 90% range indicates that the vast majority of weak layers associated with PC and RP fractures were shallow (Table 5.1). Since there is a strong correlation between the hand hardness of a snowpack layer and its depth (Section 4.3.2), it is not surprising that the median weak layer hand hardness for PC and RP fractures (F and 4F-, respectively) was lower than for SP, SC and B fractures (4F, 4F and 4F+, respectively). Similarly, density correlates with weak layer depth (Section 4.3.2), which explains why the median weak layer density for PC and RP fractures (97 and 118 $kg\,m^{-3}$, respectively) was also lower than for SP, SC and B fractures (168, 185 and 176 $kg\,m^{-3}$, respectively).

The median weak layer thickness was lowest for SP fractures (1.3 cm), followed by SC fractures (5 cm). Resistant planar fractures, on the other hand, had the largest median weak layer thickness (11 cm). In Table 5.3 the weak layer thickness for SP and SC fractures is compared for the two most common persistent weak layer crystals (SH and FC) associated with slab avalanches in the Columbia Mountains

Table 5.4: *Percentage of crystal type by fracture character for the layers adjacent to the weak layer. Crystal type is grouped by Storm (PP, DF and RG), FC, Cr and Other (DH, SH, WG and I).*

	Crystal Type La				Crystal Type Lb			
Fracture character	Storm %	FC %	CR %	Other %	Storm %	FC %	CR %	Other %
PC	85.2	2.2	9.8	2.6	87.4	6.2	4.3	2.0
RP	72.9	1.9	20.5	4.3	71.8	6.2	15.1	6.6
SP	79.0	7.8	10.6	2.4	47.0	23.1	26.5	3.2
SC	55.5	18.3	22.7	3.4	54.3	32.2	10.1	3.4
B	64.2	20.8	10.4	4.0	56.3	19.3	19.9	2.8

of British Columbia (Hägeli and McClung, 2003). Clearly, the median weak layer thickness for these persistent weak layers was significantly larger for SC fractures than for SP fractures.

Finally, the compression test score correlates with weak layer depth as well (N = 10313, $R_s = 0.73$, $p < 10^{-8}$). This is consistent with the median number of taps being lowest for PC fractures and highest for B fractures. However, even though SC fractures were mostly associated with deeper weak layers (Median = 40 cm, $R_{90\%}$ = 3-135 cm), the median number of taps was rather low (13 taps), which was comparable to RP fractures (12 taps).

Properties of the layers adjacent to the weak layer

The majority of the layers adjacent to weak layers that failed in compression tests consisted of *Storm* snow (PP, DF and RG), regardless of fracture character (Table 5.4). Crusts comprised a smaller percentage of the layers adjacent to PC fractures (9.8% above and 4.3% below) than for other types of fractures. Faceted crystals were also commonly observed in layers adjacent to weak layers associated with SP, SC, and B fractures. Consequently, the median crystal size for the adjacent layers was

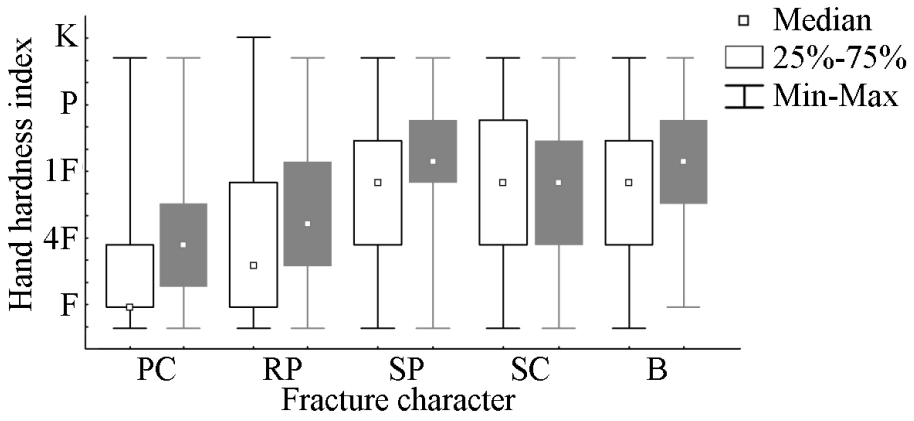

Figure 5.4: *Hand hardness index by fracture character for the layer above (black and white) and layer below (grey) the weak layer by fracture character.*

relatively small and comparable for all fracture types (Tables 5.1 and 5.2).

The hand hardness by fracture character for the layers adjacent to the weak layer is shown in Figure 5.4. Except for RP fractures, the layer above the weak layer was generally softer (i.e. lower hand hardness) than the layer below the weak layer (Tables 5.1 and 5.2). The median hand hardness for the layers adjacent to the weak layer increased from PC to RP to SP, SC and B. A similar trend was also present for the density of the adjacent layers (Tables 5.1 and 5.2).

The crystal size of the adjacent layers was similar for each fracture type (Tables 5.1 and 5.2). However, E_{La} was often larger for PC and RP fractures than for SP, SC and B fractures. Similarly, there was little difference in the thickness of the layers adjacent to the weak layer by fracture character (Tables 5.1 and 5.2).

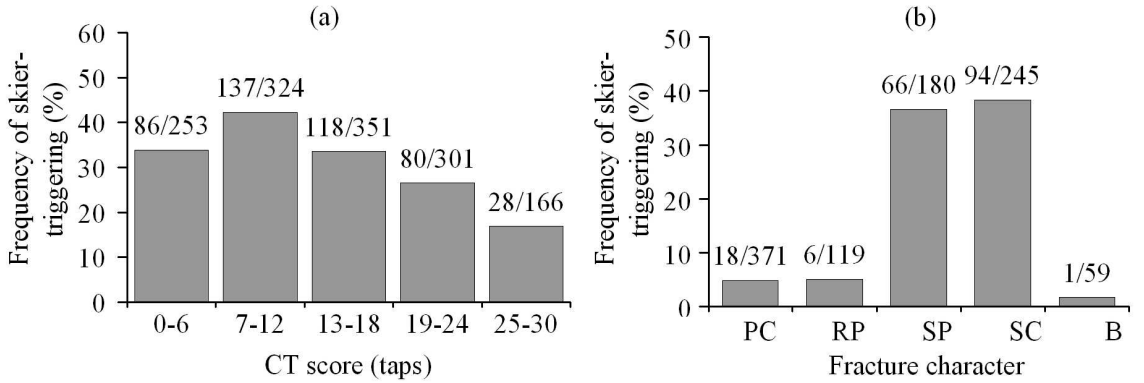

Figure 5.5: *Frequency of skier-triggering by (a): compression test score and (b): fracture character. The compression test score is grouped in five bins: 0-6 taps, 7-12 taps, 13-18 taps, 19-24 and 25-30 taps.*

Differences in snowpack properties between the adjacent layers and the weak layer

The median difference in crystal size between the weak layer and the adjacent layers was smaller for PC, RP and B fractures than for SP and SC fractures (Tables 5.1 and 5.2). Moreover, the median of ΔE_{Lb} was equal or larger than the median of ΔE_{La}, for all fracture characters, which means that typically, the crystal size difference is largest between the weak layer and the layer below.

Likewise, the median difference in hand hardness between the weak layer and the adjacent layers was smaller for PC and RP fractures than for SP, SC as well as B fractures. Furthermore, the median difference in the hand hardness index Δh_{La} was smaller than Δh_{Lb} (Table 5.1 and 5.2).

5.3.2 Comparison of stable and unstable fractures

The frequency of skier-triggering for all observed fractures on skier-tested slopes by compression test score, as well as by fracture character, is shown in Figure 5.5. The

frequency of skier-triggering increased from 33% for compression test scores ranging from zero to six taps to 42% for compression test scores ranging from seven to twelve taps. Thereafter, the frequency of skier-triggering decreased to 17% for compression test scores ranging from 25 to 30 taps (Fig. 5.5(a)). Clearly, layers that fracture with a high compression test score are less likely to be the failure plane of a slab avalanche ($N = 2276$, U-test $p = 10^{-4}$).

There was also a difference between the fracture character of stable and unstable fractures. As can be seen in Figure 5.5(b), sudden fractures (SP and SC) were more often the failure layer of a skier-triggered slab avalanche than PC, RP or B fractures. In order to compare the fracture character associated with stable and unstable weak layers, fractures were classified as either sudden (SP and SC) or not sudden (PC, RP and B). Using the Mann-Whitney U-test it was found that the fracture character of unstable fractures was significantly different from that of stable fractures ($N = 1318$, U-test $p = 10^{-9}$). Unstable weak layers were typically associated with sudden fractures.

Figure 5.6 shows the frequency of skier-triggering by fracture character grouped by compression test scores in the easy, moderate and hard ranges. The majority of the weak layers that were the failure plane of slab avalanches produced sudden fractures in compression tests, regardless of the compression test score. However, the frequency of skier-triggering for SP and SC fractures decreased from 56% and 48% respectively in the easy range, to 27% and 19% respectively in the hard range. On the other hand, PC, RP and B fractures were rarely the failure plane of slab avalanches. Moreover, none of the compression test results in the hard range that produced PC, RP or B fractures were the failure layer for slab avalanches.

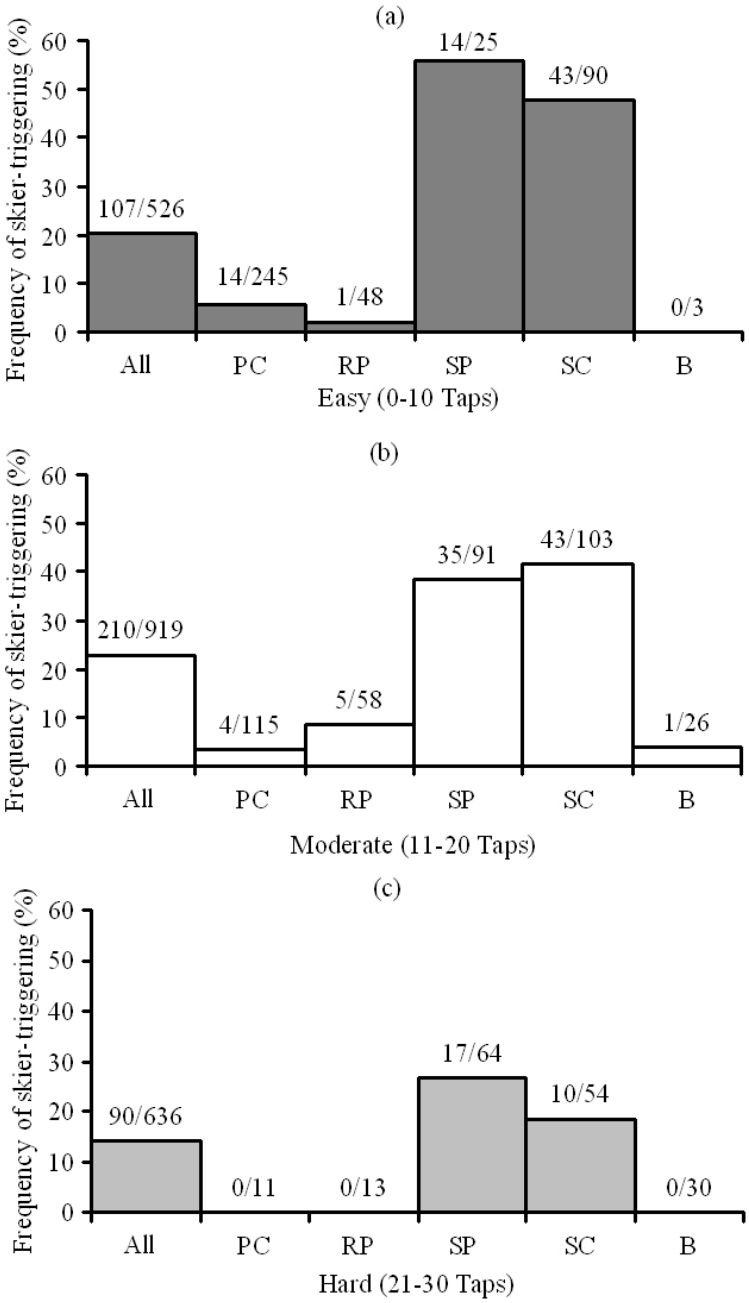

Figure 5.6: *Frequency of skier-triggering by fracture character for compression test results in the easy (0-10 taps), moderate (11-20 taps) and hard (21-30 taps) range. The first column (All) for each range shows the frequency of skier triggering for all fractures, including unclassified fractures and fractures that were classified using the old classification system.*

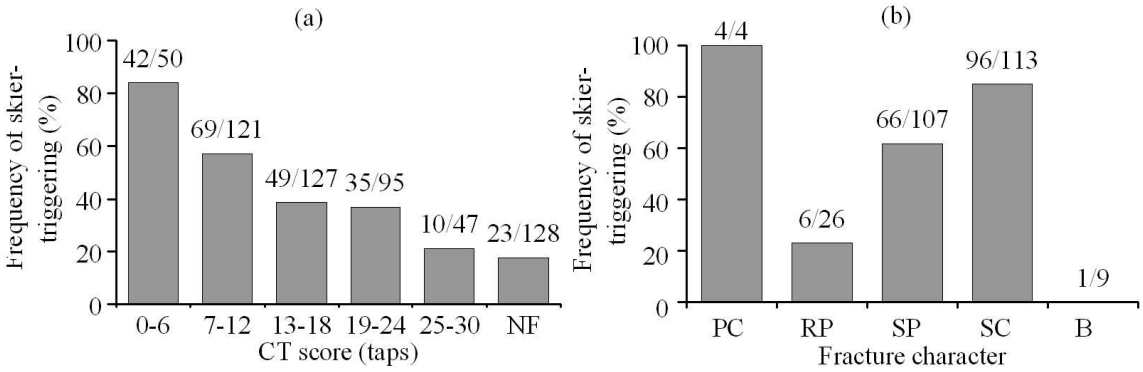

Figure 5.7: *Frequency of skier-triggering for the primary weakness in compression tests. (a) Frequency of skier-triggering by compression test score. The frequency of skier-triggering for primary weaknesses that did not produce a fracture (NF) is also shown. (b) Frequency of skier-triggering by fracture character. The compression test score is grouped in five categories: 0-6 taps, 7-12 taps, 13-18 taps, 19-24 and 25-30 taps.*

5.3.3 Comparison of stable and unstable primary weaknesses

The frequency of skier-triggering for primary weaknesses by compression test score, as well as by fracture character, is shown in Figure 5.7. The frequency of skier-triggering decreased from 64% for compression test scores ranging from zero to six taps to 21% for compression test scores ranging from 25 to 30 taps (Fig. 5.7(a)). Unstable primary weaknesses had a significantly lower compression test score that stable primary weaknesses ($N = 440$, U-test $p = 10^{-12}$). Furthermore, as can been seen in Figure 5.7 (a), the frequency of skier-triggering for primary weaknesses that did not produce a fracture in the compression tests (NF) was 18%.

As can be seen in Figure 5.7 (b), the frequency of skier-triggering was highest for PC fractures (100%). However, only four PC fractures were recorded on primary weaknesses in compression tests. These were recorded on two separate skier-tested slopes on which small (Size 0.5) slab avalanches were initiated. Furthermore, sudden

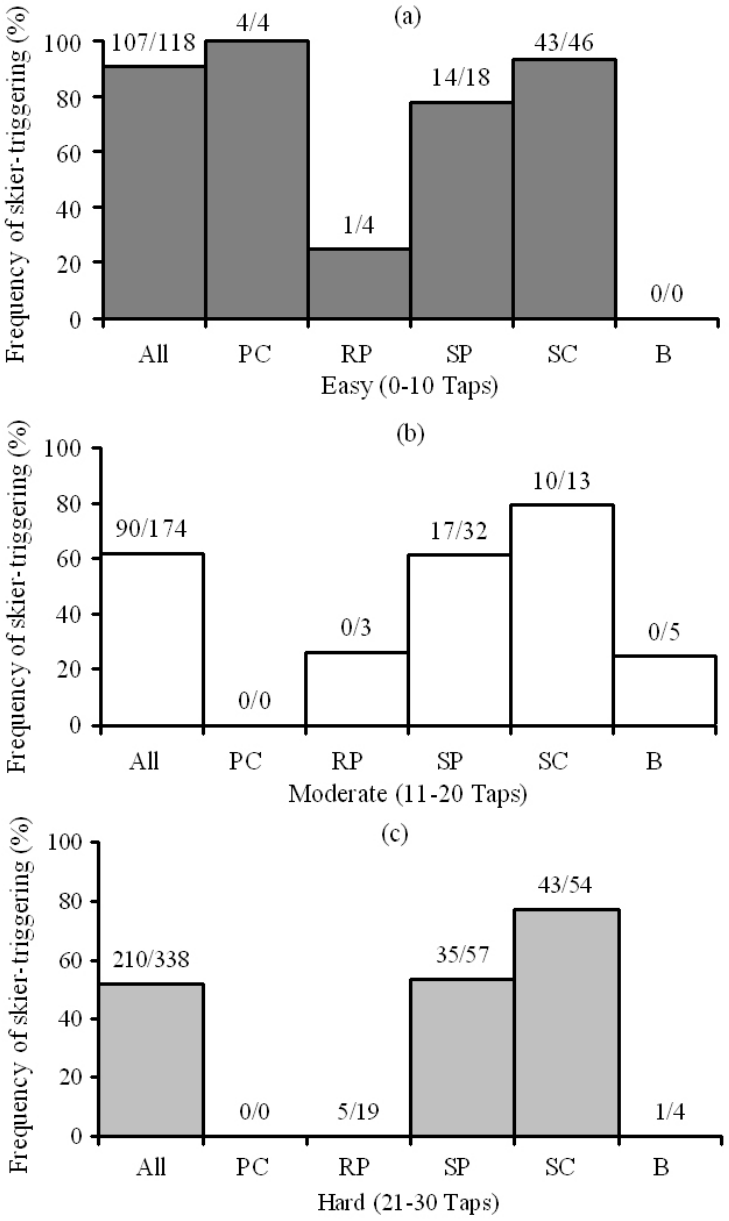

Figure 5.8: *Frequency of skier-triggering for the primary weakness by fracture character for compression test results in the easy (1-10 taps), moderate (11-20 taps) and hard (21-30 taps) range. The first column (All) for each range shows the frequency of skier-triggering for all fractures, including unclassified fractures and fractures that were classified using the old classification system.*

fractures (SP and SC) were more often the failure plane of slab avalanches than RP or B fractures. Furthermore, it was found that there was a significant difference in fracture character between stable and unstable primary weaknesses ($N = 269$, U-test $p = 0.001$), in that unstable primary weaknesses were primarily associated with sudden fractures.

Figure 5.8 shows the frequency of skier-triggering by fracture character grouped by compression test scores in the easy, moderate and hard range. As can be seen, in the easy range, the frequency of skier-triggering was highest for PC (100%) and SC (93%) fractures, followed by SP fractures (78%). The frequency of skier-triggering for RP fractures was much lower (25%) and no B fractures were recorded. In the moderate range however, the frequency of skier-triggering of PC was lower (36%), whereas the frequency of skier-triggering for SP and SC fractures was still much higher (61% and 80%, respectively). Finally, in the hard range, only sudden fractures (SP and SC) were associated with unstable primary weaknesses, and these were skier-triggered 61% and 80%, respectively.

5.3.4 Fracture character associated with remotely triggered avalanches and whumpfs

As mentioned earlier, whumpfs and remotely triggered slab avalanches are of particular interest because these represent snowpack conditions that favour widespread fracture propagation. In Figure 5.9, the percentage of each fracture type is shown for primary weaknesses associated with whumpfs and remotely triggered slab avalanches. The majority of fractures in compression tests associated with whumpfs were classified as SC fractures, whereas remotely triggered slab avalanches were most often

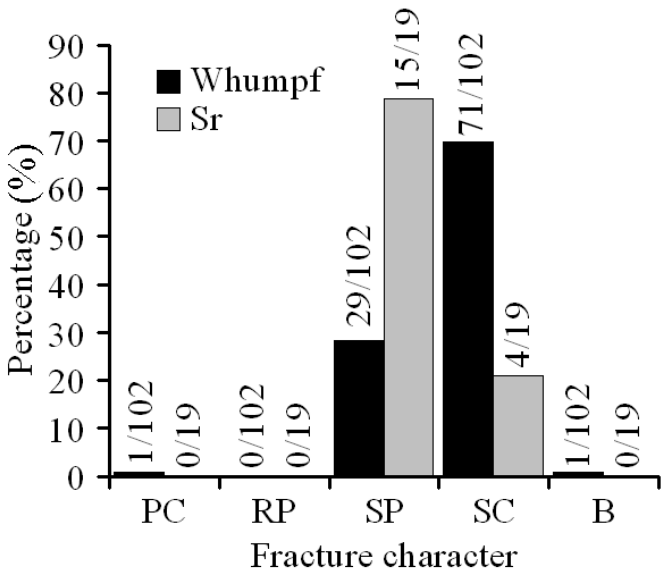

Figure 5.9: *Fracture character in compression tests for whumpfs and remotely triggered slab avalanches.*

associated with SP fractures. Furthermore, no PC, RP or B fractures were associated with remotely triggered slab avalanches and only one PC and one B fracture with a whumpf.

5.3.5 Rutschblock test

There were not as many fracture character observations from the rutschblock test (63 classified fractures) as from the compression test. As can be seen in Figure 5.2 (b), the majority of fractures in rutschblock tests was classified as SP, which was partly due to an observation bias, as mentioned earlier. Observations on the rutschblock release type, described as whole block (W), most of the block (M) or only an edge of the block (Ed), were only recorded since the winter of 2003-2004. However, many rutschblock data were available without fracture character, or utilizing the old

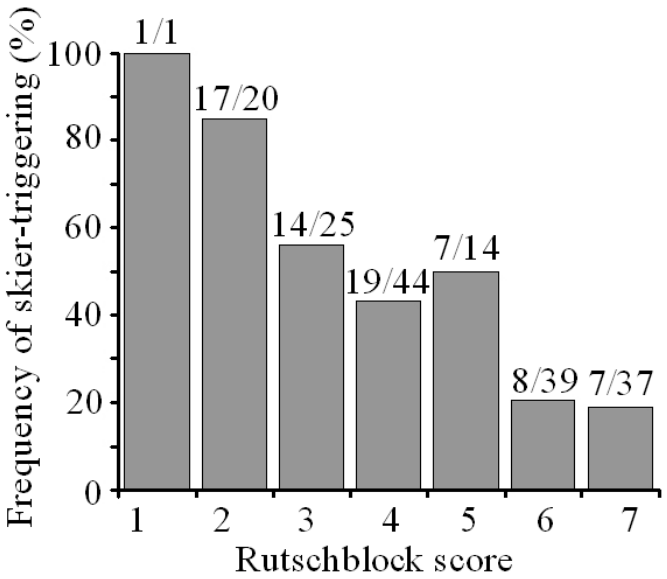

Figure 5.10: *Frequency of skier-triggering for the primary weakness by rutschblock score.*

fracture classification scheme. Consequently, there were significantly more data on rutschblock score than on fracture character or release type for rutschblock tests performed on skier-tested slopes.

The frequency of skier-triggering by rutschblock score is shown in Figure 5.10. The only observed rutschblock with a score of 1 was on a slope where a slab was skier-triggered. Nonetheless, the frequency of skier-triggering decreased with increasing rutschblock score, from 100% for RB1 to 19% for RB7, which is assigned to a rutschblock that did not produce a fracture (see Table 3.3). Furthermore, there was a significant difference between the rutschblock score of stable and unstable fractures ($N = 143$, U-test $p = 8\ 10^{-6}$). The frequency of skier-triggering by fracture character and release type in rutschblock tests is shown in Figure 5.11. Clearly, the frequency of skier-triggering was highest for SP and SC fractures. No primary weak-

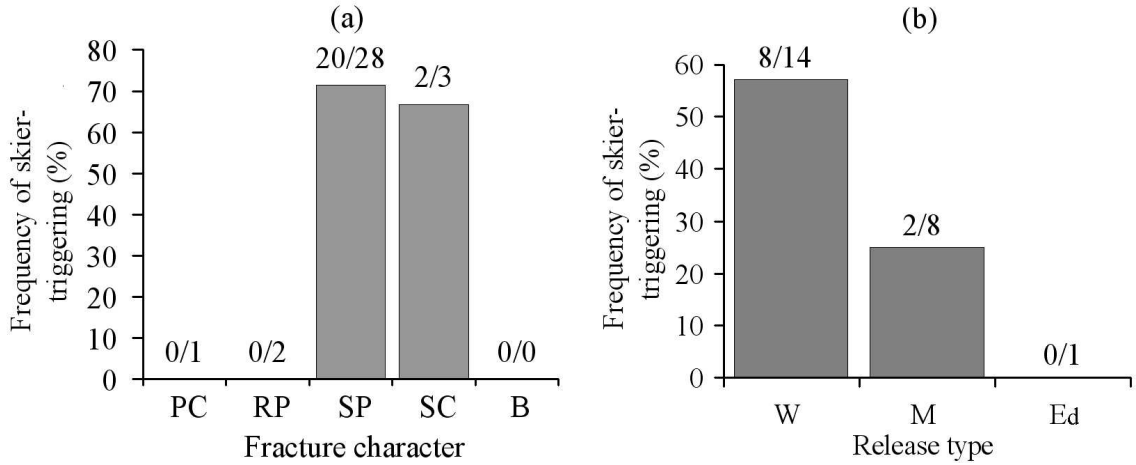

Figure 5.11: *(a) Fracture character in rutschblock tests on skier-tested slopes. (b) Release type in rutschblock tests on skier-tested slopes.*

nesses that produced PC or RP fractures in rutschblock tests were associated with skier-triggered slabs, and despite the limited data, there was a significant difference between the fracture character of stable and unstable fractures ($N = 34$, U-test $p = 0.016$). Finally, the majority of skier-triggered primary weaknesses resulted in the release of the whole block (Figure 5.11 (b)), yet there was no significant difference in release type between unstable and stable fractures ($N = 24$, U-test $p = 0.155$). However, as mentioned earlier, very few data were available on fracture character and release type in rutschblock tests.

5.3.6 Deep tap test and fracture propagation test

The fracture propagation test was modelled after a modified compression test that a ski guide was using in the mid 1990s to test deep weak layers (Jamieson, 2003). Once finished with the compression test, the ski guide levelled the test column above a deep weak layer that had not fractured, and loaded it like a compression test (taps).

For the deep tap test and the fracture propagation test, the weak layer was notched, the amount of damping snow was fixed.

The fracture propagation test and rutschblock test have been used extensively by Campbell (2004) to study the spatial variability of fracture properties (drop hammer energy, fracture character and rutschblock release type) across slopes that were representative of avalanche start zones. Sixteen of the 23 propagation test arrays had a single fracture character of either SP (15 arrays) or SC (1 array). Twenty-two of the 29 rutschblock arrays had consistent SP fracture character. Furthermore, the DHE was found to be less variable than the score in similar arrays of stability tests (e.g. Stewart, 2002). These results support the hypotheses of Johnson and Birkeland (2002) that shear quality (related to fracture character) is related to fracture propagation and should be less variable within slopes than stability test results. The most significant factors correlating with DHE were found to be weak layer depth and weak layer thickness, where areas with deeper weak layers and thinner surface hoar weak layers tended to have higher DHE.

In order to assess the effect of the notch, Campbell (2004) performed standard propagation tests beside 25 x 30 cm test columns without notches. The median DHE for the standard propagation test was significantly lower which indicates that the notch has a significant effect. The thickness of the notch (which may affect the notch radius and hence the stress concentration at the crack tip) was tested with side-by-side tests notched with either a crystal screen ($\approx$ 1 mm radius) or a snow saw ($\approx$ 3 mm radius). The difference was significant with more energy being required to propagate fractures initiated from thicker notches. For this study, a snow saw was used to notch the propagation tests since it was easier to cut a notch of consistent

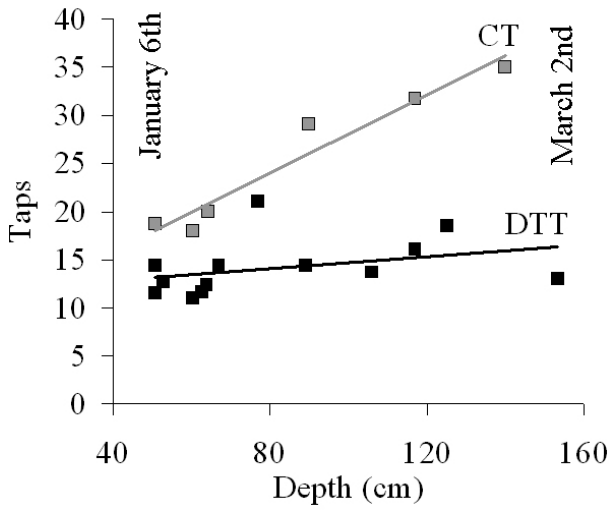

Figure 5.12: *Average compression test score (grey) and deep tap test score (black) as function of depth for a buried surface hoar weak layer (031225 SH) observed from January 6th to March 2nd 2003 at Mt. Fidelity.*

depth (5 cm) because the blade of a typical snow saw is approximately 5 cm wide. These trials showed that the propagation test has some characteristics expected for a test of propagation propensity. Campbell (2004) concluded that more development of the fracture propagation test is required and recommended that correlations with avalanche activity be attempted.

In this section, results from deep tap tests (DTT) and fracture propagation tests (FPT) are presented. This included the comparison of the DTT and the FPT results with compression test results. Furthermore, the number of taps and the drop hammer energy for persistent weak layers, measured at regular study sites, were compared to avalanche activity in the surrounding area.

Comparison of deep tap test and fracture propagation test results with compression test results

In order to compare the average deep tap test score with the average compression test score for adjacent tests, the Wilcoxon matched-pairs signed-ranks test (Walpole and others, 2002: 605) was used. The number of taps for the deep tap tests was significantly lower than for adjacent compression tests ($N = 57$, $p < 10^{-8}$). As can be seen in Figure 5.12 for a buried surface hoar weak layer at Mt. Fidelity (021225 SH layer), there was no significant increase in deep tap test score with depth ($N = 13$, $R_s = 0.55$, $p = 0.054$), whereas the compression test score increased more significantly with depth ($N = 6$, $R_s = 0.94$, $p = 0.005$). Furthermore, there was only a weak correlation between the average compression test score and the average deep tap test score for all tests ($N = 57$, $R_s = 0.29$, $p = 0.030$). Similarly, the drop hammer energy of persistent weak layers increased much less with depth than the compression test score. Furthermore, the drop hammer energy did not correlate strongly with compression test score of adjacent tests ($N = 38$, $R_s = 0.12$, $p = 0.47$). Finally, there was a significant correlation between the deep tap test score and the drop hammer energy ($N = 62$, $R_s = 0.50$, $p = 10^{-5}$), as can be seen in Figure 5.13. Since the deep tap test and the fracture propagation test are essentially similar tests, this was expected.

In Table 5.5, snowpack properties are correlated with compression test score, drop hammer energy and deep tap test score. Scores from compression tests had the strongest correlation with weak layer depth ($R_s = 0.69$), indicating that the number of taps required to fracture deep weak layers is higher than for shallow weak layers. Since depth has a strong influence on the hand hardness, shear strength and density

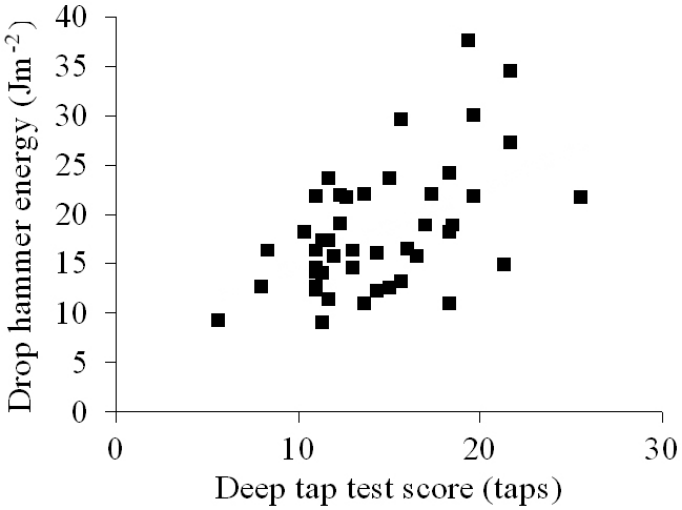

Figure 5.13: *Average drop hammer energy by average deep tap test score.*

of snowpack layers (Section 4.3.2), it comes as no surprise that these snowpack properties (i.e. Σ, h_{WL}, ρ_{WL}, h_{La}, ρ_{La}, h_{Lb} and ρ_{Lb}) had significant positive correlations with compression test score. Furthermore, deeper weak layers are generally older, hence the significant positive correlation with CT score. On the other hand, three snowpack variables had significant negative correlations with compression test score: E_{Lb}, Th_{WL} and E_{La}. This indicates that larger crystals in the adjacent layers (which often means a shallower weak layer) and thicker weak layers require a lower number of taps to fracture in compression tests.

The DTT and FPT results also exhibited significant positive correlations with the depth of the weak layer (Table 5.5). However, for both the DTT and the FPT, other snowpack variables had stronger correlations with these test results. For the deep tap test, the strongest positive correlation was with weak layer hardness ($R_s = 0.5$, $p = 10^{-16}$). For the fracture propagation test, the strongest positive correlation was with weak layer thickness, contrary to results reported by Campbell (2004) who

Table 5.5: Correlations between snowpack variables and compression test score (CT score), deep tap test score (DTT score) and drop hammer energy (DHE). Spearman Rank order correlations were used to determine associations between snowpack variables measured on an ordinal scale (i.e. CT score, DTT score, hand hardness and differences in hand hardness). Other variables were correlated using the Pearson product-moment linear correlation, and these variables are marked with an asterisk.

	CT score				DTT score				DHE		
variable	N	R	p	variable	N	R	p	variable	N	R	p
D_{WL}	5791	0.69	$< 10^{-16}$	h_{WL}	235	0.5	10^{-16}	$^{*}Th_{WL}$	175	0.54	10^{-14}
Σ	1950	0.63	$< 10^{-16}$	ρ_{La}	188	0.49	10^{-13}	h_{WL}	175	0.45	10^{-9}
h_{WL}	5561	0.58	$< 10^{-16}$	D_{WL}	235	0.43	10^{-12}	$^{*}\Sigma$	100	0.51	10^{-8}
ρ_{WL}	1915	0.57	$< 10^{-16}$	Age	228	0.36	10^{-8}	$^{*}Age$	154	0.41	10^{-7}
ρ_{Lb}	3446	0.56	$< 10^{-16}$	ρ_{WL}	12	0.9	$5\ 10^{-5}$	$^{*}Th_{Lb}$	172	0.27	10^{-5}
h_{Lb}	5480	0.55	$< 10^{-16}$	ρ_{Lb}	191	0.26	$3\ 10^{-4}$	$^{*}Th_{La}$	172	0.23	10^{-5}
ρ_{La}	3200	0.49	$< 10^{-16}$	h_{La}	232	0.25	10^{-4}	$^{*}D_{WL}$	175	0.2	0.009
Age	2677	0.4	$< 10^{-16}$	Σ	135	0.22	0.009	$^{*}E_{La}$	160	0.19	0.018
h_{La}	5350	0.38	$< 10^{-16}$	E_{La}	221	0.17	0.013	h_{Lb}	172	0.12	0.109
Th_{La}	5389	0.16	$< 10^{-16}$	h_{Lb}	232	0.16	0.016	$^{*}\rho_{Lb}$	143	0.1	0.249
ΔE_{Lb}	4597	0.12	10^{-15}	Th_{Lb}	232	0.13	0.041	h_{La}	172	0.07	0.334
Th_{Lb}	5511	0.06	10^{-5}	E_{Lb}	198	0.13	0.063	$^{*}E_{Lb}$	148	-0.02	0.778
Δh_{Lb}	5266	0.05	10^{-4}	Th_{La}	232	0	0.993	ρ_{La}	133	-0.17	0.055
E_{WL}	5573	0.05	10^{-4}	Th_{WL}	235	-0.1	0.128	$^{*}\rho_{WL}$	24	-0.58	0.003
Δh_{La}	5127	0.02	0.147	Δh_{La}	232	-0.24	10^{-4}	Δh_{La}	172	-0.3	10^{-5}
ΔE_{La}	4486	0.02	0.241	Δh_{Lb}	232	-0.33	10^{-7}	Δh_{Lb}	172	-0.33	10^{-5}
E_{Lb}	4642	-0.09	10^{-10}	ΔE_{Lb}	198	-0.39	10^{-8}	$^{*}\Delta E_{La}$	160	-0.46	10^{-7}
Th_{WL}	5791	-0.17	$< 10^{-16}$	E_{WL}	235	-0.42	10^{-11}	$^{*}E_{WL}$	175	-0.41	10^{-8}
E_{La}	4516	-0.22	$< 10^{-16}$	ΔE_{La}	221	-0.43	10^{-11}	$^{*}\Delta E_{Lb}$	148	-0.49	10^{-10}

found a negative correlation for a larger data set of predominantly buried surface hoar layers. However, when only persistent weak layers (FC, DH and SH) were considered, the correlation was not significant ($N = 130$, $R_p = 0.25$, $p = 0.136$).

Overall, DTT and FPT results were significantly correlated with hand hardness, shear strength, age and depth of the weak layer, similar to the compression test results. Since the properties of snow change with depth (related to the age of the weak layer), this comes as no surprise. However, substantial differences were observed for snowpack variables that exhibited negative correlations. For both the deep tap test and the fracture propagation test, differences in hand hardness and crystal size, as well as weak layer crystal size, had significant negative correlations with DTT and FPT results. As mentioned in Section 4.5, differences in hand hardness are probably related to the interface fracture energy. Large differences in crystal size indicate poor bonding and the crystal size difference typically increased with increasing weak layer crystal size (Section 4.3.2). These negative correlations therefore suggest that the deep tap test and the fracture propagation test results relate more to propagation propensity than compression test results.

The majority of fractures in deep tap tests and fracture propagation tests were sudden fractures (SP and SC). Only very few RP fractures (4 and 1 for the DTT and the FPT, respectively) and no PC fractures were observed in these tests. Furthermore, nine fractures in the deep tap test and 16 fractures in the fracture propagation test were classified as a non-planar break.

The mean number of taps, as well as the mean drop hammer energy associated with each fracture character are shown in Table 5.6. The mean drop hammer energy for non-planar break fractures was significantly higher than for SP and SC fractures

Table 5.6: *Mean number of taps and drop hammer energy by fracture character. The number of observations (N) as well as the minimum (Min) and maximum (Max) number of taps or drop hammer energy for each fracture character are also shown.*

	Number of taps				Drop hammer energy (Jm^{-2})			
Fracture Character	N	Mean	Min	Max	N	Mean	Min	Max
RP	4	18	11	28	1	14.1		
SP	157	13.9	1	29	81	20.7	4.2	49
SC	63	13.2	2	23	56	19.1	5.4	54.4
B	9	16.2	12	21	16	48.3	25.7	81.5

($N = 153$, U-test $p = < 10^{-8}$). This was not the case for the mean number of taps in the deep tap test ($N = 220$, U-test $p = 0.105$). On the other hand, there was no significant difference in the mean number of taps ($N = 220$, U-test $p = 0.088$) and the mean drop hammer energy ($N = 137$, U-test $p = 0.514$) for SP and SC fractures.

Test score and regional avalanche activity

In Figure 5.14 the number of taps and the drop hammer energy for two persistent weak layers, measured at regular study sites, are related to avalanche activity in the surrounding area on the same layer. As can be seen in Figure 5.14 (a), for a buried surface hoar weak layer (030215 SH), the number of reported avalanches decreased after reaching a maximum at eight days. On the other hand, the number of taps necessary to fracture the weak layer in a deep tap test did not increase over time. However, the first measurements were performed after nine days. This weak layer did not produce any fractures in compression tests after approximately 12 days. However, there were still reports of avalanche activity on this buried surface hoar weak layer up to 28 days after burial.

Similarly, the DHE associated with a weak layer composed of faceted crystals (021121 FC) observed at the Mt. St Anne study site, showed no increase as the

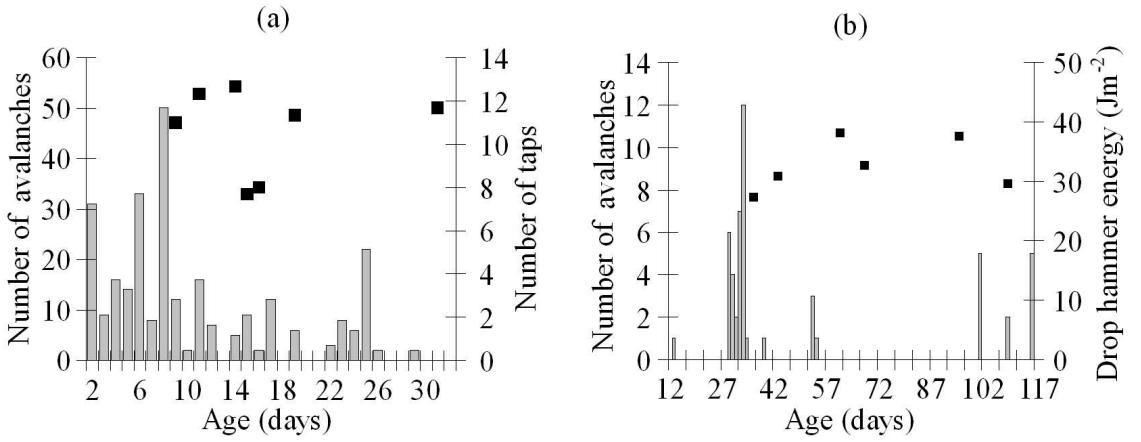

Figure 5.14: *Comparison of DTT and FPT test results with regional avalanche activity. (a) Comparison of the number of taps (black markers) in the deep taps test with avalanche activity (bars) on a buried SH weak layer (030215 SH). The age of the weak layer is the time since burial. (b) Comparison of the drop hammer energy (black markers) in the fracture propagation test with avalanche activity (bars) on a weak layer composed of facetted crystals (021121 FC).*

winter progressed, as can be seen in Figure 5.14 (b). The avalanche activity soon after burial was not reported, as this layer was formed in November. However, there were many avalanches after approximately 30 days, after which the avalanche activity diminished (Figure 5.14 (b)). Yet there were still reports of avalanches on this specific layer up to 111 days after burial.

The drop hammer energy associated with a persistent weak layer (030119 SH) that did not produce as many avalanches in the region as the preceding two persistent weak layers is shown in Figure 5.15. Again, there was no increasing trend in the drop energy over time. The reported avalanche activity on this persistent weak layer was generally low, and most avalanches were reported within the first ten days after burial.

In these three time series, the avalanche activity generally diminished with time,

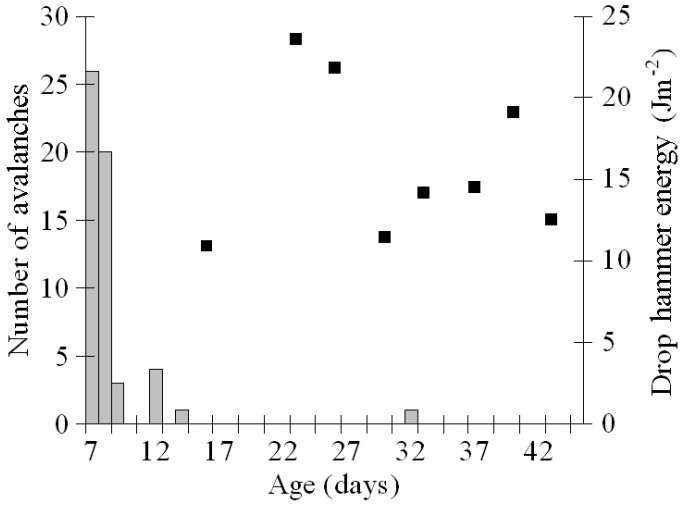

Figure 5.15: *Comparison of drop hammer energy (black marker) with avalanche activity (bars) for a buried surface hoar weak layer (030119 SH).*

whereas the number of taps in the deep tap test, or the drop hammer energy in the fracture propagation test, did not exhibit increasing trends with time.

5.4 Discussion

The comparison of stable and unstable fractures in compression test results revealed that fracture character has high predictive merit (Section 5.3.2). Johnson and Birkeland (2002) stated that reducing the uncertainty associated with "conditionally stable" stability tests (i.e. compression test scores in the hard range) is crucial to improve the interpretation of stability test results for avalanche forecasting. Clearly, incorporating fracture character into compression test interpretations can reduce some of these uncertainties, since sudden fractures (SP and SC) are more often the failure layer of slab avalanches (Figure 5.6).

For primary weaknesses however, the predictive merit of fracture character was

limited (Section 5.3.3). However, because the primary weaknesses on skier-tested slopes that were not skier-triggered were often identified through use of stability tests, there was a strong bias towards sudden fractures in the data of stable primary weaknesses. Nevertheless, only very few PC, RP fractures and no B fractures were associated with unstable primary weaknesses. Occasionally primary weaknesses produced two or more different types of fracture in adjacent compression tests (field researchers generally performed three compression tests at each profile site). It must be pointed out that none of the weak layers that fractured *consistently* as PC or RP were the failure layer of slab avalanches. Furthermore, all unstable primary weaknesses associated with PC and RP fractures also produced at least one SP fracture in adjacent compression tests.

To understand why sudden fractures identify layers that are more susceptible to skier-triggering, the snowpack properties associated with fracture character are discussed in relation to fracture initiation and fracture propagation. Most PC and RP fractures were in the easy or moderate range and were associated with shallow, soft weak layers consisting of PP, DF or RG crystals. Although these conditions are favourable for fracture initiation (Section 4.5), the frequency of skier-triggering was low for these types of fracture. This is because the differences in hand hardness and crystal size were generally small. This indicates that there is little stress concentration at the interfaces of the weak layer, hindering fracture initiation and fracture propagation. Moreover, the layer above the weak layer was usually soft (less stiff) and therefore less conducive to fracture propagation in the weak layer (Section 4.5).

PC and RP fractures are however different from one another. PC fractures are characterized by the gradual compression of the weak layer over several loading steps

(Table 3.4). Physically, the fracture involves gradual rearrangement of the weak layer crystals due to the external loading (see Section 6.3.1). Seventeen percent of the weak layers exhibiting PC fractures consisted of SH crystals, which are generally thin weak layers (< 1 cm) consisting of one layer of crystals (Jamieson and Schweizer, 2000). The gradual compression of such thin weak layers would not be noticeable, which indicates that soft layers above and below the weak layer can be involved in the fracturing process as well. RP fractures on the other hand, are thin, mostly planar fractures at the interface between the weak layer and one of the adjacent layers. These fractures are caused by the rearrangement of the crystals at the interface (see Section 6.3.1) and require one or more loading steps to cross the column. In most cases the block of snow does not slide easily on the weak layer, indicating that not all the bonds between the weak layer and the adjacent layer are fractured or that there are minor irregularities (non-planarities) in the fracture surface. Moreover, the weak layer depth ($N = 981$, U-test $p < 10^{-6}$) as well as the hardness of the weak layer ($N = 970$, U-test $p = 10^{-5}$) and the adjacent layers (La: $N = 730$, U-test $p = 10^{-8}$; Lb: $N = 972$, U-test $p = 10^{-8}$) were significantly larger for RP fractures than for PC fractures.

Most sudden fractures (SP and SC) were associated with harder and deeper weak layers. These are less favourable snowpack conditions for fracture initiation partly because the stresses below the skier reduce rapidly with depth, and partly because harder, deeper weak layers are generally stronger. However, the median depth for these fractures was still well within the range for skier-triggering (Figure 4.9) and persistent weak layers, commonly associated with sudden fractures, are more often the failure layer of skier-triggered slab avalanches (e.g. Schweizer and

Jamieson, 2001). Additionally, the larger hand hardness difference indicates stress concentration in the weak layer and the larger relative crystal size indicates less bonding (Colbeck, 2001), facilitating fracture initiation and propagation. Finally, the layer above the weak layer was harder and therefore stiffer, which promotes fracture propagation (see Section 4.5).

There are some important differences between SP fractures and SC fractures. Persistent weak layers causing SC fractures were significantly thicker than weak layers causing SP fractures (Table 5.3). Moreover, the median number of taps was significantly lower for SC fractures than for SP fractures ($N = 2080$, U-test $p < 10^{-6}$). Finally, the failure layers of whumpfs produced more SC fractures than SP fractures in compression tests (Figure 5.9). Whumpfs are generally regarded as good indicators of high instability (e.g. McClung and Schearer, 1993) since conditions are favourable for widespread fracture propagation. This suggests that the amount of collapse during fracture may contribute to fracture propagation, probably because additional gravitational energy from the slab is available at the crack tip.

Most snowpack properties for non-planar breaks are similar to those for SP fractures (Tables 5.1 and 5.2). However, the hardness difference between the adjacent layers and the weak layer was significantly lower for B than for SP fractures (La: $N = 627$, U-test $p = 10^{-8}$; Lb: $N = 646$, U-test $p = 10^{-5}$). Moreover, the difference in crystal size between the weak layer and the adjacent layers was significantly smaller for B fractures than for SP fractures (La: $N = 597$, U-test $p < 10^{-8}$; Lb: $N = 494$, U-test $p < 10^{-8}$). The fact that B fractures rarely occurred in the failure layer of nearby slab avalanches indicates that a large hardness difference and relative crystal size favour slab avalanche release.

None of the slab avalanches associated with PC and RP fractures were remotely triggered avalanches and only one PC fracture was associated with a whumpf. Moreover, nearly all classified fractures on the failure layer of eight slab avalanches larger than size 1.5 were sudden fractures (96%). Finally, only one B fracture was associated with a whumpf. This further indicates that the snowpack properties for PC, RP and B fractures are typically not favourable for widespread fracture propagation.

5.4.1 Evolution of fracture character for weak snowpack layers

The median depth of weak layers by fracture character (Tables 5.1 and 5.2), as well as the median hardness, density and compression test score, suggests that the fracture character of some weak layers may evolve as they age and are buried more deeply.

In general, the hardness of snowpack layers increases with depth (see Figure 4.4 (b)). However, weak layers gain strength and hardness slower than the surrounding layers. For shallow depths, the hardness difference between the weak layer and the soft adjacent layers will usually be very low (PC and RP fractures). As weak layers get buried deeper in the snowpack, the hand hardness difference between the weak layers and their adjacent layers increases (SP and SC fractures). Over time, the hardness of weak layers slowly increases, decreasing the hand hardness difference (B fractures). Persistent weak layers gain strength much slower than non-persistent weak layers (storm snow), suggesting that the transition in fracture character would be much faster for storm snow weak layers than for persistent weak layers.

University of Calgary field researchers have observed that soon after burial (e.g. the first day), many persistent weak layers do not produce compression test results. However, when the slab over the weak layer thickens and becomes more cohesive,

persistent weak layers generally produce SP fractures, or SC fractures if the weak layer is relatively thick. Finally, once a weak layer is buried deep enough in the snowpack, it stops producing stability test results because insufficient stress from dynamic surface loading reaches the weak layer.

Observations on the evolution of fracture character for storm snow weak layers are very limited. Nevertheless, field researchers have observed that initially most storm snow layers produce PC fractures. As the overlying snow becomes more cohesive, many storm snow interfaces evolve to RP fractures, followed by breaks and no fractures, within days. However, during the initial stages of the evolution, some slabs can become cohesive faster (and comprised of smaller particles) than the weak layer (e.g. weak layer of large PP), thereby increasing the hand hardness differences and differences in crystal size. These weak layers would evolve into SP or SC fractures, indicating that at this stage, skier-triggered slab avalanches are more likely (Fig. 5.5).

An example of the evolution of fracture character, for a thin weak layer (approximately 1 cm) that consisted of faceted crystals on top of a crust observed on Mt. Fidelity, is shown in Figure 5.16. This weak layer was formed after a cold storm deposited dry snow on top of a moist snow layer, which subsequently froze. The hand hardness difference between the weak layer and the layer above did not change much over time. However, Δh_{Lb} decreased from 3 on the first day to 1.3 after 16 days (Fig. 5.16(b)). While descending from the study slope on the third day, researchers from the University of Calgary triggered several small avalanches (Size 0.5) on this weak layer. As can be seen in Figure 5.16(a), the fracture character recorded on that day was mostly SP. However, on the first day, the recorded fracture character was

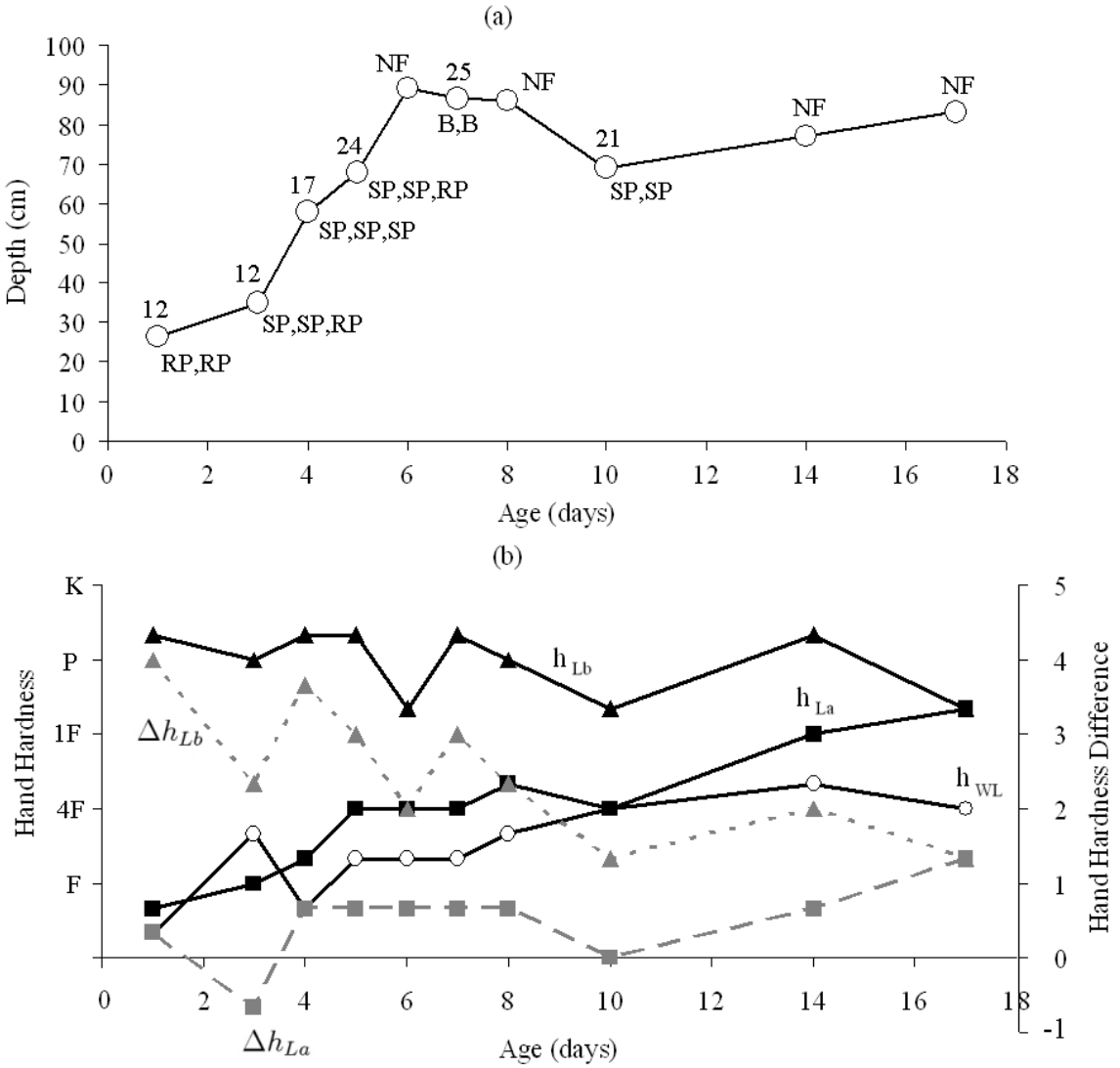

Figure 5.16: *Evolution of snowpack parameters by age, for a weak layer consisting of faceted crystals buried on 040312 observed on Mt. Fidelity. (a): Depth of the weak layer as well as the average compression test score (above, NF = no fracture) and recorded fracture character (below). (b): Hand hardness index of the weak layer and the adjacent layers (black) as well as the difference in hand hardness index between the adjacent layers and the weak layer (grey).*

mostly RP. Clearly, changes in snowpack conditions resulted in an evolution of the fracture character from mostly RP to mostly SP within three days, and then to B and NF (Fig. 5.16(a)). However, the weak layer did produce two SP fractures after 10 days even though two days earlier it did not produce any compression test results. This was probably because more stress from tapping on the shovel was transmitted to the weak layer in compression tests as the slab had densified with no additional precipitation.

5.4.2 Rutschblock test

The vast majority of fractures in rutschblock tests were classified as sudden fractures. Therefore, the predictive merit of fracture character in rutschblock tests was limited. However, PC and RP fractures were observed more often in compression tests than in rutschblock tests because these fractures are difficult to observe on the front (lower) wall of a rutschblock test. Similarly, despite the fact that the release type of most rutschblock tests associated with skier-triggered avalanches was classified as whole block (W), the release type of rutschblock tests was not significantly different for unstable and stable rutschblocks (Section 5.3.5). However, very few data on fracture character and release type were available for rutschblock tests performed on skier-tested slopes.

In Figure 5.17 the percentage of fracture character and release type by rutschblock score is shown for all rutschblock tests (performed on regular study slopes as well as on skier-tested slopes). As expected, most fractures in rutschblock tests were SP fractures, regardless of rutschblock score (Figure 5.17 (a)). The percentage of rutschblock tests in which most of the block was released increased with increasing

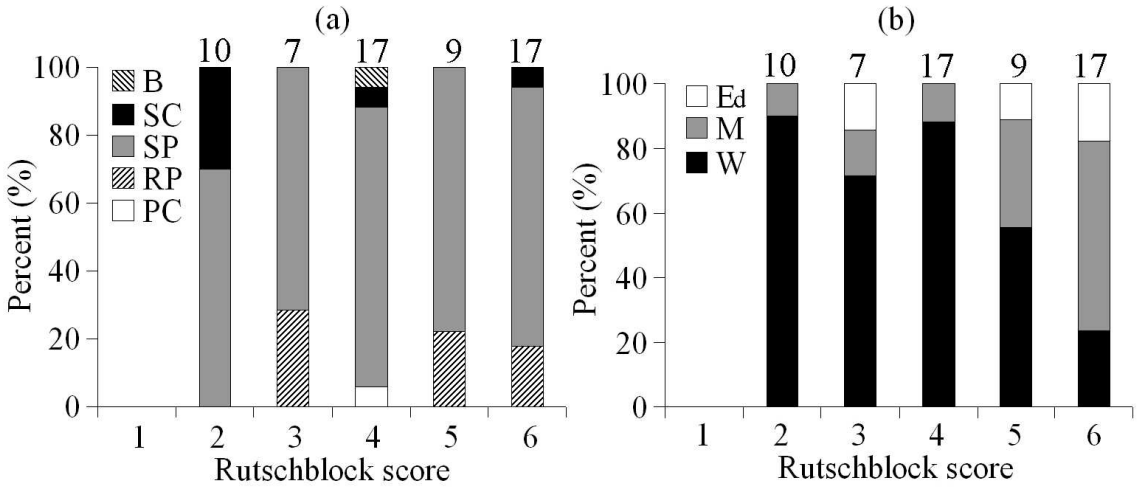

Figure 5.17: *(a) Percentage of observed fracture character by rutschblock score. (b) Percentage of observed release type by rutschblock score. The number of total observations for each loading step is shown above the bars.*

rutschblock score, whereas rutschblock tests in which the whole block released became less frequent with increasing RB score (Figure 5.17 (b)). This suggests that for rutschblock tests the release type could potentially have higher predictive merit than fracture character, since the frequency of skier-triggering also decreased with increasing rutschblock score (Figure 5.10). Furthermore, Schweizer and Jamieson (2003b) reported that typically when the whole block was released in a rutschblock test, significantly more adjacent slopes were skier-triggered. Clearly, more data will be needed to confirm these findings.

5.4.3 Deep tap test and fracture propagation test

Comparison of deep tap test and fracture propagation test results with compression test results showed that there was no significant correlation between the score in the deep tap test or fracture propagation test with that of adjacent compression tests.

This comes as no surprise since all but 15 cm of incompressible snow overlying the weak layer was removed for the DTT and FPT. Therefore, more energy is delivered at the weak layer after each loading step compared to compression tests, in which some energy is used to compact the overlying snow column.

Fractures in deep tap tests and fracture propagation tests were mostly sudden fractures. Nevertheless, some RP and B fractures were observed and the average DHE was significantly higher for B fractures than for SP and SC fractures. Campbell (2004) reported that the propagation test has some characteristics expected for a test of propagation propensity, since the notch had a significant effect on the test results. Furthermore, correlation analysis of compression test, deep tap test and fracture propagation test results with snowpack properties showed that the DTT and FPT were significantly affected by hand hardness and crystal size differences, as well as weak layer crystal size. This suggests that the deep tap test and the fracture propagation test results relate to propagation propensity. This is also consistent with the fact that sudden fractures were more often associated with slab avalanches than B fractures, which required significantly more energy in the FPT.

However, for persistent weak layers measured at regular study sites, no significant increases were observed in the number of taps or the DHE with time, suggesting that the fracture propagation propensity for persistent weak layers did not change much over time. Comparing the number of taps from DTT, or the DHE, with avalanche activity did not produce threshold values above which avalanche activity was minimal. Generally, avalanche activity on a specific weak layer decreased with time, whereas the DTT score and DHE only marginally increased with time. However, it must be noted that DTT and FPT tests could only be performed on weak layers

that were "older" (i.e. deeper in the snowpack), since the overlying snow had to be incompressible. Therefore, no DTT or FPT test could be performed when the weak layers were shallow, which is when the avalanche activity was highest. Furthermore, as weak layers age, fracture initiation becomes infrequent due to an increase in depth. However, since avalanche professionals usually recognize unstable snowpack conditions, route selection becomes more conservative when stability is low and therefore not many skier-triggered avalanches are reported.

Nonetheless, these results suggest that the propagation propensity of persistent weak layers, if indeed measured by the DTT and the FPT, does not change much over time, and therefore slab properties, such as thickness and hand hardness, play a major role in fracture initiation and propagation. This is somewhat consistent with field observations on avalanche activity on persistent weak layers. These types of weak layers are relatively common in the Columbia Mountains, and can produce avalanches for many weeks, suggesting that the propagation propensity remains high. Generally speaking, skier-triggered avalanches become less frequent as persistent weak layers get buried deeper in the snowpack. Nevertheless, even deep persistent weak layers can produce avalanches, provided the fracture is initiated by a skier in an area where the weak layer is more shallow. This also suggests that the propagation propensity remains high. In some instances, persistent weak layers have been known to release slab avalanches in the spring, after many weeks of inactivity on this layer. One such layer, described by Jamieson et al. (2001), formed in November 1996 and consisted of faceted crystals on top of a crust. Intermittent dry slab avalanches occurred until mid-March 1997. However, many wet slab avalanches were reported to have released naturally on this particular layer in May and June 1997, suggesting that the weak

layer conditions were still favourable for fracture propagation. However, some other factors may be at play as well, since spring conditions are typically characterized by strong melt-freeze cycles which can substantially change slab properties and weak layer properties.

These results are therefore inconclusive since they neither confirm nor deny the predictive merit of either the deep tap test or the fracture propagation test as field tests for propagation propensity.

5.5 Conclusions

With the proposed classification system the five most common types of fractures in stability tests were identified. The data show that fracture character is a valuable addition to the compression test score since most failure layers of slab avalanches produce sudden fractures (SP and SC) in compression tests. For the rutschblock test however, the release type might be a better descriptor, since observations on fracture character are not as precise as in the compression test score.

The analysis of fracture character in combination with snow profile data suggests that the typical snowpack characteristics for SP and SC fractures favour slab avalanche release in the data studied. Moreover, there is an indication that the larger slope normal displacement in SC fractures promotes widespread fracture propagation. On the other hand, typical snowpack properties for PC, RP and B fractures do not appear to favour fracture propagation. Furthermore, fracture character observations in DTT and FPT tests indicated that the drop hammer energy to propagate the initial fracture (notch) for sudden fractures was significantly lower than for non-

planar breaks, which is consistent with these observations. However, the usefulness of the DTT and the FPT as a field test for propagation propensity was inconclusive, since no relation was found between these test results and regional avalanche activity.

Finally, tracking the evolution of potential weak layers through fracture character appears useful. During the initial stages of the slab becoming cohesive, fracture character can provide information on the potential for avalanches to occur.

Chapter 6

High-speed photography of fractures in weak snowpack layers

6.1 Introduction

It is now widely accepted that the fractures that release slab avalanches initiate at a weak layer (or interface) underlying a cohesive slab (e.g. Schweizer et al., 2003). Theoretical models generally assume that slab avalanche release is caused by rapid propagation of a brittle shear fracture in a weak snowpack layer (e.g. McClung, 1979b, 1981, 1987; Bader and Salm, 1990). However, there are still no consistent *in situ* measurements of propagating fractures in weak snowpack layers. Such measurements are essential to verify theoretical models and improve the understanding of failure initiation and slab avalanche release.

A study on the dynamic response of the snow cover has shown that the additional stress introduced by a skier decreases with depth (Schweizer et al., 1995b). In the same study, a video sequence of a fracture caused by rapid surface loading was analyzed. This was probably the first directly photographed observation of a fracture in a weak snowpack layer. The deformation measurements showed that a fracture in weak interface was associated with both slope parallel and slope normal displacement. The slope normal displacement caused by the fracture was measured to be 0.47 cm. Unfortunately, no further tests were reported.

Johnson et al. (2004) used geophones placed on the snow surface on low angle terrain to measure the vertical displacement of the snow surface due to a propagating fracture in a weak snowpack layer. This was the first direct measurement on a fracture propagating through a weak layer. The vertical displacement was approximately 0.1 cm and the fracture speed was measured to be 20±2 m s^{-1}.

For this study, a portable high-speed camera was used to photograph *in situ* fractures in weak snowpack layers. Fractures in various field tests (compression, rutschblock and cantilever beam tests) and on skier-tested slopes were photographed at an interval of 4 *m*s in order to observe fractures propagating in weak snowpack layers directly. The aim was to obtain displacement measurements at the time of fracture and also fracture speed measurements, which is one way to verify theoretical models. Parts of the analysis presented in this chapter have been accepted for publication in a special issue of Cold Regions Science and Technology.

6.2 Methods

6.2.1 Field tests and equipment

To observe fractures in weak snowpack layers, a portable high-speed digital video camera was used during the winters of 2002-2003 and 2003-2004. This camera (MotionMeter) records at 250 frames per second, which allowed for detailed observation of fractures. The high-speed camera has a 658 x 496 pixel Charge-Coupled Device (CCD) array and a cyclic internal memory that can store up to 8.5 seconds of images at 250 frames per second. Video images were converted into digital format prior to analysis. Since the camera was used to observe *in-situ* fractures in weak snow-

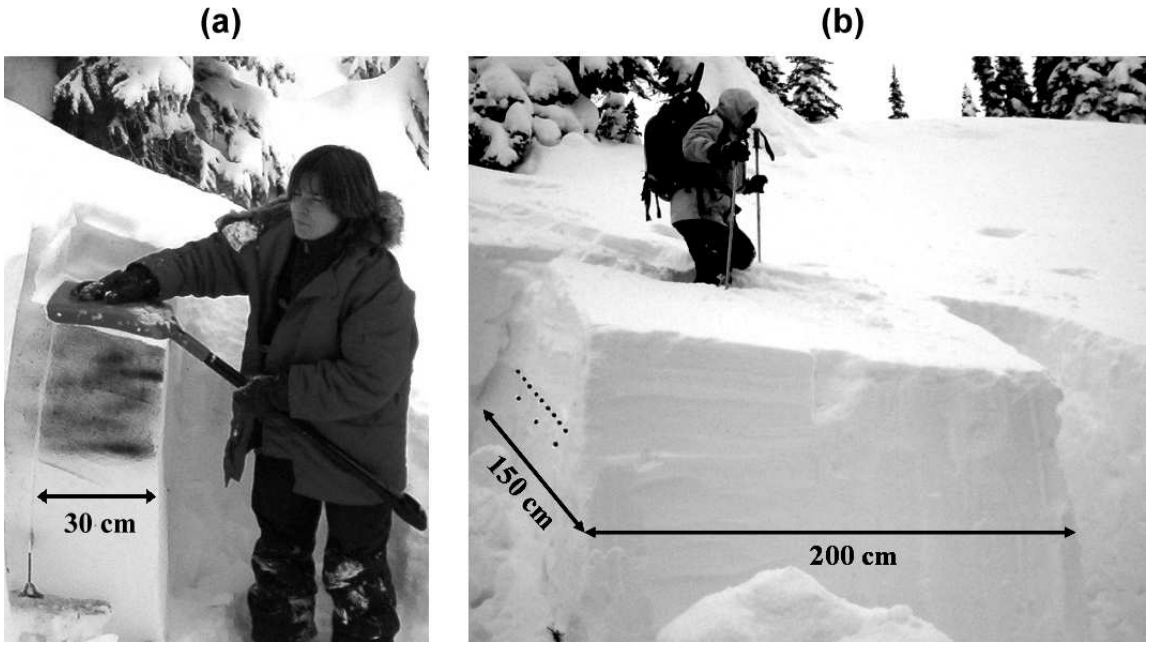

Figure 6.1: *Fractures in weak snowpack layers were photographed in compression tests (a) and rutschblock tests (b). Black powder was used to increase the contrast in most photographed compression tests. Markers were inserted in the vertical snow wall above and below the weak layer to analyze the motion of the slab in rutschblock tests.*

pack layers, the images were stored on a portable computer in the field. In order to store the images on the portable computer, an external analog capture device (Dazzle Digital Video Creator 80) was used. This device attaches to the Universal Serial Bus (USB) port on the portable computer and converts the Composite Video signal (RCA) from the high-speed camera to digital images. The digitized images were stored onto the hard drive with a resolution of 320 x 240 pixels, the maximum resolution of the external analog capture device.

Different types of fractures, classified according to the fracture classification scheme introduced in Section 3.4, were photographed in compression tests (Figure 6.1 (a)). In order to observe fractures in weak layers, black powder (photocopy

toner) was blown on the snow around the weak layer or black markers (rubber corks) were carefully placed in the snow above the weak layer (Figure 6.1). The high-speed camera was mounted on a tripod, aimed at the weak layer of interest on one of the sides of the compression test column, and the compression test was performed until the weak layer fractured. Due to the relatively small size of the test column and the loading method, the compression test could not be used to analyze propagating fractures. In total, 28 fractures in 27 compression tests were photographed with the high-speed camera. However, only four of these tests had markers in the snow above the weak layer.

Propagating fractures were photographed in larger tests such as the rutschblock test (RB), the cantilever beam test (CB) as well as on skier-tested slopes (ST). In standard rutschblock tests (Figure 6.1 (b)), a 1.5 x 2 m block of snow was loaded by a skier (e.g. Föhn, 1987). However, for this study most rutschblock tests were performed with a larger block (e.g. 4 x 3 m). In order to observe the response of the slab to the propagating fracture, a row of black markers was inserted on the side of the rutschblock (Figure 6.1 (b)). The markers were placed 5 cm above the weak layer of interest and a distance d apart (5, 10 or 20 cm). Markers were also placed under the weak layer. In some rutschblock tests, a second row of markers was inserted in the snow, 10 cm above the first row of markers. The rutschblock test was performed until the weak layer fractured and the block released. Fractures were photographed in nine rutschblock tests.

Cantilever beam tests (Figure 6.2 (a)) consisted of an isolated beam of snow that was 30 cm wide and approximately 2 m long in the down-slope direction and contained a weak layer. The slab was rapidly undercut along the weak layer using a

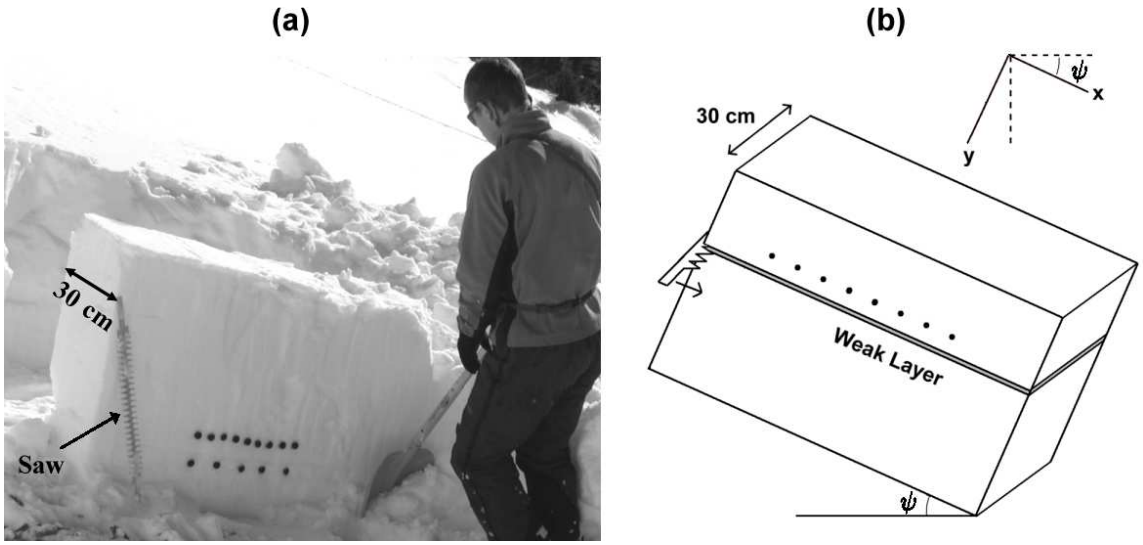

Figure 6.2: *The cantilever beam test was used to photograph propagating fractures. (a) Black markers were inserted in the vertical snow wall above and below the weak layer in a 30 cm wide and 2 m long rectangular column. (b) The slab was undercut along the weak layer using a 2 cm wide saw. For analysis, a coordinate system with a slope parallel x and slope normal y component was used as shown for a slope angle ψ.*

2 cm wide saw (Figure 6.2 (b)). This technique was introduced by Johnson (2000), who described several such cantilever beam tests, performed on level study sites. In these tests, the fracture propagated 30 to 60 cm horizontally along the weak layer before being stopped by the tensile fracture through the slab. The cantilever beam tests performed for this study were on steeper slopes and the slab was undercut in the down-slope direction (Figure 6.2 (b)). As for the rutschblock test, a row of markers was inserted in the vertical snow wall above the weak layer to observe displacements in the slab due to the propagating fracture and markers were placed under the weak layer. In total, three cantilever beam tests were successfully photographed.

On skier-tested slopes, an up-slope trench, typically 4 m long, was dug prior to testing. This was done in order to expose the weak layer for photography. In

order to test the slope, a skier traversed the slope with considerable speed while pressing down on his skies. As described earlier, a row of markers was placed in the snow above the weak layer and markers were also placed under the weak layer. Occasionally, a second row of markers was inserted in the snow above the first row. In all, six skier-tested slopes were photographed.

Additionally, at each test site, a snow profile was observed to obtain information about hand hardness, crystal type, crystal size, layer thickness, temperature and density of the snow layers (Canadian Avalanche Association, 2002). This information was used to correlate the measured variables with snowpack properties.

6.2.2 Image analysis

Particle tracking software (Crocker and Grier, 1996) was used to analyze the digitized images of photographed tests with black markers in the snow above the weak layer (Figure 6.3 (a)). In the analysis, the markers were numbered down-slope, starting with the uppermost marker in the video frame, as shown in Figure 6.3 (a). The image analysis consists of three stages. First, a spatial bandpass filter is used to identify the markers in the digitized images (Figure 6.3 (b)). This filter detects gaussian-like features of radius w by smoothing the image (boxcar average over a region of $2w + 1$) and subtracting the background (Crocker and Grier, 1996). Secondly, coordinates are assigned to the centroid of each marker (Figure 6.3 (c)). This is done by identifying local brightness maxima within a distance w. The last step is to identify the markers in all images so that the position of all markers is known at any given time. By 'connecting the dots' the trajectory for each marker can be determined (Figure 6.3 (d)). Linking particle distribution to trajectories is only

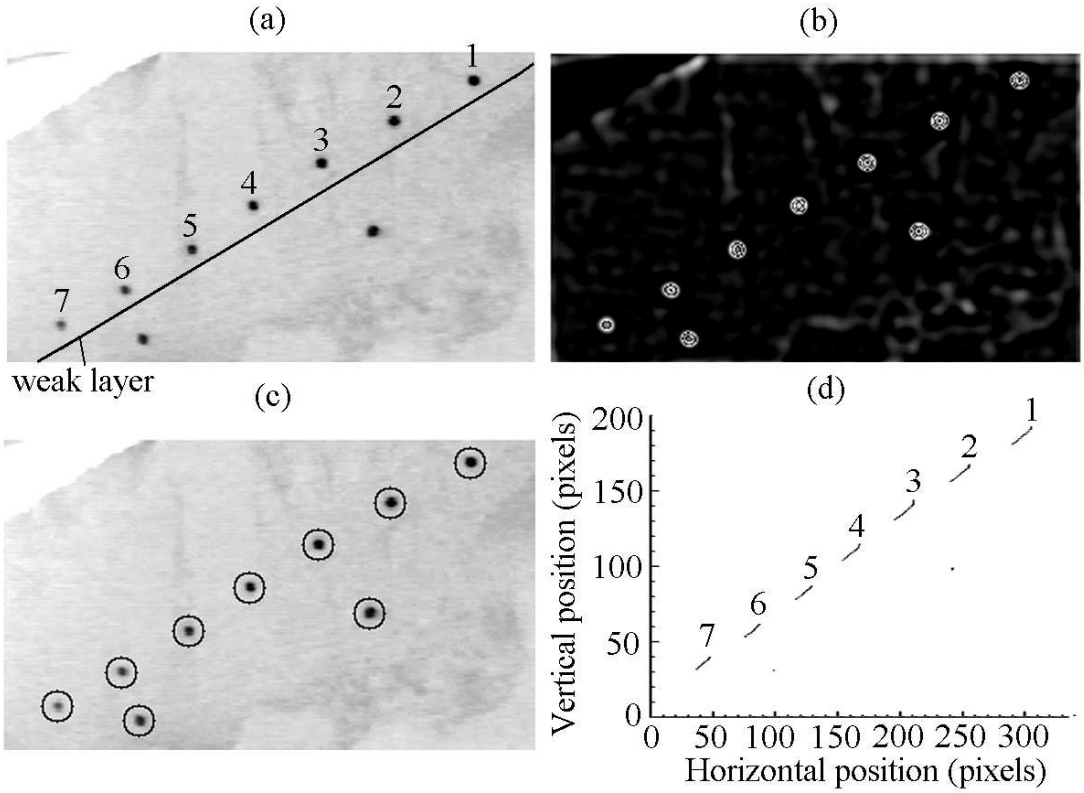

Figure 6.3: *Stages of image analysis. (a) An image of black markers, with a radius of 3 pixels, in the vertical snow wall above the weak layer on a skier-tested slope. (b) A spatial bandpass filter is used to identify gaussian-like features. (c). Coordinates are assigned to the centroid of each detected feature by identifying local brightness maxima. (d) By connecting the centroid in each image the trajectory of each marker is determined.*

possible if the particle displacement in one time step is sufficiently smaller than the particle spacing d. However, this was not a constraint, since the marker spacing was on the order of 5 cm and the typical particle displacement in one time step was on the order of 1 mm or less.

When analyzing the trajectories of the markers, a coordinate system with slope parallel (x) and slope normal (y) axes was used (Figure 6.2 (b)). In such a coordinate system, a collapsing fracture results in slope parallel (Δx) and slope normal (Δy)

displacement of the overlying slab. The displacement of a marker was calculated as the departure from the initial position:

$$\Delta x(t) = x(t) - X_0 \tag{6.1}$$

$$\Delta y(t) = y(t) - Y_0 \tag{6.2}$$

where the initial position (X_0, Y_0) was determined by averaging the position of the marker over 50 frames prior to movement. The speed (v_x,v_y) and the acceleration (a_x,a_y) of a marker in the slope parallel and slope normal direction could readily be calculated from the displacement curves:

$$v_x(t) = \frac{\Delta x(t) - \Delta x(t - \Delta t)}{\Delta t} \tag{6.3}$$

$$v_y(t) = \frac{\Delta y(t) - \Delta y(t - \Delta t)}{\Delta t} \tag{6.4}$$

$$a_x(t) = \frac{v_x(t) - v_x(t - \Delta t)}{\Delta t} \tag{6.5}$$

$$a_y(t) = \frac{v_y(t) - v_y(t - \Delta t)}{\Delta t} \tag{6.6}$$

where Δt is the time between two subsequent images (i.e. $\Delta t = \frac{1}{250}$ s).

The displacement of the markers was caused by several effects leading to differences in the slope parallel and slope normal displacement of the markers. The fracturing weak layer usually caused the overlying slab to be displaced in both the slope normal and the slope parallel direction. In most tests however, the slab moved down-slope after the weak layer had fractured, resulting in additional slope parallel displacement. The slope normal displacement therefore "levelled out" after the weak layer had fractured, to an approximately constant maximum value of Δy_{max}. The

slope parallel displacement on the other hand, generally did not reach a maximum value since slope parallel displacements caused by the down-slope slab movement could not be separated from the displacement caused by the fracturing of the weak layer. The calculated speed of the markers was therefore different in both directions. The speed of the markers in the slope parallel direction generally increased as the slab moved down-slope, eventually reaching an approximately constant value when the slab moved down-slope. The slope normal speed of the markers on the other hand, reached a maximum value $v_{y_{max}}$ as the weak layer fractured, after which v_y decreased. Finally, the acceleration of the markers generally reached a maximum value in both the slope parallel ($a_{x_{max}}$) and the slope normal ($a_{y_{max}}$) direction.

6.2.3 Accuracy of the displacement measurements

Digitized images suffer from a range of imperfections including nonuniform contrast and noise, which influences the accuracy of the particle tracking software. The particle tracking software performs best for particles with a radius between 2 and 30 pixels. Therefore, the choice of the magnification (i.e. apparent marker size) is a trade-off between the size of the field of view and degree of image contrast and apparent particle size. For a low magnification (i.e. small particle radius), the field of view is increased. However, the image contrast is decreased, thereby increasing the signal to noise ratio. For this study, the particle radius ranged from 2 to 20 pixels, resulting in a magnification ranging from 0.6 cm/pixel to 0.06 cm/pixel. Crocker and Grier (1996) describe a model for evaluating the performance of the brightness-weighted centroid estimation from digitized microscope images, based on the magnification and the particle radius. However, this method cannot be applied

to the images in this study since more significant variations were introduced due to uneven illumination of the field of view, much larger than present in microscope images. Furthermore, additional noise was introduced by the analog capture device (Section 6.2.6). Therefore, the accuracy ϵ for each test was estimated by calculating the standard deviation in the initial position of the markers. The accuracy was typically on the order of 0.02 cm and ranged from 0.01 cm to 0.1 cm.

6.2.4 Fracture speed calculation

For propagating fractures there is a retardation between the displacement of subsequent markers, as is shown schematically for Δy in Figure 6.4 (a) and (b). For a given displacement Δy_*, the time t_i, corresponding to the time when $\Delta y_i(t) = \Delta y_*$ for Marker i, is expected to be proportional to the initial position X_{0i}. Assuming a constant fracture propagation velocity (i.e. $t_2 - t_1 = t_3 - t_2 = ... = t_N - t_{N-1}$), the fracture speed $V_{\Delta y_*}$ is the slope of the line between X_{0i} and t_i (Figure 6.4 (c)) and is equal to the propagation speed of the advancing fracture. However, due to inaccuracies in the displacement data, a single value of Δy_* can lead to an inaccurate fracture speed calculation. In order to avoid this, the fracture speed $V_{\Delta y_*}$ was calculated for a wide range of Δy_* values, sampled at an interval of $\frac{\epsilon}{2}$ (Figure 6.4 (d)). An estimate of the propagation speed was then obtained by averaging the calculated fracture speed $V_{\Delta y_*}$ for $\epsilon < \Delta y_* \leq \frac{1}{2}\Delta y_{max}$, and is referred to as $\overline{V_{\Delta y}}$. A maximum value of $\frac{1}{2}\Delta y_{max}$ was chosen in order to account for any attenuation in the slope normal displacement (e.g. Figure 6.13).

Similarly, a fracture speed estimate $\overline{V_{\Delta x}}$ was calculated from the slope parallel displacement measurements. However, as mentioned earlier, the slab above the weak

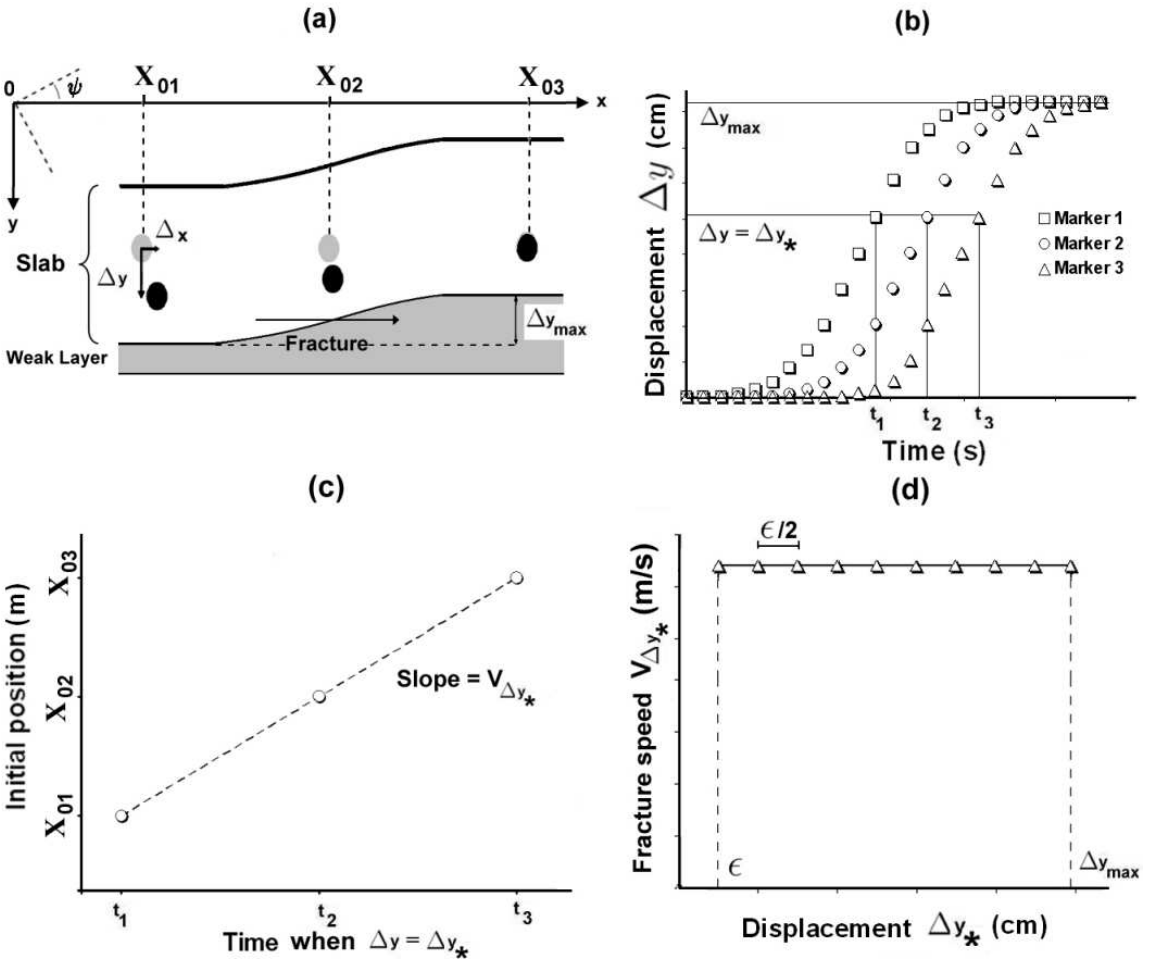

Figure 6.4: *Stages of the fracture speed calculations. (a) Schematic representation of the slope parallel (Δx) and slope normal (Δy) displacement of three markers due to a propagating collapsing fracture on a slope (not to scale). (b) Schematic slope normal displacement curves. The slope normal displacement reaches a maximum value of Δy_{max} after the weak layer has fractured. The time t_i, corresponding to the time when $\Delta y = \Delta y_*$ for Marker i, is used in the fracture speed calculation. (c) The propagation speed $V_{\Delta y_*}$ is equal to the slope of the line between the initial positions X_{0i} and the time t_i for a displacement of $\Delta y = \Delta y_*$, assuming a constant propagation velocity. (d) The fracture speed is calculated for a range of values of Δy_* sampled at an interval of $\frac{\epsilon}{2}$.*

layer usually moved down-slope after the weak layer had fractured. Therefore, the slope parallel displacement of the markers did not reach a maximum value. Nevertheless, in order to obtain fracture speed estimates from the slope parallel displacement, the same limits were used as for the calculation of $\overline{V_{\Delta y}}$.

6.2.5 Accuracy of fracture speed measurements

The accuracy of the fracture speed calculations was limited by the size of the field of view, as well as the accuracy of the displacement measurements. The maximum fracture speed that can be resolved from the digitized images is limited by the size of the field of view: $V_{max} = \frac{(N-1)d}{\Delta t}$, where N is the number of markers, d is the marker separation distance, and Δt is the time between two subsequent digitized images (i.e. $\frac{1}{250}$ s). The accuracy in the displacement measurement ϵ on the other hand, limited the particle tracking precision. The rate of displacement of a marker during the initial stages of fracture was on the order of 10 cm/s. Therefore, the typical displacement of a marker between two subsequent images was 0.04 cm, on the order of ϵ. The accuracy of the times t_i used in calculating the fracture speed was therefore equal to Δt. Hence, the relative measurement error in the maximum resolvable fracture speed was 100%. Measurement errors in the marker separation distance d were on the order of 1% or less, and did not affect the accuracy of the fracture speed calculations. The measurement error ϵ_V for the calculated fracture speed $V_{\Delta x_*}$ and $V_{\Delta y_*}$ was therefore estimated using the maximum resolvable fracture speed as a reference:

$$\frac{\epsilon_V}{V_i} = \frac{V_i}{V_{max}} \tag{6.7}$$

where V_i is either $V_{\Delta x_*}$ or $V_{\Delta y_*}$.

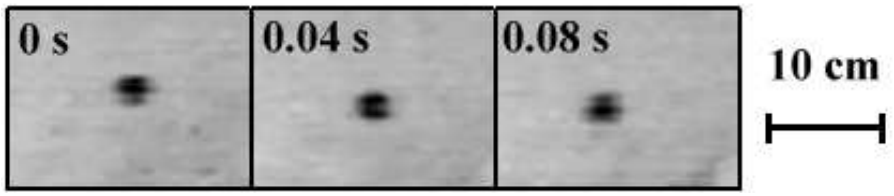

Figure 6.5: *Images of a moving marker at three different times showing uneven pixel clipping at the edges of the marker, leading to errors in the determination of the centroid of the marker.*

6.2.6 Image restoration and data filtering

During movement of the markers, uneven pixel clipping at the edges of the markers (Figure 6.5) introduced additional fluctuations in the displacement data. This was caused by interference of the images with static noise bands introduced by the capture device (Figure 6.6). As can be seen in Figure 6.6 for an image taken with the lens covered, apart from time varying noise introduced by thermal variations in the CCD array, static horizontal noise bands were introduced by the analog capturing device. Uneven pixel clipping was found to be a significant constraint on the accuracy of the displacement measurements during movement and was dependent on the apparent marker size in the digitized images and the rate of displacement of the marker. Moreover, due to the accelerated movement of the markers during the initial stages of the displacement, the fluctuations in the displacement measurements were not constant. Furthermore, the static noise bands were different in each experiment.

In order to reduce unwanted fluctuations in the displacement measurements caused by uneven pixel clipping, it was necessary to remove the noise bands from the digitized images. Two methods for correcting the digitized images were explored. First, a correction function $C(y')$ was constructed by calculating the average pixel

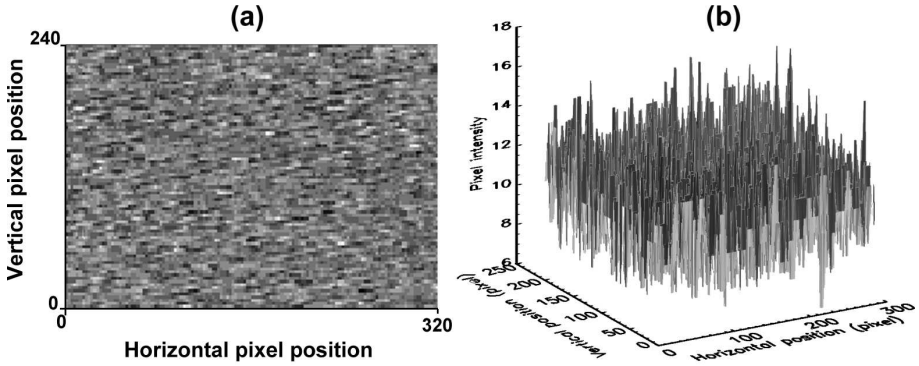

Figure 6.6: *The use of the analog capture device introduced additional noise to the digitized images. (a) Example of an image taken with a covered lens. The pixel intensity was scaled from 0 to 255 to accentuate the noise level. (b) Pixel intensity by horizontal and vertical pixel position for the same image. The mean pixel intensity was 11.*

intensity in the vertical direction of the first 50 images, prior to movement:

$$C(y') = \frac{1}{50}\sum_{i=1}^{50}\left(\frac{1}{N_{x'}}\sum_{x'=0}^{N_{x'}-1} I(x',y')\right)_i \tag{6.8}$$

where $I(x', y')$ is the video signal (i.e. pixel intensity at location (x',y')) and $N_{x'}$ the number of pixels in the horizontal direction (320). The correction function $C(y')$ was used to construct a background image which was removed from the digitized images. As can be seen in Figure 6.7, this method was reasonably effective in removing the horizontal noise bands. However, it did not correct the pixel clipping problems at the edges of the markers. A second method, using a Fast Fourier Transform (see below) to filter out the specific frequencies of the noise bands, did not produce better results.

Since image restoration prior to analysis was not successful, methods for reducing the scatter in the displacement measurements (Δx, Δy) were considered. Three techniques were evaluated: moving average filters, Fast Fourier Transforms and curve fitting.

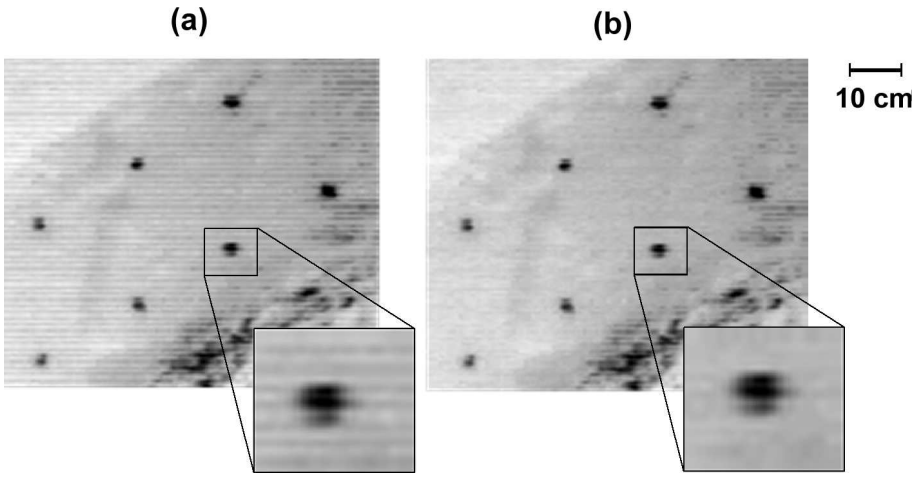

Figure 6.7: *Image restoration by removing the horizontal noise bands. (a) Original digitized image showing horizontal noise bands causing uneven pixel clipping at the edges of a marker. (b) Reconstructed image obtained by removing the constructed background image from the original digitized image showing no reduction in pixel clipping.*

The simplest way to reduce high-frequency noise is with local averaging, which is called a moving average filter (e.g. Castleman, 1996). The value of a signal $f(t)$ at a given time t_* is converted to the average value over a distance N_* around t_*:

$$F(t_*) = \frac{1}{N_*} \sum_{t=t_*-\frac{1}{2}(N_*-1)}^{t_*+\frac{1}{2}(N_*-1)} f(t) \tag{6.9}$$

where $f(t)$ is the raw data (i.e. $\Delta x(t)$ or $\Delta y(t)$), N_* is the width of the moving average filter, also called the degree or the order of the filter, and $F(t_*)$ is the resulting average value at time t_*. Higher order filters removed more scatter, at the expense of loss of detail, whereas lower order filters did not adequately reduce the scatter in the data (Figure 6.8 (a)). A seven point moving average was found to be effective in reducing most fluctuations in the displacement data without significant loss of detail.

The Fast Fourier Transform (FFT) is a computational method to determine the

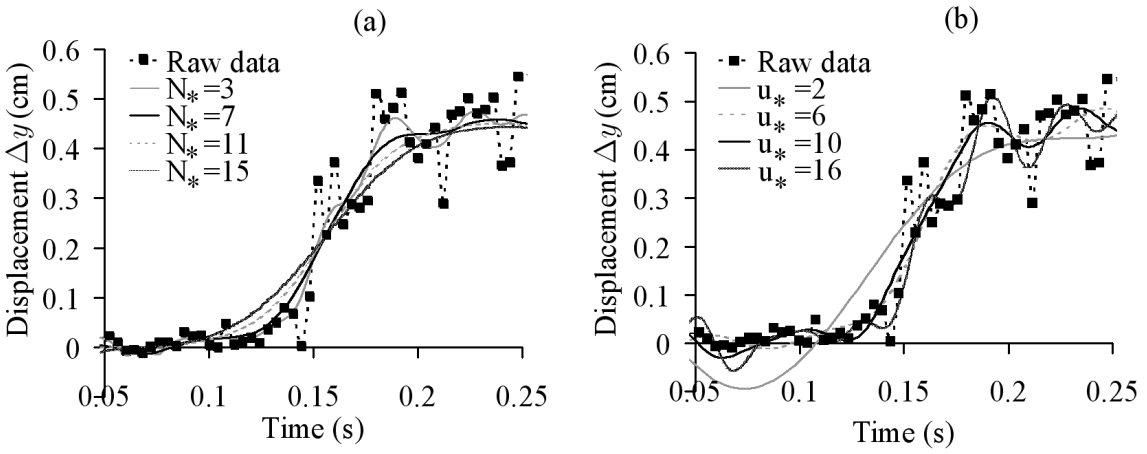

Figure 6.8: *Two techniques used to reduce the scatter in the displacement data. (a) Example of raw slope normal displacement measurements and moving average curves of various degrees N_*. Scatter in the displacement curve, introduced by uneven pixel clipping, was reduced by this filters. A seven point moving average reduced most displacement fluctuations. (b) Example of raw slope normal displacement measurements and low-pass filtered curves for various cut-off frequencies u_*. A low-pass filter with a cut-off frequency of $u_* = 10$ suppressed most displacement fluctuations.*

Fourier transform of a discrete signal from the time domain $f(t)$ to the frequency domain $F(u)$:

$$F(u) = \frac{1}{N_t} \sum_{t=0}^{N_t-1} f(t) e^{\frac{-i2\pi ut}{N_t}} \tag{6.10}$$

for $u = 0, 1, ..., N_t - 1$ and where N_t is the number of samples (e.g. Pratt, 2001). By applying a low-pass filter in the frequency domain, high-frequency fluctuations above a cut-off frequency u_* were removed by setting the high-frequency portion of the amplitude spectrum to zero: $F_*(u) = F(u)$ for $u < u_*$ and $F_*(u) = 0$ otherwise. The filtered signal $f_*(t)$ in the time domain was obtained by performing the inverse Fourier transform from the filtered signal $F_*(u)$ in the frequency domain:

$$f_*(t) = \sum_{u=0}^{N_t-1} F_*(u) e^{\frac{i2\pi ut}{N_t}} \tag{6.11}$$

for $t = 0, 1, ..., N_t - 1$. As for the moving average filter, higher order low-pass filters

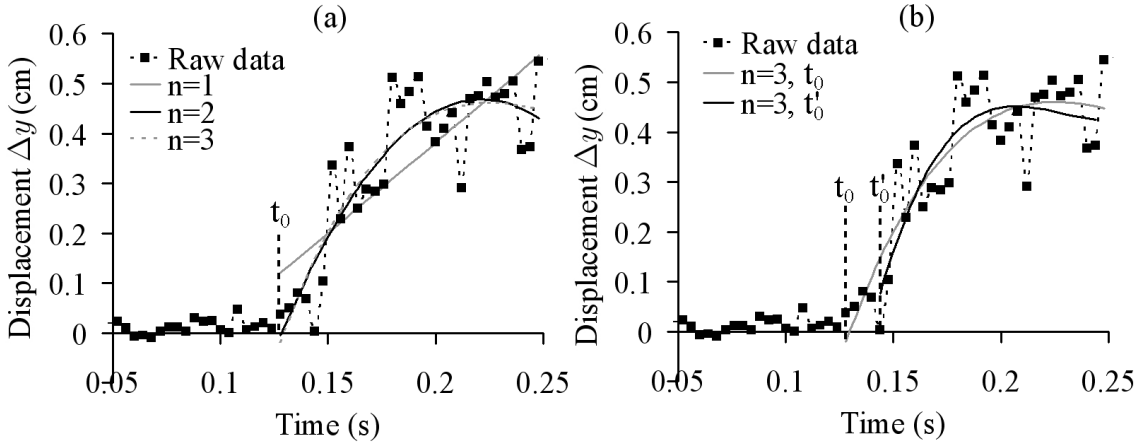

Figure 6.9: *(a) Polynomial functions of the first, second and third order were fitted to the slope normal displacement data. Only data from when the markers were moving was used ($t > t_0$). (b) Third order polynomial fit for different portions of the data. Selecting a different t_0 value affected the polynomial fit to the experimental data.*

(i.e. lower u_*) removed more scatter at the expense of loss of detail and lower order filters did not adequately remove the scatter in the displacement data, as can be seen in Figure 6.8 (b). A cut-off frequency of $u_* = 10$ was found to be most effective.

Finally, two types of functions were fit to the experimental displacement data using a least squares fit: polynomial functions and the Butterworth function. Polynomial functions of the first, second and third order were fitted to the displacement data, using only data from when the markers were in motion ($t > t_0$). Higher order polynomials generally were a better fit to the experimental data (Figure 6.9 (a)). However, it was not always obvious when the markers started moving. As can be seen in Figure 6.9 (b), selecting a different portion of the data (i.e. different t_0) affected the polynomial fit.

The Butterworth function on the other hand was fitted to the entire displacement data, yet only for the slope normal displacement. The Butterworth function is defined

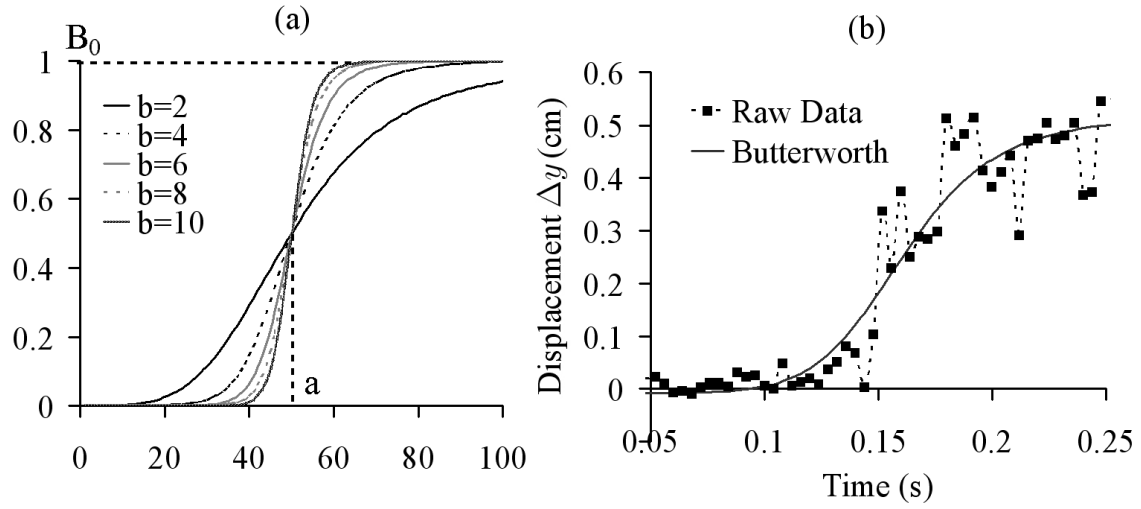

Figure 6.10: *The Butterworth function was used as a fit to the experimental data. (a) The effect of the power b is shown for a Butterworth function with and amplitude* $B_0 = 1$ *and a centre* $a = 50$*. (b) Least squares fit of the Butterworth function to slope normal displacement data.*

as:

$$B(t) = \frac{B_0}{1 + \left(\frac{a}{t}\right)^{2b}} \tag{6.12}$$

where B_0 is the amplitude, a the centre and the power b determines the steepness of the function, as seen in Figure 6.10 (a). This function is commonly used as a low-pass or high-pass filter (e.g. Pratt, 2001). The Butterworth function had a reasonable fit to the experimental data (Figure 6.10 (b)). The fit could be improved by only using a certain portion of the data. However, as for the polynomial function fitting, no method was available to select an adequate portion of the data objectively.

Overall, these filtering methods were successful in reducing the scatter in the displacement data. The moving average filter, as well as the low-pass filter produced reliable results since there was no selection bias. However, fitting polynomial functions or the Butterworth function to the experimental data did not result in reliable

filtered data since the fit was dependent on the portion of the data that was used for the least squares fit. Therefore, only the moving average and the low-pass filtering techniques were used in the analysis.

6.2.7 Influence of data filtering on calculated parameters

Displacement data were used to calculate the speed and acceleration of the markers and the propagation speed of the fracture. These parameters could generally not be calculated from the raw data, therefore the filtered data were used. However, since detailed information was lost due to the data filtering, the values of the calculated parameters were affected by the data filtering. In this Section, the influence of the data filtering on the calculated parameters is discussed and highlighted by showing examples of raw data and filtered data. These examples were chosen because the data were representative of other experiments. Furthermore, the trends shown below were very similar in all experiments.

Due to scatter in the raw data, the calculated marker speeds from the raw data did not result in useable values (Figure 6.11 (a)). As the scatter was removed by data filtering, trends appeared in the calculated marker speeds. These trends were unchanged by the moving average filter (Figure 6.11 (b)), whereas no consistent trends were observed with the low-pass filtered data (Figure 6.11 (c)). For the moving average filter, the values of the calculated marker speed only decreased slightly for higher order filters (Figure 6.11 (b)).

Similarly the calculated accelerations of individual markers were affected by the data filtering. As can be seen in Figure 6.12 (a), the calculated marker accelerations from the raw data were highly variable. As with marker speeds, trends emerged

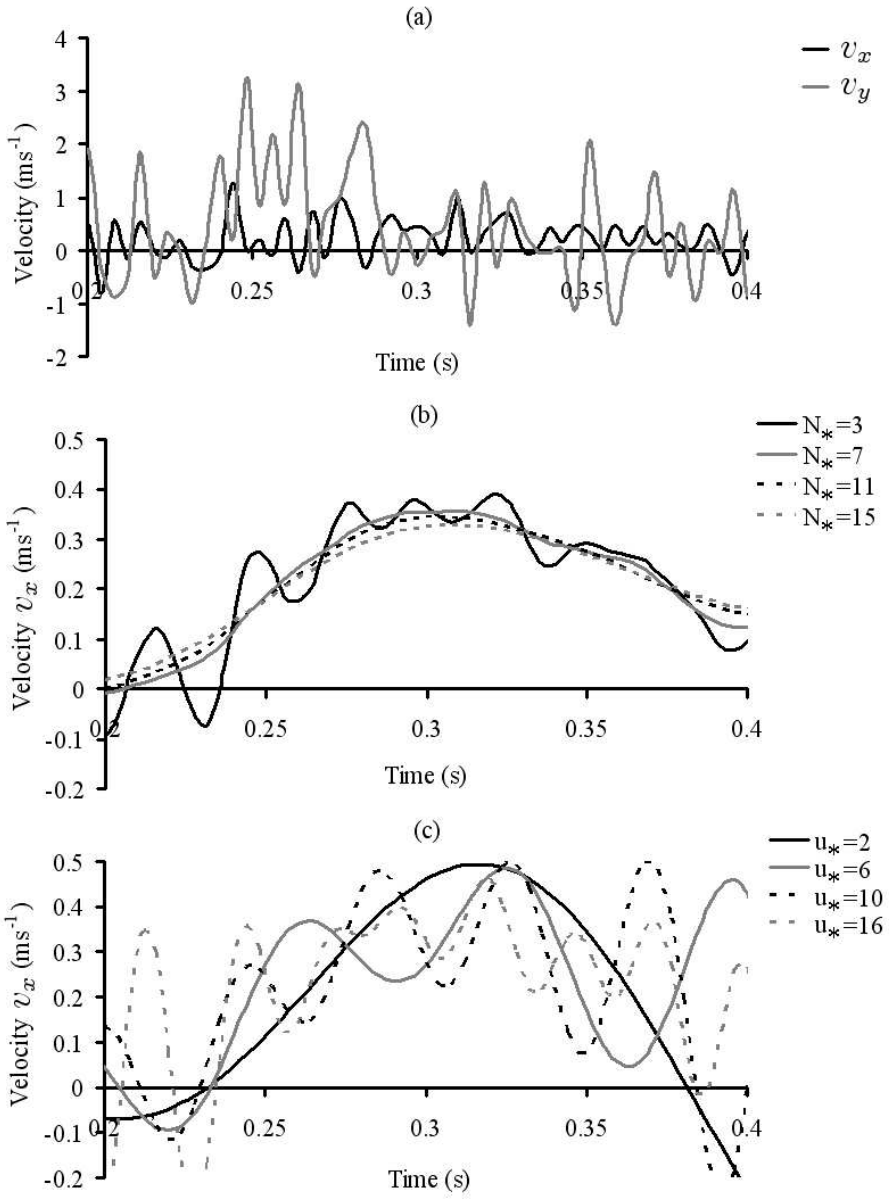

Figure 6.11: *The calculated marker speed (test CTB in Table 6.2) was affected by the data filtering. (a) Example of calculated marker speed from raw data in the slope parallel (black) and slope normal (gray) direction. (b) Slope parallel marker speed calculated from data filtered by using moving average filters of various orders N_*. (c) Slope parallel marker speed calculated from data filtered by using low-pass filters with various cut-off frequencies v_*.*

when using a moving average filter to reduce the scatter in the displacement data (Figure 6.12 (b)), whereas no consistent trends were observed in the low-pass filtered calculated accelerations (Figure 6.12 (c)). However, for the moving average filter, the values of the calculated marker accelerations decreased for higher order filters (i.e. larger N_*), as high resolution time information was lost with additional averaging. Furthermore, the influence of the moving average on the calculated marker acceleration was more pronounced for markers that were displaced over a short period of time, since the width of the moving average filter was relatively more important for these markers than for markers that were displaced over a longer period of time. The values of the calculated acceleration are therefore only an estimate of the actual acceleration of the markers.

Finally, the speed of propagating fractures was calculated from the displacement measurements of rows of markers, as described in Section 6.2.4. The scatter in the raw data was often too large to obtain reliable fracture speed measurements. Therefore, the moving average and low-pass filtered data were used when calculating fracture speeds. However, due to inherent inaccuracies in the filtered data, it was not possible to determine whether or not the fracture was accelerated. Therefore, the fracture speed calculation should be considered as an average fracture speed throughout the field of view.

In Table 6.1 the values of the calculated fracture speed $\overline{V_{\Delta x}}$ and $\overline{V_{\Delta y}}$ are shown for various orders of the moving average filter as well as various cut-off frequencies for the low-pass filter. The values of $\overline{V_{\Delta x}}$ were affected by the data filtering as the values were dependent on the order of the filter. The calculated fracture speed values obtained from the slope normal displacement on the other hand, were virtually not

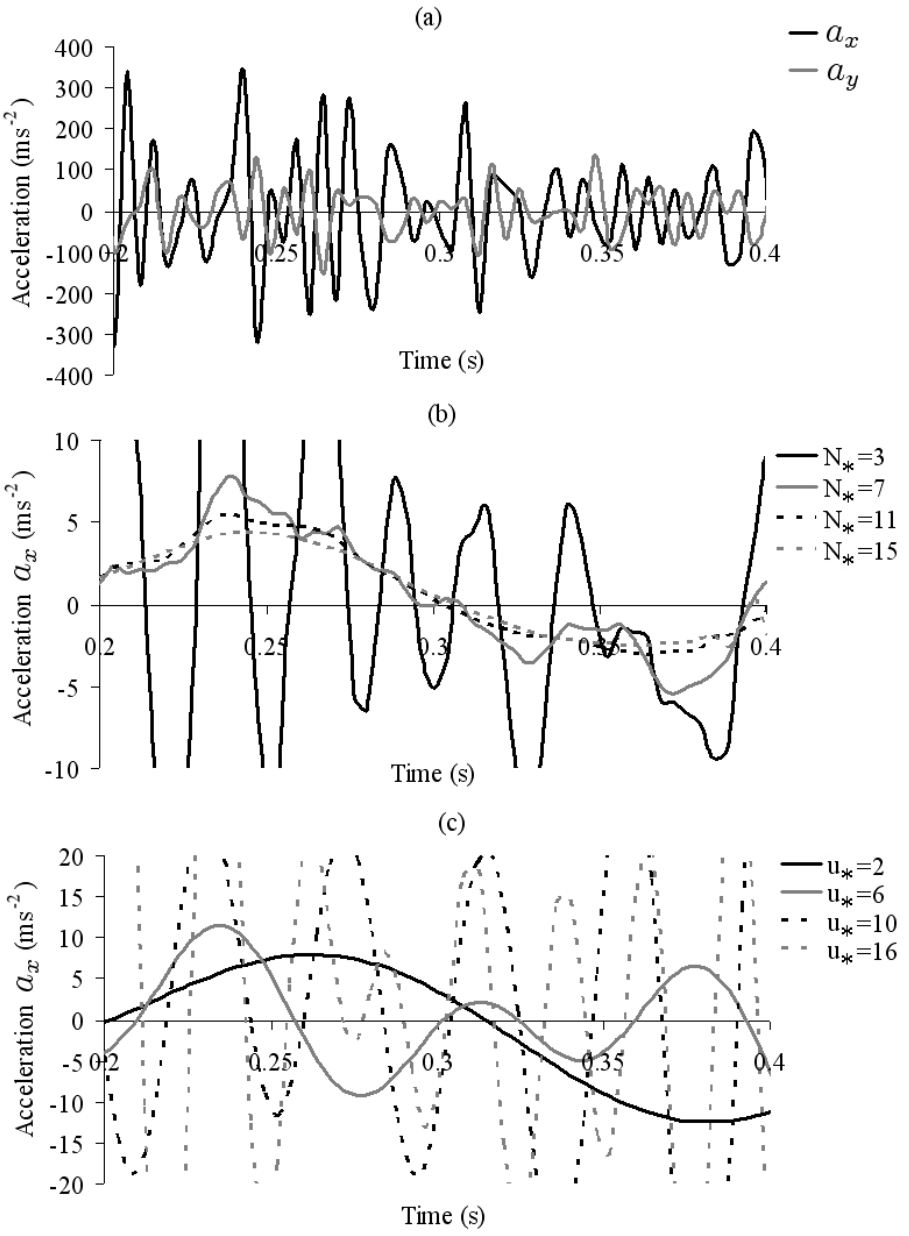

Figure 6.12: *The calculated marker acceleration (test CTB in Table 6.2) was affected by the data filtering. (a) Example of calculated marker acceleration from raw data in the slope parallel (black) and slope normal (gray) direction. (b) Slope parallel marker acceleration calculated from data filtered by using moving average filters of various orders N_*. (c) Slope parallel marker acceleration calculated from data filtered by using low-pass filters with various cut-off frequencies v_*.*

Table 6.1: *Example of calculated fracture speed values* $\overline{V_{\Delta x}}$ *and* $\overline{V_{\Delta y}}$ *(test STE in Table 6.5) for various orders of the moving average filter* (N_*) *and various cut-off frequencies for the low-pass filter* (u_*).

Moving Average			Low-pass		
N_*	$\overline{V_{\Delta x}}$ (m s^{-1})	$\overline{V_{\Delta y}}$ (m s^{-1})	u_*	$\overline{V_{\Delta x}}$ (m s^{-1})	$\overline{V_{\Delta y}}$ (m s^{-1})
3	29±5	25±5	2	110±38	25±3
5	34±10	26±4	3	88±24	21±3
7	35±10	26±3	6	87±23	23±3
9	38±14	26±2	8	48±32	26±4
11	40±10	25±2	10	27±25	26±3
15	42±13	24±3	16	33±20	26±6
21	46±12	23±3	21	29±10	25±5

affected by the data filtering, and the measurement errors were smaller than those for $\overline{V_{\Delta x}}$, showing that the fracture speed calculations from the slope normal displacement were more reliable than the $\overline{V_{\Delta x}}$ values.

Overall, filtering the displacement data affected the various parameters calculated from the displacement measurements. The moving average filter was found to be the most reliable filtering method since trends in the marker speed and acceleration were unchanged and fracture speed calculations from the slope normal displacement were not significantly affected. Fracture speed calculations obtained from the slope parallel displacement on the other hand, were more variable and had greater measurement errors. Furthermore, the low-pass filtered data did not reveal any trends in the marker speed or acceleration. This was found to be the case in all the experiments. Therefore, in the analysis, parameters were calculated from the seven point moving average filtered data.

6.3 Results

Displacement measurements of tests that are not shown in this section can be found in Appendix A.

6.3.1 Observations of fractures in compression tests

Four fractures in compression tests were photographed with black markers in the snow wall above the weak layer (Table 6.2). The size of the field of view ranged from 20 cm in test CTA to 40 cm in test CTD. Furthermore, the quality of the digitized images from test CTD was compromised by uneven illumination, resulting in an accuracy of only 0.1 cm.

A fracture in a buried surface hoar layer (CTA) that was judged as Sudden Planar (Table 3.4) and tested on a level study site, resulted in a maximum slope normal displacement of 0.28 ± 0.05 cm, whereas the slope parallel displacement was undetectable. Three Sudden Collapse fractures in a weak layer consisting of faceted crystals, were performed on a 30^0 slope. The measured Δy_{max} for these tests ranged from 1.3±0.1 cm to 1.7±0.1 cm and Δx did not level off as the test column moved down-slope. Therefore, the values of Δx_{max} in Table 6.2 are the average slope parallel displacements in the last frame, which are primarily affected by the length of the videos.

Figure 6.13 shows images of the markers at the start and at the end of compression test CTC (Table 6.2), as well as the displacements Δx and Δy of three markers. The slope parallel displacement increased steadily after the weak layer fractured and the compression test column moved down-slope. The slope normal displacement on the

Table 6.2: *Measurements from photographed fractures in compression tests. Slope angle in degrees (ψ), observed fracture character (Char), weak layer crystal type (F) and weak layer thickness measured vertically (Th) are given. Furthermore, the accuracy of the displacement measurements (ϵ), the average slope parallel displacement in the last frame (Δx_{max}) and the average maximum slope normal displacement after fracture (Δy_{max}) are shown. The maximum speed $v_{x_{max}}$ and $v_{y_{max}}$ and maximum acceleration a_x and a_y were derived from the seven point moving average displacement data. Tests in which the slab moved down-slope after fracture are marked with an asterisk.*

Test	ψ	Char	F	Th (cm)	ϵ (cm)	Δx_{max} (cm)	Δy_{max} (cm)	$v_{x_{max}}$ (m s^{-1})	$v_{y_{max}}$ (m s^{-1})	$a_{x_{max}}$ (m s^{-2})	$a_{y_{max}}$ (m s^{-2})
CTA	0	SP	SH	0.7	0.03	0.01±0.04	0.22±0.04	0.03±0.02	0.06±0.02	0±1	3±1
CTB*	30	SC	FC	5.5	0.02	3.4±0.1	1.3±0.1	0.39±0.02	0.17±0.02	4±1	6±1
CTC*	30	SC	FC	5.5	0.04	3.3±0.1	1.7±0.1	0.42±0.03	0.20±0.03	7±2	8±2
CTD*	30	SC	FC	5.5	0.1	4.7±0.1	1.3±0.1	0.41±0.09	0.15±0.08	7±3	7±3

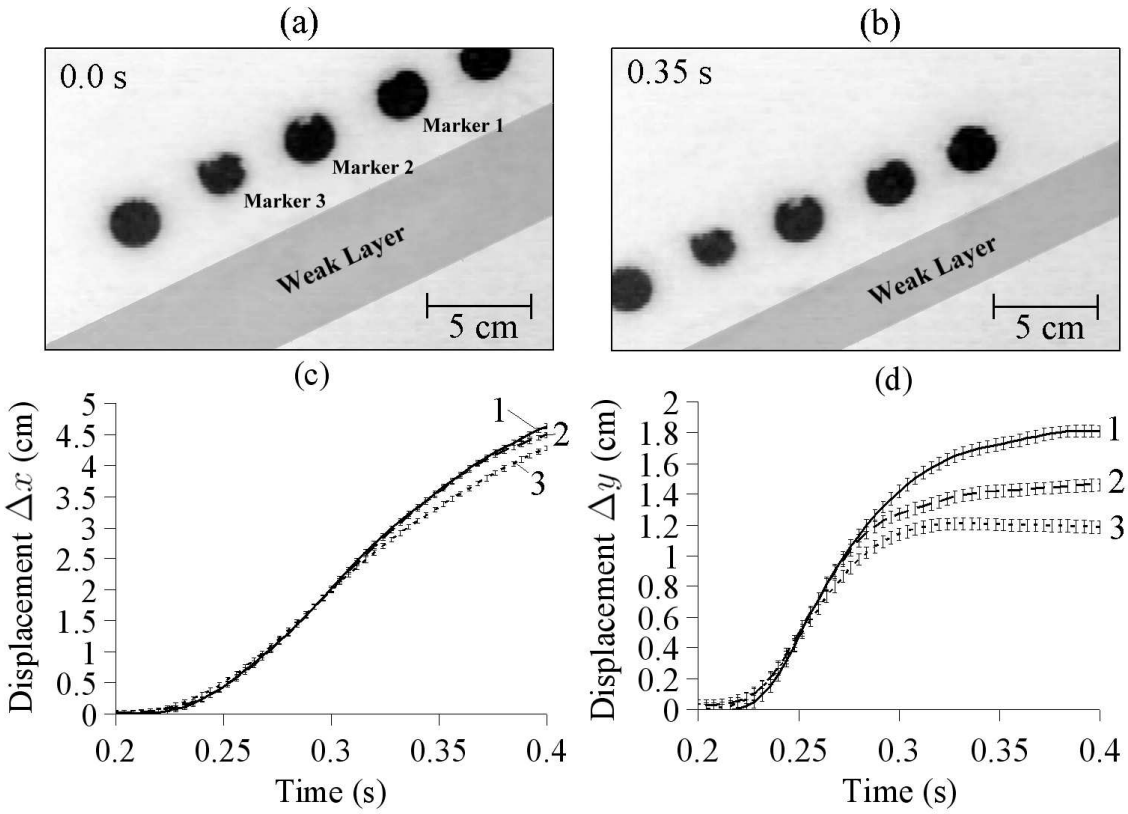

Figure 6.13: *(a) Image of markers at the start of compression test CTC. (b) Image of markers at the end of the compression test. (c) Slope parallel displacement. (d) Slope normal displacement. The accuracy of the displacement measurements for this test was 0.01 cm.*

other hand, increased steadily up to 0.8 cm at $t \approx 0.26$ s, after which the rate of collapse decreased (i.e. attenuation) until an average maximum value of 1.3±0.1 cm was reached after approximately 0.1 s. As seen in Figure 6.13, the displacement of Marker 1 was largest. This was caused by tilting of the compression test column when it moved down-slope after the weak layer had fractured.

The markers were observed to start moving in both the slope parallel and the slope normal direction simultaneously, as can be seen in Figure 6.14 (a) for Marker 1 from test CTC. The speed and the acceleration of Marker 1, calculated from the

seven point moving average displacement, are shown in Figure 6.14 (b) and (c). During the initial stages of displacement (i.e. $t < 0.25$ s), the speed of Marker 1 was similar in both directions (Figure 6.14 (b)). However, at t $\approx$ 0.25 s, v_y reached a maximum value and started decreasing (i.e. attenuation) while v_x still increased (i.e. column sliding down-slope) until a maximum value at t $\approx$ 0.31 s was reached. Thereafter v_x decreased as the compression test column moved further down-slope and started tilting. On the other hand, both the slope parallel and slope normal acceleration of Marker 1 reached a maximum value at t $\approx$ 0.23 s (Figure 6.14 (c)). However, the slope normal acceleration of Marker 1 decreased more rapidly than the slope parallel acceleration, as expected since the compression test column moved down-slope after fracture.

The maximum speed and acceleration of the markers in the slope parallel ($v_{x_{max}}$ and $a_{x_{max}}$, respectively) and slope normal direction ($v_{y_{max}}$ and $a_{y_{max}}$, respectively) are shown in Table 6.2. These were calculated from the seven point moving average displacement data. The maximum speed of the markers in the slope normal direction was somewhat lower for test CTA (0.06 ± 0.02 m s^{-1}) than for test CTB, CTC and CTD. The maximum slope parallel speed of the markers on the other hand, was undetectable in test CTA since there was no slope parallel displacement. For test CTB, CTC and CTD however, $v_{x_{max}}$ was larger than $v_{y_{max}}$ as the compression test column moved down-slope after the weak layer fractured. The maximum acceleration in the slope parallel direction of the markers in test CTA was lower than $a_{y_{max}}$. This comes as no surprise since there was no slope parallel displacement of the markers in this test. However, this was not the case for tests CTB, CTC and CTD, for which $a_{y_{max}} \approx a_{y_{max}}$.

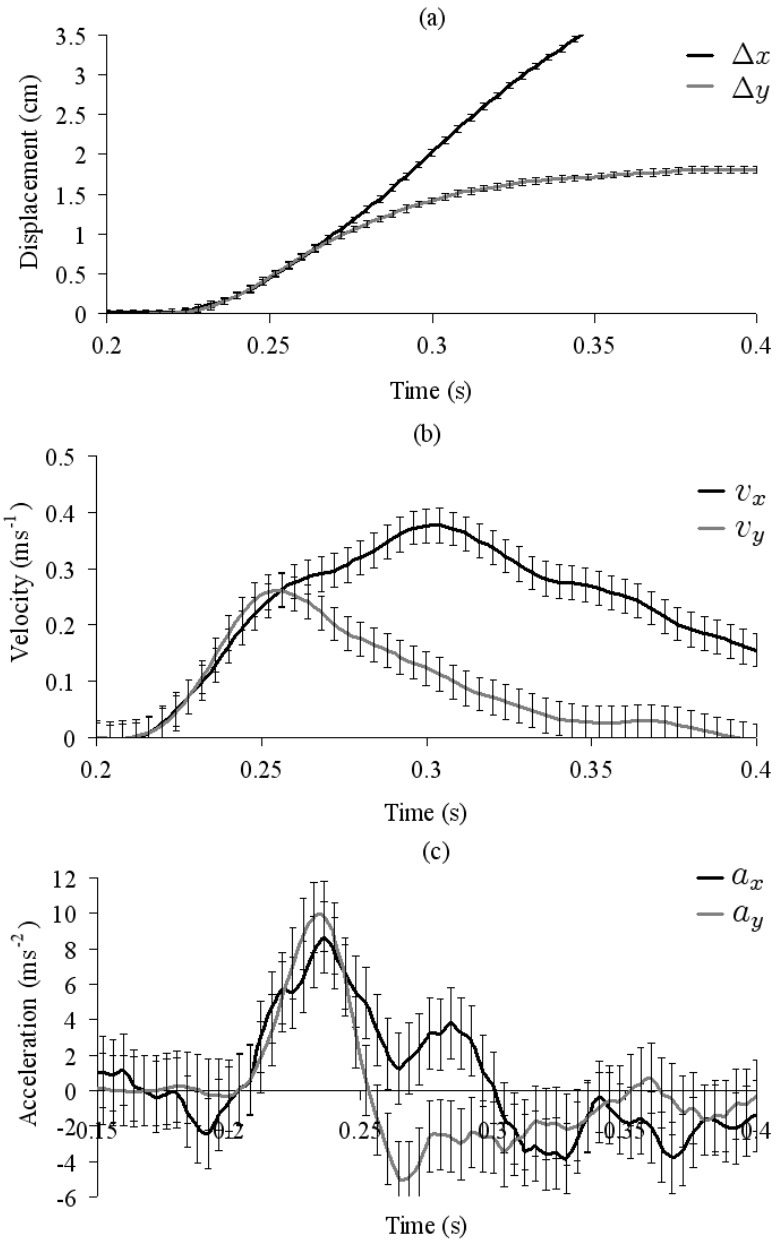

Figure 6.14: *(a) Seven point moving average slope parallel (Δx) and slope normal displacement (Δx) of Marker 1 in test CTC (Figure 6.13). The accuracy of the displacement measurements was 0.04 cm. (b) Slope parallel (v_x) and slope normal (v_y) marker speed. (c) The acceleration of the markers in the slope parallel (a_x) and slope normal direction (a_y). Error bars indicate the uncertainty in the calculated velocity and acceleration. These were approximated as the standard deviation in the seven-point moving average velocity and acceleration over 50 frames prior to movement.*

In the majority of the photographed compression tests no markers were used, but black powder was blown on the snow to increase contrast. No quantitative analysis of these images can be done. Nevertheless, crushing of the weak layer was observed in each test (i.e. slope normal displacement), regardless of the fracture character. Furthermore, the mechanism that caused different fracture types was observed in the images. For Progressive Compression and Sudden Collapse fractures, the fracture occurred through the thickness of the whole weak layer. In PC fractures, the crystals in the weak layer were rearranged after each loading step, resulting in progressive crushing of the weak layer. For SC fractures on the other hand, the critical loading step resulted in an obvious displacement of the overlying slab by a sudden and extensive rearrangement of the crystals throughout the weak layer (Figure 6.15 (a)). Images of the only photographed Resistant Planar fracture showed that the fracture occurred at the lower interface of a weak layer due to rearrangement of the crystals at the interface, resulting in slope normal displacement of the overlying slab ($<$ 1 cm). Sudden Planar fractures were only photographed in weak layers composed of buried surface hoar crystals. The fractures appeared to occur due to rupturing of the bonds between the weak layer and the adjacent layers, as proposed by Jamieson and Schweizer (2000), causing the crystals in the weak layer to tilt resulting in collapse (Figure 6.15 (b)). These layers were thin ($<$ 1 cm) resulting in only limited slope normal displacement of the overlying slab.

6.3.2 Observations of fractures in cantilever beam tests

Three fractures in cantilever beam tests were photographed with black markers in the snow wall above the weak layer (Table 6.3). In these tests, the field of view ranged

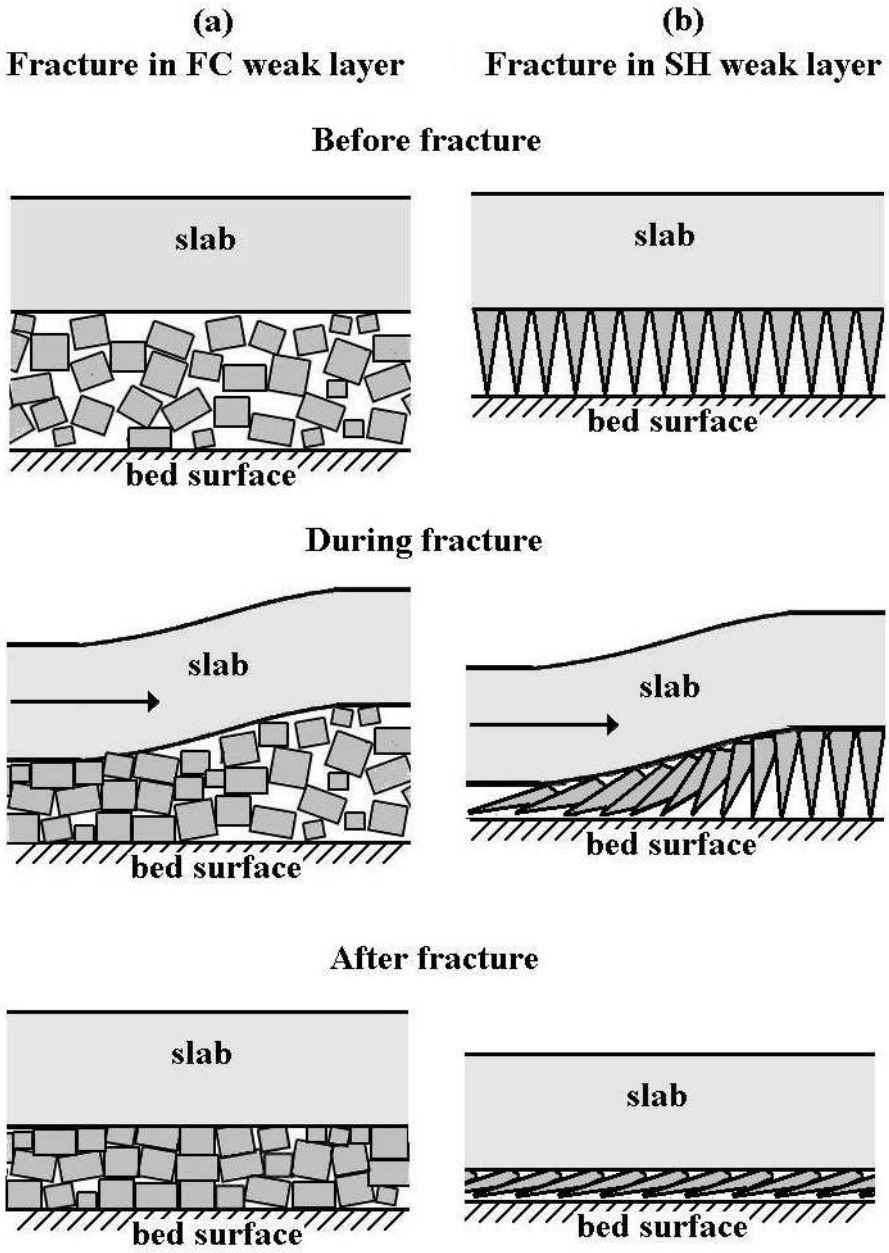

Figure 6.15: *Schematic micro-mechanical diagram of two different fracture mechanisms (not to scale). (a) Fracture in a weak layer composed of faceted crystals. Breaking of bonds causes extensive rearrangement of the crystals throughout the weak layer resulting in slope normal displacement. (b) Fracture in buried surface hoar weak layer. Breaking of bonds causes rotation of the surface hoar crystal resulting in slope normal displacement.*

Table 6.3: *Measurements from photographed fractures in cantilever beam tests (CB). Slope angle in degrees (ψ), observed fracture character (Char), weak layer crystal type (F), weak layer thickness measured vertically (Th), depth of the weak layer measured vertically (D), the accuracy of the displacement measurements (ϵ), the number of markers that were displaced (N) and the marker separation (d) are given. The maximum displacement Δx_{max} and Δy_{max}, maximum speed $v_{x_{max}}$ and $v_{y_{max}}$, maximum acceleration a_x and a_y and the average fracture speed $\overline{V_{\Delta x}}$ and $\overline{V_{\Delta y}}$ were derived from the seven point moving average displacement measurements of the markers. The test in which the slab moved down-slope after fracture is marked with an asterisk.*

Snowpack conditions and experimental parameters									
Test	ψ	Char	F	Th (cm)	D (cm)	ρ_{slab} (kg m^{-3})	ϵ (cm)	N	d (cm)
CBA	20	SP	SH	1.5	69	213	0.04	5	5
CBB	20	SP	SH	1.5	69	213	0.02	5	5
CBC*	34	SP	SH	0.7	85	193	0.02	6	10
Motion data									
Test	Δx_{max} (cm)	Δy_{max} (cm)	$v_{x_{max}}$ (m s^{-1})	$v_{y_{max}}$ (m s^{-1})	$a_{x_{max}}$ (m s^{-2})	$a_{y_{max}}$ (m s^{-2})	$\overline{V_{\Delta x}}$ (m s^{-1})	$\overline{V_{\Delta y}}$ (m s^{-1})	
CBA	0.1±0.05	0.4±0.1	0.03±0.03	0.12±0.03	1±1	3±1	3±2	20±8	
CBB	0.06±0.03	0.15±0.05	0.01±0.02	0.04±0.02	1±1	3±1	5±3	16±6	
CBC*	1.82±0.06	0.35±0.05	0.13±0.03	0.06±0.02	4±1	2±1	-25±16	20±5	

from 40 cm in test CBA to 75 cm in test CBC. In test CBC, the fracture propagated through the whole length of the cantilever beam causing down-slope displacement of the slab. In tests CBA and CBB however, the fracture propagated through the photographed section of the beam without propagating through the whole beam. Therefore, all markers in the field of view were displaced. Furthermore, there was no down-slope displacement of the slab after the weak layer had fractured, and the slope parallel displacement reached a maximum value after the weak layer had fractured. In these tests, the maximum slope parallel displacement (0.1 ± 0.05 cm and 0.06 ± 0.03 cm for CBA and CBB, respectively) was lower than the maximum slope normal displacement (0.4 ± 0.1 cm and 0.15 ± 0.05 cm for CBA and CBB, respectively).

The markers in tests CBA and CBB started moving in both direction simultaneously. In test CBC however, the markers further away from the saw-cut (Marker 5 and 6) were displaced in the slope parallel direction prior to slope normal displacement. As seen in Figure 6.16(b) and (c), Marker 1 started moving in both directions simultaneously, which was not the case for Marker 6. This particular cantilever beam test (CBC) was interesting since the fracture was observed to step from one buried surface hoar weak layer into a second buried surface hoar layer 5 cm below the first one (Figure 6.16 (a)). This phenomenon is sometimes observed at fracture lines where multiple weak layers are present in the snowpack and is commonly referred to as a fracture "stepping down".

In Figure 6.17 the displacements of markers placed above the weak layer in cantilever beam test CBA are shown. Markers were also placed under the weak layer. The displacement of these markers was undetectable. Clearly, there was a retardation between the displacement of markers located up-slope compared to those

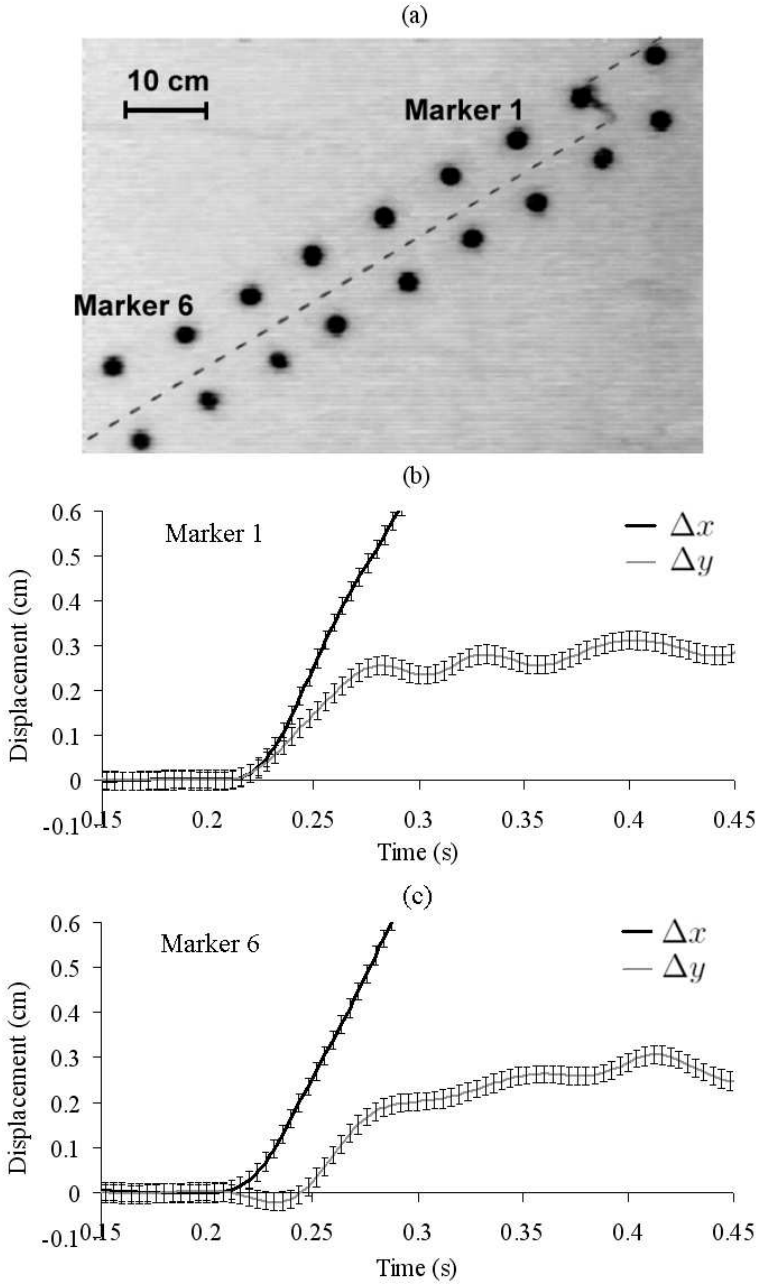

Figure 6.16: *(a) Image of a fracture 'stepping down' from one buried surface hoar layer to a second buried surface hoar layer below it in test CBC. The dashed line indicates where the weak layers were fractured. (b) Seven point moving average displacement measurements from Marker 1. (c) Seven point moving average displacement measurements from Marker 6. Both slope parallel displacement (black) and the slope normal displacement (grey) are shown. The accuracy of the displacement measurements in this test was 0.02 cm.*

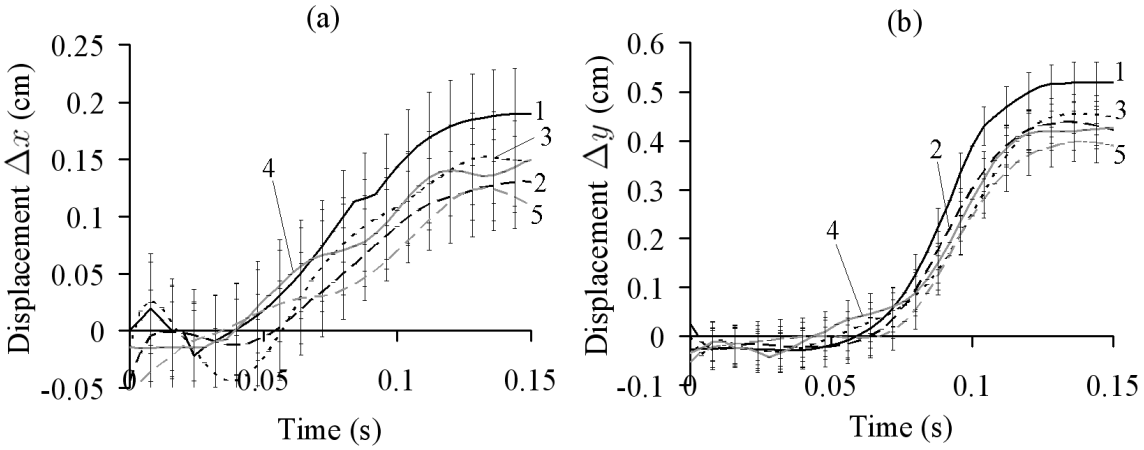

Figure 6.17: *Seven point moving average of the displacement of a row of five markers placed five cm above a buried surface hoar weak layer in cantilever beam test CBA. The marker separation d was five cm. (a) Slope parallel displacement. (b) Slope normal displacement. The accuracy of the displacement measurements for this test was 0.04 cm.*

farther down-slope, as seen in Figure 6.17. Furthermore, the maximum slope normal displacement for Marker 1 (0.52±0.04 cm) was greater than that of Marker 5 (0.40±0.04 cm), indicating that Δy_{max} decreased with the distance from the leading edge of the saw-cut. Similarly, the maximum slope parallel displacement for Marker 1 (0.19±0.04 cm) was greater than that of Marker 5 (0.11±0.04 cm). This was likely due to influences from the saw-cut as the distance between Marker 1 and the leading edge of the saw-cut was approximately 7 cm and the saw that was used for cutting the weak layer was 2 cm thick. Moreover, this behaviour was not observed in tests CBB and CBC, in which the first marker was further away from the edge of the saw-cut.

The fracture speeds calculated from the seven point moving average displacement data of the markers in cantilever beam test CBA are shown in Figure 6.18. The values of $V_{\Delta y_*}$ were relatively constant for Δy_* between 0.04 ($=\epsilon$) and 0.2 cm ($=\frac{1}{2}\Delta y_{max}$).

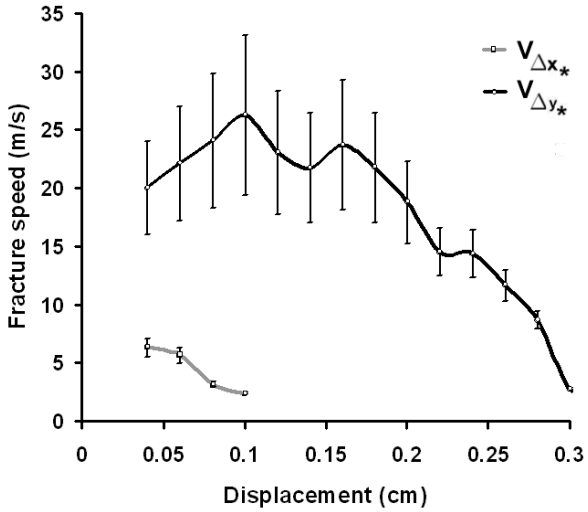

Figure 6.18: *Fracture speed measurements obtained from the seven point moving average displacement shown in Figure 6.17. The accuracy was* $\epsilon = 0.04$ *cm and the maximum displacements after fracture were* Δy_{max}*=0.4±0.1 cm and* Δx_{max}*=0.1±0.05 cm.*

For values of Δy_* larger than 0.2 cm, the calculated fracture speed $V_{\Delta y_*}$ decreased. On the other hand, the fracture speed calculated from the slope parallel displacement was much lower and could only be calculated for a limited range of displacement values. Averaging the values of $V_{\Delta y_*}$ for $0.04 \leq \Delta y_* \leq 0.2$ cm resulted in a fracture speed of $\overline{V_{\Delta y}} = 22 \pm 8$ m s^{-1}, whereas $\overline{V_{\Delta x}} = 4 \pm 2$ m s^{-1} for $0.04 \leq \Delta x_* \leq 0.1$.

The fracture speed calculations from tests CBB and CBC resulted in similar results (Table 6.2), with lower values for $\overline{V_{\Delta x}}$ than for $\overline{V_{\Delta y}}$. However, in test CBC, the slope parallel displacement curves were more closely packed than those shown in Figure 6.17 and initially Marker 6 was displaced before Marker 1, resulting in a highly variable negative fracture speed values (i.e. fracture propagating up-slope?) for small displacements. For larger displacements (i.e. $\Delta x_* > 0.7$ cm) however, the fracture speed was found to be positive.

Finally, the maximum *slope parallel* speed and acceleration of the markers (Table 6.3), calculated from the seven point moving average displacement, was larger in test CBC than in cantilever beam tests CBA and CBB. The maximum *slope normal* speed and acceleration on the other hand, were similar in all cantilever beam tests.

6.3.3 Observations of fractures in rutschblock tests

Fractures in weak snowpack layers, initiated by a skier dynamically loading the snow surface, were observed in nine rutschblock tests (Table 6.4). Only two rutschblock tests, RBA and RBB, were 'standard' rutschblock tests (i.e. 1.5 m by 2 m). All other rutschblock tests were performed with a larger block, typically 3 m by 3 m. The size of the field of view in the rutschblock tests ranged from 45 cm for tests RBA and RBB to 140 cm in test RBI. In RBG, the rutschblock did not slide down-slope after fracture and Δx_{max} in Table 6.4 represents the maximum slope parallel displacement after fracture. In all other tests, the rutschblock did slide down-slope and Δx_{max} represents the slope parallel displacement in the last frame. Furthermore, some rutschblock tests were photographed with two rows of markers inserted in the vertical snow wall above the weak layer. For these tests (RBC, RBD and RBE), measurements from the second row of markers are also shown in Table 6.4.

The maximum slope normal displacement was similar for most photographed fractures in rutschblock tests, except for tests RBE and RBG, in which the fracture was not confined to the weak layer. The maximum slope normal displacement was largest for test RBB (0.51±0.02 cm) and smallest for test RBF (0.15±0.05 cm). In test RBE, the maximum slope normal displacement after fracture increased with the distance from the loading point, ranging from 0.1±0.02 cm to 0.27±0.02 cm.

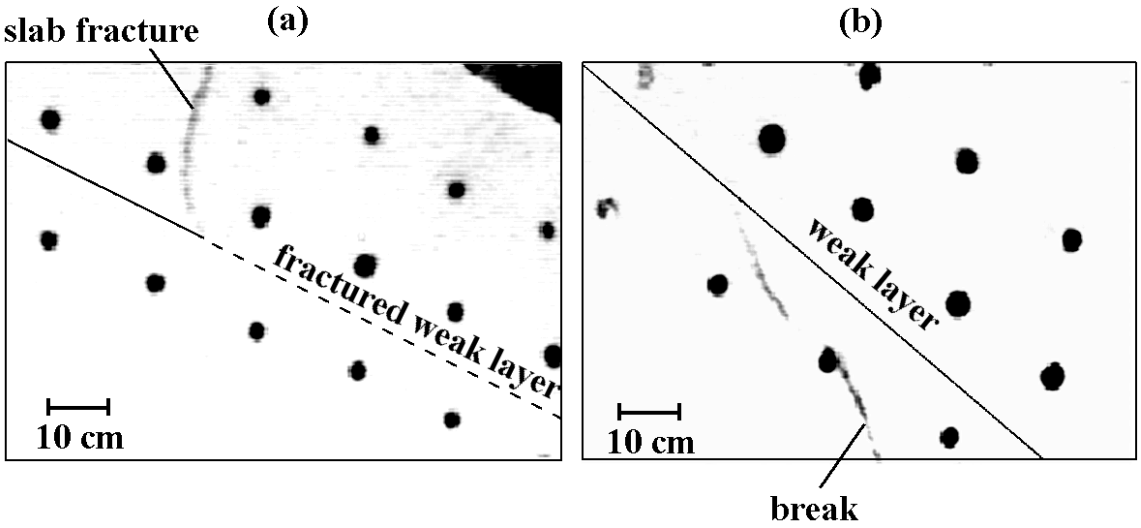

Figure 6.19: *Images of markers at the end of two rutschblock tests (RBE and RBG) in which the fracture was not confined to the weak layer. (a) A fracture through the slab in test RBE below which the weak layer had fractured. The area where the weak layer had fractured is indicated by a dashed line. (b) An irregular fracture in test RBG, classified as a Break, fractured several snowpack layers, without fracturing the primary weak layer.*

Measurements from a second row of markers, placed 10 cm above the first one, resulted in similar results (Table 6.4). In this test, there was a tensile fracture through the slab below which the weak layer had fractured (Figure 6.19 (a)). This fracture was classified as a Resistant Planar fracture and only a part of the rutschblock was displaced. In test RBG, the weak layer did not fracture. However, as seen in Figure 6.19 (b), the skier caused an irregular fracture, which was described as a Break, through various snowpack layers. The slope normal displacement of the markers in this test was negative, indicating that the rutschblock was displaced upwards as the rutschblock slid over the irregular fracture surface.

The displacements from the row of markers closest to the weak layer in test RBD is shown in Figure 6.20. The displacements of the markers were different in the

Table 6.4: *Measurements from photographed fractures in rutschblock tests (RB). Notations as in Table 6.3. Test RBF and RBG were each performed on a 'weak interface' (inter). Tests in which the slab moved down-slope after fracture are marked with an asterisk.*

Snowpack conditions and experimental parameters									
Test	ψ	Char	F	Th (cm)	D (cm)	ρ_{slab} (kg m^{-3})	ϵ (cm)	N	d (cm)
RBA*	19	SP	SH	1.5	69	213	0.03	5	5
RBB*	21	SP	SH	1.5	69	213	0.01	5	5
RBC*	37	SP	FC	0.4	53	105	0.03	5 and 2	20 and 40
RBD*	40	SP	SH	0.8	90	158	0.02	5 and 3	10 and 10
RBE*	24	RP	FC	0.4	53	105	0.02	3 and 2	20 and 40
RBF*	33	SP	DF	inter	72	103	0.03	2	20
RBG	37	B	DF	inter	72	103	0.03	3	20
RBH*	40	SP	SH	1.5	36	113	0.1	4	20
RBI*	42	SP	SH	1.5	36	113	0.1	5	20

Motion data								
Test	Δx_{max} (cm)	Δy_{max} (cm)	$v_{x_{max}}$ (m s^{-1})	$v_{y_{max}}$ (m s^{-1})	$a_{x_{max}}$ (m s^{-2})	$a_{y_{max}}$ (m s^{-2})	$\overline{V_{\Delta x}}$ (m s^{-1})	$\overline{V_{\Delta y}}$ (m s^{-1})
RBA*	1.97±0.03	0.33±0.03	0.27±0.03	0.08±0.02	4±1	3±1	18±14	19±7
RBB*	3.06±0.05	0.51±0.02	0.29±0.03	0.1±0.03	5±1	4±1	2±5	26±7
RBC*	7.8±0.1	0.29±0.04	0.41±0.03	0.07±0.03	6±1	3±1	30±18	17±4
	7.8±0.1	0.27±0.04	0.41±0.03	0.06±0.03	5±1	2±1	-	-
RBD*	3.2±0.1	0.29±0.05	0.22±0.03	0.05±0.02	2±1	2±1	40±13	23±5
	3.3±0.1	0.28±0.06	0.21±0.03	0.05±0.02	2±1	2±1	21±15	23±4
RBE*	2.3±0.1	0.1 to 0.27	0.22±0.03	0.04±0.02	5±1	1±1	-	-
	2.3±0.1	0.14 to 0.24	0.21±0.03	0.04±0.02	6±1	2±1	-	-
RBF*	3.3±0.1	0.12±0.05	0.42±0.02	0.07±0.02	6±1	3±1	-	-
RBG	0.21±0.03	-0.9±0.1	0.11±0.03	-0.09±0.02	6±1	-2±1	-	-
RBH*	3.5±0.1	0.5±0.1	-	-	-	-	-	-
RBI*	5.2±0.1	0.4±0.1	-	-	-	-	-	-

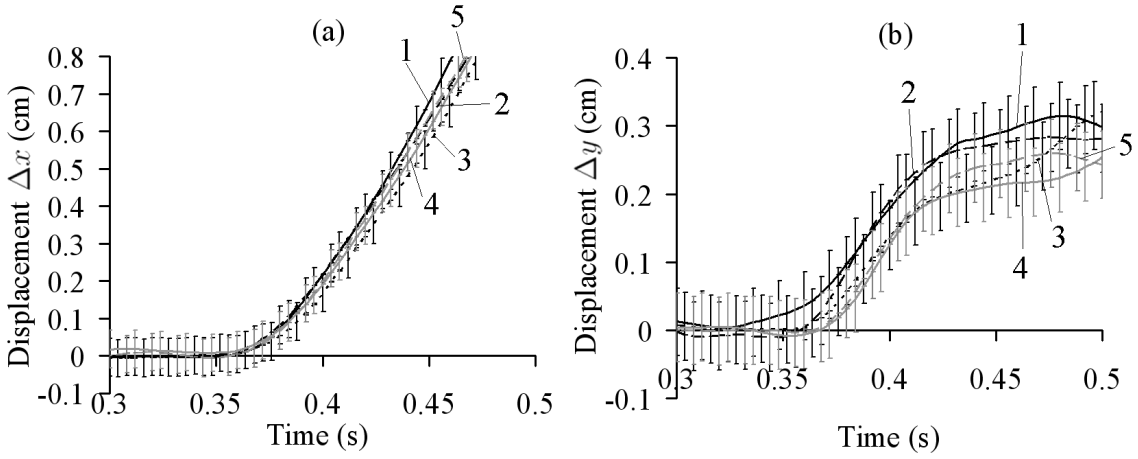

Figure 6.20: *Seven point moving average displacement of a row of five markers placed five cm above a buried surface hoar weak layer in rutschblock test RBD. The Marker separation d was 10 cm. (a) Slope parallel displacement. (b) Slope normal displacement. The accuracy of the displacement measurements for this test was 0.05 cm.*

slope parallel and slope normal directions. As seen in Figure 6.20, Δx increased with time as the rutschblock moved down-slope, whereas Δy reached a maximum value of 0.3±0.1 after the weak layer had fractured. Furthermore, the markers were observed to start moving in both the slope parallel and the slope normal direction simultaneously. This was also observed in rutschblock tests RBA, RBB and RBG. However, in tests RBE, RBF, RBH and RBI, the markers were observed to start moving in the slope parallel direction first. Finally, in rutschblock test RBC, some markers were observed to start moving in both directions simultaneously, while others started moving in the slope parallel direction first.

In all rutschblock tests, the maximum slope parallel speed of the markers was larger than the maximum slope normal speed (Table 6.4). Similarly, the maximum slope parallel acceleration of the markers was larger than $a_{y_{max}}$, except for test RBD. For this rutschblock test, $a_{x_{max}}$ and $a_{y_{max}}$ were similar and these maximum values

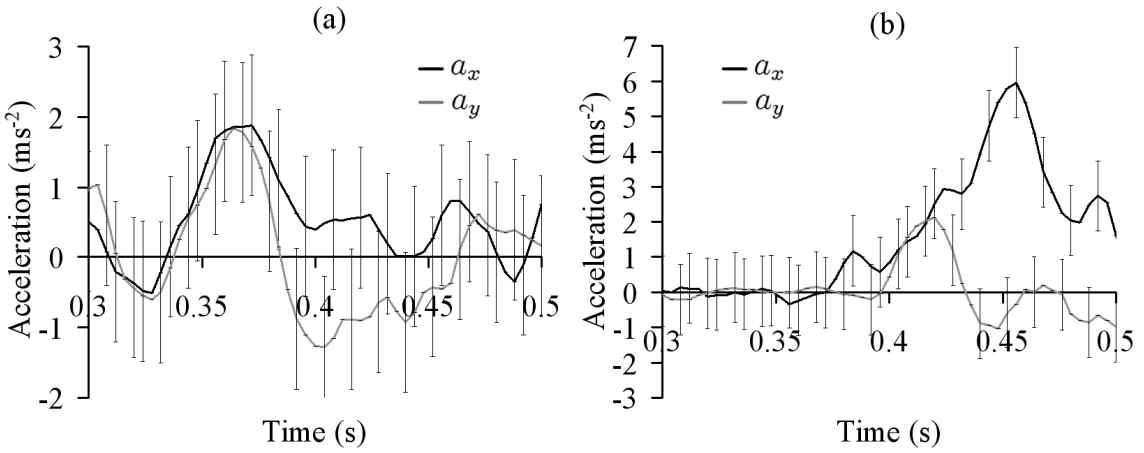

Figure 6.21: *Marker acceleration in the slope parallel (a_x) and slope normal direction (a_y) for: (a) Marker 2 in rutschblock RBD and (b) Marker 2 in rutschblock RBC.*

were reached at approximately the same time. Thereafter, the acceleration in the slope normal direction decreased more rapidly than a_x (Figure 6.21 (a)). In all other rutschblock tests however, the maximum slope parallel acceleration was reached after the maximum slope normal acceleration, as is shown for Marker 2 in rutschblock test RBC in Figure 6.21 (b).

Fracture speed measurements were obtained from four photographed fractures in rutschblock tests (RBA-RBD) in which the fracture propagated through the whole length of the weak layer and the block released (Table 6.4). Three other photographed rutschblock tests (RBF, RBH and RBI) also resulted in the release of the block after fracture. However, it was not possible to calculate the fracture speed for these tests. Only two markers in the field of view of test RBF were displaced, not allowing for reliable fracture speed calculations. For both tests RBH and RBI, the static horizontal noise bands in the digitized images were much more pronounced than usual. The scatter in the displacement data during movement of the markers

was therefore much larger than usual, making fracture speed calculations, as well as marker speed and acceleration calculations, highly variable and unreliable. These two tests were performed on the same day. Finally, two fractures in tests RBE and RBG did not result in fracture speed estimates because the fractures were not confined to the weak layer, as described earlier.

The fracture speed calculations obtained from the seven point moving average displacement data of both rows of markers placed above the weak layer in rutschblock test RBD are shown in Figure 6.22. The values of $V_{\Delta y_*}$ from both rows of markers were relatively constant for Δy_* between 0.02 ($=\epsilon$) and 0.15 cm ($=\frac{1}{2}\Delta y_{max}$). For values of Δy_* larger than 0.15 cm, the calculated fracture speed $V_{\Delta y_*}$ decreased. On the other hand, the fracture speed calculated from the slope parallel displacement was much more variable and different for both rows of markers. Averaging the values of $V_{\Delta y_*}$ for $0.02 \leq \Delta y_* \leq 0.15$ cm resulted in a fracture speed of $\overline{V_{\Delta y}} = 23 \pm 5$ m s^{-1} for the first row and 23$\pm$4 m s^{-1} for the second row of markers, whereas the calculated $\overline{V_{\Delta x}}$ was 40$\pm$13 m s^{-1} and 22$\pm$13 m s^{-1} for the first and second rows of markers for $0.02 \leq \Delta x_* \leq 0.15$.

The calculated fracture speed values $\overline{V_{\Delta y}}$ shown in Table 6.4 for all four rutschblock tests ranged from 26$\pm$7 m s^{-1} for test RBB to 17$\pm$4 m s^{-1} for RBC. On the other hand, the fracture speed values obtained from the slope parallel displacement were more variable, ranging from 2$\pm$5 m s^{-1} for test RBB to 31$\pm$15 m s^{-1} for test RBD. Furthermore, the calculated value of $\overline{V_{\Delta y}}$ was identical for both rows of markers in test RBD (23$\pm$5 m s^{-1} and 23$\pm$4 m s^{-1}, respectively), whereas $\overline{V_{\Delta x}}$ was not (40$\pm$13 m s^{-1} and 22$\pm$15 m s^{-1}, respectively). Finally, as mentioned earlier, the values of $\overline{V_{\Delta y}}$ were not significantly affected by the data filtering, whereas the values of $\overline{V_{\Delta x}}$

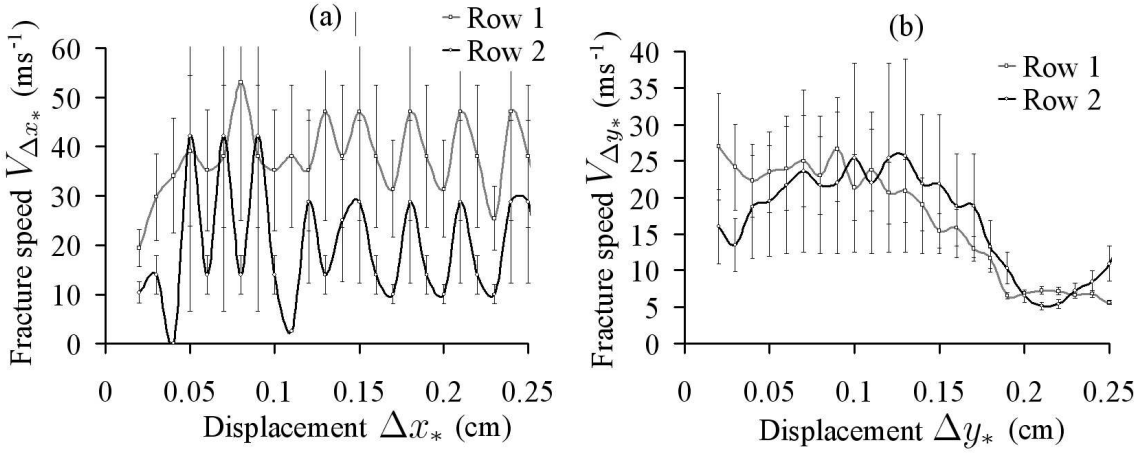

Figure 6.22: *Fracture speed obtained from the seven point moving average displacement measurement from two rows of markers placed above the weak layer in test RBD. Row 1 (gray) was closest to the weak layer (5 cm above) and Row 2 (black) was 10 cm above Row 1. (a) Fracture speed obtained from the slope parallel displacement. (b) Fracture speed obtained from the slope normal displacement. The accuracy of the displacement measurements for this test was 0.02 cm and Δy_{max} was approximately 0.3 cm.*

varied more significantly with increased filtering.

6.3.4 Observations of fractures on skier-tested slopes

Fractures initiated by a rapidly moving skier were photographed on six skier-tested slopes (Table 6.5). The horizontal length of the field of view ranged from 120 cm for test STD to 240 cm for test STB and was larger than in the previously described tests, resulting in generally lower accuracies for the displacement measurements. Three of these skier-tested slopes (STA, STB and STC) did not release a slab avalanche and Δx_{max} in Table 6.4 represents the maximum slope parallel displacement after fracture. On skier-tested slopes STD, STE and STF however, the slab was skier-triggered and Δx_{max} represents the slope parallel displacement in the last frame.

Table 6.5: *Measurements from photographed fractures on skier-tested slopes (ST). Notations as in Table 6.3. Tests in which the slope was skier-triggered are marked with an asterisk.*

Snowpack conditions and experimental parameters									
Test	ψ	Char	F	Th (cm)	D (cm)	ρ_{slab} (kg m^{-3})	ϵ (cm)	N	d (cm)
STA	34	SP	SH	2	62	105	0.1	6	20
STB	31	SP	SH	1.3	69	136	0.1	2	20
STC	41	SP	FC	0.4	39	118	0.06	3 and 3	20 and 20
STD*	32	SP	SH	2.1	49	175	0.05	5	20
STE*	33	SC	DH	5 to 10	42	212	0.06	5 and 4	20 and 20
STF*	44	SP	SH	0.8	94	132	0.08	5	20

Motion data								
Test	Δx_{max} (cm)	Δy_{max} (cm)	$v_{x_{max}}$ (m s^{-1})	$v_{y_{max}}$ (m s^{-1})	$a_{x_{max}}$ (m s^{-2})	$a_{y_{max}}$ (m s^{-2})	$\overline{V_{\Delta x}}$ (m s^{-1})	$\overline{V_{\Delta y}}$ (m s^{-1})
STA	9.6 to 0.3	2.3 to 0.2	-	-	-	-	-	-
STB	7.4 to 4.8	0.3±0.1	-	-	-	-	-	-
STC	3±0.1	0.41±0.06	0.17±0.02	0.07±0.02	5±1	3±1	51±16	21±9
	2.2±0.1	0.33±0.06	0.12±0.02	0.06±0.02	3±1	3±1	21±7	23±8
STD*	4.2±0.1	0.5±0.1	0.41±0.02	0.08±0.02	4±1	3±1	21±8	21±6
STE*	3.6±0.1	1.1±0.1	0.33±0.02	0.15±0.02	5±1	5±1	33±20	25±4
	3.6±0.1	1.2±0.2	0.32±0.02	0.16±0.02	5±1	4±1	-53±40	23±5
STF*	3.6±0.1	0.4±0.1	0.17±0.02	0.09±0.02	5±1	3±1	30±7	21±8

Furthermore, on two skier-tested slopes (STC and STE), two rows of markers were inserted in the vertical snow wall above the weak layer. Measurements from both rows of markers are shown in Table 6.5 for these tests. As before, the maximum speed and acceleration of the markers in both directions were also calculated. However, due to the lower accuracy of the displacement measurement in these tests, the trends in the acceleration were less distinct.

Skier-tested slopes that were not skier-triggered

Images from three skier-tested slopes that did not release a slab avalanche (STA, STB and STC) showed that the skier fractured the weak layer as he pressed down on his skis while attempting to trigger the slab. These observations clearly show that a skier can fracture a weak layer without releasing a slab avalanche.

The seven point moving average displacement measurements of the markers in test STA are shown in Figure 6.23. The quality of the images was compromised by uneven illumination, resulting in an accuracy of only 1 mm, making marker speed and acceleration calculations impossible. This was also the case for test STB, which was performed on the same day as test STA. Markers 1 to 6 were displaced by the skier, whereas Markers 7 and 8 did not move. The distance over which the weak layer was fractured in test STA was estimated from photos as being 3±0.2 m. Markers placed under the weak layer did not exhibit any detectable displacement.

The displacement of the markers in test STA are shown in Figure 6.23. Marker 1 was the closest to the skier's skis (approximately 70 cm) and both Δx and Δy were the greatest for this marker: 9.6±0.1 cm and 2.5±0.1 cm, respectively. Furthermore, the displacement of the markers decreased with the distance from the skier (Figure

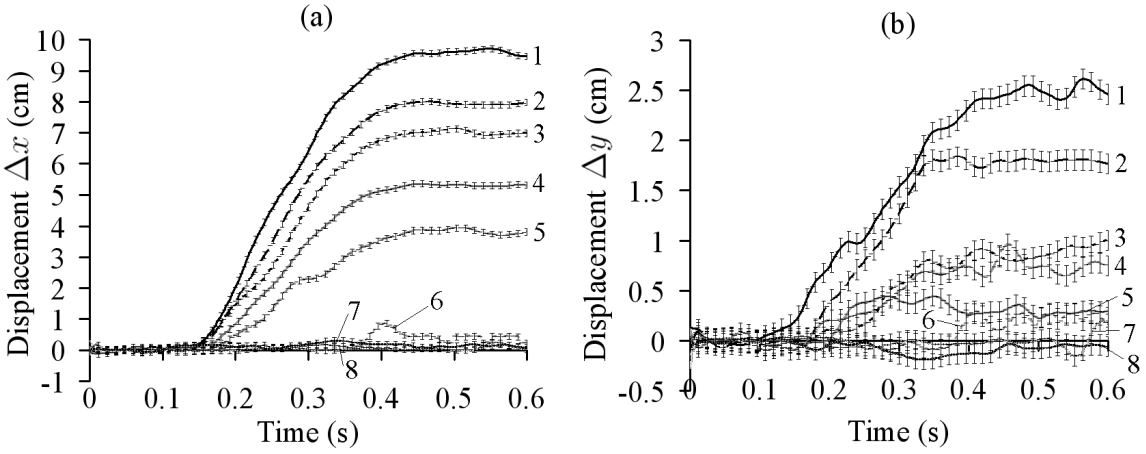

Figure 6.23: *Seven point moving average displacement of markers placed 5 cm above a buried surface hoar weak layer on a skier-tested slope that did not release a slab avalanche (STA). The Marker separation d was 20 cm and Marker 1 was closest to the skier (approximately 70 cm). (a) Slope parallel displacement. (b) Slope normal displacement. The accuracy of the displacement measurements for this test was 0.1 cm.*

6.23). The slope parallel displacement ranged from 9.6±0.1 cm to 0.3±0.1 cm and the slope normal displacement ranged from 2.5±0.1 cm to 0.2±0.1 cm for Marker 1 and Marker 6, respectively. Finally, Markers 2, 3 and 4 were observed to start moving in the slope parallel direction first whereas Markers 1, 5 and 6 started moving in both directions simultaneously.

The initial slope parallel distance between Marker 1 and Marker 6 was 100±1 cm, leading to a slope parallel strain of 9.3±0.1 %. As seen in Figure 6.23, the markers were in motion for 0.25±0.05 s, resulting in an approximate slope parallel strain rate of 0.37±0.06 s^{-1}, well within the brittle range (e.g. Narita, 1980). Furthermore, approximately slope normal compressive fractures were observed in the video as the slab was compacted.

Similar results were found for test STB. However, for this test only two markers in

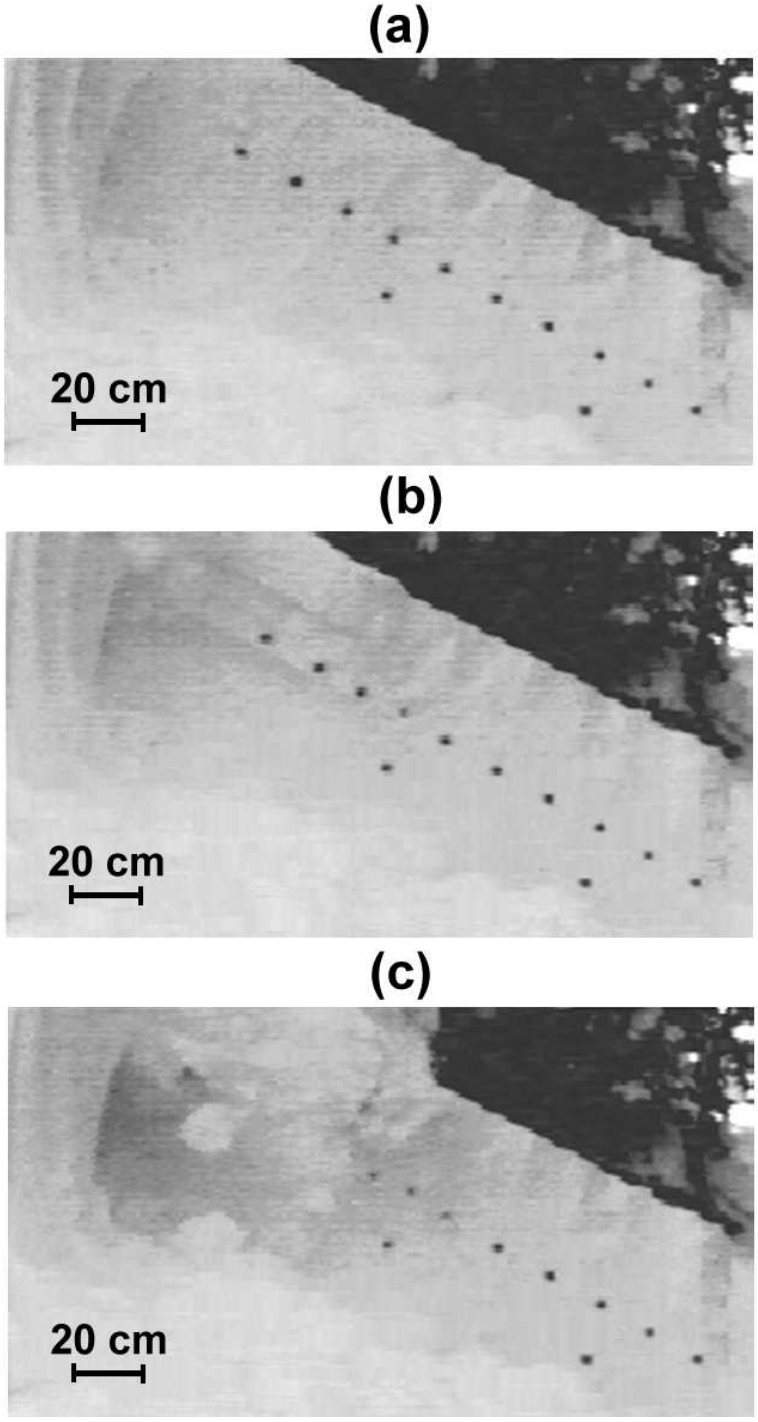

Figure 6.24: *Three images of the markers placed above a buried surface hoar weak layer on skier-tested slope STB. This slope did not release a slab avalanche. (a) Image prior to testing the slope. (b) Image showing fractures induced by the skier in the slab and a fracture in the weak layer below the row of markers. (c) Snow from the skier obscured the markers soon after the markers started moving.*

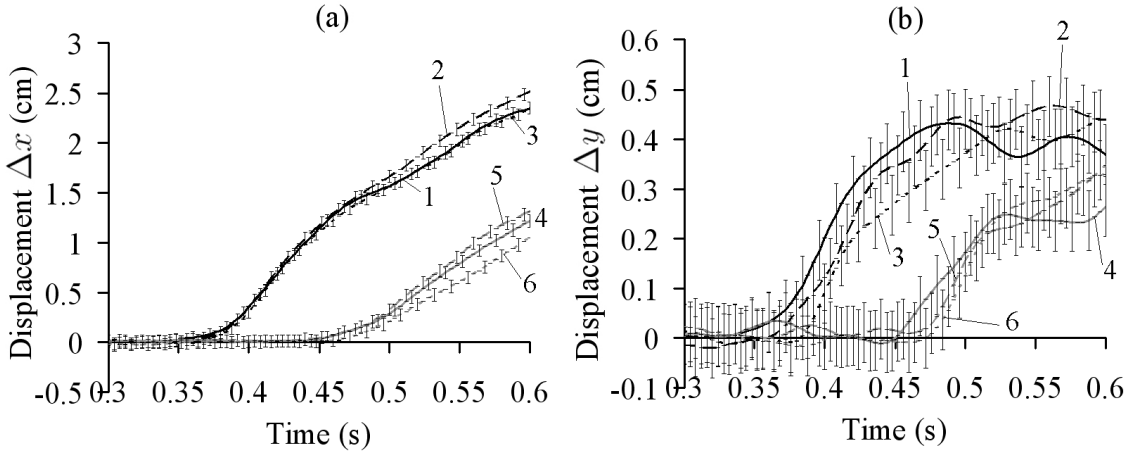

Figure 6.25: *Seven point moving average displacement of markers placed 5 cm above a buried surface hoar weak layer on a skier-tested slope that did not release a slab avalanche (STC). The Marker separation d was 20 cm and Marker 1 was closest to the skier. (a) Slope parallel displacement. (b) Slope normal displacement. The accuracy of the displacement measurements for this test was 0.06 cm.*

the field of view were displaced, and these could only be tracked over a short period of time as snow from the skier obscured the view of the markers soon after the markers had started moving (Figure 6.24 (c)). Nonetheless, the slope parallel displacement of the marker closest to the skier (approximately 120 cm) was larger than that of the second marker further away from the skier (Table 6.5). The slope parallel strain rate was calculated to be $0.65 \pm 0.06\ s^{-1}$. On the other hand, there was no significant difference in the slope normal displacement of the two markers. Furthermore, the markers were observed to start moving in the slope parallel direction first. As can be seen in Figure 6.24 (b), there was a fracture in the slab parallel to the fracture in the weak layer, probably at a weak interface in the slab. Furthermore, a compressive fracture through the slab was also observed in the video and the weak layer was not fractured beyond this compressive fracture through the slab.

The displacements of the markers on the third skier-tested slope that did not

release a slab avalanche (STC) were much different. For this test, the displacement of the markers was not affected by the distance to the skier. As seen in Figure 6.25, the first three markers were displaced approximately 0.1 s before the last three markers. Furthermore, all the markers were displaced in both directions simultaneously. The images clearly show that initially only part of the slab was displaced (Markers 1 to 3). A compressive fracture through the slab was observed in the video between Markers 3 and 4, after which the second part of the slab was displaced as well (Markers 4 to 6). Measurements from the first three markers are shown separately from those from the last three markers in Table 6.5. The maximum slope normal displacement for the first three markers (0.41±0.06 cm) was somewhat larger than that of the last three markers (0.33±0.06 cm).

Skier-triggered slopes

Three slopes that were skier-tested resulted in the release of a slab avalanche (STD, STE and STF). For test STD, a small slab avalanche was initiated above the crown of a recently skier-triggered slab avalanche and the propagating fracture was photographed. For test STE, a small slab avalanche was initiated on slope with a weak layer consisting of depth hoar crystals at the base of the snowpack. This layer was variable in thickness, ranging from 5 to 10 cm (Table 6.5). For test STF, a slab avalanche was initiated while isolating a block of snow for a large rutschblock test. A field worker was using a saw to isolate the upper section of a large rutschblock, which had only been dug out on the side of the camera, when the slab avalanche was initiated. The fracture in the weak layer propagated over a considerable distance (approximately 70 m), releasing a medium sized slab avalanche (Size 2.5).

The displacements of the markers in test STF are shown in Figure 6.26. Again, the slope normal displacement reached a maximum value after the weak layer had fractured, whereas the slope parallel displacement increased as the slab moved down-slope. The maximum slope normal displacement of the markers was 0.4±0.1 cm. This was similar to the maximum slope normal displacement in test STD (Table 6.5). On the other hand, Δy_{max} for the markers in test STE was much larger (1.1±0.1 cm and 1.2±0.2 cm for the first and the second row of markers, respectively). Furthermore, on these three skier-triggered slopes most markers were observed to start moving in both directions simultaneously, while some started moving in the slope parallel direction first. Finally, on all skier-triggered slopes, the maximum slope parallel speed of the markers was larger than the maximum slope normal speed (Table 6.5), as the slab moved down-slope after the weak layer had fractured. The maximum slope parallel acceleration of the markers was generally equal or larger than $a_{y_{max}}$.

The calculated fracture speed values $\overline{V_{\Delta y}}$ from the three skier-triggered slab avalanches were similar, ranging from 21±6 m s^{-1} for test STD to 25±4 m s^{-1} for STE. On the other hand, the fracture speed values obtained from the slope parallel displacement were more variable and had a larger measurement uncertainty. For test STE, the values of $\overline{V_{\Delta y}}$ calculated from both the rows of markers were very similar, whereas the values of $\overline{V_{\Delta x}}$ were not (Table 6.5). Furthermore, as mentioned before, the values of $\overline{V_{\Delta y}}$ were not significantly affected by the data filtering, whereas the values of $\overline{V_{\Delta x}}$ varied more significantly with increased filtering, indicating that the $\overline{V_{\Delta y}}$ values were more reliable. Fracture speed calculations from skier-tested slope STC (Table 6.5) also resulted in values of $\overline{V_{\Delta y}}$ similar to those from the skier-triggered

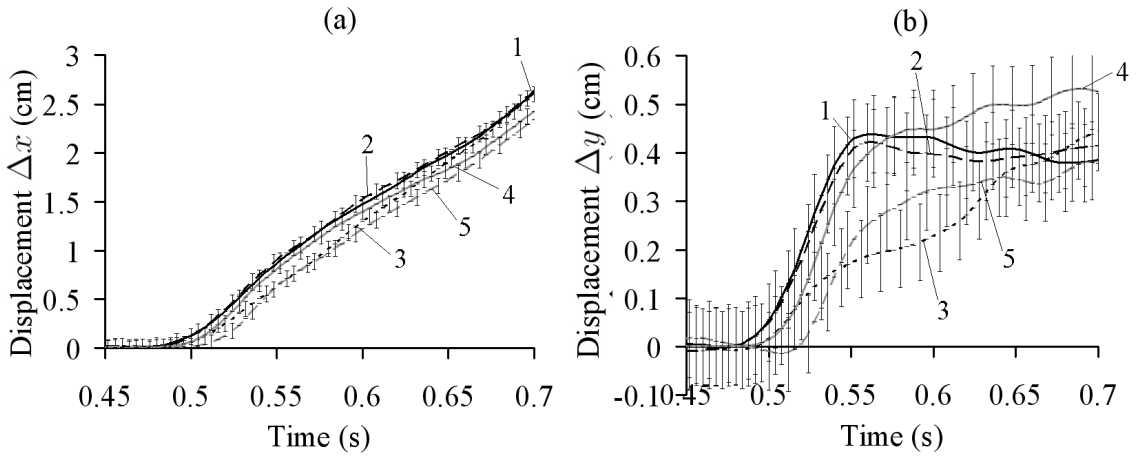

Figure 6.26: *Seven point moving average displacement of markers placed 5 cm above a buried surface hoar weak layer on a skier-tested slope that did release a slab avalanche (STF). The Marker separation d was 20 cm. (a) Slope parallel displacement. (b) Slope normal displacement. The accuracy of the displacement measurements for this test was 0.08 cm.*

slab avalanches.

6.3.5 Fracture speed estimates from avalanche videos

Fracture speed calculations were obtained from eleven videos of slab avalanches recorded with a standard video camera (Table 6.6) at 30 frames per second. These videos originated from a documentary which aired in 1997 on the Discovery Channel (Raging Planet - Avalanche; AV6, AV7 and AV8), an avalanche education video by Bruce Tremper of the Forest Service Utah Avalanche Forecast Center published in 1994 (Winning the avalanche game; AV3, AV4 and AV5), from videos shot by the avalanche control crew at Glacier National Park during artillery avalanche control (AV9, AV10 and AV11) and from University of Calgary research staff (AV1 and AV2). Four of these slab avalanches were skier-triggered (AV1, AV2, AV3 and AV4). All other slab avalanches were initiated by an explosive charge. In order to calculate

Table 6.6: *Calculated fracture speed (V) from videos of slab avalanches recorded with a standard video camera. The trigger of the slab avalanche is given, as well as the distance between the trigger point and the stauchwall. In video AV5, four distinct stauchwalls appeared (see Figure 6.27) leading to four fracture speed values.*

Video	Trigger		Distance (m)	V (m s^{-1})
AV1	Skier		5±0.25	15±6
AV2	Skier		5.25±0.25	17±8
AV3	Skier		6±0.5	16±7
AV4	Skier		8±1	20±8
AV5	Explosive	1	56±23	27±13
		2	90±45	28±14
		3	88±44	27±13
		4	104±52	23±12
AV6	Explosive		50±25	19±9
AV7	Explosive		26±3	32±10
AV8	Explosive		26±13	17±8
AV9	Explosive		64±32	19±9
AV10	Explosive		35±17	16±8
AV11	Explosive		54±27	26±13

fracture speed from these videos, several quantities had to be estimated: the time of fracture initiation, the time at which the fracture had propagated to a location where a perimeter fracture (visible at the surface) was apparent and a scaling factor for the images.

First, the time at which the fracture initiated was estimated. For avalanches initiated by explosives, this was fairly straightforward. The explosion was always associated with a dust cloud (Figure 6.27), and the time of fracture initiation, assumed to be the time when the explosive charge detonated, was estimated within an accuracy of ± 1 frame (i.e. ± 0.03 s). For skier-triggered slab avalanches on the other hand, it was more difficult to determine the time at which the fracture was

initiated. However, in all cases the skier jumped on the snow surface to release the slab avalanche. The time at which the skier's skis came in contact with the snow surface was assumed the time at which the fracture was initiated. It was estimated within an accuracy of ± 3 frames (i.e. ± 0.1 s).

Second, the time at which the fracture had propagated through the whole weak layer and the slab avalanche released was determined. The first signs of the slab avalanche sliding down-slope were generally at the stauchwall (see Section 1.2) and was estimated within an accuracy of ± 5 frames. However, for the skier-triggered slab avalanches, the field of view was generally much smaller, allowing for more detailed images, and the time at which the fracture had propagated through the whole weak layer was estimated within an accuracy of ± 3 frames.

Finally, an object was used to scale the images. For skier-triggered avalanches, the skier was used as a scaling object. The height of the skier was assumed to be 1.75±0.25 m. Similarly, for video AV7 (Table 6.6) a person was used as a scaling object. However, for the other slab avalanches initiated by explosives, the dust cloud emanating from the explosion was used as a scaling reference. The height of the plume was assumed to be 10±5 m, a value obtained from video AV7. The scaling object was used to calculate the distance from the trigger point (i.e. skier or explosive) to the stauchwall, which in turn was used to calculate the fracture speed.

Figure 6.27 shows a sequence of images from video AV5 in which the detonation of an explosive charge led to the release of a slab avalanche. Since the avalanche was triggered by an explosive, the time of fracture initiation was assumed to be the time at which the explosive charge detonated (Figure 6.27 (a)). As the fracture propagated through the weak layer, four distinct stauchwalls appeared at three different times

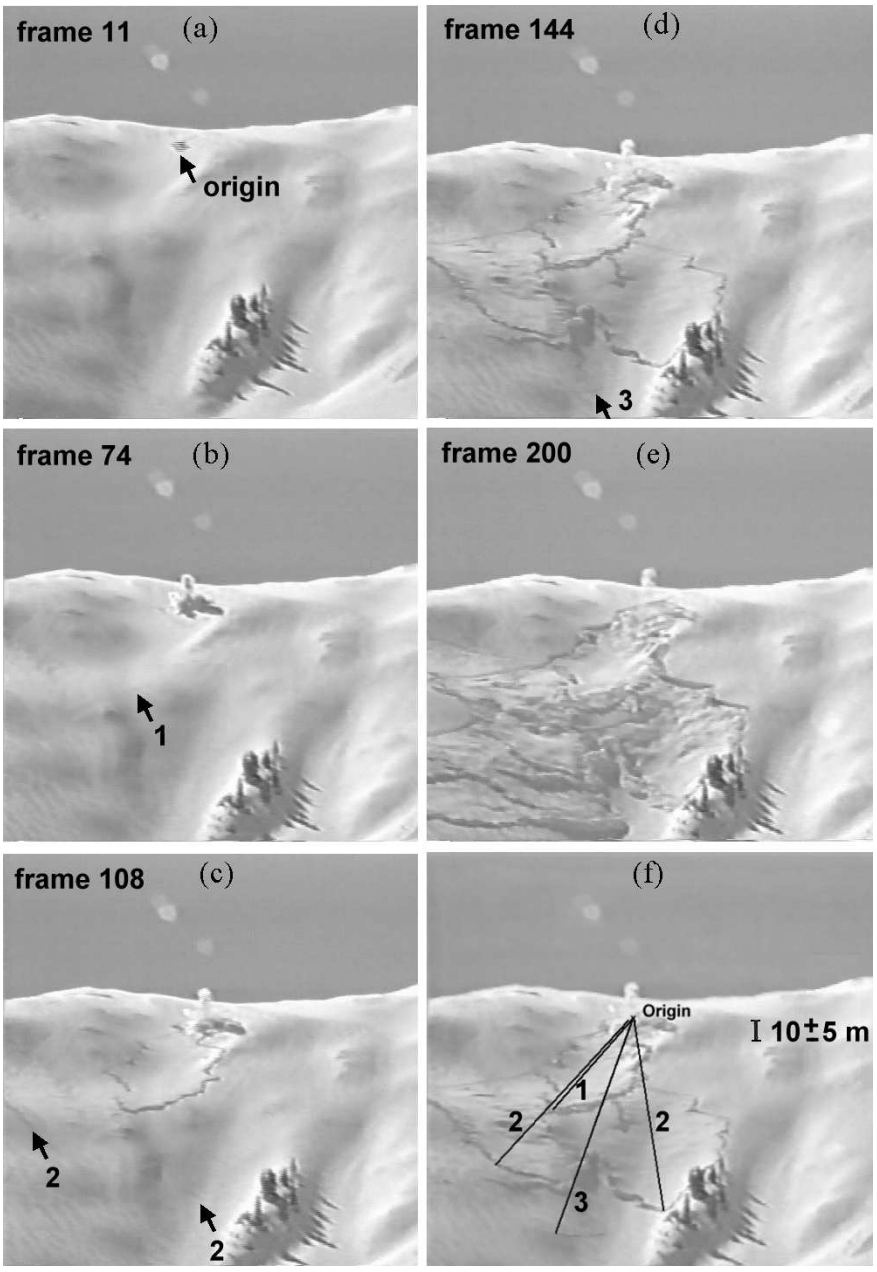

Figure 6.27: *Sequence of images from video AV5 showing the initiation of a slab avalanche by the detonation of an explosive charge. The images were recorded at a frame rate of 30 frames per second (digitized from educational avalanche video with permission of photographer: Winning the avalanche game, 1994). (a) First sign of the explosion. (b) First sign of the first stauchwall (1). (c) First sign of two additional stauchwalls (2). (d) First sign of the lowest stauchwall (3). (e) The cohesive slab breaks up and moves down-slope. (f) The size of the dust cloud was used to scale the distance between the trigger point and the various stauchwalls.*

(Figure 6.27 (b), (c) and (d)) resulting in the release of a large slab avalanche (Figure 6.27 (e)). The dust cloud emanating from the explosion was used as a scaling object to determine the distance between the trigger point and the various stauchwalls (Figure 6.27 (f)). The distance between the trigger point and the lower stauchwall was estimated to be 104±52 m (Table 6.6), which is a realistic value for a large slab avalanche. As can be seen in Table 6.6, the calculated fracture speeds for this video were 27±13 m s^{-1}, 28±14 m s^{-1}, 27±13 m s^{-1} and 23±12 m s^{-1}, respectively.

The fracture speed estimates obtained from the videos of slab avalanches, as well as the distance between the trigger point and the stauchwall, are shown in Table 6.6. The slab avalanches initiated by skiers were much smaller than the avalanches triggered with explosives. Nevertheless, all fracture speed estimates were similar, ranging from 15±6 m s^{-1} to 32±10 m s^{-1} for video AV1 and AV7, respectively. Obviously, these fracture speed calculations are only rough estimates. Furthermore, no information on slab properties or weak layer properties were available.

6.4 Discussion

6.4.1 Displacement, velocity and acceleration

Displacement measurements were obtained from photography of fractures in weak snowpack layers with black markers in the snow above the weak layer. In order to obtain marker velocity and acceleration, seven-point moving average displacement data were used. However, the data filtering affected the values of the calculated velocity and acceleration of the markers (Section 6.2.7). These effects were more pronounced for the calculated marker acceleration. The absolute values of the marker

velocity and especially the marker acceleration should therefore not be considered very accurate.

In most tests the slab moved down-slope after the weak layer fractured. The slope parallel displacement caused by the down-slope slab movement could not be separated from the displacement caused by the fracturing of the weak layer. The maximum slope parallel displacement was therefore primarily affected by the length of the video, as Δx increased with time (e.g. Figure 6.26), and of limited interest. For all tests in which the slab moved down-slope Δx_{max} was larger than Δy_{max}.

The slope parallel marker speed as well as the slope parallel marker acceleration reached a maximum value within the length of the video (e.g. Figure 6.14 and Figure 6.21) and were therefore not affected by the length of the video. Nonetheless, the maximum slope parallel marker speed and acceleration were mainly determined by the motion of the slab after the weak layer had fractured. In cantilever beam test CBA and CBB, $v_{x_{max}}$ and $a_{x_{max}}$ were much lower than $v_{y_{max}}$ and $a_{y_{max}}$ (Table 6.3). However, in rutschblock test RBA and RBB, performed on the same slope and on the same day, both $v_{x_{max}}$ and $a_{x_{max}}$ were larger than $v_{y_{max}}$ and $a_{y_{max}}$ (Table 6.4). The main difference between these tests, apart from the obvious difference in loading method, was that in both test RBA and RBB the slab moved down-slope after fracture, which was not the case for CBA and CBB. Furthermore, in all other tests in which the slab above the weak layer slid down-slope $v_{x_{max}}$ was larger than $v_{y_{max}}$ and $a_{x_{max}}$ was equal or larger than $a_{y_{max}}$. Therefore, the slope parallel speed and acceleration relate to the slab moving down-slope and hold little information about the initial fracture propagating through the weak layer.

Photography of different types of fractures in field tests has shown that fracturing

of a weak layer caused slope parallel and slope normal displacement of the overlying slab. The amount of slope parallel displacement at the time of fracture appeared to be dependent on slope angle since markers in a compression test performed on a level study site (CTA) did not display any detectable slope parallel displacement. On the other hand, markers in cantilever beam tests on a 20^{0} slope (CBA and CBB), where the fracture propagated approximately 0.5 m without releasing the overlying slab, were displaced in both directions simultaneously. Furthermore, Δy was larger than Δx, by about a factor of 3 (Table 6.3). This is consistent with the idea of free fall motion of the slab during fracture, in which case the slope parallel displacement during fracture is equal to $\Delta y \tan \psi$. For tests CBA and CBB, the slope angle was 20^{o}, hence $\Delta x = \Delta y \tan 20 \approx 0.36 \Delta y$, in good agreement with the displacement values shown in Table 6.3. The maximum slope parallel speed and acceleration were also 1/3 the maximum slope normal speed and acceleration. However, only three observations were available since in all other tests the slab slid down-slope after fracture.

Results from cantilever beam tests (CBA, CBB and CBC) showed that the slope normal displacement was caused by the fracture of the weak layer and not by compaction of the snow due to external loading on the snow surface, since in cantilever beam tests no external load was applied on the slab. The weak layer fractured due to stress concentration at the edge of the saw-cut caused by the weight of the unsupported slab. Therefore, the trajectories of the markers only reflect the response of the slab to the propagating fracture. Slope normal displacement was observed in all cantilever beam tests, and was similar to that in other field tests. Furthermore, displacement measurements from tests with two rows of markers in the snow above

the weak layer (RBC, RBD, RBE and STE) showed that there was no detectable difference in the maximum slope normal displacement of both rows of markers. This indicates that there was no snow compaction in the slab between the rows of markers, and the slope normal displacement was entirely caused by the fracture in the weak layer.

Slope normal displacement was observed in all fractures, regardless of slope angle or fracture character. It was greatest for Sudden Collapse fractures (CTB, CTC, CTD and STE), for which Δy_{max} ranged from 1.1±0.1 cm (STE) to 1.7±0.1 cm (CTB). This is consistent with the definition of SC fractures (Table 3.4). However, most fractures were classified as Sudden Planar fractures. The maximum slope normal displacement of these fractures ranged from 0.15±0.05 cm (CBB and RBF) to 0.51±0.02 cm (RBB). Based on these limited data, it can be concluded that a fracture classified as Sudden Collapse typically results in slope normal displacement of the overlying slab of $\Delta y_{max} > 1$ cm.

The majority of the SP fractures were in buried surface hoar weak layers and a thin weak layer of faceted crystals, which had a layer thickness sufficiently large to account for the amount of collapse. In rutschblock test RBF however, a weak interface fractured. Weak interfaces are different from weak layers in that the weakness is an interface between two relatively thick snowpack layers and has no detectable thickness. Nevertheless, the maximum slope normal displacement for test RBF (0.12±0.05 cm) was similar to that of the other SP fractures. The maximum slope normal displacement was on the order of the grain size scale (i.e. typically 0.5-1.5 mm for non-persistent snow crystals). This suggests that up to a few "layers" of crystals are involved in the fracturing process. This explains why weak interfaces do not have a

detectable thickness.

Prior to this study, there were only a few field observations on the slope normal displacement caused by fractures in weak layers. In 1973, Truman reported a collapse of 1 to 2 cm at the sites of firn quakes. Schweizer et al. (1995b) reported deformation measurements from a rammrutsch test (a quantifiable version of the compression test) causing a fracture in a weak interface. They reported a slope normal displacement of 0.47 cm at the time of fracture. Finally, field measurements (Johnson, 2000) showed that the average vertical displacement of the slab at whumpf sites (i.e. fracture propagation on low angle terrain without slab avalanche release) varied from 0.08 to 1 cm. Similarly, the difference in weak layer thickness between the whumpfed and unwhumpfed sites in Table 4.13 ranged from 0.1 to 1.5 cm. These values are in good agreement with the measured values for the maximum slope normal displacement from photographed fractures in weak layers on level terrain and on steeper slopes.

In most tests, all markers were observed to start moving in the slope parallel slope normal directions simultaneously (CTA, CTB, CTC, CTD, CBA, CBB, RBA, RBB, RBD, STC and STE). This indicates that the fracture of the weak layer, or interface, was not a pure slope parallel shear fracture and had a compressive component. On the other hand, in five tests all markers were observed to start moving in the slope parallel direction first (RBE, RBF, RBH, RBI and STB), which is what one would expect for an initial slope parallel shear fracture. However, the fracture in test RBE was not confined to the weak layer (Figure 6.19 (a)), tests RBH and RBI had unusually large scatter in the displacement data and STB was a skier-tested slope where the fracture did not propagate and no slab avalanche was released. In five additional tests (CBC, RBC, STA, STD and STF), some markers were displaced

in both directions simultaneously while other markers were displaced in the slope parallel direction first.

However, there was a significant negative correlation (N = 27, R_p = -0.58, p = 0.002) between the relative number of markers that were displaced in the slope parallel direction first ($\frac{N_{\Delta x first)}}{N}$) and the magnification. This indicates that these observations were significantly affected by the tracking precision. Tests in which markers were displaced in the slope parallel direction first had lower magnifications, and therefore more pronounced uneven pixel clipping. The compression tests (CTA-CTD) as well as tests CBA, CBB, RBA and RBB had a large magnification, and the measurements were therefore less affected by uneven pixel clipping. In these tests, all markers were observed to start moving in both the slope parallel and slope normal directions simultaneously, indicating that fractures in weak snowpack layers are likely mixed mode fractures with both a compressive and a slope parallel shear component.

6.4.2 Dynamic impact of a skier and fracture propagation

Displacement measurements on skier-tested slopes that did not release a slab avalanche (STA, STB and STC) showed the dynamic deformation a skier introduces into the snowpack. On skier-tested slopes STA and STB, the impact of the skier decreased with distance since the displacements (Δx and Δy) of markers farther away from the skier were less. The maximum measured slope normal displacement in STA was 2.3±0.1 cm, much larger than the measured values for propagating fractures (Tables 6.3, 6.4 and 6.5), and larger than the weak layer thickness (2 cm). Moreover, the displacements of markers placed under the weak layer were undetectable. This indi-

cates that the slope normal displacement was caused by fracturing of the weak layer as well as by slope normal compaction of snow between the markers and the weak layer. Furthermore, there was also slope parallel snow compaction caused by brittle compressive fractures in the slab. Large deformations were introduced in the slab by the dynamic loading of the skier. Although the weak layer was fractured, multiple compressive fractures were observed throughout the slab as well. This shows that a skier can fracture a weak layer while skiing without releasing a slab avalanche.

Similar characteristics were observed on skier-tested slope STB. However, only two markers were displaced and tracked over a short period of time. Nonetheless, there was also slope parallel snow compaction caused by brittle compressive fractures in the slab. However, there was also a second fracture in the slab (Figure 6.24 (b)), parallel to the weak layer, at a weak interface in the slab. This shows that skiers can readily fracture weak layers and weak interfaces throughout the upper portion of the slab ($\approx$ upper 70 cm) when skiing, provided the slab is soft (roughly a hand hardness of 1F or less).

On skier-tested (not triggered) slope STC however, the slab behaved differently. The displacement of the first three markers, and the last three markers, was more similar to that of the markers on skier-triggered slopes (Figure 6.26). The maximum slope normal displacement as well as $v_{y_{max}}$ and $a_{y_{max}}$ were similar to those obtained from skier-triggered slopes (Table 6.5). Furthermore, the calculated fracture speed values $\overline{V_{\Delta y}}$ were also similar to those obtained from skier-triggered slopes. However, a compressive fracture between Marker 3 and Marker 4 on skier-tested slope STC impeded the advance of the fracture in the weak layer beyond this point. After the compressive fracture, the unsupported portion of the slab pushed against the lower

part of the slab, which was still attached to the weak layer. This caused the weak layer to fracture beyond the initial fracture 0.1 s later (Figure 6.25). The second fracture propagated out of the field of view, but did not propagate very far as no slab avalanche released.

These results show that skiers can fracture weak layers without releasing a slab avalanche. Theoretical estimates of critical crack size for self-propagating fractures range from 0.1 to approximately 2 m (e.g. Kirchner et al., 2002; Bazant et al., 2003; Schweizer et al., 2003). From photographs taken before and after ski-test STA, the distance over which the weak layer fractured was estimated at 3.0±0.2 m, larger than most theoretical predictions for the minimum size for self-propagating fractures. This indicates the importance of slab properties for fracture propagation. In itself, a large fracture (i.e. 3 m) in a weak layer is not sufficient for fracture propagation and slab avalanche release.

On all the skier-tested slopes that were not skier-triggered, the fracture in the weak layer did not exceed the lowest fracture through the slab. This indicates that the slab plays a crucial role in delivering the energy to the tip of the fracture in the weak layer. When a discontinuity appears in the slab (i.e. a compressive fracture through the slab for down-slope propagation or a tensile fracture for up-slope propagation), no energy is delivered at the crack tip, and fracture propagation stops.

This is consistent with the author's field observations at crown fractures. On skier-tested slopes that were skier-triggered, the weak layer was observed to be intact up-slope from the crown fracture (Figure 6.28). This suggests that the propagating fracture through the weak layer was stopped by the tensile fracture through the

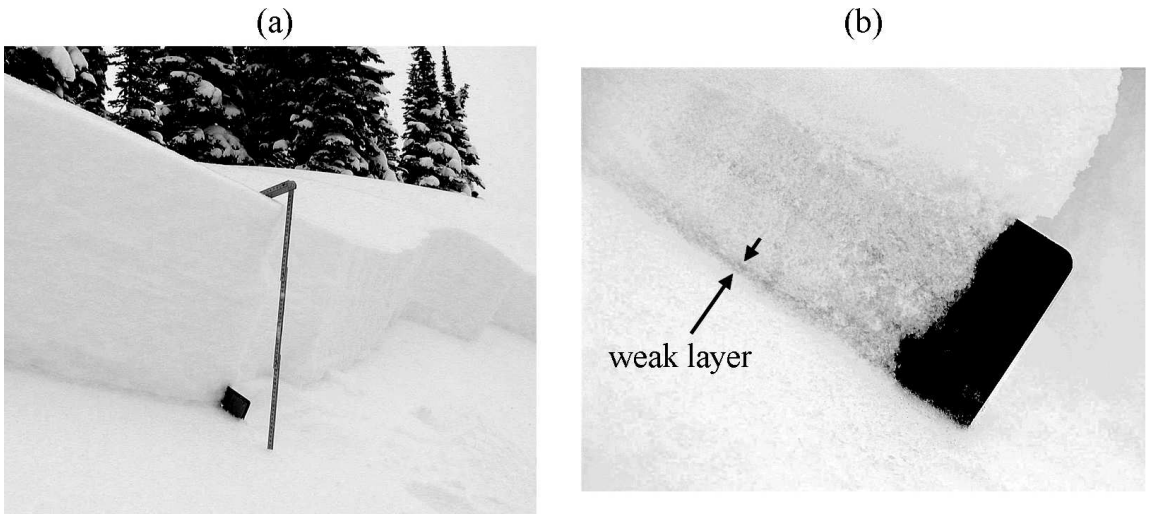

Figure 6.28: *Crown fracture of a human-triggered slab avalanche (STF). (a) Photo (ASARC) of the crown fracture taken soon (15 min.) after the avalanche had released at Mt. Fidelity on 8 March 2004 . The crown was approximately 55 cm deep. (b) Close-up photo (ASARC) showing the weak layer which was observed to be intact up-slope from the crown-fracture.*

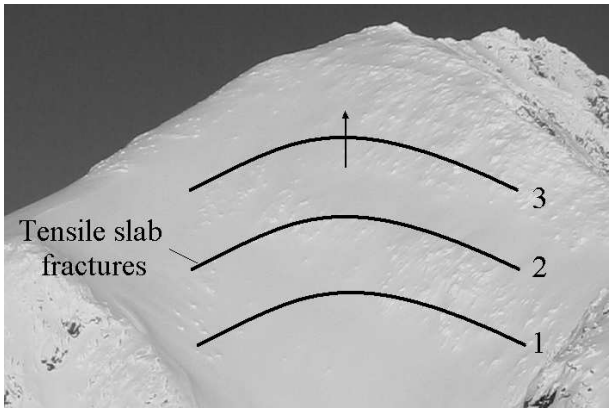

Figure 6.29: *Schematic representation of "echelon" fractures through the slab as the fracture through the weak layer propagates up-slope ahead of the tensile fractures through the slab.*

slab. Fracture of the weak layer below the slab generates zones of compression and tension in the overlying slab due to the gravitational pull on the unsupported slab. Therefore, the upper part of the slab will be in tension, whereas the lower part will be in compression. Snow is stronger in compression than in tension (e.g. Mellor, 1975) and since snow at the surface is generally of lower density and hand hardness than snow deeper in the snowpack, a tensile fracture most likely initiates at the snow surface rapidly propagating through the slab, thereby stopping the advancing fracture. Hence, crown fractures often appear at convexities in the terrain (e.g. ridge top), where increased stress at the snow surface will promote tensile fracture through the slab.

However, on some occasions, tensile fractures through the slab, similar to the crown fracture, have been observed to appear with approximately constant spacing as the fracture through the weak layer propagates up-slope (Figure 6.29) until the final crown fracture appears, typically at convexities in the terrain (B. Jamieson, personal communication). These so called "echelon" fractures are rather uncommon (i.e. less than 5% of slab avalanches). In these instances, fractures in weak layers propagate ahead of tensile fractures through the slab (B. Jamieson, personal communication).

An example of such a slab avalanche in shown in Figure 6.30. The failure layer of this slab avalanche was a buried surface hoar weak layer, at a depth of approximately 60 cm and the overlying slab was relatively hard (h_{slab}=P-). The release of this large skier-triggered slab avalanche (Size 3) resulted in the sympathetic release of another slab avalanche, indicating that conditions were very favourable for widespread fracture propagation. As can bee seen in Figure 6.30 (a), the fracture through the weak layer had propagated to the top of the sharp ridge, where the final crown fracture

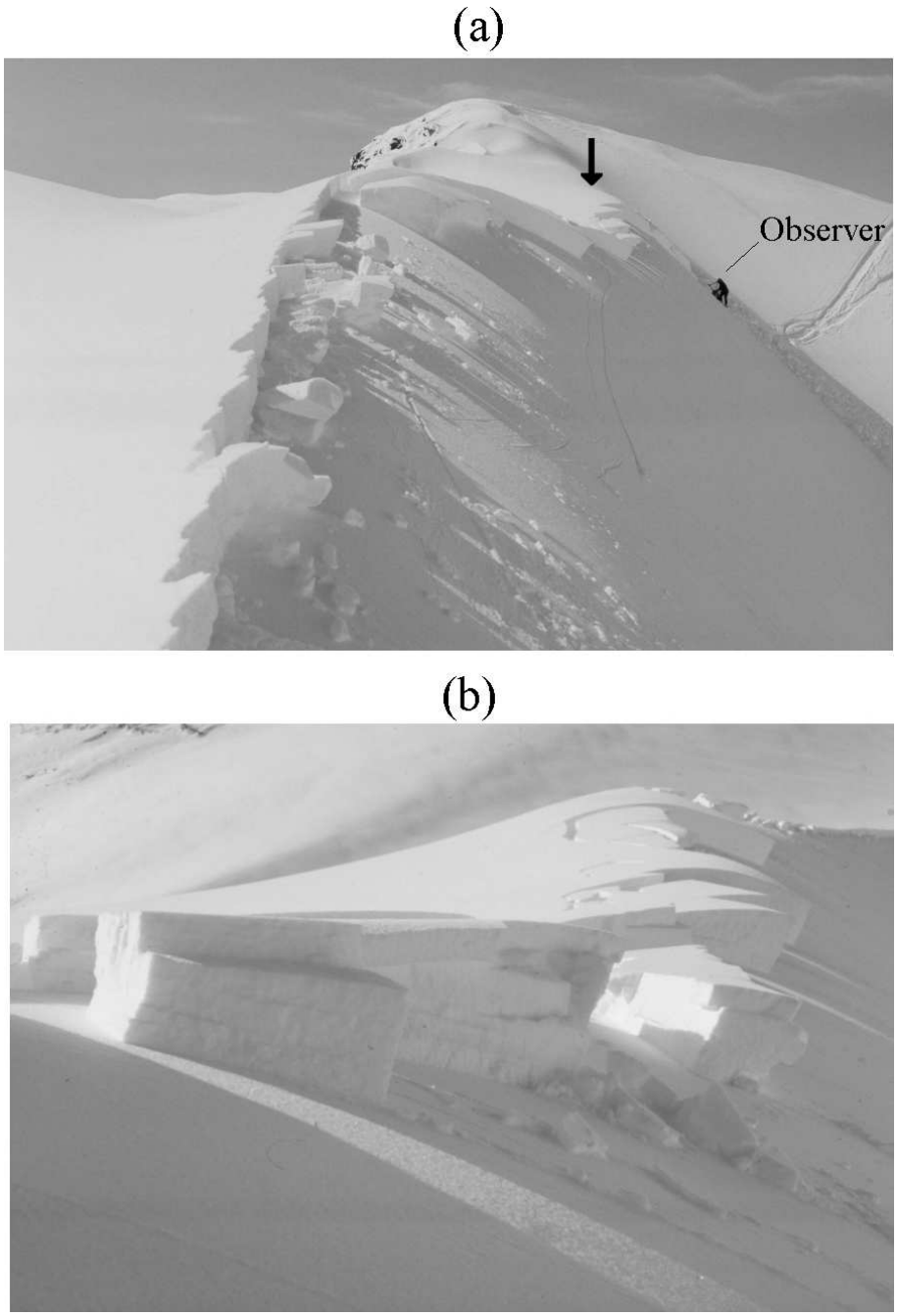

Figure 6.30: *Crown fracture of a human-triggered slab avalanche. (a) Photo (B. Jamieson) of the crown fracture at the top of a sharp ridge. The crown was approximately 60 cm deep. The arrow indicates where the second photo was taken. (b) Photo (B. Jamieson) showing that the fracture through the weak layer had propagated over the ridge, ahead of the final crown fracture.*

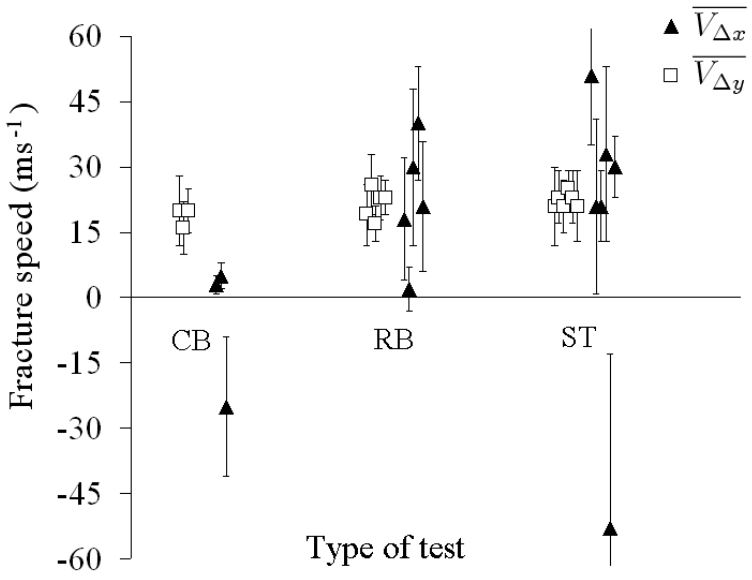

Figure 6.31: *Measured fracture speed (black and white markers) with measurement uncertainty (error bar) by test method.*

appeared probably due to increased tensile stress at the sharp convexity. However, as seen in Figure 6.30 (b), where the ridge was not as sharp, the fracture through the weak layer had propagated over the ridge, ahead of the final crown fracture.

6.4.3 Fracture speed

Fracture speed measurements were estimated from the slope normal displacement, whereas the fracture speed calculations from the slope parallel displacement were more variable, and influenced by the data filtering. Furthermore, due to inaccuracies in the displacement measurements, it was not possible to determine whether the propagation was stationary or accelerated. Therefore, the fracture speed measurements should be considered cautiously.

The measured fracture speed $\overline{V_{\Delta y}}$ ranged from 17 m s^{-1} to 26 m s^{-1}, with a mean

of 21 m s^{-1}. Furthermore, despite the fact that these fracture speed measurements were obtained from tests of different sizes and with different loading methods, the $\overline{V_{\Delta y}}$ results showed little dependence on the test method (Figure 6.31). On the other hand, $\overline{V_{\Delta x}}$ ranged from -53 m s^{-1} to 50 m s^{-1}, with a mean of 14 m s^{-1} and showed dependence on the test method. The calculated values of $\overline{V_{\Delta x}}$ were lowest for the cantilever beam tests. However, there were no substantial differences in $\overline{V_{\Delta x}}$ between rutschblock tests and skier-tested slopes.

The reason for the differences between $\overline{V_{\Delta x}}$ and $\overline{V_{\Delta y}}$ lies in the fact that the slope parallel displacement and marker speed was generally larger than the slope normal displacement and marker speed, because the slope parallel displacement caused by the fracture of the weak layer could not be separated from the slope parallel displacement of the slab sliding down-slope. Therefore, the effects of uneven pixel clipping were accentuated in the slope parallel direction. This also explains why the values of $\overline{V_{\Delta x}}$ were more affected by the data filtering than $\overline{V_{\Delta y}}$.

There was a trend for the fracture speed $\overline{V_{\Delta y}}$ to increase with increasing Δy_{max}, as seen in Figure 6.32. This result suggests that the speed of propagating fractures increases with slope normal displacement. The correlation between $\overline{V_{\Delta y}}$ and Δy_{max} was almost significant ($N = 11$, $R_p = 0.59$, $p = 0.058$). However, when only weak layers composed of buried surface hoar were considered, there was a significant positive correlation between $\overline{V_{\Delta y}}$ and Δy_{max} ($N = 10$, $R_p = 0.72$, p = 0.019). This suggests that the slope normal displacement (due to crushing of the weak layer) plays a fundamental role in the fracturing process of weak snowpack layers and thus the initiation of slab avalanches. Fracture propagation occurs when the energy release rate is greater than the fracture resistance. The surplus of released energy can be

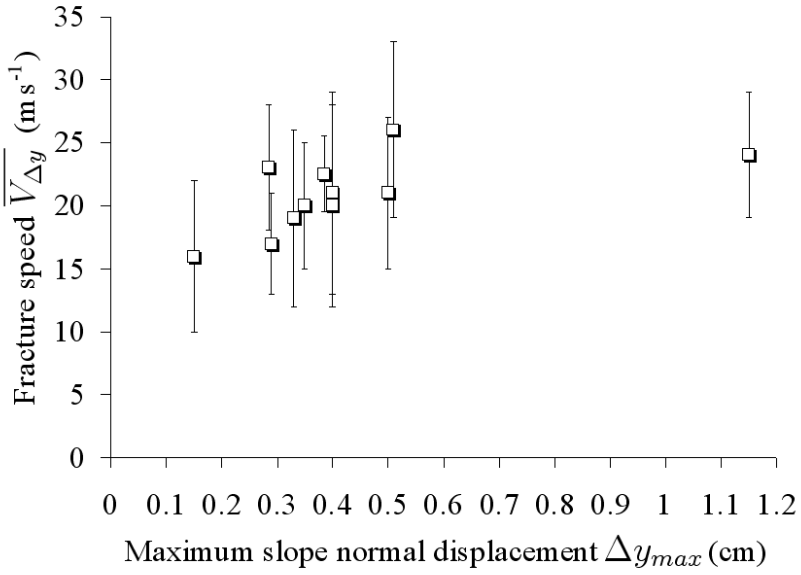

Figure 6.32: *Fracture speed measurements obtained from the slope normal displacement ($\overline{V_{\Delta y}}$) with measurement uncertainty (error bars) by maximum slope normal displacement at the end of fracture (Δy_{max}).*

converted into kinetic energy, and consequently can contribute to the speed at which the fracture will propagate (e.g. Broek, 1986). A larger slope normal displacement results in the release of more potential energy, which could explain the increase in fracture speed with increasing Δy_{max} for buried surface hoar layers.

The estimated fracture speed values from the avalanche videos (Table 6.6) were in good agreement with the calculated fracture speed values from the high-speed photography slope normal displacement data. Despite the relatively crude method to determine the fracture speed from the videos of slab avalanches, the estimated fracture speeds were very similar in all the videos and ranged from 15 m s^{-1} to 32 m s^{-1}, with a mean of 22 m s^{-1}. Furthermore, there was a significant correlation between the estimated size of the slabs and the fracture speed ($N = 12$, $R_p = 0.62$,

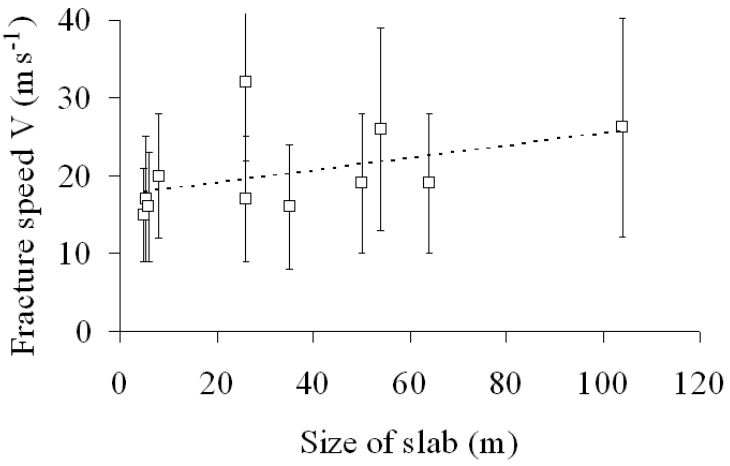

Figure 6.33: *Fracture speed measurements obtained from avalanche videos (V) with measurement uncertainty (error bars) by the estimated size of the slab avalanche.*

$p = 0.035$), as shown in Figure 6.33. Since larger slab avalanches were typically associated with stiffer (harder) slabs (Section 4.5.2), this suggests that the stiffness of the slab affects the propagation speed.

There is only one other published fracture speed measurement (Johnson et al., 2004). The measured fracture speed was 20 ± 2 m s^{-1} which was obtained from measurements over a distance of 8 m. This is in excellent agreement with the calculated fracture speed values from the high-speed photography data as well as the estimated fracture speed from the avalanche videos. Furthermore, there are several reports on firn quakes in Antarctica and North America in which the fracture speed was estimated. Truman (1973) estimates the propagation velocity to be 6 m s^{-1} for a slab thickness between 0.15 to 0.3 m, which is roughly comparable to the present results. On the other hand, Den Hartog (1982) reports propagation velocities on the order of the speed of sound in the air (≈ 300 m s^{-1}) for firn quakes with a slab thickness of probably over 3 m. However, these slabs were much thicker, and very likely much

more dense, than the slabs tested in this study.

6.4.4 Verification of theoretical models

McClung (1979b, 1981, 1987) proposed a theory where shear fracture in the weak layer, precipitated by strain softening, leads to fracture in the weak layer and slab avalanche release. The basic premise behind the theory, which is based on earlier work by Palmer and Rice (1973) for unconsolidated clay slabs, is that shear stress imposed by the overlying slab creates a shear band in the weak layer. Slow strain softening at the tip of the band follows, until a critical length is reached and the fracture becomes brittle and propagates rapidly. No slope normal displacement is assumed along the entire length of the shear band and the propagation velocity is limited by half the shear wave velocity c_s in the body of the slab (McClung, 1979b). For a linear-elastic body the velocity of shear waves is given by (e.g. Kolsky, 1963):

$$c_s = \sqrt{\frac{\mathcal{G}}{\rho}} \tag{6.13}$$

where $\mathcal{G}$ is the shear modulus given by $\mathcal{G} = \mathcal{E}/2(1+\nu)$, with ν the Poisson ratio, and ρ is the density of the material (i.e. ρ_{slab} or ρ_{La}).

Bader and Salm (1990) explored shear fracture propagation in a weak layer. They introduced the term super-weak zone where shear stresses from the overburden snow are not supported. Bader and Salm concluded that without such a pre-existing super-weak zone, avalanche release is unlikely, even with the additional load introduced by a skier. Stress concentrations at the edge of the super-weak zone causes an increase in size until a critical length is reached and rapid brittle fracture propagation follows. Again, no slope normal displacement is assumed, and the propagation speed

is assumed to be on the order of the shear wave velocity c_s.

In 2000, B. C. Johnson proposed a theory for fracture propagation on low angle terrain. The theory is based on a compressive fracture of the weak layer, generating a flexural wave in the overlying slab. Energy is transferred through the slab, progressively collapsing the weak layer, with the stiffness of the slab controlling the speed of propagation. The model is based on the theory of flexural waves travelling through a beam. This flexural wave model was recently refined by describing the behaviour of the slab on low angle terrain with the differential equation for the transverse bending of thin plates (Heierli, submitted) rather than a beam. Free fall motion is assumed directly after fracture and the solution of the differential equation is a localized disturbance that propagates without change of form, wavelength or velocity. These are characteristics of a solitary wave (Dodd et al., 1982), which is not a wave in the usual sense. The propagation velocity on flat terrain is given by:

$$c_f^4 = \frac{g}{2b}\frac{\mathcal{D}}{\rho_{slab}\mathcal{H}} \tag{6.14}$$

where g is the gravitational acceleration, $\mathcal{D}$ is the flexural rigidity of the plate (slab), b the amount of collapse (i.e. $b = \Delta y_{max}$) and $\mathcal{H}$ the slope normal depth of the weak layer. The coefficient $\mathcal{D}$ depends on the elastic modulus $\mathcal{E}$ and Poisson's ratio ν of the slab.

$$\mathcal{D} = \frac{\mathcal{E}\mathcal{H}^3}{12(1-\nu^2)} \tag{6.15}$$

The wavelength of the solitary wave is given by $\lambda = \sqrt{\frac{2b}{g}}c_f$. For fracture propagation on a slope ψ, the gravity term in Equation 6.14 becomes $g\cos\psi$.

In order to verify the theoretical models, the calculated fracture speed $\overline{V_{\Delta y}}$ is compared with the theoretical prediction given by Equations 6.13 and 6.14. In order

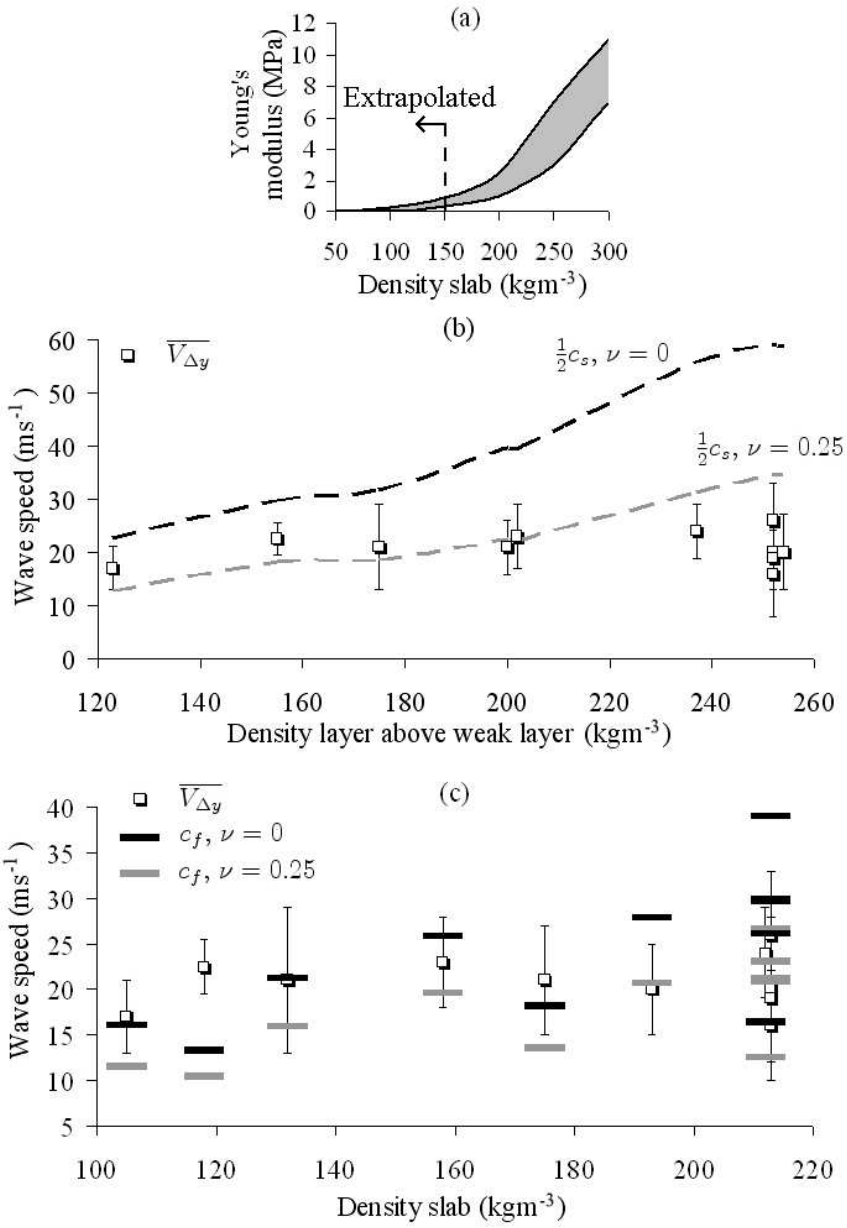

Figure 6.34: *(a) Estimates of the elastic modulus $\mathcal{E}$ (after Shapiro et al., 1997). For snow with a density lower than 150 kg m^{-3} (indicated with a dashed line), the elastic modulus was estimated by extrapolation. (b) Measured $\overline{V_{\Delta y}}$ values (markers) and half the shear wave velocity ($\frac{c_s}{2}$) for Poisson's ratio $\nu = 0$ and $\nu = 0.25$ by slab density. (c) Measured $\overline{V_{\Delta y}}$ values (markers) and flexural wave velocity ($\frac{c_s}{2}$) for Poisson's ratio $\nu = 0$ and $\nu = 0.25$ by slab density.*

to calculate propagation speed for the various waves, the elastic modulus $\mathcal{E}$ was estimated from Shapiro et al. (1997) as shown in Figure 6.34 (a). Furthermore, according to Mellor (1975), Poisson's ratio for low density snow ranges between 0 and 0.25. In Figure 6.34 (b) and (c), half the shear wave velocity ($\frac{c_s}{2}$) and the flexural wave velocity (c_f) as well as the measured $\overline{V_{\Delta y}}$ values are shown for a Poisson's ratio between 0 and 0.25.

The calculated shear wave velocity $\frac{c_s}{2}$ was on the order of the measured fracture speed $\overline{V_{\Delta y}}$ for lower densities (i.e. < 200 kg m^{-3}), whereas for higher densities the experimental data were lower than $\frac{c_s}{2}$. Furthermore, the increase in c_s with density is greater than in the experimental data ($N = 11$, $R_p = 0.11$, $p = 0.737$).

The calculated flexural wave speeds (Figure 6.34 (c)), were in reasonable accordance with the experimental results. However, inspection of Equation 6.14 reveals the flexural wave speed decreases with increasing slope normal displacement, contrary to what was found with the experimental data on buried surface hoar layers (Figure 6.32). For clarity, the theoretical estimates of c_f, as well as the measured fracture speed values are shown in Table 6.7. The calculated flexural wave velocities were within the measurement uncertainty of $\overline{V_{\Delta y}}$, with the exception of tests STC, STE and CBB. Test STC was a skier-tested slope which did not release a slab avalanche and it is likely that the skier had some influence on the propagating fracture. In test STE, a weak layer composed of depth hoar was fractured. This fracture resulted in a large slope normal displacement (1.2 cm). It is likely that some of the slope normal displacement was caused by the "erosion" of the weak layer after fracture by the down-slope sliding of the slab, in which case Equation 6.14 would underestimate the propagation speed.

Table 6.7: *Measured fracture speed $\overline{V_{\Delta y}}$, and corresponding range of calculated flexural wave velocity c_f for Poisson's ratio $\nu = 0$ and $\nu = 0.25$ given by Equation 6.14.*

Test	Slab density (kg m^{-3})	Δy_{max} (cm)	$\overline{V_{\Delta y}}$ (m s^{-1})	c_f (m s^{-1})
RBC	105	0.29±0.04	17±4	12-16
STC	118	0.39±0.03	22±3	10-13
STF	132	0.4±0.1	21±8	16-21
RBD	158	0.29±0.6	23±5	20-26
STD	175	0.5±0.1	21±6	14-18
CBC	193	0.35±0.05	20±5	21-28
STE	212	1.2±0.2	24±5	13-17
CBA	213	0.4±0.1	20±8	21-30
CBB	213	0.15±0.05	16±6	26-39
RBA	213	0.33±0.03	19±7	23-28
RBB	213	0.51±0.02	26±7	21-26

High-speed photography of fractures in weak snowpack layers in this thesis, as well as by Schweizer et al. (1995b), has shown that there is a compressive component associated with the fracture. Slope normal displacement was observed in all fractures, regardless of slope angle. The theoretical models proposed by McClung (1979b, 1981, 1987) and Bader and Salm (1990) do not take into account any slope normal displacement of the overlying slab. The fracture in the weak layer is assumed to be a pure shear fracture, which was not observed in all tests. The values of the shear wave velocity, as calculated with Equation 6.13, were comparable to the measured fracture speed. However, measurements of the shear wave velocity (Smith, 1965) show that the theoretical estimates are too low, and c_s is likely larger than the measured fracture speed $\overline{V_{\Delta y}}$.

The theoretical model introduced by B. C. Johnson (2000) and refined by Heierli (submitted) is based on compressive fracture of the weak layer coupled with a flexural wave through the slab. Crushing of the weak layer (i.e. slope normal displacement)

was observed in each test. Slope normal displacement was also observed for the only fracture in a weak interface, which had no detectable thickness. The slab undoubtedly bends when this occurs, creating a flexural wave. Furthermore, the measured fracture speeds are a better fit to the flexural wave speed than to half the shear wave speed (Figure 6.34). This suggests that fracture propagation on a slope is coupled to a flexural wave through the slab. While the weak layer can fracture in shear, the fracture would be coupled to a propagating flexural wave in the overlying slab.

6.4.5 Energy considerations

During collapse, potential energy is released. In order for the fracture to propagate, the amount of energy released must be greater than the fracture resistance. The energy balance at the crack tip is given by (e.g. Broek, 1986: 168):

$$U_g^f + U_g^s + U_E + E_{kin} = W_f \tag{6.16}$$

where U_g^f is energy supplied by the vertical displacement of the slab, U_g^s is the energy of the slab sliding down-slope, U_E is the elastic energy released, E_{kin} is the kinetic energy and W_f is the work of fracture. Jamieson and Johnston (1992b) argued that U_g^s and E_{kin} do not fully contribute to fracture propagation and lag behind the crack tip. The energy supplied by the vertical displacement of the slab per unit area is given by:

$$U_g^f = mg\frac{\Delta y_{max}}{\cos\psi} \tag{6.17}$$

where m is the mass per unit area (i.e. $\rho_{slab}Th_{slab}$) and ψ the slope angle. The energy (or work of fracture per unit area) required to fracture the weak layer can be estimated using data from Föhn et al. (1998). They measured the force and displacement required to fracture a weak layer, using a shear frame. The shear stress to cause brittle fracture increased almost linearly with strain. Similarly, laboratory studies (Akitaya, 1974; Narita, 1980; Fukuzawa and Narita, 1993) have shown that for brittle fracture the stress increases almost linearly with strain (i.e. $\tau = \mathcal{G}\gamma$). Furthermore, laboratory studies performed by Singh (1980) showed that the strain at fracture was relatively constant (i.e. $\tau/\mathcal{G} \approx$ constant), independent of density. For buried surface hoar weak layers, Föhn et al. (1998) found an average slope parallel displacement of 0.3 mm at the time of fracture.

No shear strength measurements were performed on the weak layers that were photographed. In order to calculate the work of fracture, the strength of the weak layer was therefore estimated from the hand hardness measurements. As was shown in Section 3.3 (see Figure 3.3), the hand hardness had a nearly linear relationship with the shear strength. For the data used in the correlation analysis in Section 4.3.2, empirical relationships between hand hardness and shear strength were found. For buried surface hoar weak layers as well as FC and DH weak layers, these were, respectively:

$$\text{Surface hoar } (N = 1035,\ p < 10^{-8}):\ \Sigma = 0.56H^{0.90} \tag{6.18}$$

$$\text{FC and DH } (N = 297,\ p < 10^{-8}):\ \Sigma = 0.46H^{0.88} \tag{6.19}$$

Assuming a displacement of 0.3 mm at the time of fracture, the energy required

Table 6.8: *Energy required to fracture the weak layer (W_f), released potential energy by the vertical displacement of the slab U_g^f and the ratio of U_g^f/W_f.*

Test	W_f (J m^{-2})	U_g^f (J m^{-2})	U_g^f/W_f
RBC	0.17	1.9	11.2
STC	0.17	2.3	13.5
STF	0.22	6.7	30.5
RBD	0.17	5.1	30
STD	0.10	4.7	47
CBC	0.28	6.7	23.9
STE	0.37	12.8	34.6
CBA	0.36	6	16.7
CBB	0.36	2.3	6.4
RBA	0.36	4.9	13.6
RBB	0.36	7.7	21.4

to fracture the weak layer can be estimated and compared to the potential energy released by the slab given by Equation 6.17. Both these quantities are shown in Table 6.8.

It is assumed that the fracture of the weak layer and the downward displacement of the slab are coupled together and propagate at the same velocity. Therefore, the potential energy released by the slab can be compared to the energy required to fracture the weak layer to determine if sufficient energy is available for fracture propagation. The energy per unit area released by the slab is much greater than the energy required to fracture the weak layer (Table 6.8). The ratio of U_g^f to W_f ranged from 6.4 to 47 with a mean of 22.6. Clearly, the gravitational energy supplied by the slab is sufficient to fracture the weak layer in shear.

6.5 Conclusions

A portable high speed camera was used to observe *in situ* fractures in weak snowpack layers directly at 250 frames per second. The mechanisms that cause different types of fracture were observed in compression tests. Furthermore, the use of markers placed in the snow wall above the weak layer allowed for detailed analysis of the displacement of the slab caused by the fracturing weak layer. Displacement measurements, with a typical accuracy of 0.02 cm, showed that fracturing of weak snowpack layers was associated with slope parallel and slope normal displacement of the overlying slab. Slope normal displacement, which ranged from 0.1 to 1.7 cm, was observed in all fractured weak layers, independent of slope angle, and was comparable to previously published results. Furthermore, slope normal displacement was also observed for a fracture in what was recorded as a weak interface, suggesting that slope normal displacement at the time of fracture is the rule rather than the exception. On the other hand, slope parallel displacement caused by the fracture in the weak layer was probably dependent on slope angle, as expected for free fall motion of the slab directly after fracture.

Photography of two skier-tested slopes that did not release slab avalanches showed that the impact of the skier decreased with distance from the skier. Both slope normal and slope parallel compaction of the overlying slab were observed. The videos show that skiers can fracture weak layers over a large distance (3 m) without releasing a slab avalanche, showing the importance of slab properties for fracture propagation. Furthermore, on three skier-tested slopes that were not triggered (Section 6.5), compressive fractures were also observed through the slab. The fracture in the weak

layers did not exceed the lowest down-slope fracture through the slab, indicating that the slab plays a crucial role in delivering the energy to the tip of the fracture in the weak layer.

Fracture speed measurements were obtained from eleven photographed propagating fractures. These data should be considered cautiously, since it was not possible to determine whether the propagation was stationary or accelerated. However, the propagation velocities $\overline{V_{\Delta y}}$ were comparable in all tests and of the order of 20 m s^{-1}, in good agreement with the only other published fracture speed measurement, as well as estimates from avalanche videos. The measured fracture speed values were comparable with theoretical values of half the shear wave velocity and the flexural wave velocity. However, collapse of the weak layer was observed in each test, which suggests that the fracture of the weak layer is coupled to a propagating flexural wave in the overlying slab. In addition, simple energy calculations suggest that the energy provided by this collapse is sufficient for fracture propagation.

Chapter 7

Conclusions

Based on the data and arguments presented in this thesis, the following conclusions can be drawn:

- The thorough analysis of snowpack properties associated with skier-triggering has shown that various snowpack variables were indicative of instability (Chapter 4), confirming results from previous studies. Weak layer properties, as well as slab properties, grain size and hand hardness differences between the weak layer and the adjacent layers were found to be indicative of instability (Sections 4.3.3 and 4.3.4). The relation between these snowpack variables and skier-triggering is complex and no single snowpack variable dominates fracture initiation or fracture propagation.

- Fracture initiation requires that sufficient skier induced stress reaches the weak layer to overcome the strength of the weak layer. The amount of stress that reaches the weak layer is reduced with the depth of the weak layer (Section 4.5.1), as well as with increasing hardness of the slab and the layer above the weak layer (Sections 4.5.2 and 4.5.3). Stress concentrations in the weak layer facilitate fracture initiation, and these increase with increasing differences in grain size and hand hardness between the weak layer and the adjacent layer, as well as for thinner weak layers (Section 4.5.1). Finally, the strength of the weak layer increases with increasing hand hardness of the weak layer as well as

with decreasing crystal size, since layers composed of larger crystals typically had a lower hand hardness (Section 4.5.1).

- For fracture propagation, the energy required for fracture has to be less than or equal to the amount of energy released per unit expansion. Interfacial fracture mechanics for solid materials suggests that the fracture energy decreases as the relative modulus of the weak layer increases, which increases as the hand hardness difference between the weak layer and the adjacent layers decreases (Section 4.5.4). Large differences in hand hardness therefore facilitate fracture propagation, which supports field observations showing an increase in frequency of skier-triggering with increasing hand hardness difference (Sections 4.3.3 and 4.3.4). Displacement measurements of photographed fractures showed that fracturing of weak snowpack layers was associated with slope parallel and slope normal displacement of the overlying slab (Chapter 6). Simple energy calculations showed that the amount of gravitational energy released by the slab during vertical displacement is sufficient to fracture the weak layer in shear (Section 6.4.5). Thicker and denser (harder) slabs are therefore more conducive to fracture propagation, which is consistent with field observations on remotely triggered slab avalanches, whumpfs as well as medium and large avalanches (Section 4.3.5).

- With the proposed classification system for fracture character in stability tests, the interpretation of these tests results can be improved (Chapter 5), since most failure layers of slab avalanches produce sudden fractures (SP and SC) in compression tests. For the rutschblock test however, the release type developed

in Switzerland is likely a better descriptor, since fracture character is not as easily observed as in the compression test score (Section 5.4.2). Furthermore, the analysis of fracture character in combination with snow profile data showed that the typical snowpack characteristics for SP and SC fractures favour slab avalanche release (i.e. fracture initiation and propagation). On the other hand, typical snowpack properties for PC, RP and B fractures do not favour fracture propagation (Section 5.4). These results support the idea put forward by Johnson and Birkeland (2002) that shear quality and hence fracture character are related to fracture propagation.

- Fracture character observations in DTT and FPT tests indicated that the drop hammer energy to propagate the initial fracture (notch) for sudden fractures was significantly lower than for non-planar breaks. However, the usefulness of the DTT and the FPT as a field test for propagation propensity was inconclusive, since no relation was found between these test results and regional avalanche activity.

- Tracking the evolution of potential weak layers through observations of fracture character can be useful. During the initial stages of the slab becoming cohesive, fracture character can provide information on the potential for avalanches to occur. Typically, changes in snowpack conditions are believed to cause an evolution of fracture character from PC to RP to SP/SC to B, exemplified by observations of the evolution of fracture character for a weak layer that consisted of faceted crystals on top of a crust observed on Mt. Fidelity (Section 5.4.1).

- Based on limited data from photographed SP and SC fractures in compression tests, a fracture classified as Sudden Collapse typically results in slope normal displacement of the overlying slab of more than one cm (Section 6.4.1). Furthermore, the fracture mechanism that causes different types of fractures was observed in photographed compression tests (Section 6.3.1).

- Displacement measurements from photographed fractures showed that fractures in weak snowpack layers exhibited slope normal displacement (i.e. crushing of the weak layer). Slope normal displacement ranged from 0.1 cm to 1.7 cm, was observed in all fractured weak layers, was independent of slope angle, and was comparable to previously published results (Section 6.4.1).

- High-speed photography of skier-tested slopes showed that skiers can fracture weak layers and interfaces without necessarily releasing an avalanche (Section 6.4.2). Photography of three skier-tested slopes that did not release a slab avalanche showed that the weak layer fractured and that there were fractures through the slab as well (Section 6.3.4). The fracture in the weak layers did not exceed the lowest down-slope fracture through the slab, indicating that the slab plays a role in delivering the energy to the tip of the fracture in the weak layer (Section 6.4.2). The slab has to be sufficiently stiff in order to supply energy to the crack tip. This is consistent with field measurements, showing that skier-triggered slab avalanches were infrequent for shallow, soft slabs, which was attributed to low stiffness (hand hardness) of the slab as well as fracture of the slab by ski penetration (Section 4.5.1).

- Fracture speed measurements were obtained from eleven photographed prop-

agating fractures (Sections 6.3.2, 6.3.3 and 6.3.4). The propagation velocities ranged from 17 m s^{-1} to 26 m s^{-1}, with a mean of 21 m s^{-1}. These values are in good agreement with the only other published fracture speed measurement (Johnson et al., 2004), as well as estimates from avalanche videos, which ranged from 15±6 m s^{-1} to 32±10 m s^{-1} (Section 6.3.5).

- In order to assess theoretical models, the measured fracture speed was compared with *theoretical estimates* for half the shear wave velocity and the flexural wave velocity (Section 6.4.4). An initial slope parallel shear fracture cannot be refuted as theoretical estimates of half the shear wave velocity were comparable to the measured fracture speed, and in *five out of 21* tests all markers were observed to start moving in the slope parallel direction first, consistent with a pure slope parallel shear fracture. However, the measured fracture speed values were also comparable with theoretical estimates of the flexural wave velocity, and collapse of the weak layer observed in *all* tests. The slab undoubtedly bends when this occurs, suggesting that the fracture of the weak layer is coupled to a propagating flexural wave in the overlying slab.

7.1 Contributions

As mentioned earlier, this thesis is part of an ongoing research project at the University of Calgary. As such, parts of the data have been used in previous studies. Table 7.1 lists the contributions this thesis has made to the overall goal of better understanding the release of skier-triggered slab avalanches and fracture propagation.

Table 7.1: Selected previous work and contributions made in this thesis

Chapter	Selected previous work	Contributions
4	Schweizer and Wiesinger, 2001; Schweizer and Jamieson, 2001, 2003a and 2003b; Schweizer et al., in press.	Analysis of a large data set (520 profiles on skier-tested slopes) confirmed and expanded results from previous studies. More detailed analysis, in particular the properties of the layers adjacent to the weak layer. Effects of snowpack variables on stability observed through the frequency of skier-triggering. Snowpack variables affect fracture initiation and fracture propagation in a complex manner.
5	Jamieson, 1999; Johnson and Birkeland, 2002; van Herwijnen and Jamieson, 2002.	Refined existing fracture classification system. Identified specific snowpack properties associated with each fracture type. Showed improved interpretation of stability test results by incorporating fracture character. Evolution of fracture character for non-persistent weak layers.
6	Schweizer et al., 1995b; B. C. Johnson, 2000; Johnson et al., 2002, 2004.	High-speed photography of fractures in weak snowpack layers in various field tests and on skier-tested slopes. Observed crack arrest under skiers. Measured displacement of the overlying slab at the time of fracture. Observed crushing of the weak layer in each fracture, suggesting mixed mode fracture. Measured the propagation speed of fractures on slopes.

7.2 Practical implications

Snow stability evaluation is considered as the essential element of avalanche forecasting (McClung and Schaerer, 1993: 124). Stability evaluation for avalanche forecasting relies on weather and snowpack data as well as avalanche observations. Snowpack data, including stability tests and snow profiles, become crucial information in the absence of avalanche occurrence data. A stability evaluation is essentially a search for signs of instability; weak layers (or interfaces) are identified and the stability of the overlying slab is evaluated. As mentioned earlier, snowpack conditions have to favour both fracture initiation and fracture propagation for the release of a skier-triggered slab avalanche.

Recent studies have emphasized the importance of indicators of fracture propagation (McCammon and Sharaf, 2005; Jamieson and Schweizer, 2005) for stability evaluations. Stability tests are widely used to identify potential failure layers. However, stability test results are primarily indicators of *fracture initiation*. Fracture character, on the other hand, can contribute information about *fracture propagation* potential in weak snowpack layers (Chapter 5). Furthermore, as discussed in Chapter 4, specific snowpack characteristics relate to *fracture initiation and fracture propagation* in a complex manner.

This means that for stability evaluations based on snowpack data, three indicators are available, relating to fracture initiation and fracture propagation. As shown in Figure 7.1, which is based on the "stability circle" developed by McCammon and Sharaf (2005), stability test results, fracture character observations and information on snowpack properties are three factors that can be considered in a stability evalua-

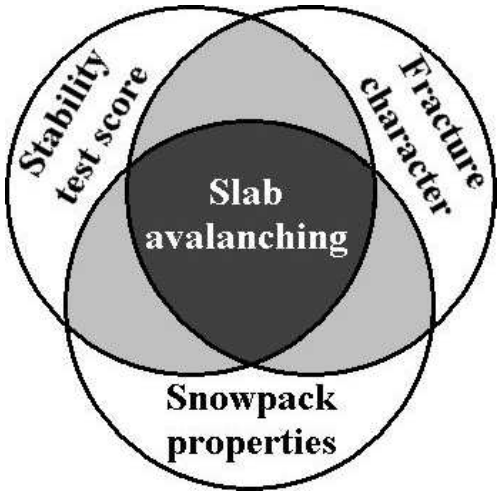

Figure 7.1: *Factors used in a stability evaluation based on snowpack data. Stability test scores are primarily indicative of fracture initiation, fracture character is primarily indicative of fracture propagation and snowpack properties indicate whether fracture initiation and fracture propagation are likely. Based on the "stability circle" developed by McCammon and Sharaf (2005).*

tion based on snowpack data. While stability test results primarily relate to fracture initiation, snowpack properties are indicative of fracture initiation and propagation and fracture character primarily relates to fracture propagation.

The interpretation of stability test results, as well as fracture character observations is relatively straightforward. However, snowprofile interpretation requires knowledge and experience. In order to quantify snowprofile interpretation, McCammon and Schweizer (2002), Schweizer et al. (in press) and Jamieson and Schweizer (2005) explored methods based on the threshold sum approach to assess snowpack stability based on layer properties. A set of layer and interface properties (i.e. depth, grain type, grain size and hand hardness of the weak layer, as well as differences in grain size and hand hardness over the failure interface) were proposed to objectively assess manual snow profiles by flagging certain characteristics of weak layers (or

interfaces). This method for analyzing snow profiles requires little experience and results in an indicator of instability. The results from Chapter 4 confirm the importance of these snowpack variables with regards to fracture initiation and fracture propagation.

Chapter 8

Recommendations for further research

Schweizer et al. (in press) explored a method based on the threshold sum approach to assess snowpack stability based on layer properties. A similar approach based on the observed frequency of skier-triggering for significant variables could be investigated. Replacing threshold values for specific variables by typical trends in the frequency of skier-triggering for these variables (e.g. Figure 4.30) might result in more accurate predictions. Alternatively, the typical distributions of snowpack characteristics could be used to determine snowpack stability. By normalizing snowpack variables with depth, deviations from typical snowpack conditions at the same depth might reveal important signs of instability.

More data will have to be collected to confirm the importance of observations on release type in rutschblock tests. Similarly, more data will help clarify the evolution of fracture character, in particular for non-persistent weak layers. However tracking non-persistent weak layers could be challenging as properties of these snowpack layers can change significantly within hours.

In this thesis, the importance of slab properties for fracture propagation has been discussed qualitatively. However, a more quantitative understanding of snowpack properties affecting fracture propagation is needed. Even though observations of fracture character, and release type for rutschblock tests, provide some qualitative information about fracture propagation, as of yet, there is no effective field test to quantify fracture propagation. Such a test is however very important, as tradi-

tional stability tests are most indicative of fracture initiation and hence have their limitations.

The flexural wave approach provides a good explanation for fracture propagation. The model introduced by Heierli is based on the differential equation for the transverse bending of thin plates. It shows analytically that the fracture occurs in form of a localized disturbance propagating with constant velocity and wavelength. However, it does not incorporate weak layer properties, as free-fall motion is used to describe the motion of the slab, which is assumed to behave as an elastic solid, directly after fracture. Furthermore, it was developed for low angle terrain, and therefore the model does not incorporate the influence of slab displacement after fracture, as observed in the videos.

Snow is a highly porous material which has been described as a granular material and most recently as a foam of ice, and is highly compressible. A simple linear elastic approximation will therefore not suffice, and modelling of weak layer fractures will require microstructural modelling of the fracture process. The energy balance at the crack tip of a propagating collapsing fracture will have to be solved in order to understand avalanche release better and devise appropriate tests. This will require knowledge about the work of fracture for collapsing fractures, as well as the stress state of the slab during fracture propagation.

High-speed photography is a very useful tool to study fractures in weak snowpack layers. Despite the technological challenges, it provided unique insight into a poorly understood phenomenon. Future work should address the origin of the noise bands in the digitized images in order to increase the accuracy of the particle tracking. This could be achieved by investigating different filters which can be used for image

restoration. Median filters (Stewart, 1985) have been used in seismic data to reject glitches on the data as well as to enhance discontinuities. The non-linear ranking-based median filter reduces noise without shifting or smoothing edges, as smoothing (i.e. moving average) filters do. Ranking the pixel intensity in windows of different sizes and keeping the difference between the brightest (or darkest) values in each can also be used to isolate features that are locally brighter (or darker) than a varying background. This so-called "top-hat" filter can be adapted to remove lines in an image (Stewart, 1985). Alternatively, thresholding operations (Hornak, 2002; 584-589) could be used to enhance the markers in the digitized images. The most widely used tools are erosion and dilation. In its simplest form, erosion removes a pixel that was thresholded to be part of a feature if it touches any background pixel, while dilatation adds a pixel to a feature if it touches the feature. Dilatation followed by erosion (so-called "closing") restores features size and fills in small holes and could be used to restore the distorted markers in the digitized images.

As technological advances are rapid, higher resolution cameras will become available which will improve the observations. A more even illumination in the field experiments would also improve the quality of the images. This could be achieved by using reflective panels to obtain an even illumination on the photographed section of the snow. More displacement measurements and fracture speed measurements will be needed to relate these quantities to specific snowpack properties.

Photography of different types of fractures has shown that there are differences in the fracture process of different types of fractures. Close-up photography of fracture in weak snowpack layers might reveal more quantifiable information about crystal deformation and the fracture process. Furthermore, by inserting numerous markers

in the slab on larger tests (e.g. skier tested slopes), the deformation of the slab could be measured more accurately, providing some information about strain within the slab.

Bibliography

Akitaya, E., 1974. Studies on depth hoar. Contributions from the Institute of Low Temperature Science, Series A, 26, pp. 1-67.

Bader, H.P., B. Salm, 1990. On the mechanics of snow slab release. Cold Regions Science and Technology, 17, pp. 287-300.

Bazant, Z.P., G. Zi, D. McClung, 2003. Size effect law and fracture mechanics of the triggering of dry snow slab avalanches. Journal of Geophysical Research, 108 (B2), 2119.

Beer, F.P., E.R. Johnston, 1985. Machanics of Materials. McGraw-Hill Inc., Toronto, Canada, 611 pp.

Benson, C.S., 1962. Stratigraphic studies in the snow and firn of the Greenland Ice Sheet. U.S.A. SIPRE Research Report, 70.

Birkeland, K.W., 1998. Terminology and predominant processes associated with the formation of weak layers of near-surface cafeted crystals in the mountain snowpack. Artic and Alpine Research, 30 (2), pp. 193-199.

Birkeland, K.W., H.J. Hansen, R.L. Brown, 1995. The spatial variability of snow resistance on potential avalanche slopes. Journal of Glaciology, 41 (137), pp. 183-189.

Birkeland, K.W., R.F. Johnson, 1999. The stuffblock snow stability test: compara-

bility with the rutschblock, usefulness in different snow climates, and repeatability between observers. Cold Regions Science and Technology, 30, pp. 115-123.

Bradley, C.C., 1970. The location and timing of deep slab avalanches. Journal of Glaciology, 9 (56), pp. 253-261.

Bradley, C.C., D. Bowles, 1967. Strength-load ratio, an index of deep slab avalanche condition. Institute of Low Temperature Science, Hokkaido University, Japan, 1 (2), pp. 1243-1253.

Broek, D., 1986. Elementary Engineering Fracture Mechanics, fourth revised edition. Kluwer Acedemic Publishers, Hingham, USA, 516 pp.

Bucher, E., 1956. Contribution to the theoretical foundations of avalanche defense construction. Snow, Ice and Permafrost Research Establishment, translation 18, 99 pp.

Canadian Avalanche Association, 2002. Observation guidelines and recording standards for weather, snowpack and avalanches. Canadian Avalanche Association, Revelstoke, B.C., Canada.

Campbell, C., 2004. Spatial variability of slab stability and fracture properties in avalanche start zones. MSc. Thesis, University of Calgary.

Camponovo, C., J. Schweizer, 1996. Measurements on skier triggering. Proceedings of the 1996 International Snow Science Workshop, Banff, Alberta, Canada, pp. 100-103.

Castleman, K.R., 1996. Digital Image Processing. Prentice Hall, Upper Saddle River, New Jersey, 665 pp.

Chalmers, T., 2001. Forecasting shear strength and skier-triggered avalanches for buried surface hoar layers. MSc Thesis. University of Calgary.

Colbeck, S.C., E. Akitaya, R. Armstrong, H. Gubler, J. Lafeuille, K. Lied, D. McClung and E. Morris, 1990. International Classification for Seasonal Snow on the Ground. International Commission for Snow and Ice, World Data Center for Glaciology, University of Colorado, Boulder, CO, USA.

Colbeck, S.C., 2001. Sintering of unequal grains. Journal of Applied Physics, 89 (8), pp. 4612-4618.

Colbeck, S.C., B. Jamieson, 2001. The formation of faceted layers above crusts. Cold Regions Science and Technology, 33 (2-3), pp. 247-252.

Conway, H., J. Abrahamson, 1984. Snow stability index. Journal of Glaciology, 30 (106), pp. 321-327.

Crocker, J.C., D.G. Grier, 1996. Methods of digital video microscopy for colloidal studies. Journal of Colloid Interface Science, 179 (1): 298-310.

de Quervain, M.R., 1966. Problems of avalanche research. Symposium at Davos, 1965, Scientific Aspects of Snow and Ice Avalanches, IAHS Publication, 69, pp. 1-8.

DenHartog, S.L., 1982. Firn quake (A rare and poorly explained phenomenon). Cold Regions Science and Technology, 6, pp. 173-174.

Dodd, R.K., J.C. Eilbeck, J.D. Gibbon, H.C. Morris, 1982. Solitons and Monlinear Wave Equations. Academic Press, New York, USA, 630 pp.

Faillettaz, J., D. Daudon, D. Bonjean, F. Louchet, 2002. Snow toughness measurements and possible applications to avalanche triggering. Proceedings of 2002 International Snow Science Workshop, Penticton, British Columbia, Canada, pp. 540-543.

Föhn, P.M.B., 1987. The rutschblock as a practical tool for slope stability evaluation. International Association of Hydrology Science Publication, 162, pp. 223-228.

Föhn, P.M.B., 1993. Characteristics of weak snow layers and interfaces. Proceedings of the 1992 International Snow Science Workshop, Breckenridge, Colorado, USA, pp. 160-170.

Föhn, P.M.B., C. Camponovo, G. Krusi 1998. Mechanical and structural properties of weak snow layers measured *in situ*. Annals of Glaciology, 26, pp. 1-6.

Fukuzawa, T., H. Narita, 1993. An experimental study on the mechanical behaviour of a depth hour layer under shear stress. Proceedings of the 1992 International Snow Science Workshop, Breckenridge, Colorado, USA, pp. 97-104.

Fuller, R., in press. Observations of an increase in slab thickness after fracture. Proceedings of 2004 International Snow Science Workshop in Jackson Hole, USA.

Geldsetzer, T., B. Jamieson, 2000. Estimating dry snow density from grain form and hand hardness. Proceedings of the 2000 International Snow Science Workshop, Big Sky, Montana, USA, pp. 121-127.

Gold, L.W., 1956. The strength of snow in compression. Journal of Glaciology, 2 (20), PP. 719-725.

Gubler, H., 1992. Mesures et modelistation pour ameliorier notre comprehension des mecanismes de formation des avalanches. La meteorologie, 7 (45), pp. 24-31.

Greene, E., K. Birkeland, K. Elder, G. Johnson, C. Landry, I. McCammon, M. Moore, D. Sharaf, C. Sterbenz, B. Tremper, K. Williams, 2004. Snow, Weather, and Avalanches: Observational Guidelines for Avalanche Programs in the United States. American Avalanche Association, Pagosa Springs, USA.

Haefeli, R., 1967. Some mechanical aspects on the formation of avalanches. Institute of Low Temperature Science, Hokkaido University, Japan, 1 (2), pp. 1199-1213.

Heierli, J., submitted. Crack propagation in a metastable snowpack as a solitary wave phenomenon. Journal of Geophysical Research.

Hägeli, P., D. M. McClung, 2003. Avalanche characteristics of a transitional snow climate - Columbia Mountains, British Columbia, Canada. Cold Regions Science and Technology, 37 (3), pp. 255-276.

van Herwijnen, A., J.B. Jamieson, 2002. Interpreting fracture characture in stability tests. Proceedings of 2002 International Snow Science Workshop, Penticton, British Columbia, Canada, pp. 514-520.

van Herwijnen, A., J.B. Jamieson, 2003. An update on fracture character in stability tests. Avalanche News, 66, Canadian Avalanche Association, Revelstoke, Canada, pp. 26-28.

Hornak, J.P., 2002. Encyclopedia of Imaging Science and Technology, Volume 1. Wiley Interscience Publication, New-York, USA, 759 pp.

Jamieson, J.B, 1995. Avalanche prediction for persistent snow slabs. PhD Thesis, University of Calgary, 255 pp.

Jamieson, J.B., 1999. The compression test - after 25 years. The Avalanche Review, 18 (1), pp. 10-12.

Jamieson, J.B., 2001. Snow avalanches. A synthesis of geological hazards in Canada, Bulletin 548, Geological Survey of Canada, pp. 81-100.

Jamieson, J.B., 2003. Fracture propagation and resistance in weak snowpack layers. Avalanche News, 67, Canadian Avalanche Association, Revelstoke, Canada, pp. 36-43.

Jamieson, J.B., 2004. Between a slab and a hard layer: Part 1 - Formation of poorly bonded crusts in the Columbia Mountains. Avalanche News 70, Canadian Avalanche Association, Revelstoke, Canada, pp. 48-54.

Jamieson, J.B., T. Geldsetzer, 1996. Avalanche Accidents in Canada. Volume 4, 1984-1996. Canadian Avalanche Association, Revelstoke, 193 pp.

Jamieson, J.B., C.D. Johnston, 1990. In-situ tensilte tests of snow-pack layers. Journal of Glaciology, 36 (122), pp. 102-106.

Jamieson, J.B., C.D. Johnston, 1992a. Snowpack characteristics associated with avalanche accidents. Canadian Geotechnical Journal 29, pp. 862-866.

Jamieson, J.B., C.D. Johnston, 1992b. A fracture-arrest model for unconfined dry slab avalanches. Canadian Geotechnical Journal 29, pp. 61-66.

Jamieson, J.B., C.D. Johnston, 1998. Snowpack characteristics for skier triggering. Avalanche News, 55, Canadian Avalanche Association, Revelstoke, Canada, pp. 31-39.

Jamieson, J.B., C.D. Johnston, 2001. Evaluation of the shear frame test for weak snowpack layers. Annals of Glaciology, 32, pp. 59-69.

Jamieson, J.B., J. Schweizer, 2000. Texture and strength changes of buried surface-hoar layers with implications for dry snow-slab avalanche release. Journal of Glaciology, 46 (152), pp. 151-160.

Jamieson, J.B., J. Schweizer, 2005. Using a checklist to assess manual snow profiles. Avalanche News, 72, Canadian Avalanche Association, Revelstoke, Canada.

Jamieson, J.B., T. Geldsetzer, C. Stethem, 2001. Forecasting for deep slab avalanches. Cold Regions Science and Technology, 33 (2-3), pp. 275-290.

Johnson, B., 2000. Remotely triggered slab avalanches. MSc. Thesis, University of Calgary, 98 pp.

Johnson, B.C., J.B. Jamieson, C.D. Johnston, 2000a. Field studies using the cantilever beam test. The Avalanche Review 18 (6), pp. 8-9.

Johnson, B.C., J.B. Jamieson, C.D. Johnston, 2000b. Field data and theory for human triggered whumpfs and remote avalanches. Proceedings of the 2000 International Snow Science Workshop, Big Sky, Montana, USA, pp. 208-214.

Johnson, B.C., J.B. Jamieson, R.R. Stewart, 2004. Seismic measurement of fracture speed in a weak snowpack layer. Cold Regions Science and Technology, 40 (1-2), pp. 41-45.

Johnson, G.T., 2000. Observations of faceted crystals in alpine snowpacks. MSc. Thesis, Department of Civil Engineering, University of Calgary, Calgary, Canada.

Johnson, R.F., K.W. Birkeland, 2002. Integrating shear quality into stability test results. Proceedings of 2002 International Snow Science Workshop, Penticton, British Columbia, Canada, pp. 514-520.

Keeler, C.M., W.F. Weeks, 1968. Investigation into the mechanical properties of alpine snow-packs. Journal of Glaciology, 7 (50), pp. 253-271.

Kezdi, A., 1974. Handbook of Soil Mechanics. Elsevier Scientific Publishing, New York, USA, 294 pp.

Kirchner, H.O.K., G. Michot, T. Suzuki, 2000. Fracture toughness of snow in tension. Philosophical Magazine A, 80 (5), pp. 1265-1272.

Kirchner, H.O.K., G. Michot, H. Narita, T. Suzuki, 2001. Snow as a foam of ice: plasticity, fracture and the brittle to ductile transition. Philosophical Magazine A, 81 (9), pp. 2161-2181.

Kirchner, H.O.K., G. Michot, J. Schweizer, 2002. Fracture toughness of snow in shear and tension. Scripta Materialia, 46, pp. 425-429.

Kolsky, H., 1963. Stress Waves in Solids. Dover Publications, New York, USA, 213 pp.

Lackinger, B., 1989. Supporting forces and stability of snow slab avalanches: a parameter study. Annals of Glaciology, 13, pp. 140-145.

Landry, C.C., J.J. Borkowski, R.L. Brown, 2001. Quantified loaded column stability test: mechanics, methodology, and preliminary trials. Proceedings of the 2000 International Snow Science Workshop, Big Sky, Montana, USA, pp. 230-237.

Louchet, F., 2001. A transition in dry-snow slab avalanche triggering modes. Annals of Glaciology, 32, pp. 285-289.

McCammon, I., J. Schweizer, 2002. A field method for identifying structural weaknesses in the snowpack. Proceedings of 2002 International Snow Science Workshop, Penticton, British Columbia, Canada, pp. 477-481.

McCammon, I., D. Sharaf, 2005. Integrating strength, energy and structure into stability decisions: So you dig a pit and then what? The Avalanche Review, 23 (3), pp. 18-19.

McClung, D.M., 1977. Direct simple shear tests on snow and their relation to slab avalanche formation. Journal of Glaciology, 19 (81), pp. 101-109.

McClung, D.M., 1979a. In-situ estimates of the tensile strength of snow utilizing large sample sizes. Journal of Glaciology, 22 (87), pp. 321-329.

McClung, D.M., 1979b. Shear fracture precipitated by strain softening as a mechanism of dry slab avalanche release. Journal of Geophysical Research, 84 (87), pp. 3519-3525.

McClung, D.M., 1981. Fracture mechanical models of dry slab avalanche release. Journal of Geophysical Research, 86 (B11), pp. 10783-10790.

McClung, D.M., 1987. Mechanism of snow slab failure from a geotechnical perspective. International Association of Hydrology Science Publication, 162, pp. 475-508.

McClung, D.M., P.A. Schaerer, 1993. The Avalanche Handbook. The Mountaineers, Seattle, 271 pp.

Mellor, M., 1975. A review of basic snow mechanics. International Association of Hydrological Sciences Pubilcation 114 (Symposium at Grindewald 1974 - Snow Mechanics), pp. 251-291.

Narita, H., 1980. Mechanical behaviour and structure of snow under uniaxial tensile strength. Journal of Glaciology, 26 (94), pp. 275-283.

National Research Council of Canada (NRCC), 1981, revised 1989. Guidelines for Weather, Snowpack and Avalanche Observations. Associate Committee on Geotechnical Research, National Research Council of Canada, Technical Memorandum 132.

Palmer, A.C., J.R. Rice, 1973. The growth of slip surfaces in the progressive failure of over-consolidated clay. Proceedings of the Royal Society London, Series A, 332, pp. 527-548.

Perla, R, 1969. Strength tests on newly fallen snow. Journal of Glaciology, 8 (54), pp. 427-440.

Perla, R., 1977. Slab avalanche measurements. Canadian Geotechnical Journal, 14 (2), pp. 206-213.

Perla, R., 1980. Avalanche release, motion and impact. Dynamics of Snow and Ice Masses, Academic Press, New York, pp. 397-464.

Perla, R.I., E.R. LaChapelle, 1970. A theory of snow slab failure. Journal of Glaciology, 75 (36), pp. 7619-7627.

Perla, R.L., R.A. Sommerfeld, 1987. On the metamorphism, morphology and microstructure of snow. Proceedings of the International Snow Science Workshop, Lake Tahoe, pp. 98-102.

Perla, R.L., T.M.H. Beck, T.T. Cheng, 1982. The shear strength index of alpine snow. Cold Regions Science and Technology, 6 (1), pp. 11-20.

Pratt, W.K., 2001. Digital Image Processing, third edition. Wiley, New York: 735 pp.

Roch, A., 1956. Mechanism of avalanche release. US Army, Snow Ice and Permafrost Research Establishment, Hanover, New Hampshire, Translation 52, 11 pp..

Roch, A., 1965. Les declenchements d'avalanches. Proceedings of the International Symposium on Scientific Aspects of Snow and Ice Avalanches, Davos, pp. 182-183.

Schweizer, J., 1993. The influence of the layered character of the snow cover on the trigering of slab avalanches. Annals of Glaciology, 18, pp. 193-198.

Schweizer, J., 1998. Laboratory experiments on shear failure of snow. Annals of Glaciology, 26, pp. 97-102.

Schweizer, J., 1999. Review of dry snow slab avalanche release. Cold Regions Science and Technology, 30, pp. 43-57.

Schweizer, J., C. Camponovo, 2001. The skier's zone of influence in triggering of slab avalanches. Annals of Glaciology, 32, pp. 314-320.

Schweizer, J., B. Jamieson, 2001. Snow cover properties for skier-triggered avalanches. Cold Regions Science and Technology, 33 (2-3), pp. 207-221.

Schweizer, J., B. Jamieson, 2003a. Contrasting stable and unstable snow profiles with resprect to skier loading. Proceedings of 2002 International Snow Science Workshop, Penticton, British Columbia, Canada, pp. 499-501.

Schweizer, J., B. Jamieson, 2003b. Snowpack properties for snow profile analysis. Cold Regions Science and Technology, 37 (3), pp. 233-241.

Schweizer, J., M. Lütschg, 2001. Characteristics of human-triggered avalanches. Cold Regions Science and Technology, 33 (2-3), pp. 147-162.

Schweizer, J., T. Wiesinger, 2001. Snow profile interpretation for stability evaluation. Cold Regions Science and Technology, 33 (2-3), pp. 179-188.

Schweizer, J., C. Fierz, J.B. Jamieson, in press. Assessing the probability of skier triggering from snow layer properties. Proceedings of 2004 International Snow Science Workshop in Jackson Hole, USA.

Schweizer, J., J.B. Jamieson, M. Schneebeli, 2003. Snow avalanche formation. Reviews of Geophysics, 41 (4), 1016.

Schweizer, J., Michot, G., Kirchner, H.O.K., in press. On the fracture toughness of snow. Annals of Glaciology, 38.

Schweizer, J., C. Camponovo, C. Fierz, P.M.B. Föhn, 1995a. Skier triggered slab avalanche release-some practical implications. Proceedings of the International Symposium: Sciences and Mountain-The contribution of Scientific Research to Snow, Ice and Avalanche Safety, Chamonix, France, 30 May - 3 June. Association Nationale pour l'Etude de la Neige et des Avalanches (ANENA), Grenoble, France, pp. 309-316.

Schweizer, J., M Schneebeli, C. Fierz, P.M.B. Föhn, 1995b. Snow mechanics and avalanche formation: Field experiments on the dynamic response of the snow cover. Surveys in Geophysics, 16, pp. 621-633.

Shapiro, L.H., J.B. Johnson, M. Sturm, G.L. Blaisdell, 1997. Snow mechanics: review of the state of knowledge and applications. CRREL report, 97-3.

Singh, H., 1980. A finite element model for the prediction of dry-slab avalanches. PhD thesis, Colorado State University, 183 pp.

Sommerfeld, R.A., 1980. Statistical models of snow strength. Journal of Glaciology, 26 (94), pp. 217-223.

Sorge, E., 1933. The scientific results of the Wegener expeditions to Greenland. The Geophysical Journal, LXXXI (4), pp. 333-334.

Stethem, C., R. Perla, 1980. Snow-slab studies at Whistler Mountain, British Columbia, Canada. Journal of Glaciology, 26 (94), pp. 85-91.

Stewart, R.R., 1985. Median filtering: Review and a new f/k analogue design. Journal of the Canadian Society of Exploration Geophysics, 21 (1), pp. 54-63.

Stewart, K.W., 2002. Spatial variability of slab stability within avalanche start zones. MSc. Thesis, Dept. of Geology and Geophysics, University of Calgary, Calgary, Canada.

Truman, 1973. Wave propagation in snow. American Journal of Physics, 41 (2), pp. 282-283.

Walpole, R. E., R.H. Myers, S.L. Myers, K. Ye, 2002. Probability and Statistics for Engineers and Scientists, Seventh Edition. Prentice Hall, Upper Saddle River, USA, 730 pp.

Wei, Y., M. Adamson, J.P. Dempsey, 1996. Ice/metal interface: fracture energy and fractography. Journal of Materials Science, 31, pp. 943-947.

Appendix A - High-speed photography displacement measurements

A.1 Introduction

In this appendix, displacement measurements of markers placed above fracturing weak layers are shown. The seven-point moving average filtered data are shown. Tests that were described in Chapter 6 are not shown. The markers are numbered down-slope, starting with the uppermost marker in the video frame. Both the slope parallel (Δx) and the slope normal (Δy) displacement curves are shown. The error bars indicate the measurement uncertainty, calculated as the standard deviation in the initial position (Section 6.2.3).

A.2 Compression tests

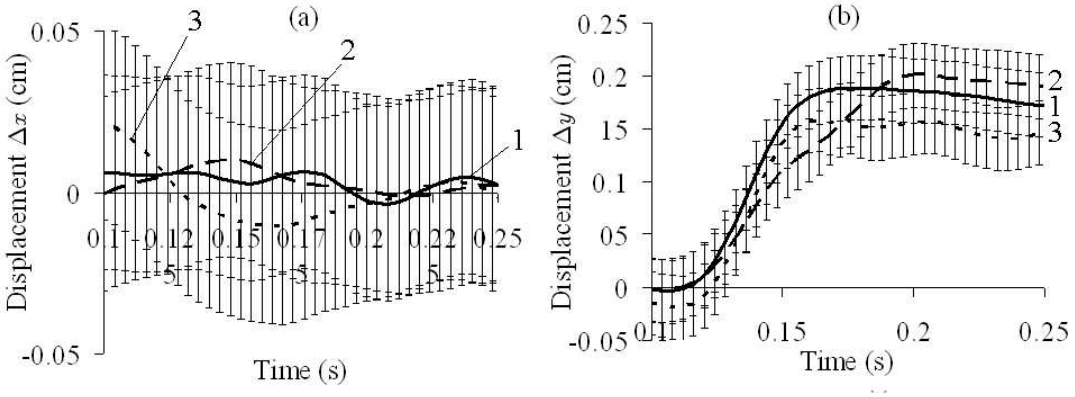

Figure A.1: *Compression test CTA. (a) Slope parallel displacement. (b) Slope normal displacement. The accuracy of the displacement measurements for this test was 0.03 cm.*

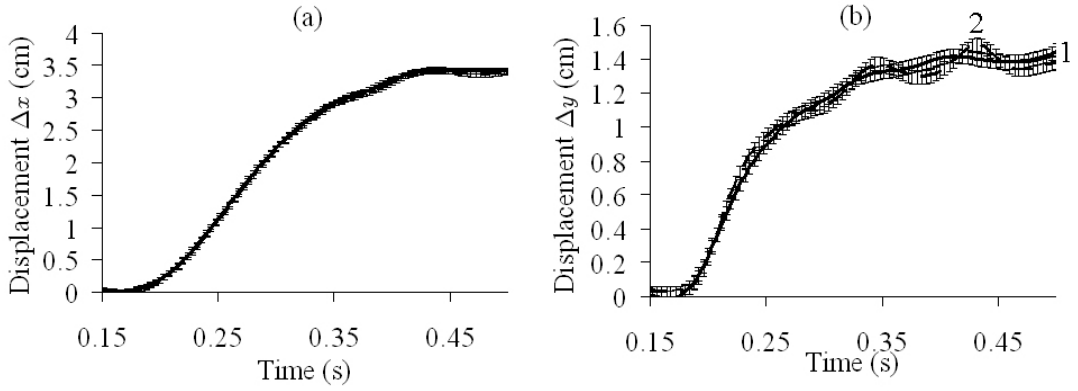

Figure A.2: *Compression test CTB. (a) Slope parallel displacement. (b) Slope normal displacement. The accuracy of the displacement measurements for this test was 0.02 cm.*

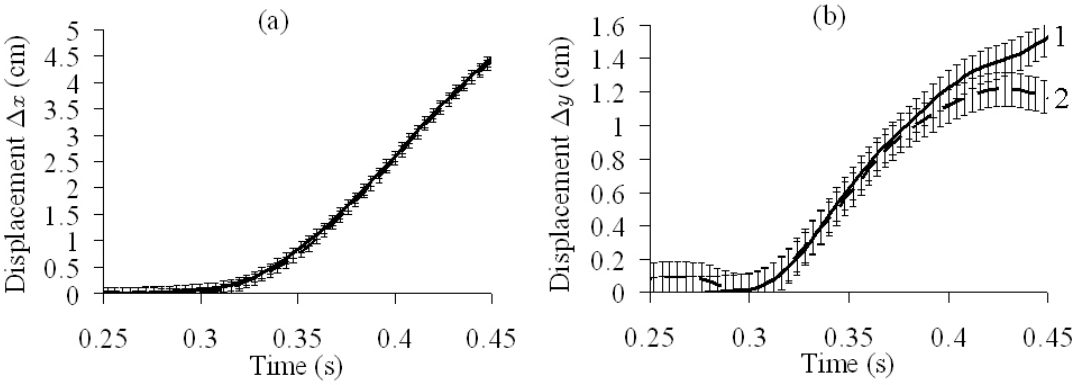

Figure A.3: *Compression test CTD. (a) Slope parallel displacement. (b) Slope normal displacement. The accuracy of the displacement measurements for this test was 0.1 cm.*

A.3 Cantilever beam test

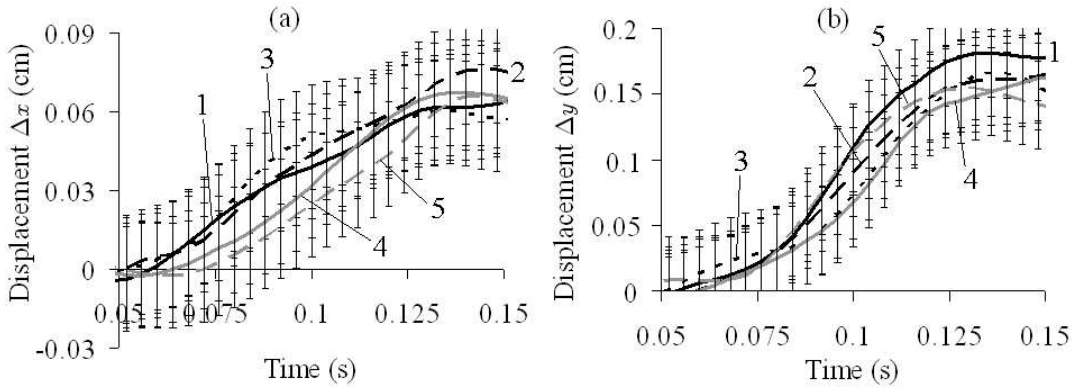

Figure A.4: *Cantilever beam test CBB. (a) Slope parallel displacement. (b) Slope normal displacement. The accuracy of the displacement measurements for this test was 0.02 cm.*

A.4 Rutschblock tests

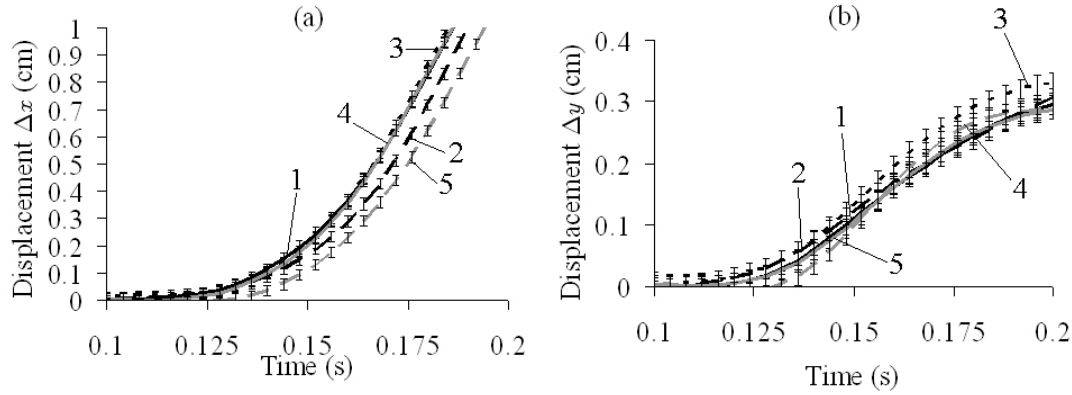

Figure A.5: *Rutschblock test RBA. (a) Slope parallel displacement. (b) Slope normal displacement. The accuracy of the displacement measurements for this test was 0.03 cm.*

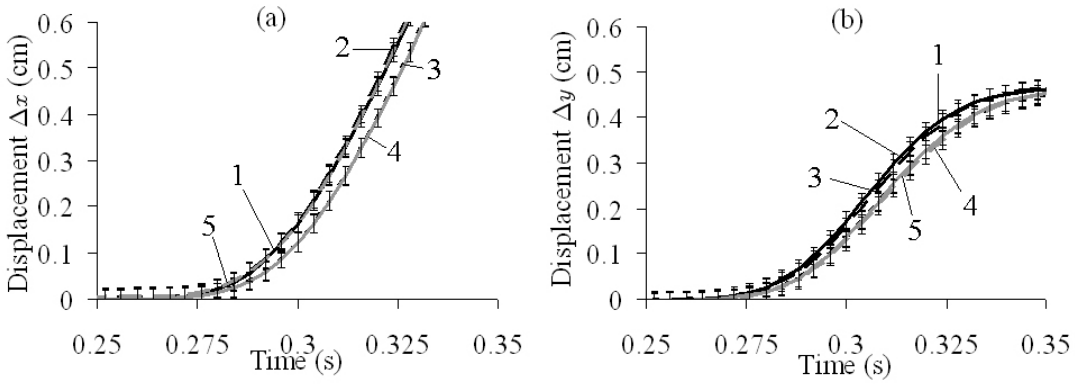

Figure A.6: *Rutschblock test RBB. (a) Slope parallel displacement. (b) Slope normal displacement. The accuracy of the displacement measurements for this test was 0.01 cm.*

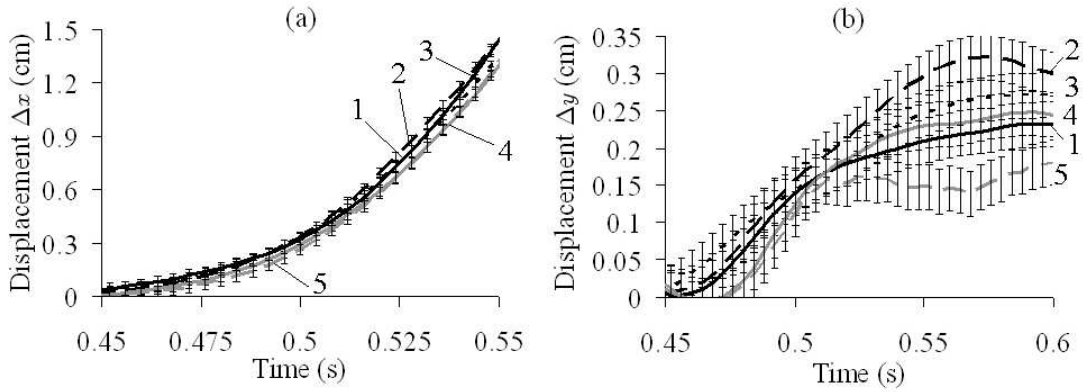

Figure A.7: *Rutschblock test RBC. (a) Slope parallel displacement. (b) Slope normal displacement. The accuracy of the displacement measurements for this test was 0.03 cm.*

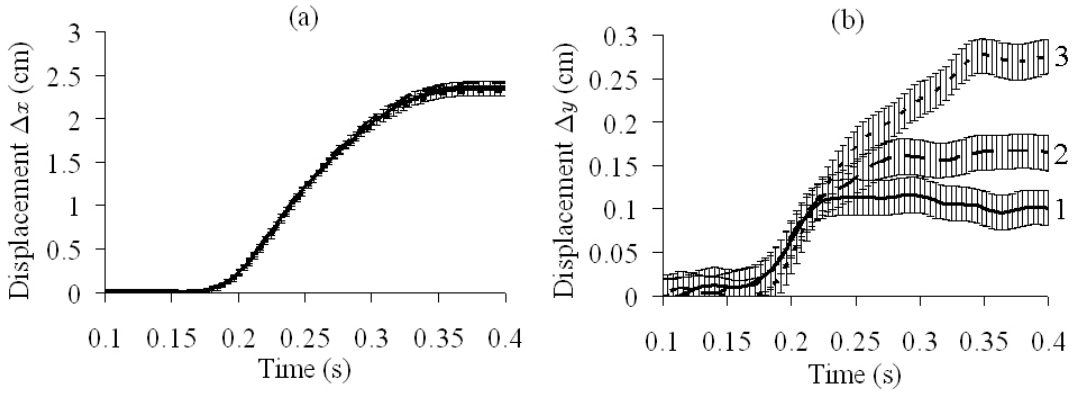

Figure A.8: *Rutschblock test RBE. (a) Slope parallel displacement. (b) Slope normal displacement. The accuracy of the displacement measurements for this test was 0.02 cm.*

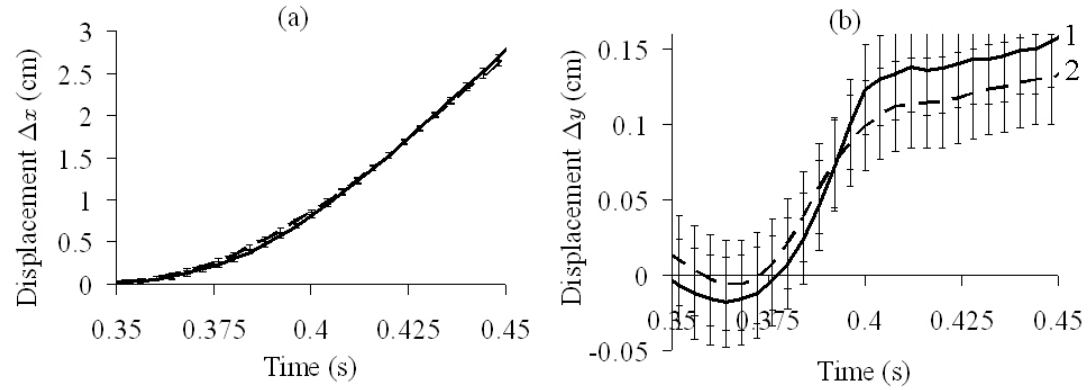

Figure A.9: *Rutschblock test RBF. (a) Slope parallel displacement. (b) Slope normal displacement. The accuracy of the displacement measurements for this test was 0.03 cm.*

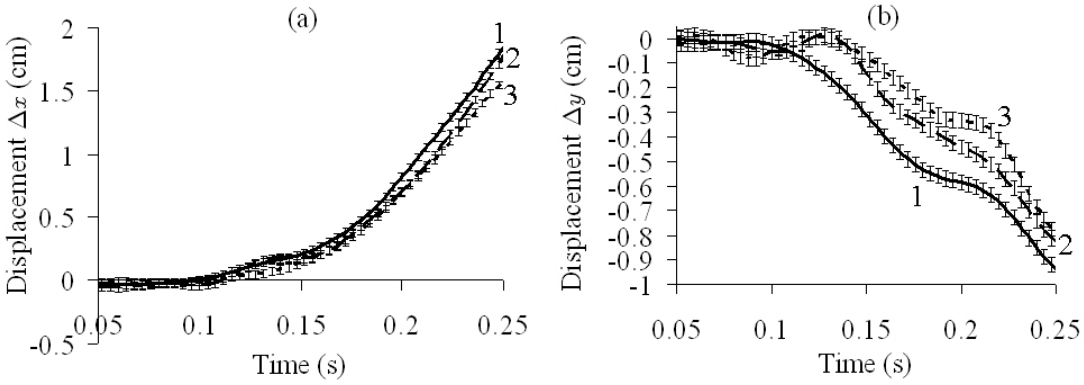

Figure A.10: *Rutschblock test RBG. (a) Slope parallel displacement. (b) Slope normal displacement. The accuracy of the displacement measurements for this test was 0.03 cm.*

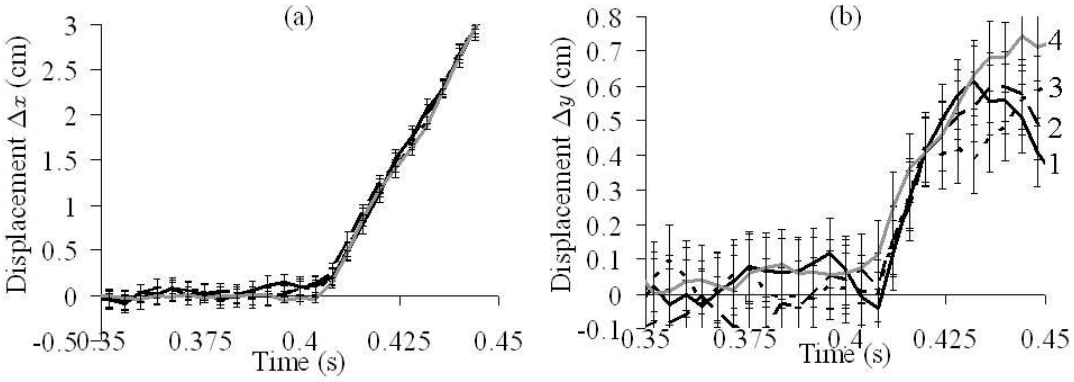

Figure A.11: *Rutschblock test RBH. (a) Slope parallel displacement. (b) Slope normal displacement. The accuracy of the displacement measurements for this test was 0.1 cm.*

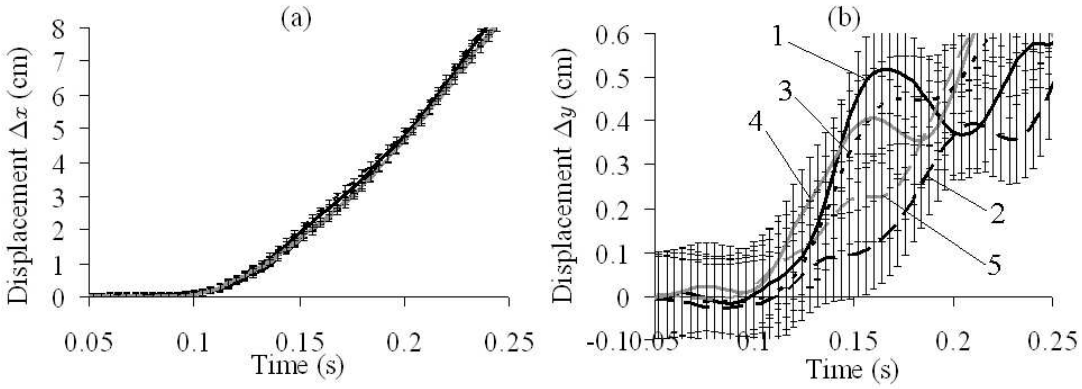

Figure A.12: *Rutschblock test RBI. (a) Slope parallel displacement. (b) Slope normal displacement. The accuracy of the displacement measurements for this test was 0.1 cm.*

A.5 Skier-tested slopes

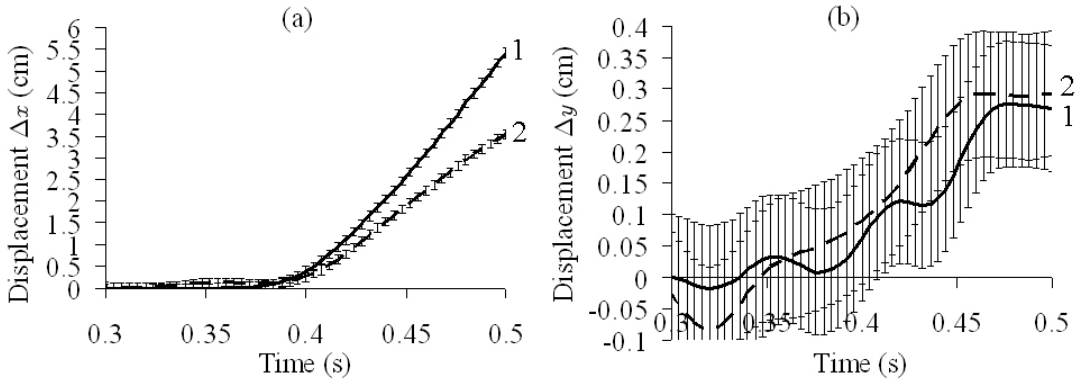

Figure A.13: *Skier-tested slope STB. (a) Slope parallel displacement. (b) Slope normal displacement. The accuracy of the displacement measurements for this test was 0.1 cm.*

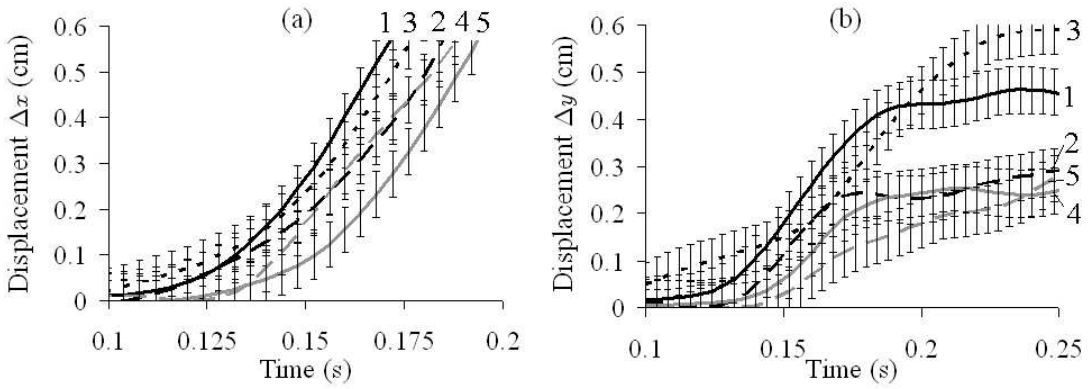

Figure A.14: *Skier-tested slope STD. (a) Slope parallel displacement. (b) Slope normal displacement. The accuracy of the displacement measurements for this test was 0.05 cm.*

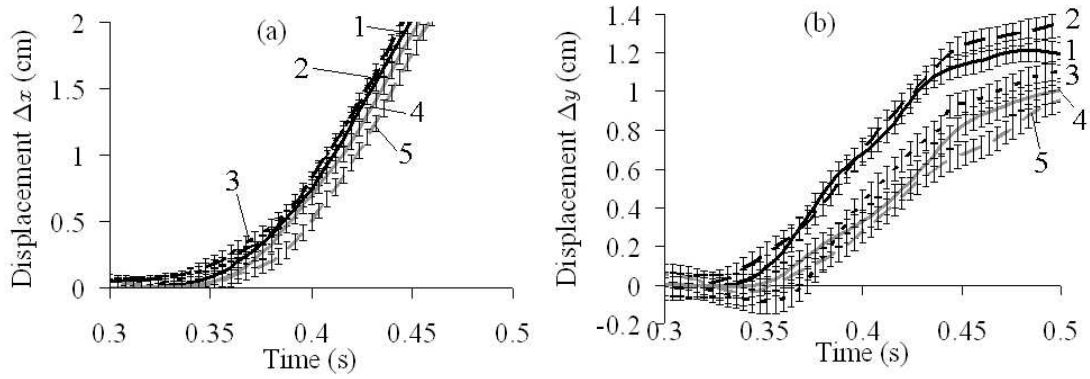

Figure A.15: *Skier-tested slope STE. (a) Slope parallel displacement. (b) Slope normal displacement. The accuracy of the displacement measurements for this test was 0.06 cm.*